

Hassan Ziad Jishi

The Fabrication and Mechanical Properties of Continuous Fiber Composite Lattice Structures

Doctoral Thesis / Dissertation

YOUR KNOWLEDGE HAS VALUE



- We will publish your bachelor's and master's thesis, essays and papers
- Your own eBook and book - sold worldwide in all relevant shops
- Earn money with each sale

Upload your text at www.GRIN.com
and publish for free



Bibliographic information published by the German National Library:

The German National Library lists this publication in the National Bibliography; detailed bibliographic data are available on the Internet at <http://dnb.dnb.de> .

This book is copyright material and must not be copied, reproduced, transferred, distributed, leased, licensed or publicly performed or used in any way except as specifically permitted in writing by the publishers, as allowed under the terms and conditions under which it was purchased or as strictly permitted by applicable copyright law. Any unauthorized distribution or use of this text may be a direct infringement of the author s and publisher s rights and those responsible may be liable in law accordingly.

Imprint:

Copyright © 2016 GRIN Verlag
ISBN: 9783668355910

This book at GRIN:

<https://www.grin.com/document/345395>

Hassan Ziad Jishi

The Fabrication and Mechanical Properties of Continuous Fiber Composite Lattice Structures

GRIN - Your knowledge has value

Since its foundation in 1998, GRIN has specialized in publishing academic texts by students, college teachers and other academics as e-book and printed book. The website www.grin.com is an ideal platform for presenting term papers, final papers, scientific essays, dissertations and specialist books.

Visit us on the internet:

<http://www.grin.com/>

<http://www.facebook.com/grincom>

http://www.twitter.com/grin_com

The Fabrication and Mechanical Properties of Continuous Fiber Composite Lattice Structures

Hassan Ziad Jishi

PhD. Thesis

May 2016



KHALIFA
UNIVERSITY

A thesis submitted to Khalifa University of Science, Technology and Research in accordance with the requirements of the degree of PhD in Engineering in the Department of Aerospace Engineering.

The Fabrication and Mechanical Properties of Continuous Fiber Composite Lattice Structures

by

Hassan Ziad Jishi

A thesis submitted in partial fulfillment of the
requirements for the degree of

**PhD in Engineering
(Aerospace Engineering)**

at

Khalifa University

Thesis Committee

Prof. Wesley J. Cantwell (Supervisor),
Khalifa University

Prof. Véronique Michaud (External
Examiner & Committee Chair),
*École Polytechnique Fédérale de
Lausanne (EPFL)*

Dr. Rehan Umer (Co-Supervisor)
Khalifa University

Dr. Kin Liao (Internal Examiner)
Khalifa University

May 2016



Abstract

Hassan Ziad Jishi, “**The Fabrication and Mechanical Properties of Continuous Fiber Composite Lattice Structures**”, PhD. Thesis, PhD in Engineering, Department of Aerospace Engineering, Khalifa University, United Arab Emirates, May 2016.

The primary aim of this research work is to examine the mechanical properties per weight density of novel core materials for use in sandwich panels. Composite lattice core sandwich structures with relative densities in the range of 3% to 35% were manufactured and tested under quasi-static compression loading conditions. Collapse strength, failure mechanisms and energy absorption characteristics of the lattice structures have been evaluated.

Since these core material shapes are unique, research involved developing suitable manufacturing methods. The study started by looking at introducing ‘simple through thickness lattice’ structure into PET foam cores. This was achieved by drilling the foam material, glass fibers were then inserted into the perforations. The panel was then infused with resin using the vacuum assisted resin transfer molding process. This was then extended to look at the possibility of removing the ‘core’ by adopting a-lost mold manufacturing procedure that would leave a free-standing lattice structure. This involved inserting reinforcing fiber tows through holes in wax blocks. Following infusion with an epoxy resin and subsequent post curing, the preforms were heated to a temperature above

that required to melt the wax, leaving well-defined lattice structures based on vertical, pyramidal, modified-pyramidal, octet configurations and others based on what are termed BCC, BCCz, FCC and F₂BCC designs.

Compression tests showed that the strength of individual struts and the corresponding cores increases with strut diameter and fiber volume fraction. Smaller diameter struts failed in buckling, whereas the larger diameter columns failed in a crushing mode involving high levels of energy absorption. Truss core structures with 4 mm diameter columns, based on 28% fiber volume fractions offered specific energy absorption values above 70 kJ/kg.

Compression tests on the four lattice structures based on BCC, BCCz, FCC and F₂BCC designs indicated that the F₂BCC lattice offered the highest compression strength of approximately 12 MPa. Although, when normalized by relative density, the BCCz lattice structure out-performed the three remaining structures. The specific energy absorption values of the lattices were relatively high, ranging from 44 kJ/kg for the BCC lattice to 80 kJ/kg for the BCCz structure. Similarly, the specific compression strengths of some of the lattices have been shown to be superior to those of more traditional core materials. An examination of the samples during testing highlighted a number of failure mechanisms, including strut buckling, fracture at the strut-skin joints and debonding of the reinforcing members at the central nodes.

The compression strength properties of the various lattice structures have been compared to currently available engineering materials, where it is noted that the properties of these lattice structures can be further increased using higher fiber volume fractions.

Micromechanical based analytical expressions for predicting the through thickness elastic properties and compression collapse strengths of all lattice structures manufactured using the lost mold technique are presented. Finally, the properties of the various lattice structures considered here were also predicted using finite element modeling techniques for comparison with analytical calculations and experimental results. The finite element predictions showed excellent agreement with the analytical calculations which validate the analytical derivations.

Indexing Terms: Lattice structures, Sandwich structures, Mechanical properties, Resin infusion, Finite Element, Composites, VARTM, Unidirectional fiber.

Acknowledgements

A special word of thanks goes to my family for their continuous support and encouragement. My father Ziad Jishi, May God give him mercy, would have been extremely proud of what I have accomplished. My mother, Laila Arslan has been very encouraging and proud and of course, this work would not have been possible without the help and patience of my wife Laila Othmane. I was also fortunate enough to be blessed with two daughters, Eleen and Mila during the period of this work.

I also would like to acknowledge my advisors Prof. Wesley J. Cantwell and Dr. Rehan. Umer for their help, support and outstanding guidance. I thank Jimmy Thomas and Bitu Scaria for their help in preparing the test specimens. Thanks to Dr. Zuheir Barsoum for his assistance in running the FE simulations.

Last but not least, the research carried out was made possible by Mubadala Aerospace and Khalifa University through funding the Aerospace Research and Innovation Center and by Khalifa University for providing a full PhD scholarship.

Declaration and Copy Right

I declare that the work in this thesis was carried out in accordance with the regulations of Khalifa University of Science, Technology and Research. The work is entirely my own except where indicated by special reference in the text. Any views expressed in the thesis are those of the author and in no way represent those of Khalifa University of Science, Technology and Research. No part of the thesis has been presented to any other university for any degree.

Author Name: Hassan Ziad Jishi

Author Signature: Hassan Ziad Jishi

Date: 25 May 2016

Copyright ©

No part of this thesis may be reproduced, stored in a retrieval system, or transmitted, in any form or by any means, electronic, mechanical, photocopying, recording, scanning or otherwise, without prior written permission of the author. The thesis may be made available for consultation in Khalifa University of Science, Technology, and Research Library and for inter-library lending for use in another library and may be copied in full or in part for any bona fide library or research worker, on the understanding that users are made aware of their obligations under copyright, i.e. that no quotation and no information derived from it may be published without the author's prior consent.

List of publications

Published papers:

1. H. Z. Jishi, R. Umer and W. J. Cantwell, Skin-core debonding in resin-infused sandwich structures, Polymer Composites, 2015.
2. H. Z. Jishi, R. Umer and W. J. Cantwell, The fabrication and mechanical properties of novel composite lattice structures, Materials & Design, vol. 91, pp.286-293, 2016.

Under review:

1. H. Z. Jishi, R. Umer, K. Ushijima and W. J. Cantwell, The mechanical properties of composite lattice structures. Submitted to Journal of Composite Structures, 2016.

In preparation for submission:

1. H. Z. Jishi, F. Almehairi, R. Umer and W. J. Cantwell, A lost mold technique for manufacturing novel lattice structures based on natural fibers.
2. H. Z. Jishi, R. Umer, Z. Barsoum and W. J. Cantwell, Numerical simulation of continuous fibers composite lattice structures.

Published conference papers:

1. H. Z. Jishi, R. Umer, Z. Barsoum and W. J. Cantwell, The mechanical properties of sandwich structures based on composite column cores, in the 20th International Conference on Composite Materials (ICCM20), Copenhagen, Denmark, 2015.

2. H. Jishi, R. Umer and W.J. Cantwell, Investigation of Skin-Core Adhesion in Resin Infused Sandwich Panels, 12th International conference on Flow Processes in Composite Materials (FPCM12), Enschede, The Netherlands, 2014.

Contents

Abstract	iii
Acknowledgements	vi
Declaration and Copy Right	vii
List of publications	viii
Contents	x
List of Figures	xiv
List of Tables	xxviii
Nomenclature	xxix
Chapter 1: Introduction	1
1.1 Overview	1
1.2 Thesis Objective	4
1.3 Thesis Outline	4
1.4 Sandwich Panel Design Concept	6
1.5 Cellular materials	7
1.5.1 Stochastic cellular materials	8
1.5.2 Periodic cellular materials	15
1.6 Manufacture	38
1.6.1 Autoclave molding	39
1.6.2 Filament winding	40
1.6.3 Resin transfer molding	40
1.7 Vacuum Assisted Resin Transfer Molding (VARTM) process	44
1.7.1 Variations of the VARTM process	45
1.7.2 VARTM process and quality of composite	49
1.8 Elastic and strength properties of composite materials	54
1.8.1 Elastic properties of composite materials	54
1.8.2 Strength properties of composite materials	54
References	64
Chapter 2: Experimental procedures	75
2.1 Introduction	75

2.2	Lattice fabrication	76
2.2.1	Consumable materials	76
2.2.2	Constituent materials.....	77
2.2.3	Preparation Process	79
2.2.4	Infusion Process	82
2.2.5	Post infusion process.....	84
2.3	Hybrid core sandwich panel studies.....	85
2.3.1	Overview	85
2.3.2	Materials and Manufacturing	86
2.3.3	Compression tests	90
2.3.4	Interfacial fracture tests.....	91
2.4	Vertical, pyramidal, and octet lattice studies	95
2.4.1	Overview	95
2.4.2	Materials and fabrication.....	95
2.4.3	Compression tests	99
2.5	BCC, BCCz, FCC and F ₂ BCC lattice studies	100
2.5.1	Overview	100
2.5.2	Materials and fabrication.....	100
2.5.3	Compression tests	103
2.6	Other lattice structures	103
	References	104
Chapter 3: Analytical Modeling.....		105
3.1	Introduction	105
3.2	Elastic properties of parent material	105
3.3	Elastic values.....	113
3.4	Strength values	115
3.5	Analytical model of the compressive response	116
3.5.1	Analytical predictions for the response of composite pyramidal truss core	116
3.5.2	Analytical predictions of the vertical column core response	125
3.5.3	Analytical predictions for the response of the modified pyramidal truss core	130
3.5.4	Summary	137
3.5.5	Analytical predictions of the response of the octahedral lattice core.....	138

3.5.6	Analytical predictions of the response of the BCC core	141
3.5.7	Analytical predictions of the response of the FCC core	146
3.5.8	Analytical predictions of the response of the BCCz core	149
3.5.9	Analytical predictions of the response of the F ₂ BCC core	156
	References	159
Chapter 4: Finite Element Analysis.....		161
4.1	Introduction	161
4.2	ANSYS FE package	161
4.3	Constitutive models for the composite material.....	162
4.3.1	Elastic response.....	163
4.3.2	Damage initiation & progression model for the fiber reinforced composites 164	
4.4	Quasi-static Finite element modelling	167
4.4.1	Modelling of lattice core sandwich structures	167
4.5	Numerical analysis results.....	178
4.5.1	Vertical lattice	178
4.5.2	Pyramidal lattice.....	180
4.5.3	Modified pyramidal lattice.....	182
4.5.4	BCC lattice.....	185
4.5.5	BCCz lattice	188
4.5.6	FCC lattice	190
4.5.7	F ₂ BCC lattice	192
4.6	Conclusions	196
	References	197
Chapter 5: Results and Discussion.....		198
5.1	Introduction	198
5.2	Resin flow and post-manufacture visual assessment	198
5.2.1	Hybrid GFRP/PET core	198
5.2.2	Vertical, pyramidal and octet lattice	201
5.2.3	BCC, BCCz, FCC and F ₂ BCC lattice	205
5.3	Compression tests.....	206
5.3.1	Hybrid GFRP/PET core	206
5.3.2	Vertical, pyramidal and octet lattice	208

5.3.3	BCC, BCCz, FCC and F ₂ BCC lattice	230
5.4	Skin-core Interfacial fracture toughness	241
5.4.1	Hybrid GFRP/PET core	241
	References	249
Chapter 6:	Conclusions and Future Work.....	251
6.1	Introduction	251
6.2	Conclusions	251
6.3	Recommended future work	255
	References	258
Appendix A		259
Appendix B		260
Appendix C		261

List of Figures

Figure 1.1: Materials used in the Boeing 787 [2].....	2
Figure 1.2: Modified Ashby materials property charts for (a) Young’s modulus and (b) Compression strength for engineering materials [10]. Composite lattice structures could fill the gap area in the low density – high stiffness and strength region.....	3
Figure 1.3: Cellular materials in nature: (a) cork, (b) balsa wood, (c) sponge, and.....	8
Figure 1.4: Three dimensional cellular material (a) open-cell polyurethane (b) closed-cell polyethylene [13].	9
Figure 1.5: Schematic diagram of an idealized cell representative of an open-cell foam [13].	10
Figure 1.6: Unit cell edges undergoing bending due to an applied compressive force [13].	11
Figure 1.7: Typical compressive stress-strain trace of a bending-dominated foam structure [19].....	12
Figure 1.8: (a) $M < 0$, if the joints are rigid the configuration becomes a bending dominated structure, (b) $M = 0$, stretch dominated structure and (c) $M > 0$, over constrained structure [19].....	14
Figure 1.9: Cellular material topologies [10, 24].....	15
Figure 1.10: Hexagonal honeycombs manufactured using an expansion process [24]	17
Figure 1.11: Elastic and shear modulus of hexagonal honeycombs and open cell foams vs. relative density [15].....	18

Figure 1.12: Schematic diagram of the slotting procedure for creating prismatic cores [26].	19
Figure 1.13: Sandwich panels based on 3D Kagome' trusses metallic lattice structures [10].	20
Figure 1.14: Tetrahedral truss structures created through a metal forming technique [24].	21
Figure 1.15: Sandwich panels based on tetrahedral trusses metallic lattice structures with a unit cell size of 10 mm [10].	22
Figure 1.16: Sandwich structures based on copper textile cores configured at (a) $0/90^\circ$ and (b) $\pm 45^\circ$ orientations [24].	23
Figure 1.17: A Non-weave approach for manufacturing cellular core structures from solid wires or hollow tubes [24].	24
Figure 1.18: (a) Pyramidal lattice structure fabricated using the hot press mold and (b) adhesively bonded between skins to for the sandwich panel [30].	25
Figure 1.19: a) Truss member are water jet cut from laminate sheets, b) truss members are snap-fitted together forming the pyramidal lattice configuration. c) The truss were fitted and adhesively bonded in milled facesheet pockets [31].	25
Figure 1.20: An Ashby strength versus density map for engineering materials [31]	26
Figure 1.21: Schematic diagram illustrating the manufacturing procedure of the stretch–bend-hybrid hierarchical composite pyramidal lattice cores [34].	27
Figure 1.22: Stretch-stretch-hybrid hierarchical composite pyramidal lattice cores [35].	27
Figure 1.23: a) Manufactured Lattice core based on carbon fiber reinforced poly-ethylene terephthalate (CPET). b) Sandwich panel with a lattice truss core bonded to stringer reinforced face sheets [32].	28

Figure 1.24: EDM Pyramidal carbon fiber reinforced epoxy lattices having a core relative density of 4.95% [34].	29
Figure 1.25: Finished semi-WBK composite core [36].	29
Figure 1.26: a) The hybrid CFRP pyramidal lattice core sandwich panel assembly, b) Photograph of manufactured sample and c) x-ray image showing the interior core structure of the panel [37].	30
Figure 1.27: a) Unit cell of an octahedral lattice configuration. b) Stress-strain curve of a stretch dominated structure [19].	31
Figure 1.28: Variation of relative modulus with relative density for various cellular materials. The line of slope 1 represents stretch-dominated structures, while slope 2 corresponds to bending-dominated materials [19].	32
Figure 1.29: Variation of relative strength with relative density for various cellular materials. Stretch dominated structures lie along a trajectory of slope 1; bending dominated structures along line of slope 2 [19].	34
Figure 1.30: layup assembly for autoclave molding of composite laminates [2].	39
Figure 1.31: Schematic of filament winding process [48].	40
Figure 1.32: Schematic of the RTM process [2].	41
Figure 1.33: Schematic of VARTM process [48].	42
Figure 1.34: Aerospace components manufactured using the VARTM process [61].	45
Figure 1.35: Schematic of a typical SCRIMP process [64].	47
Figure 1.36: Schematic of the VAP setup [61].	48
Figure 1.37: Schematic of the CAPRI setup and processing steps [61].	48
Figure 1.38: Schematic of compaction pressure variation during VARTM infusion [51].	52

Figure 1.39: Matrix splitting (brooming).....	56
Figure 1.40: a) Initial buckling of fibers, b) development of cracks on the lower edge and c) a fully-formed kink band [83].....	57
Figure 1.41: Elastic micro-buckling modes: (a) Initial configuration (b) Shear mode and (c) Extensional mode.....	58
Figure 1.42: a) Kink band geometry and b) kink band failure in unidirectional carbon-epoxy composite [88].....	60
Figure 2.1: Four lattice structures (progressing from simple to complex) that have been manufactured. (a) Vertical column, (b) modified pyramidal truss, (c) BCCz lattice and (d) an octet structure.	80
Figure 2.2: (a) Wax block showing threading pattern of carbon fiber (b) Perforated PET foam core with holes reinforced with glass fibers.	81
Figure 2.3: Threaded samples showing fibers extending over the skins through the holes.	82
Figure 2.4: Perforated foam core with holes reinforced with glass fiber tows.	82
Figure 2.5: Photograph illustrating laboratory set-up of the VARTM infusion process.	83
Figure 2.6: Schematic of the VARTM process used to infuse the skins and core.....	84
Figure 2.7: Summary of the step-by-step procedures used in the VARTM process and lost mold technique.....	84
Figure 2.8: Hybrid composite core structure consisting of a unidirectional GRFP lattice with PET foam configured as the core of a sandwich panel with glass fiber composite face sheets.....	85
Figure 2.9: (a) Materials B and D unit cell with vertical truss arranged in a 25.4mm square pattern (b) Materials C and E with truss positioned in a 12.7mm square pattern.....	86

Figure 2.10: (a) Schematic of the configuration of sandwich panels investigated in this study. (b) Schematic of the patterns for the through-thickness fiber reinforcement in (i) Materials D and E and (ii) Material F.	88
Figure 2.11: Schematic of the VARTM manufacturing set-up.	89
Figure 2.12: Stacking procedure completed in preparation for vacuum bagging and infusion.	90
Figure 2.13: The hybrid core under compression loading.	91
Figure 2.14: Schematic of the three point bend test used to characterize the interfacial fracture toughness of the sandwich structures.	92
Figure 2.15: Plot of compliance against the cube of crack length of the specimen from (a) Material B, (b) Material C.	93
Figure 2.16: Schematic diagram showing the locations of the 2, 2.5, 3, and 4 mm diameter holes in the test samples. The edge lengths of the squares is nominally 30 mm. All dimensions are in mm.	96
Figure 2.17: Schematic drawings of the two procedures used to thread the samples.	96
Figure 2.18: Schematic of the VARTM process used to infuse the skins and core.	97
Figure 2.19: Idealized images of (a) a pyramidal structure and (b) a modified pyramidal structure, reinforced with a central vertical member.	98
Figure 2.20: Computer generated image of an octet truss structure.	99
Figure 2.21: Schematic of the compression test used to characterize the axial strength of the manufactured core structure.	99
Figure 2.22: Schematic of the unit cell topologies: (a) the BCC unit cell and (b) the BCCz unit cell (c) the FCC unit cell and (d) the F ₂ BCC lattice.	101

Figure 2.23: (a) Schematic drawings of the procedure used to thread the samples. The fibers extend through the holes and then between the wax core and the skins. (b) Threaded samples showing fibers extending over the skins through the holes.	102
Figure 2.24. Schematic of the VARTM process used to infuse the lattice structures.....	103
Figure 3.1: Unidirectional fiber-reinforced composite [1].....	106
Figure 3.2: Randomly distributed fibers in the cross-section of a strut with $V_f=51\%$	108
Figure 3.3: Fiber tows through the core oriented at an angle.	111
Figure 3.4: Estimated longitudinal modulus for materials having various fiber volume fractions. Experimental results are based on the 3-point bend test performed on rods having circular cross-sections.	114
Figure 3.5: Schematic of a unit cell of the 4-legged pyramidal core.	116
Figure 3.6: Schematic of (a) unit cell (b) deflection of a single truss of the pyramidal core upon application of a uniaxial compressive load (c) the free-body diagram of a truss subjected to compression and shear.	118
Figure 3.7: Schematic diagram of a vertical column core	125
Figure 3.8: Schematic of (a) unit cell (b) deflection of single column within the core upon application of a uniaxial compressive load.	127
Figure 3.9: Sketch of a unit cell of the 4-legged pyramidal core.....	130
Figure 3.10: Schematic of (a) unit cell (b) deflection of a single inclined truss and the vertical truss of the pyramidal core upon application of a uniaxial compressive load (c) the free-body diagram of a truss subjected compression and shear.....	132
Figure 3.11: Structure of an octahedral lattice core. The red struts represent the octahedron core.....	138

Figure 3.12: Schematic of a BCC unit cell.	141
Figure 3.13: Schematic showing (a) deflection of a BCC cell upon application of a uniaxial compressive load (b) the free-body diagram of a strut subjected to compression and shear (c) due to symmetry the BCC resembles the pyramidal lattice unit cell.....	142
Figure 3.14: Schematic of a FCC unit cell.....	146
Figure 3.15: Schematic of a BCC-z unit cell.	149
Figure 3.16: Schematic showing (a) deflection of a BCCz core upon application of a uniaxial compressive load (b) the free-body diagram of a strut subjected to compression and shear (c) the free-body diagram of half a vertical strut subjected.	150
Figure 3.17: Schematic of a F_2 BCC unit cell.....	156
Figure 4.1: Single strut illustrating fiber orientation.....	163
Figure 4.2: BEAM188 element geometry [8]	168
Figure 4.3: Loading direction, boundary conditions and assembly of the pyramidal lattice core.....	169
Figure 4.4: The FE mesh for the BCC unit cell.	170
Figure 4.5: Typical mesh generated for the numerical analysis.....	171
Figure 4.6: Failure stress and CPU time are plotted against element size for the pyramidal pin-jointed lattice core having a strut diameter of 3 mm and a $V_f = 0.06$	172
Figure 4.7: Failure stress and CPU time are plotted against element size for the F_2 BCC lattice.....	173
Figure 4.8: Failure stress and CPU time are plotted against step size for the end-clamped pyramidal lattice core.....	174

Figure 4.9: The failure stress and CPU time are plotted against step size for the F_2BCC lattice.	175
Figure 4.10: An imperfection sensitivity analysis study for the pyramidal lattice model.	177
Figure 4.11: An imperfection sensitivity analysis study for the $BCCz$ lattice model.	178
Figure 4.12: Numerical and micro-mechanical predictions of the elastic modulus of the vertical lattice core.	179
Figure 4.13: Strength predictions based on Euler buckling and plastic micro-buckling failure modes and FE models.	179
Figure 4.14: Initial elastic modulus of the pyramidal lattice based on numerical and analytical models. The modulus increases linearly with increasing relative density.	181
Figure 4.15: Numerical and analytical predictions of the pin-jointed pyramidal lattice compression strength.	181
Figure 4.16: FE model and analytical predictions of the rigid-jointed pyramidal lattice compression strength.	182
Figure 4.17: FE model and analytical predictions for the initial stiffness of a modified pyramidal lattice core.	183
Figure 4.18: Strength predictions for the pin-jointed modified pyramidal core. The failure mode shifts from elastic buckling to plastic microbuckling for cores having a relative density above 0.04%	184
Figure 4.19: Strength predictions based of edge-clamped modified pyramidal model. For relative densities above 0.009 the core fails due to plastic micro-buckling.	185
Figure 4.20: Initial stiffness predictions based for a BCC lattice constructed from pin-jointed and rigid-jointed struts.	186

Figure 4.21: Compression strength of a BCC lattice with rigid-jointed struts.	187
Figure 4.22: Compression strength of a BCC lattice with pin-jointed struts.	187
Figure 4.23: FE model and analytical predictions for the initial stiffness of the BCCz lattice structure.	188
Figure 4.24: Strength predictions for the pin-jointed BCCz core. The failure mode shifts from elastic buckling to plastic microbuckling for cores having a relative density above 0.045%	189
Figure 4.25: Strength predictions based on the rigid-jointed BCCz lattice model.	189
Figure 4.26: Numerical and micro-mechanical predictions of the elastic modulus for an FCC lattice. The initial modulus increases linearly with increasing relative density.	190
Figure 4.27: Strength predictions based on a rigid-jointed FCC lattice model. The failure mode shifts from elastic buckling to plastic micro buckling for cores having a relative density above 0.045%	191
Figure 4.28: Strength predictions for the pin-jointed FCC core. At relative densities over 0.16%, the core fails due to plastic microbuckling.	191
Figure 4.29: Numerical and micro-mechanical predictions of the Elastic modulus.	192
Figure 4.30: Strength predictions based on Euler buckling and plastic micro-buckling failure modes compared to FE model results.	193
Figure 4.31: Strength predictions based on a rigid-jointed F_2 BCC structure. Elastic buckling of the struts is the predicted failure mode for relative densities below 0.07. At relative densities above 0.30, the struts fail due to plastic micro-buckling.	194
Figure 4.32: Numerical predictions for the specific initial stiffness of the various lattice core configurations.	195

Figure 4.33: Numerical predictions for the specific compression strength of the various lattice core configurations.	195
Figure 5.1: (a) Top face sheet with in-plane flow, (b) Bottom face sheet with in-plane and radial flow through the holes from top to bottom.	199
Figure 5.2: Cross-sections of manufactured samples with filled holes. (a) Materials B, (b) Materials C, (c) Material D-D, (d) Material D-S, (e) Material E-D, (f) Material E-S, (g) Material F-D, (h) Material F-S.	200
Figure 5.3: The unit cell of a column truss core based on an array of 4 mm diameter columns.	201
Figure 5.4: Photograph of a 6 x 6 column core based on 2.5 mm diameter struts.	202
Figure 5.5: Photographs of (a) a pyramidal structure and (b) a modified pyramidal structure, reinforced with a central vertical member.	202
Figure 5.6: (a) Various views of a structure based on three octet unit cells, (b) A photograph of an octet truss unit cell structure	203
Figure 5.7: Optical micrographs of individual columns (a) 2 mm diameter, $V_f = 0.51$ (b) 2.5 mm diam. $V_f = 0.28$ (c) 3 mm diam. $V_f = 0.28$, (d) 4 mm diam. $V_f = 0.28$	204
Figure 5.8. Photographs of the BCCz, the F_2 BCC, the BCC and FCC lattice structures following manufacture.	205
Figure 5.9: Axial compression stress strain-curves for Materials A, B, and C.	206
Figure 5.10: Axial compression response of Materials A, D-S, E-S and F-S.	207
Figure 5.11: Summary of the compression strengths of the core materials.	208
Figure 5.12: Schematic drawings of the two procedures used to thread the samples.	208

Figure 5.13: Stress-strain traces for individual columns (a) 2.5 mm diameter and (b) 3 mm diameter. $V_f = 0.42$. Dashed line = Configuration A and Solid line = Configuration B....	210
Figure 5.14: Stress-strain traces of individual columns of 4 mm diameter. $V_f = 0.28$. Dashed line = Configuration A and Solid line = Configuration B.....	211
Figure 5.15: Variation of specific compression strength with slenderness ratio for single columns. The samples are based on Configuration B.	212
Figure 5.16: Stress-strain traces for multiple columns (a) 3 mm diameter and (b) 4 mm diameter. $V_f = 0.28$. Dashed line = Configuration A and solid line = Configuration B. ...	215
Figure 5.17: The variation of specific compression strength with slenderness ratio for the truss cores. $V_f = 0.28$	216
Figure 5.18: Stress-strain traces for multiple columns (i) 2 mm diameter and (ii) 4 mm diameter. $V_f = 0.28$. Dashed line = experiment and solid line = FE model.	217
Figure 5.19: The variation of SEA as a function of slenderness ratio for the truss cores..	218
Figure 5.20: Typical stress-strain traces following compression tests on single columns based on different fiber volume fractions (a) 3 mm diameter columns (b) 4 mm diameter columns.	220
Figure 5.21: Photographs of individual 3 mm diameter columns at various stages of testing: (i) neat resin, (ii) $V_f = 8\%$ and (iii) $V_f = 12\%$	222
Figure 5.22: Photographs of individual 4 mm diameter columns during testing:.....	222
Figure 5.23: The variation of failure stress with fiber volume fraction for the 3 and 4 mm diameter columns. The solid lines correspond to the predictions of Euler buckling theory based on the properties at a given fiber volume fraction.	223

Figure 5.24: Typical stress-strain traces following compression tests on core structures based on arrays of columns with diameters of 2.5, 3 and 4 mm.	224
Figure 5.25: Stages of deformation in truss core based on 3 mm diameter columns. The crosshead displacement is shown under each figure.	225
Figure 5.26: Stages of deformation in truss core based on 3mm diameter columns.	225
Figure 5.27: The variation of compression strength with slenderness ratio for the truss cores. The solid line corresponds to the prediction offered by Euler theory.	226
Figure 5.28: The variation of the compression strength of the core structures with column slenderness ratio.	227
Figure 5.29. Summary of the specific strengths of the pyramidal and modified pyramidal structures. The photos show plain and modified samples during testing. Open columns = experiment and hatched columns = FE modeling.	228
Figure 5.30: Photographs of an octet truss structure (a) prior to testing and (b) following compression testing. The sample height is 56 mm.	229
Figure 5.31. (a) Stress-strain traces for the BCC lattice structure (b) photographs showing the deformation modes with increasing strain.	231
Figure 5.32. (a) Stress-strain traces for the BCCz lattice structure (b) photographs showing the deformation modes with increasing strain.	232
Figure 5.33. (a) Stress-strain traces for the FCC lattice structure (b) photographs showing the deformation modes with increasing strain.	233
Figure 5.34. (a) Stress-strain traces for the F ₂ BCC lattice structure (b) photographs showing the deformation modes with increasing strain.	235

Figure 5.35. Summary of the Young's modulus properties of the four lattice structures. Included in the figure are the experimentally-determined values of modulus as well as those predicted by the analytical and FE models,	236
Figure 5.36. (a) Comparison of the compression strengths of the four lattice structures and (b) comparison of the specific compression strengths (experimental data) of the lattices.	238
Figure 5.37. Summary of the specific energy absorption values of the four lattice structures.	239
Figure 5.38: Typical load-displacement traces for Materials A, B and C.	242
Figure 5.39: Fracture surfaces of Materials A, B, and C following interfacial failure.	243
Figure 5.40: Typical load-displacement traces for Materials D-D, E-D and F-D.....	244
Figure 5.41: Photograph of the edge of Material F-D during interfacial fracture testing..	245
Figure 5.42: Typical load-displacement traces for Materials D-S, E-S and F-S.	245
Figure 5.43: Fracture surfaces of Materials D-D, E-D and F-D following interfacial failure.	246
Figure 5.44: Summary of the interfacial fracture properties of the sandwich structures...	248
Figure 6.1: An Ashby diagram of strength versus density for engineering materials. The measured compression strengths of the various lattice cores are included [1].	254
Figure 6.2: An Ashby diagram including the FE model predictions for compression strengths of the various lattice cores made from a material having a 51% fiber volume fraction [1].....	255
Figure 6.3: An Ashby diagram including the FE model predictions for the elastic modulus of the various lattice cores made from a material having a 51% fiber volume fraction [1].	256

Figure B.1: a) Top view of a single skin sandwich structure (S^4), b) skin free side of the S^4 structure, c) lattice wheel d) Natural fiber reinforced airfoil and Carbon fiber reinforced airfoil.....260

Figure C.1: Photographs showing (a) Jute fibers passing through the holes in the wax mold in a continuous fashion, (b) Natural fiber sheets forming the airfoil skin placed around the mold, (c) airfoil stack sealed in a vacuum bag in preparation for the infusion process (d) and flow front on one side of the airfoil during the VARTM process.....262

Figure C.2: Snapshots showing the progression of resin through the reinforcement with the blue and red colors indicating dry and resin rich regions respectively.....263

List of Tables

Table 1.1: Resin infusion patents overview [62].	46
Table 2.1: Summary of hole separation, fiber volume fraction in the perforations and overall core density for the various materials.	87
Table 3.1: Constituent materials elastic properties	106
Table 3.2: Elastic properties for materials having three different fiber content.	113
Table 3.3: Summary of the strength characteristics for materials having 28% and 42% fiber volume fraction.	115
Table 3.4: Pyramidal lattice elastic and strength properties	124
Table 4.1: Summary of elastic properties of CFRP materials manufactured at three different fiber volume fractions.	164
Table 4.2: Summary of strength characteristic data for the CFRP materials (*Assumption)	165
Table 4.3: Summary of the fracture energy data for the truss material (lower bound and upper bound values correspond to materials having $V_f = 0.14$ and $V_f = 0.48$ respectively)	167
Table A.1: Summary of the mechanical properties used in this study (a) elastic properties and (b) strength characteristics.....	259

Nomenclature

BCC	Body centered cube
CAPRI	Controlled Atmospheric Pressure Resin Infusion
CFRP	Carbon fiber reinforced plastic
EDM	Electrical discharge machining
FCC	Face centered cube
GFRP	Glass fiber reinforced plastic
LCM	Liquid composite molding
NFRP	natural fiber reinforced plastic
PET	Polyethylene terephthalate
RTM	Resin transfer molding
SCRIMP	Seamann Composites Resin Infusion Molding Process
UD	Unidirectional
VAP	Vacuum-Assisted Process
VARTM	Vacuum resin assisted transfer molding
WBK	Woven bulk Kagome'

Chapter 1: Introduction

1.1 Overview

Despite the development of highly efficient turbofan and turboprop engines with lower emissions and the improvements achieved in fuel efficiency through the adoption of advanced aircraft technology, the increase in air traffic volume is overshadowing all the above improvements and resulting in a net increase in pollution emission coming from the aviation sector. The reduction of structural weight of future aircraft provides one avenue to achieve significant reduction in fuel consumption and an increase in payload, as a result, there is a growing drive in the aerospace sector to develop increasingly lightweight, high performance load-bearing, multifunctional structures. In addition for the structure to be light weight, other properties such as high stiffness, high strength and multifunctional capability are important, especially for aerospace applications. Materials, such as aluminum alloys and titanium, have been the favorite choice of aerospace structural materials for many years due to their high stiffness to weight ratio [1]. However, the advent of relatively newly developed materials such as fiber reinforced composites are causing a paradigm shift in favor of these new materials for aerospace structural applications, due to their ability to achieve significant weight reductions, while maintaining superior mechanical properties, in comparison to their metallic counterparts. Commercial aircraft, military craft, helicopters, business jets, general aviation aircraft and space craft all make substantial use of composites. As a result, there is a growing drive in the aerospace sector to develop increasingly lightweight, high-performance load-bearing, multifunctional structures. The

recent introduction of the Boeing 787 represents an excellent example, with composites representing fifty percent (by weight) of the aircraft structure. Another example is the Airbus A350XWB, making more extensive use of advanced composite components than its predecessors.

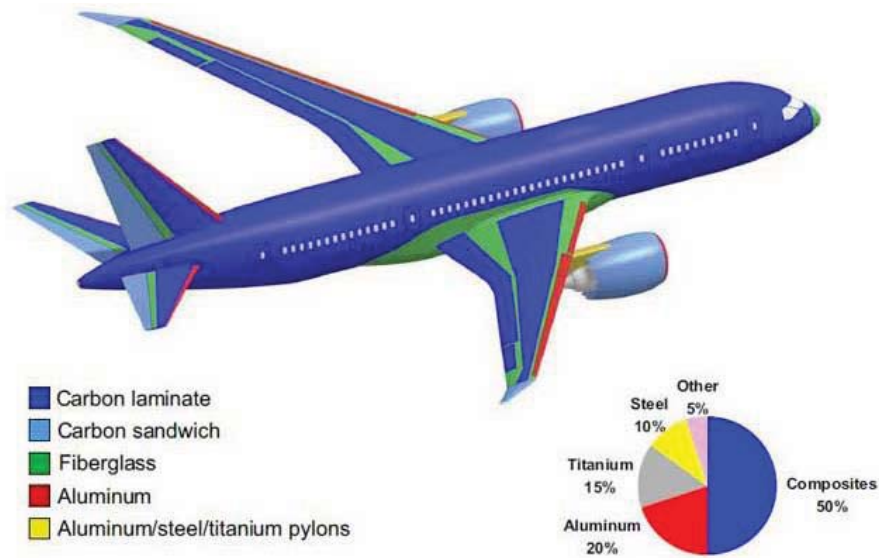


Figure 1.1: Materials used in the Boeing 787 [2].

Traditionally, many lightweight aircraft components have been based on sandwich structures, consisting of composite skins bonded to honeycomb or foam cores. More recently, there has been a growing interest in the potential offered by lattice core structures in the design and manufacture of ultra-light sandwich panels for high-performance engineering applications. The stiffness and strength properties of these lattice structures depend on the materials of which they are made and their topology. Metallic lattice structures, based on architectures such as the Kagome' structure [3], pyramidal designs [4] and the octet truss configuration [5] have been examined. A number of manufacturing techniques have been used to produce these metallic structures including a rapid processing and brazing procedure [6], investment casting [7] and selective laser melting [8].

Subsequent mechanical testing has shown that many of these structures offer a range of attractive mechanical properties [3–9]. Recently, attention has focused on developing composite lattice structures that should, in principle, out-perform their metallic counterparts. Here, a new manufacturing technique is developed to fabricate ultra-light composite lattice structures and hybrid foam reinforced with composite lattice structures in addition to characterizing their mechanical properties mainly in compression and develop analytical models to predict their mechanical properties for comparison with numerical predictions and experimental results. These new composite lattice structures offer the potential to fill the gap between the currently available engineering materials and the unattainable material space. This is illustrated in the existing gap within the modified Ashby diagrams for strength vs. density and stiffness vs. density shown in Figure 1.2. The goal here is to develop a manufacturing technique that will enable the fabrication of composite based lattice structures with properties that can fill these observed gaps.

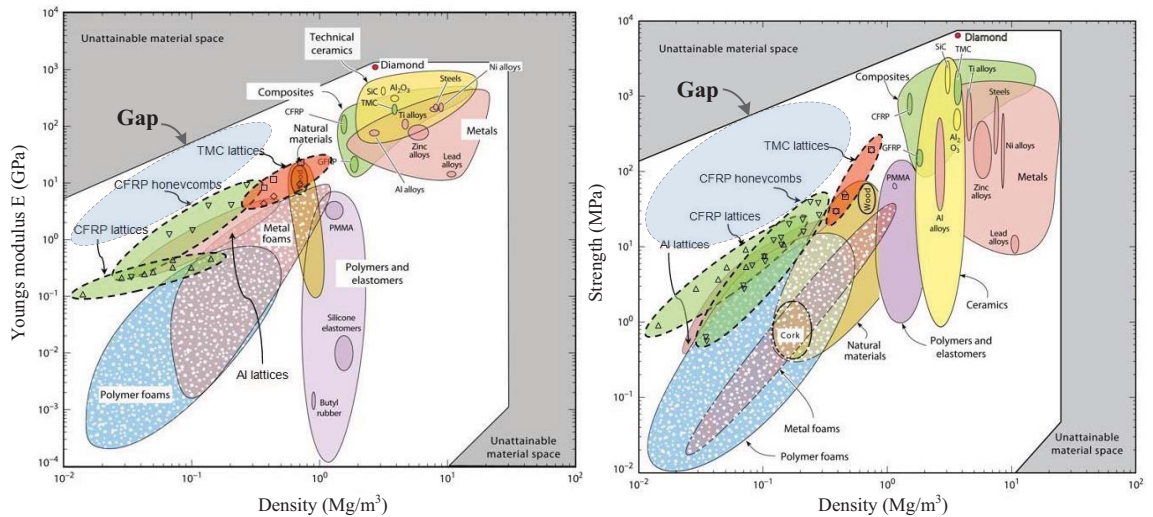


Figure 1.2: Modified Ashby materials property charts for (a) Young's modulus and (b) Compression strength for engineering materials [10]. Composite lattice structures could fill the gap area in the low density – high stiffness and strength region.

1.2 Thesis Objective

The primary objective of this work is (1) to investigate the possibility of fabricating millimeter size, all composite lattice core sandwich panels with superior specific strength/stiffness properties; (2) to develop a viable method for manufacturing these lattice based core structures; (3) to investigate their mechanical properties and failure mechanism as a function of the constituent material properties and core geometry; (4) to develop analytical models for predicting the elastic stiffness and collapse strength of these structures and (5) to carry out numerical simulations for comparison with experimental results and for validating the analytical models.

The potential significance of this work is that it will enable the manufacture of composite lattice structures of various complexity. Given the potential of these composite structures in filling the gap area in the low density – high stiffness and strength region in Figure 1.2, their performance will be experimentally determined. s

1.3 Thesis Outline

The remainder of this thesis is organized as follows:

- **Chapter 1: Literature Review;** continues to examine the sandwich panel concept based on cellular materials, their mechanical properties and manufacturing techniques including the vacuum assisted resin transfer molding (VARTM) process.
- **Chapter 2: Experimental Procedure;** presents the lost mold technique for manufacturing the lattice core structures and includes details of the experimental procedures used in measuring the mechanical properties.

- **Chapter 3: Analytical Modeling;** develops the micromechanical models for the mechanical performance of the lattice structures in response to compression loading.
- **Chapter 4: Finite Element Analysis;** provides details about relevant aspects involved in developing the finite element models the results of which are then compared with the analytical predictions.
- **Chapter 5: Results and Discussion;** includes discussion of the results of all lattice structures considered in this study.
- **Chapter 6: Conclusions and Future Work;** then discusses the significance of these results in the context of the goals of this work and provides an outline for future work.

1.4 Sandwich Panel Design Concept

Sandwich construction is emerging as the structural design of choice, due to its ability to provide excellent mechanical properties at minimal weight. A sandwich panel consists typically of three layers; a lightweight core between two relatively thin face-sheets. The core material being low in density plays a fundamental role in providing a strong, stiff and lightweight sandwich structure design when placed between two face-sheets. Typically, cores are made of metallic or non-metallic honeycomb, cellular foams, balsa wood, and trusses while commonly-used materials for face-sheets are laminated composites and metals [2]. The task of the face-sheets is to carry almost all of the bending and in-plane loads in addition to providing high surface quality and good impact performance. The mechanical requirement of the core is to prevent the movement of the face-sheets relative to each other and stabilize them against wrinkling or buckling while defining the flexural stiffness, out of plane shear and compressive properties. Additional functions of the core include thermal and acoustic insulation and energy absorption during impact. This task distribution in the sandwich construction enables high stiffness and strength for lightweight panels and parts. A wide range of core materials for use in sandwich composites are available. Each core material provides particular properties suitable in various conditions. Currently, there is a strong interest in developing lightweight, high-performance structures for enhanced aerospace design. More recently, there has been a growing interest in the use of foldcore structures and lightweight lattice architectures for use in aerospace design. The unique and attractive properties offered by cellular materials based on lattice truss topologies have, in recent years, been investigated by a number of authors [3, 5–7, 11, 12]. Previous work has shown that such lattices exhibit stiffness and strength properties that

scale linearly with density, ρ . This is in contrast to polymer and metal foams, whose strength and stiffness properties scale as $\rho^{3/2}$ and ρ^2 respectively. A brief review of cellular materials follows.

1.5 Cellular materials

A cellular material consists of an interconnected network of solid struts or plates that make up the faces and edges of the cell [13]. The properties of the cellular structure depend directly on the shape and structure of the cell. The most important structural characteristic of such structures is relative density, ρ , defined as the density of the cellular structure divided by the density of the solid of which it is made [13]. Light weight structures characterized by a low density cellular material configured as the core with a denser outer surface are very common in nature [14]. Few examples include cork, wood, sponge, plant stems, trabecular bone and bird beaks [14]. Cork and balsa wood consists of closed cells resembling a honeycomb, Figure 1.3 (a) and (b). Others, such as sponge and bone are an open network of struts with multi-node connection. This naturally-occurring construction allows for structures with good mechanical properties at low weight. They are essentially stiff, strong, lightweight and multifunctional structural form of a sandwich construction. If it were not for this design, trees for example, would not be able to withstand the bending loads from wind and would collapse under its own weight.

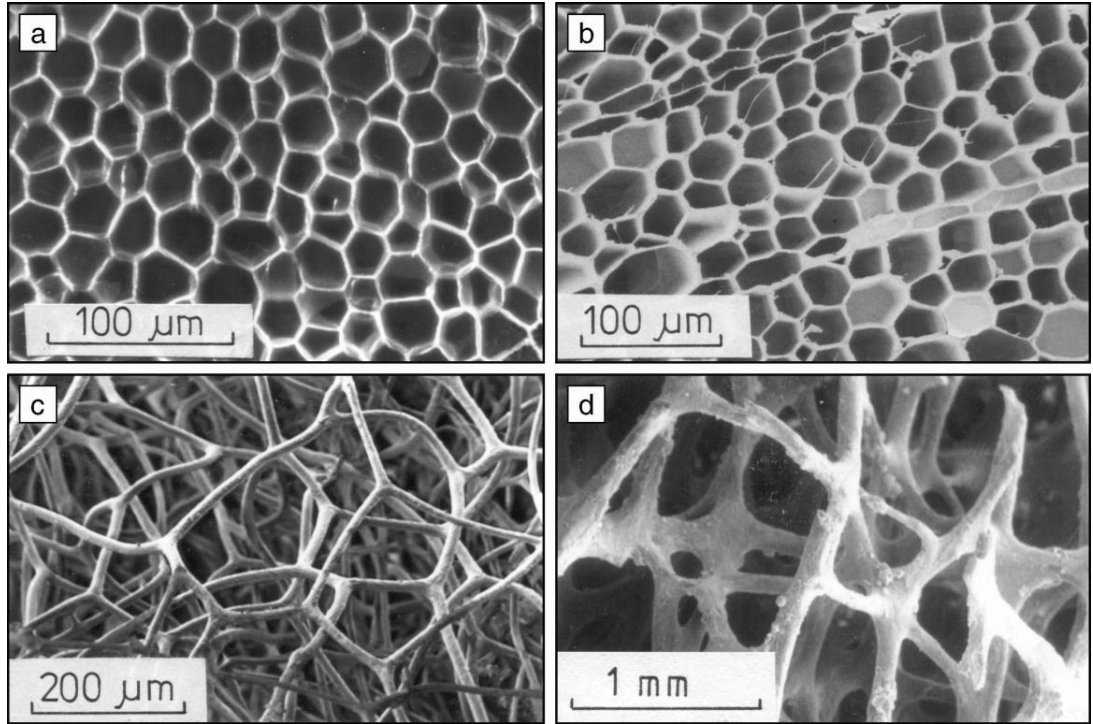


Figure 1.3: Cellular materials in nature: (a) cork, (b) balsa wood, (c) sponge, and (d) trabecular bone [13].

Inspired by the lessons learned from nature, synthetic cellular materials have evolved. Currently, a wide range of cellular solids are being manufactured including foams, honeycombs, prismatic materials, and truss structures. All cellular solids are generally categorized as being open cell or closed cell with stochastic or periodic topologies [15].

1.5.1 Stochastic cellular materials

Figure 1.4 illustrates two examples of man-made stochastic cellular structures. They are foam structures that are characterized by having a random microstructure distribution or pattern. Two sub-types can be distinguished, open cell and closed cell stochastic architecture. In the first, the material has been formed into struts that join at vertices

forming the cell edges as in Figure 1.4a. In the second, the cell faces are sealed by a solid membrane (Figure 1.4b).

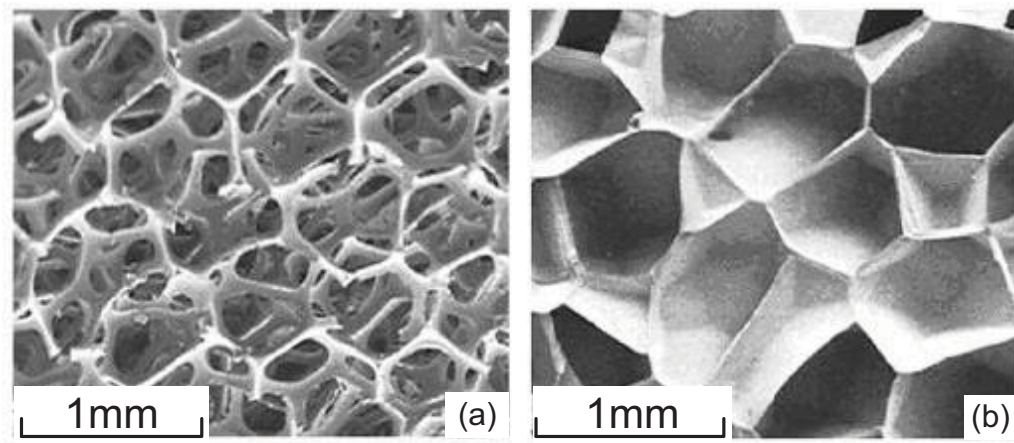


Figure 1.4: Three dimensional cellular material (a) open-cell polyurethane (b) closed-cell polyethylene [13].

Foam materials are typically made from diverse materials such as polymers, metals, ceramics, glasses and composites. Cellular metals for example are manufactured by foaming of liquid metal by injecting a gas or by the decomposition of a gas releasing particles [16]. Polymeric foams are produced in a process that involves the nucleation and growth of gas bubbles in a polymer matrix [17]. Due to the random nature of the manufacturing process, statistical variations in cell size and shape exist leading to non-uniform distribution of material in the cell walls/edges. This leads to considerable density and mechanical properties fluctuation within the foam structure [16].

Generally, factors influencing the structural properties of cellular material properties are found to be dependent on relative density, properties of the solid of which the cellular structure is made, cell type (open/closed), shape and topology [16, 18]. Gibson and Ashby [13] derived the micromechanical response of an open-cell foam using an idealized unit

cell. The model was based on a cubic array with edges of length L and square cross-section of side t (Figure 1.5).

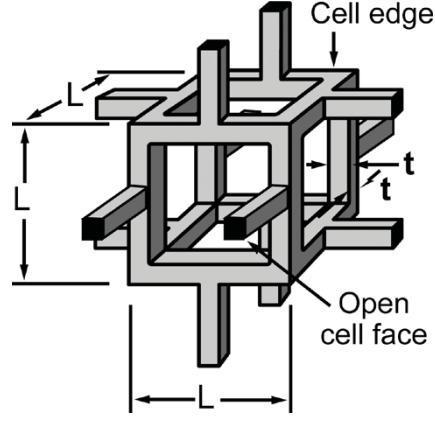


Figure 1.5: Schematic diagram of an idealized cell representative of an open-cell foam [13].

With $t \ll L$, the relative density of the cell in terms of the unit cell key geometric dimensions is given by:

$$\frac{\rho^*}{\rho_s} \propto \left(\frac{t}{L}\right)^2 \quad (1.1)$$

where ρ^* is the density of the foam and ρ_s is the density of the parent material of which it is made. When a compressive force, F , is applied at the unit cell mid-point as shown in Figure 1.6, the edges bend with a deflection, δ . Using standard beam theory; the elastic deflection δ is proportional to $FL^3/E_s I$ where E_s is the elastic modulus of the material of the beam and I is the second moment of area of the beam and is given by $I \propto t^4$.

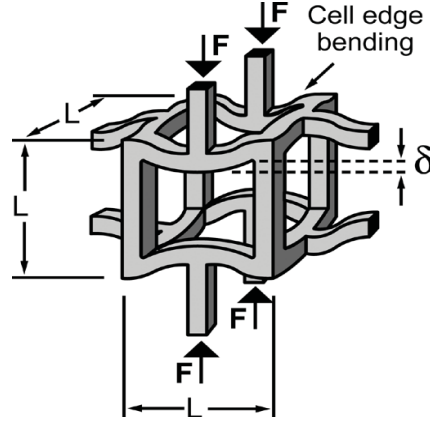


Figure 1.6: Unit cell edges undergoing bending due to an applied compressive force [13].

The applied force F is related to the remote compressive stress σ by $F \propto \sigma L^2$. The compressive strain ϵ sustained by the unit cell is related to displacement by $\epsilon \propto \delta/L$. Using the above relations, it follows that the elastic modulus $E = \sigma/\epsilon$ of a foam with a bending dominated behavior is given as [13]:

$$\frac{E}{E_s} \propto \left(\frac{\rho^*}{\rho_s} \right)^2 \quad (1.2)$$

Using a similar approach, the collapse strength of an open cell foam structure can be approximated as [13]:

$$\frac{\sigma_{pl}^*}{\sigma_{ys}} \propto \left(\frac{\rho^*}{\rho_s} \right)^{3/2} \quad (1.3)$$

This bending dominated behavior can be extended to most closed-cell foam materials with resulting stiffness and strength predictions that follow the same scaling laws as Equations 1.3 and 1.4 [18]. This arises from the fact that the cell faces are very thin relative to the cell struts. Consequently, the cell membranes fail at very low stresses with little contribution to stiffness and strength, leaving the cell edges to carry the majority of the load [18]. Equations 1.2 and 1.3 demonstrate that a decrease in relative density in foam materials is

accompanied by a rapidly decreasing strength and stiffness, since they scale as $\rho^{3/2}$ and ρ^2 respectively. A typical compressive stress-strain curve for a bending-dominated foam is illustrated in Figure 1.7. The initial elastic behavior is dictated by the bending of the cell edges. Once the elastic limit is reached, the cell edges begin to fail either by elastic buckling, plastic yielding or brittle fracture, depending on the nature of the cell material. This failure continues at a constant rate, as observed in the long collapse plateau stress portion of the curve. Once the collapse process is almost complete, the opposing cell walls come into full contact and continued loading compresses the solid material, resulting in a rapid increase in stress.

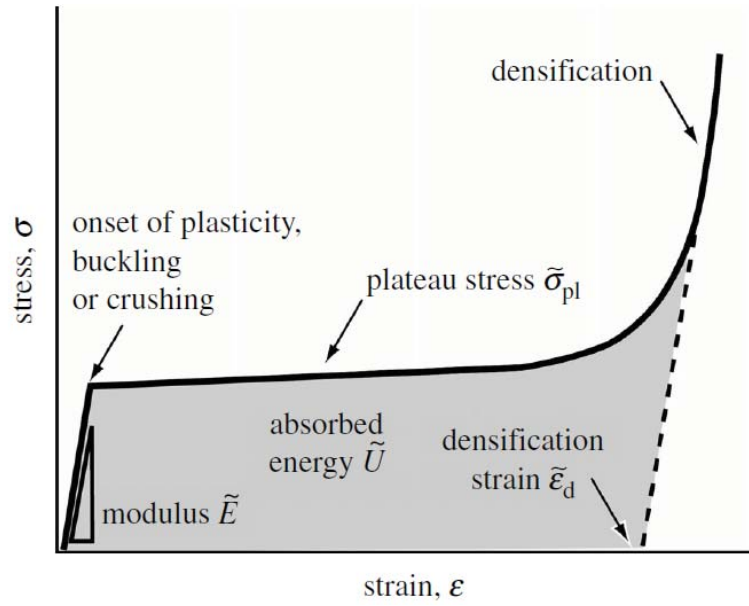


Figure 1.7: Typical compressive stress-strain trace of a bending-dominated foam structure [19].

The material is not fully utilized in bending-dominated cellular materials such as foams. Therefore, such materials exhibit lower specific stiffness and strength properties compared to stretch-dominated structures [20]. However, the long flat plateau stress in their stress-

strain curves is an attractive property for energy-absorbing applications [19]. Foam is the material of choice for the main impact-absorbing element of the motorcycle helmet [13].

The struts in Figure 1.5 are arranged in a way that allows them to bend under an applied load resulting in reduced stiffness and strength properties. They can be reconfigured to become optimally constrained in a way that prevents bending, resulting in a stretch-dominated structure. This can be explored through an understanding of Maxwell's Criterion of structural rigidity [21]. A structure constructed from b struts joined by j frictionless joints is said to be statically and kinematically determinate when the following condition for a two dimensional structure is met:

$$M = b - 2j + 3 = 0 \quad (1.4)$$

In three dimensions, the equivalent condition is:

$$M = b - 3j + 6 = 0 \quad (1.5)$$

Figure 1.8(a) illustrates an example for the case when $M < 0$, the truss will fold up when loaded, making it a *mechanism* without stiffness or strength. If the joint were rigid, the bars would bend when loaded as in the configuration of the idealized cell model in Figure 1.5. The truss configuration in Figure 1.8(b) is an example for the case of $M = 0$ in which the truss members would carry tension or compression when loaded, making a stretch-dominated structure. This would be the case whether the hinges were free to rotate or rigid. Rigid hinges have little influence because slender structures are much stiffer when stretched rather than when bent [19]. For this reason, stretch-dominated structures have a high structural efficiency; bending-dominated structures have lower efficiency [19].

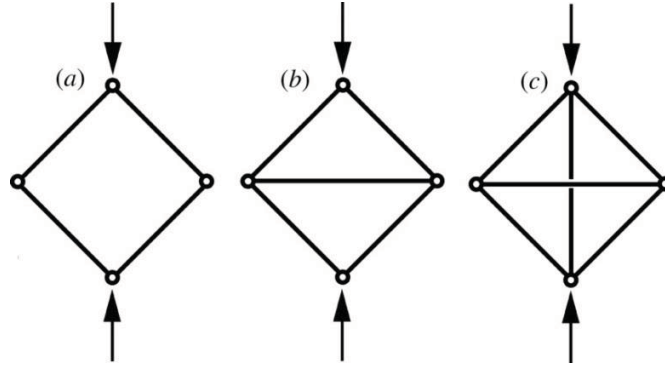


Figure 1.8: (a) $M < 0$, if the joints are rigid the configuration becomes a bending dominated structure, (b) $M = 0$, stretch dominated structure and (c) $M > 0$, over constrained structure [19].

Figure 1.8c is an over-constrained truss configuration with $M > 0$. If the horizontal truss is elongated or shortened, the truss configuration would be in a state of self-stress, even in the absence of external loads. Maxwell's criteria given in Equations 1.4 and 1.5 is a necessary but generally not a sufficient condition for rigidity, as it doesn't account for the possibility of states of self-stress and of *mechanism* [19]. The generalized form of Maxwell's equation in three dimensions is given by [22]:

$$M = b - 3j + 6 = s - m \quad (1.6)$$

where s is the number of self-stress states and m is the number of mechanisms. A frame is considered statically and kinematically-determinate (rigid) when $s = m = 0$.

An examination of Equation 1.6 reveals that a vanishing left-side only indicates that the number of mechanisms and states of self-stress are equal, not that each equals zero.

This explains the nature of Maxwell's rule as a necessary rather than sufficient condition. However, Maxwell's criterion gives a prescription for designing a stretch-dominated structure.

1.5.2 Periodic cellular materials

Microstructures of periodic architecture include either three dimensional micro-truss assemblies referred to as, a lattice structure, or two dimensional periodic channels, referred to as prismatic materials or honeycombs [23]. Generally, periodic cellular materials have a highly porous structure with 20% or less of their interior volume occupied by solid [24]. They are characterized by an ordered structure of repeating a unit cell geometry. Periodic materials can be divided into three main groups, namely honeycomb, prismatic and lattice cellular structures as shown in Figure 1.9.

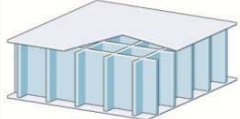
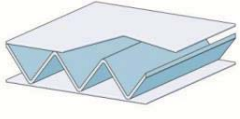
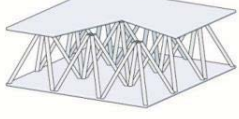
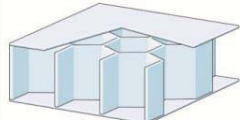
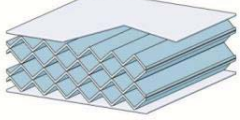
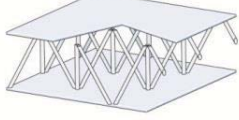

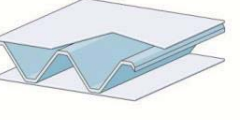
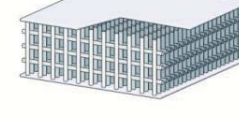
i) Honeycomb	ii) Prismatic	iii) Truss
a) Square 	a) Triangular 	a) Pyramidal 
b) Hexagonal 	b) Diamond 	b) Tetrahedral 
c) Triangular 	c) Navtruss 	c) Colinear (square) 

Figure 1.9: Cellular material topologies [10, 24]

An advantageous property of periodic cellular materials is that they are often stretch-dominated structures, in which the stiffness and strength scale linearly with relative density. Synthetic honeycombs are based upon the efficient design of a honeybee's nest [15]. It is a structure made up of regular arrays of prismatic hexagonal open cells. It represents a two dimensional cellular solid as the hexagonal unit cells pack to fill a plane in two dimensions.

Honeycombs can be made from square, triangular, or hexagonal shaped unit cells in addition to other variations Figure 1.9 (a, b and c). Part of a sandwich panel construction, honeycomb cores with unit cell walls arranged perpendicular to the face sheet form a closed cell structure. Honeycomb cores are manufactured from a variety of materials for sandwich structures, depending on the application. For low stiffness and strength applications (such as domestic internal doors) they are made from paper and card. For aerospace applications that require high stiffness, and strength with minimum weight, they are constructed from Nomex paper or aerospace grade aluminum. Hexagonal honeycombs are manufactured using an expansion process (Figure 1.10). In this process large thin sheets of the material are printed with alternating parallel thin strips of adhesive and the sheets are stacked in a heated press while the adhesive cures. The stack of sheets is then sliced through the thickness and these slices are gently stretched and expanded to form the sheet of continuous hexagonal cell shapes. This in-plane expansion process results in two of the six cell walls having double thickness, consequently, the honeycomb will have different mechanical properties in the 0° and 90° directions of the sheet [13]. Another approach involves the assembly of slotted strips of material to create square or triangular honeycombs that are less anisotropic than their hexagonal counterpart [25].

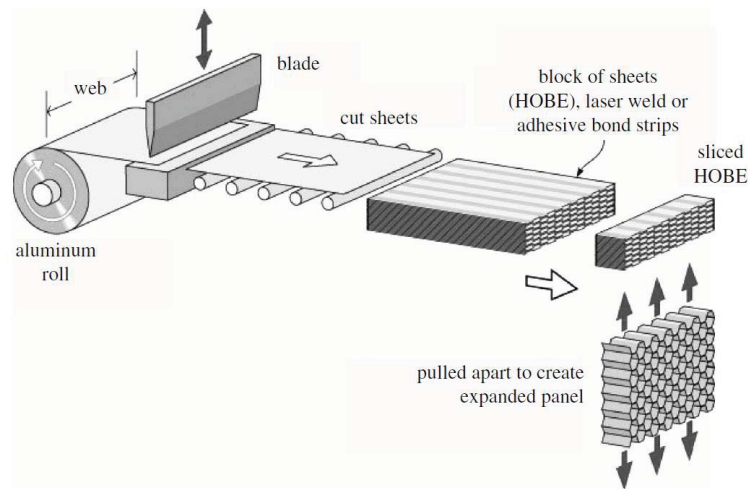


Figure 1.10: Hexagonal honeycombs manufactured using an expansion process [24]

Properties of honeycomb materials depend on the relative density, the properties of the solid of which the cellular structure is made, the cell shape and the topology [16, 18]. In general, honeycomb materials produce one of the highest strength to weight ratios of any structural material. When compressed in-plane, the cell walls bend, giving a linear elastic behavior up to a critical load upon which the cells fail by elastic buckling, plastic yielding or brittle fracture. In tension, the cell walls bend, as in compression, up to a critical load and fractures if the cell material is brittle or plastically yields if ductile. When loaded out-of-plane, parallel to the axis of the unit cells, the cell walls will extend or compress resulting in a much higher modulus and collapse strength [13]. Figure 1.11 compares the out-of-plane performance of a hexagonal honeycomb to an open-cell foam structure. It is noted that the elastic modulus of the foam is significantly lower than the honeycomb at low relative densities. A similar trend is observed with yield strength. These differences are the result of the foam's low structural efficiency arising from the bending-dominated behavior of the cell edges and, to a lesser degree, due to the presence of microscopic defects (depending on the manufacturing process) within the foam micro structure [15].

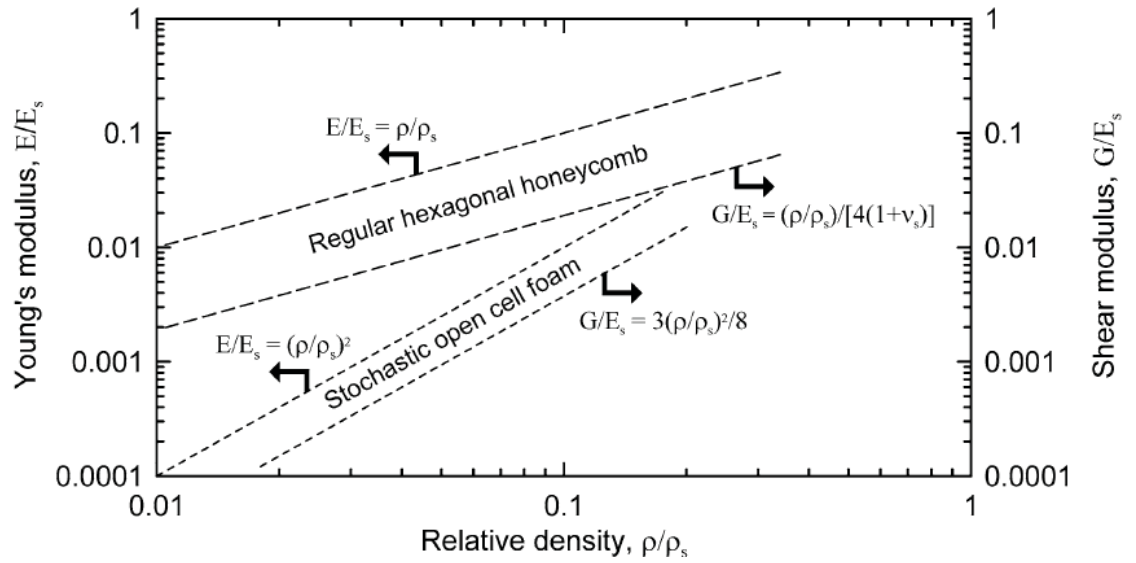


Figure 1.11: Elastic and shear modulus of hexagonal honeycombs and open cell foams vs. relative density [15].

Prismatic core structures are made of plate or sheet elements that form the edges of the unit cell. They are essentially honeycomb structures, rotated 90° about their horizontal, resulting in open channels (open cell) in one direction and a closed cell structure in the remaining orthogonal directions, as observed in Figure 1.9ii. The open channels enable excellent ventilation characteristics, avoiding problems associated with water accumulation, which is common in closed cell core materials, such as honeycombs and foams. Prismatic cores come in various unit cell topologies, including triangular, diamond, navtruss or a Y-truss corrugation. Metallic corrugated cores are manufactured using a corrugation method. In this process, a thin sheet of material is continuously bent by pressing or folding to form the corrugation patterns [24]. Some metals can be corrugated through an extrusion process [24]. Alternatively, a slotting procedure is used in which sheets of the core material are cut into rectangles, cross-slotted, assembled in arrays and joined by brazing (or adhesive bonding) to construct the prismatic cells [26]. The slotting procedures can be used to

fabricate prismatic metallic or composite cores, while the corrugation method is limited to metallic materials only.

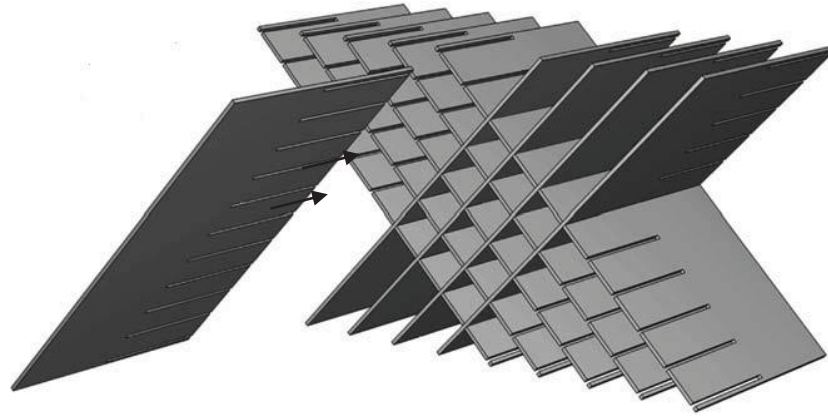


Figure 1.12: Schematic diagram of the slotting procedure for creating prismatic cores [26].

In another approach, a hot press is used to produce composite corrugated cores in which the pre-preg material is placed between upper and lower molds and cured [27].

The out-of-plane compression and shear strength of triangular and diamond corrugated cores were investigated and found to have lower specific strengths compared to square-honeycomb and pyramidal sandwich cores, due to a weak buckling mode [26]. In contrast, the longitudinal shear strength and energy-absorption capacity were comparable to square-honeycomb cores, offering significant potential for applications in sandwich panel construction [26].

Materials with a periodic microstructural architecture of micro-truss assemblies are referred to as lattice materials. They are characterized by having an open-cell architecture, since they are constructed from a regular repetition of slender beams leaving three dimensional interconnected void spaces. The slender beams or trusses can be of any cross-sectional shape, including circular, square, hollow or I-beam sections. In one study, hierarchical composite pyramidal lattice core were manufactured with struts based on foam-core

sandwich struts [28]. Micro-lattice truss architectures can be configured in various arrangements, such as pyramidal [6], textile [11], tetrahedral [7], 3-D Kagome' [3], octahedral [5] and other lattice topologies.

Various methods have been developed for the manufacture of metallic-based lattice structures involving casting, forming, and textile weaving techniques [29]. In investment casting, the truss core and face-sheets are made from wax or polymer by injection molding, 3-D printing or any other rapid prototyping techniques. This pattern is then coated with a layer of ceramic shell by dipping into ceramic casting slurry. Once the ceramic coating is dried, the wax or polymer is removed by melting leaving a hollow mold that reflects the final sandwich panel configuration. This is then filled with liquid metal and after the molten metal has cooled, the ceramic mold can be broken and the casting removed. Sandwich panels based on a three dimensional Kagome' [3] and tetrahedral [7] lattice core were manufactured using the investment casting method as illustrated in Figure 1.13.

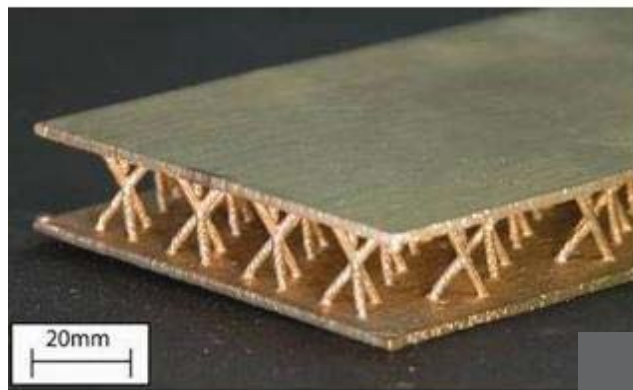


Figure 1.13: Sandwich panels based on 3D Kagome' trusses metallic lattice structures [10].

Metal forming techniques involve a sheet of metal that is perforated using die stamping, laser or water jet cutting and subsequently deformed by bending or folding to reflect the

desired core configuration, as shown in Figure 1.14. The truss pattern is then bonded between two face-sheets.

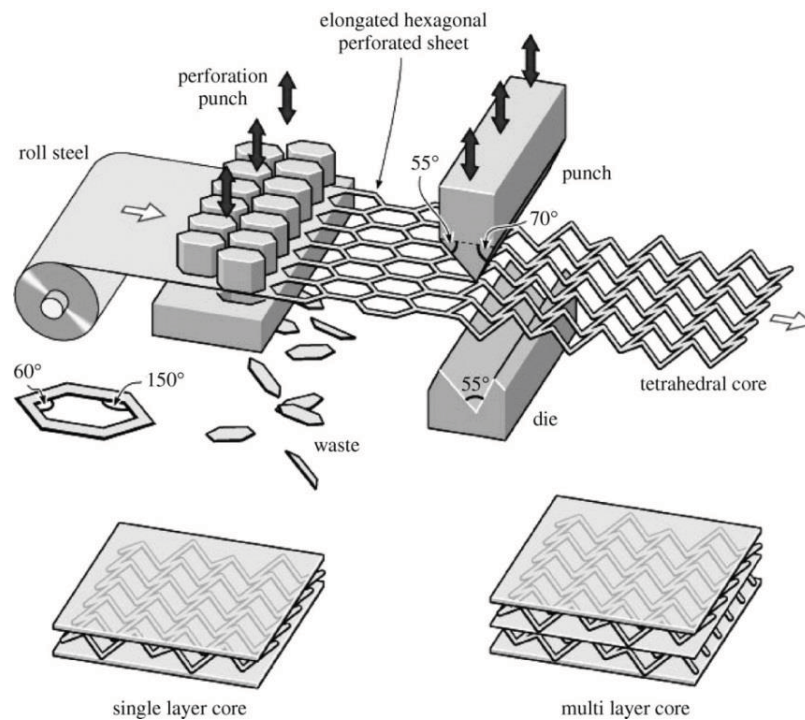


Figure 1.14: Tetrahedral truss structures created through a metal forming technique [24].

A 6061-T6 aluminum octahedral lattice structure is illustrated in Figure 1.15. It was constructed from multiple layers of tetrahedral structure that were manufactured by metal forming techniques. The nodes were bonded using a brazing process.

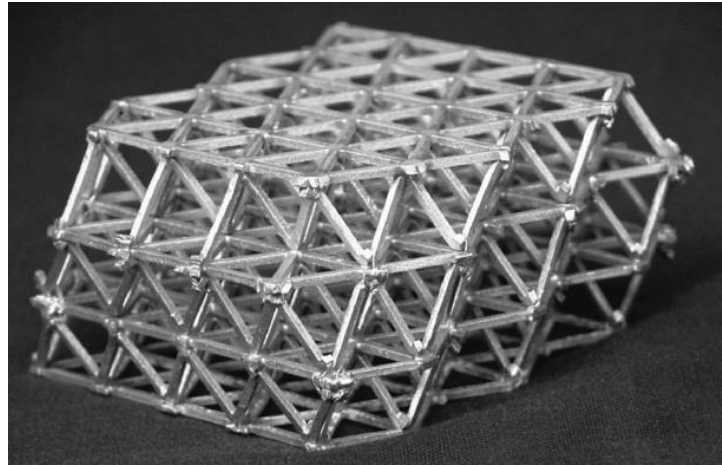


Figure 1.15: Sandwich panels based on tetrahedral trusses metallic lattice structures with a unit cell size of 10 mm [10].

In another approach, metal based truss structures were made from weaving and braiding of metallic wires [29]. It is considered a simple and cost-effective approach as it virtually does not involve any waste material. Any metal alloy that can be drawn into a wire can be utilized. The metal textiles are then stacked and bonded to create the periodic cellular core. By varying the orientation of the metallic woven fabrics, different topologies can be achieved, as illustrated in a $0/90^\circ$ and $\pm 45^\circ$ configurations of copper textile core sandwich structures shown in Figure 1.16.

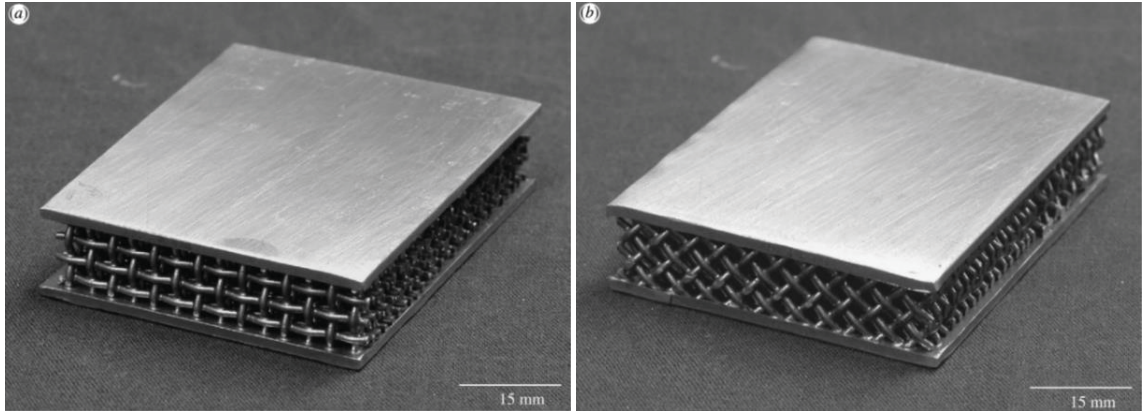


Figure 1.16: Sandwich structures based on copper textile cores configured at (a) $0/90^\circ$ and (b) $\pm 45^\circ$ orientations [24].

Weaving of metallic tubes to form the textile layer is more difficult, as they tend to buckle when plastically bent. Alternatively, a non-weaving approach can be utilized [29]. The wires, could be hollow or solid, are stacked in a slotted tool that maintains the wire spacing and orientation. The wires or hollow tubes are bonded or welded together and to the face sheets to achieve a square or diamond lattice topologies as illustrated in Figure 1.17. Manufacturing of hollow pyramidal lattice core structures is made possible through high precision drilling methods [29]. Core configurations based on hollow trusses make for a more efficient use of the material and has been identified as the one of the strongest cores, hence, making it an attractive design [6].

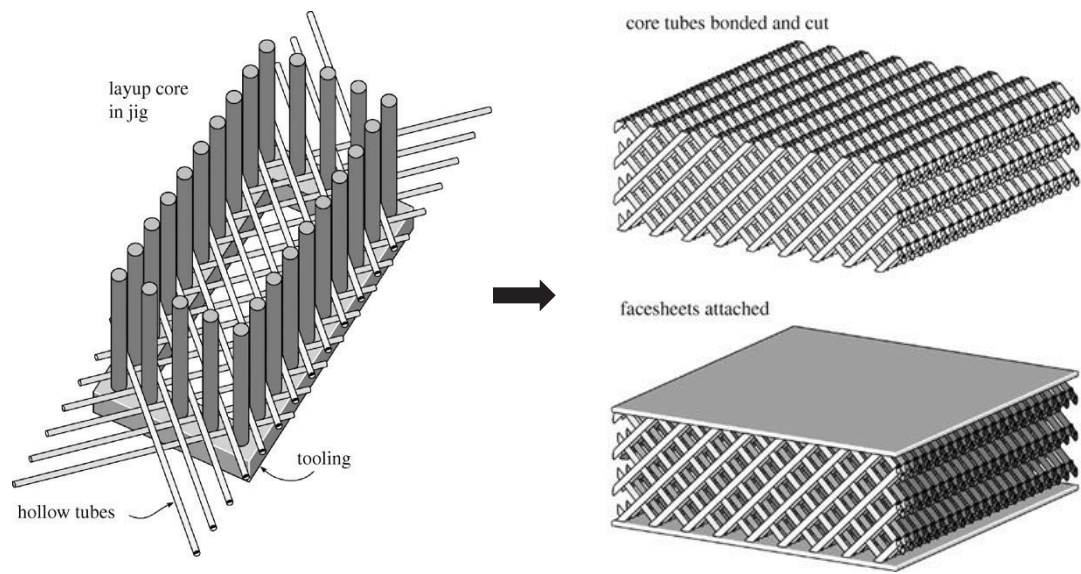


Figure 1.17: A Non-weave approach for manufacturing cellular core structures from solid wires or hollow tubes [24].

Recently, attention has focused on developing composite lattice structures that should, in principle, out-perform their metallic counterparts. Investment casting, folding, weaving and braiding methods are suitable for metallic-based lattice structures. In response, techniques for manufacturing of composite based lattice core structure have been developed. Recently, techniques such as hot press molding [30], mechanical interlocking [31] and folding and cutting flat sheets of composite material sheet [32] have been used to produce composite lattice structures of varying complexity. The hot press molding procedure involves the placement of pre-preg layers between a multi-part mold. Once the pre-preg has cured the carbon fiber composite pyramidal truss structures is removed from the mold and attached between two face-sheets using an adhesive as shown in Figure 1.18. In a similar approach called the hot-embossing method, the pre-pregs were placed in a mold with both ends embedded into the top and bottom face-sheets to form a single structure [33]. Once cured, the mold is removed, leaving a free standing pyramidal lattice core sandwich structure.

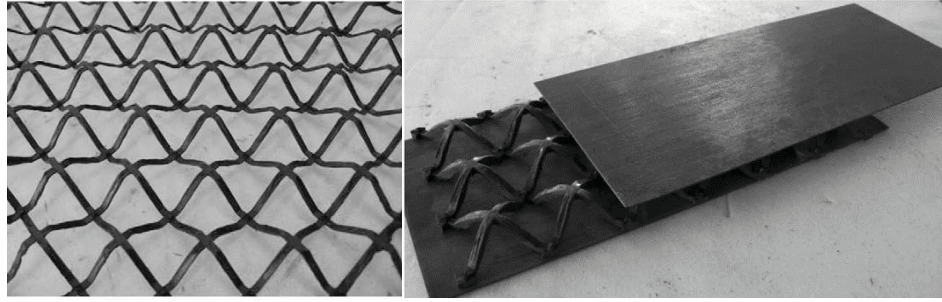


Figure 1.18: (a) Pyramidal lattice structure fabricated using the hot press mold and (b) adhesively bonded between skins to for the sandwich panel [30].

Another fabrication method that was investigated involves pultruded composite rods that are adhesively bonded to face sheets containing a series of pre-drilled holes to form the pyramidal truss members [31]. Following this, truss patterns were cut from unidirectional sheets and adhesively bonded into milled slots in the skins. These procedures were rejected as a result of premature failure of the bonds. A third technique proved more successful. Here, a semi-continuous truss pattern was cut from 0° , 90° panels using a water-jet cutting facility. The pyramidal structure was then formed by snap-fitting the members together and the skins were then bonded. A schematic diagram of the snap fitting approach is illustrated in

Figure 1.19.

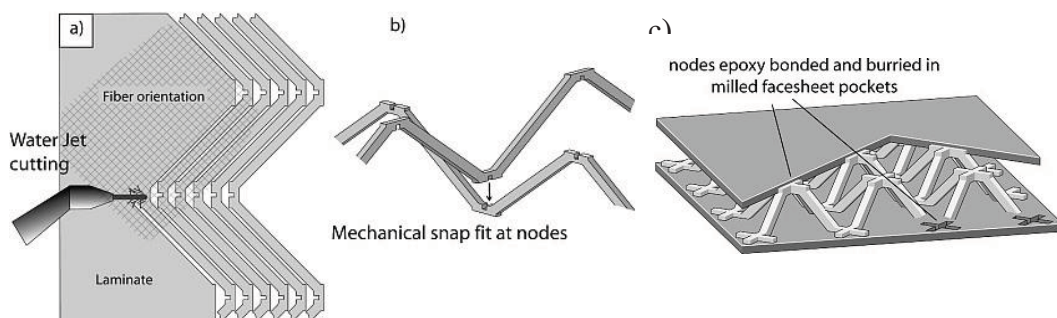


Figure 1.19: a) Truss member are water jet cut from laminate sheets, b) truss members are snap-fitted together forming the pyramidal lattice configuration. c) The truss were fitted and adhesively bonded in milled facesheet pockets [31].

The resulting pyramidal structures offered attractive mechanical properties when tested in compression [31], the results of which are plotted on an Ashby diagram of strength versus density shown in Figure 1.20. Here, although impressive, it is clear that the measured values fall below the limit associated with the unattainable materials space. This discrepancy was attributed to the inefficient use of material in the nodes and the onset of delamination from the nodal connections.

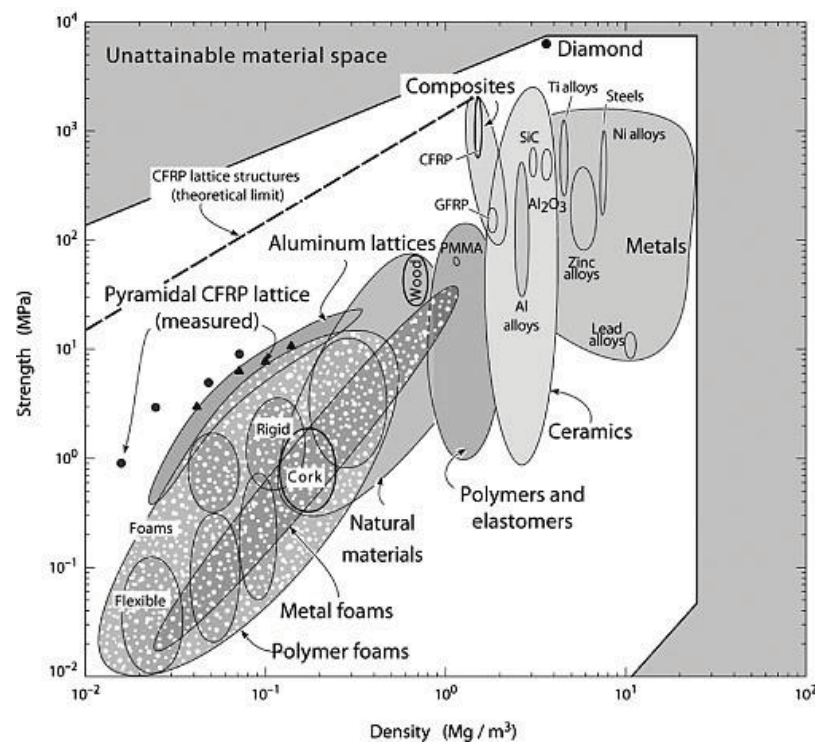


Figure 1.20: An Ashby strength versus density map for engineering materials [31]

Stretch–bend–hybrid hierarchical composite pyramidal lattice cores were manufactured using two different core configurations [34]. In the first approach (Figure 1.21a), a flat foam core sandwich plate produced by hot pressing was cut into strips. The strips were then snap-fitted together and incorporated with face-sheets by slot insertion at the nodes and adhesively bonded. In the second approach (Figure 1.21b), corrugated foam sandwich plate

was fabricated using a corrugated steel mold. Strips were then cut from the corrugated foam sandwich plate fit together by slot insertion at the pyramidal nodes.

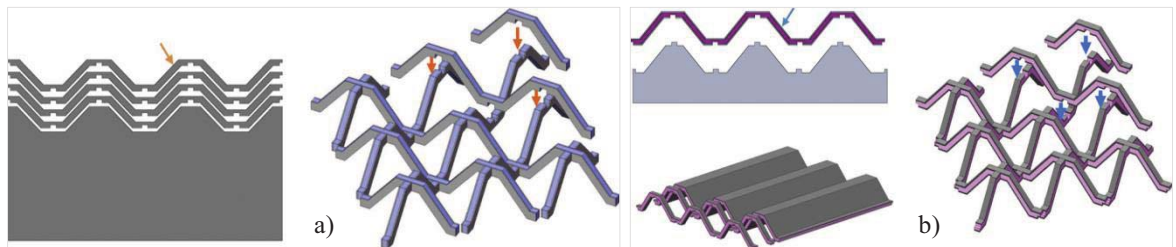


Figure 1.21: Schematic diagram illustrating the manufacturing procedure of the stretch-bend-hybrid hierarchical composite pyramidal lattice cores [34]

Further, the same authors manufactured what are termed stretch-stretch-hybrid hierarchical composite lattice cores, by employing a two-step approach that involved assembling pyramidal lattice sandwiches into macroscopic truss configurations [35]. The hierarchical pyramidal lattice structure is illustrated in Figure 1.22.

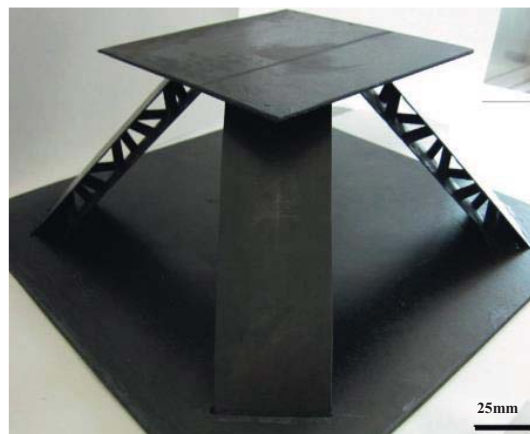


Figure 1.22: Stretch-stretch-hybrid hierarchical composite pyramidal lattice cores [35].

A more recent manufacturing route for lattice truss core material is based on carbon fiber reinforced thermoplastic polymer resin to produce lattice cores in a three step procedure [32]. Initially, the corrugated plate shape is fabricated by hot forming using corrugated

molds. Slots are then machined into the corrugated sheet at a predefined width and separation. Finally, the sheet is expanded into its final shape (Figure 1.23a). The fabricated core is then hot-bonded to stringer reinforced face-sheets, as illustrated in Figure 1.23b for a poly-ethylene terephthalate fiber reinforced poly-ethylene terephthalate. Experimental measurements revealed that the through thick compression strengths of these core were comparable to high end metallic cores.

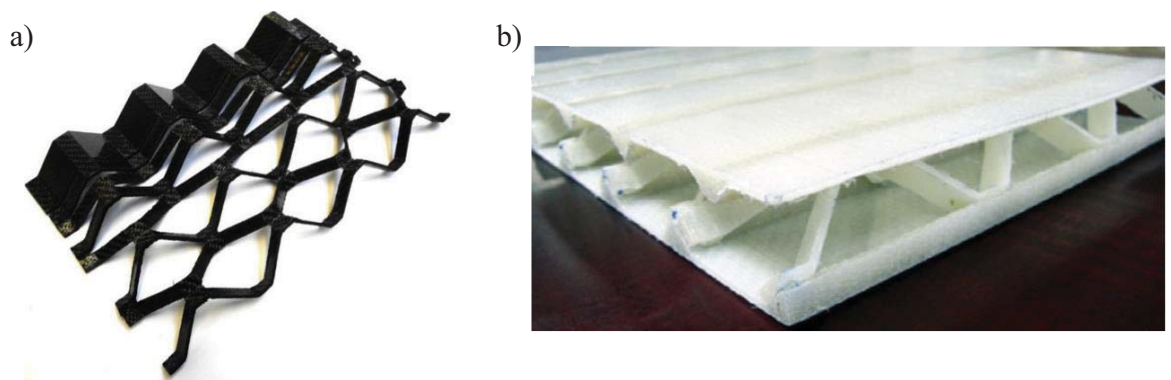


Figure 1.23: a) Manufactured Lattice core based on carbon fiber reinforced poly-ethylene terephthalate (CPET). b) Sandwich panel with a lattice truss core bonded to stringer reinforced face sheets [32].

Pyramidal carbon fiber reinforced epoxy lattices were also manufactured by means of electrical discharge machining (EDM) [30]. A flat top corrugated sheet of the composite material was manufactured by pressing in a hot mold. Near-pyramidal truss cores were created using an EDM plunge cutting technique that employed a suitably-shaped cuprite electrode. The face-sheets were finally adhesively bonded to the top and bottom of the manufactured core. Measured compression strengths were found to be lower than theoretical predictions due to debonding between the core and face sheets.



Figure 1.24: EDM Pyramidal carbon fiber reinforced epoxy lattices having a core relative density of 4.95% [34].

Using pultruded unidirectional fiber-reinforced composite rods, a semi-wire woven bulk Kagome' (WBK) structure was manufactured [36]. In this approach, straight rods were used to build the out of-plane struts, while helically-formed wires from carbon yarns held in a steel frame were used to build the in-plane struts. The entire assembly was then dipped in a pool of epoxy resin and allowed to cure at room temperature with this process repeated multiple times. The steel frames were then removed from the assembly leaving a finished semi-WBK composite core. All manufactured types failed by premature collapse at the ends of the pultruded rods under compression.

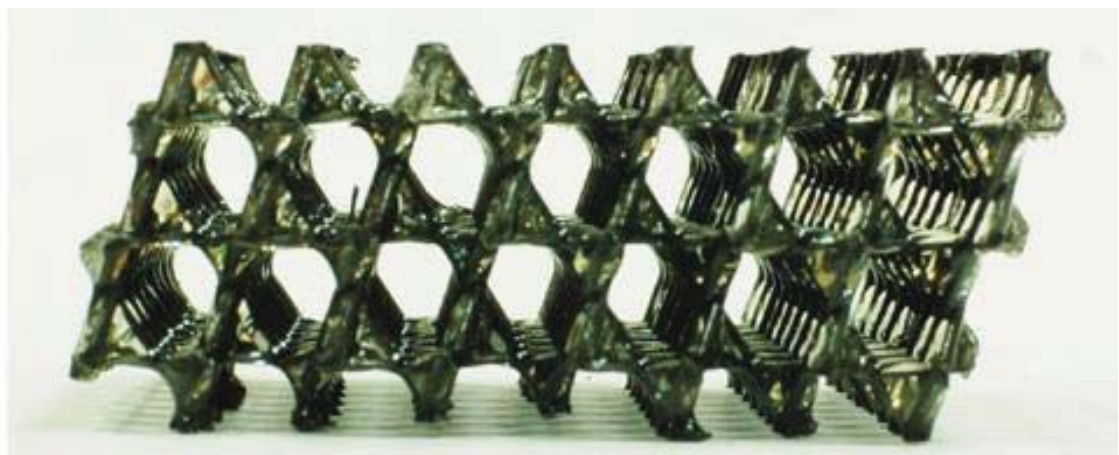


Figure 1.25: Finished semi-WBK composite core [36].

Finally, hybrid core carbon fiber composite sandwich panels have been assembled from a braided carbon fiber pyramidal lattice with polymer foam inserts configured as the core of the sandwich panel [37]. The dry assembly begins by stitching the braid to the face sheets, while overlapping the foam inserts as illustrated in Figure 1.26. The entire stack is sealed in a vacuum bag and infused with resin using the Vacuum Assisted Resin Transfer Molding (VARTM) procedure.

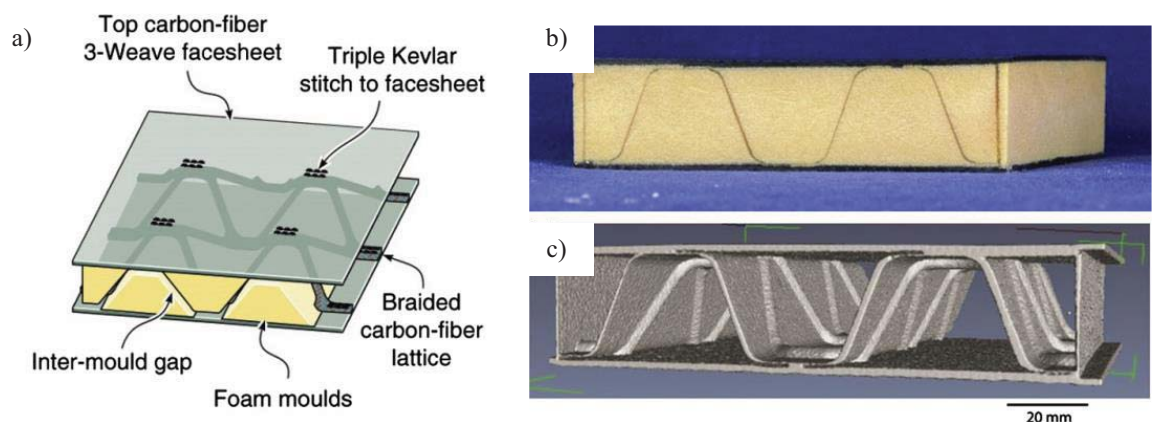


Figure 1.26: a) The hybrid CFRP pyramidal lattice core sandwich panel assembly, b) Photograph of manufactured sample and c) x-ray image showing the interior core structure of the panel [37].

Generally, the principle feature in periodic lattice core structures is that when the panel is subjected to a load, the core members stretch or compress without significant bending. Figure 1.27 illustrates a unit cell of an octahedral micro-lattice structure. It is an example of a structure having $M = 18$ with many states of self-stress but no *mechanism*, therefore, its mechanical response is stretch-dominated [19]. Using the same approach used in deriving the stiffness and strength relations as a function of density, stretch-dominated micro-truss lattice materials can be shown to have stiffness and strength properties that are linearly proportional to relative density as follows,

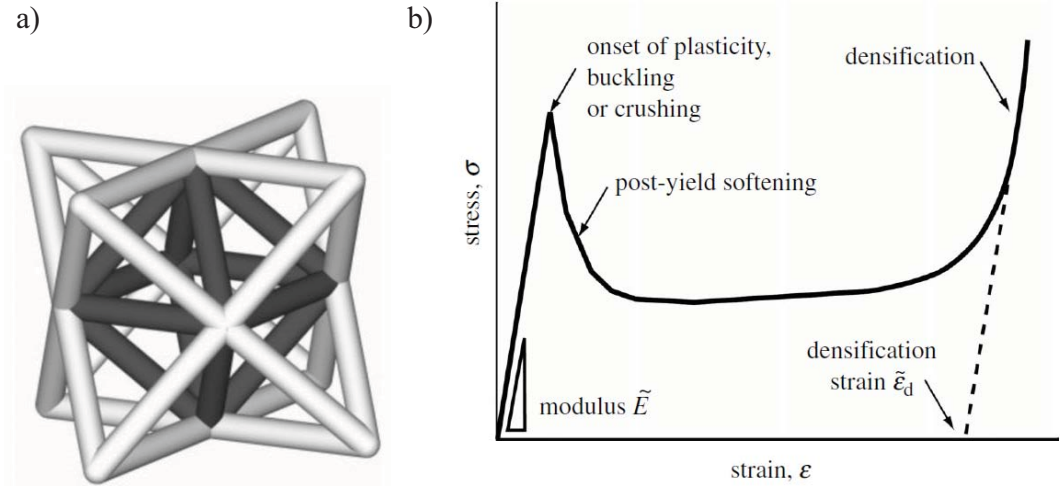


Figure 1.27: a) Unit cell of an octahedral lattice configuration. b) Stress-strain curve of a stretch dominated structure [19].

$$\frac{E}{E_s} \propto \left(\frac{\rho^*}{\rho_s} \right) \quad (1.7)$$

The lattice struts continue to deform elastically up to the yield point, upon which the material fails due to plastic yielding, or fracturing, depending on the nature of the parent material. The collapse strength in a plastic stretch-dominated truss is:

$$\frac{\sigma_{pl}^*}{\sigma_{ys}} \propto \left(\frac{\rho^*}{\rho_s} \right) \quad (1.8)$$

It is evident from Equations 1.7 and 1.8 that the elastic modulus and initial collapse strength of a stretch-dominated cellular material are significantly higher than those of bending-dominated materials having the same relative density. Figure 1.27b illustrates a typical stress-strain trace of a stretch-dominated structure demonstrating the post-yield softening. This makes such structures less attractive for energy-absorbing applications that require the post-failure stress-strain curve to have a long flat plateau as observed in bending-dominated structures. The relative modulus is plotted against relative density for a

various cellular materials, as observed in Figure 1.28. The dashed lines represent the behavior of an ideal stretch and bending-dominated lattices.

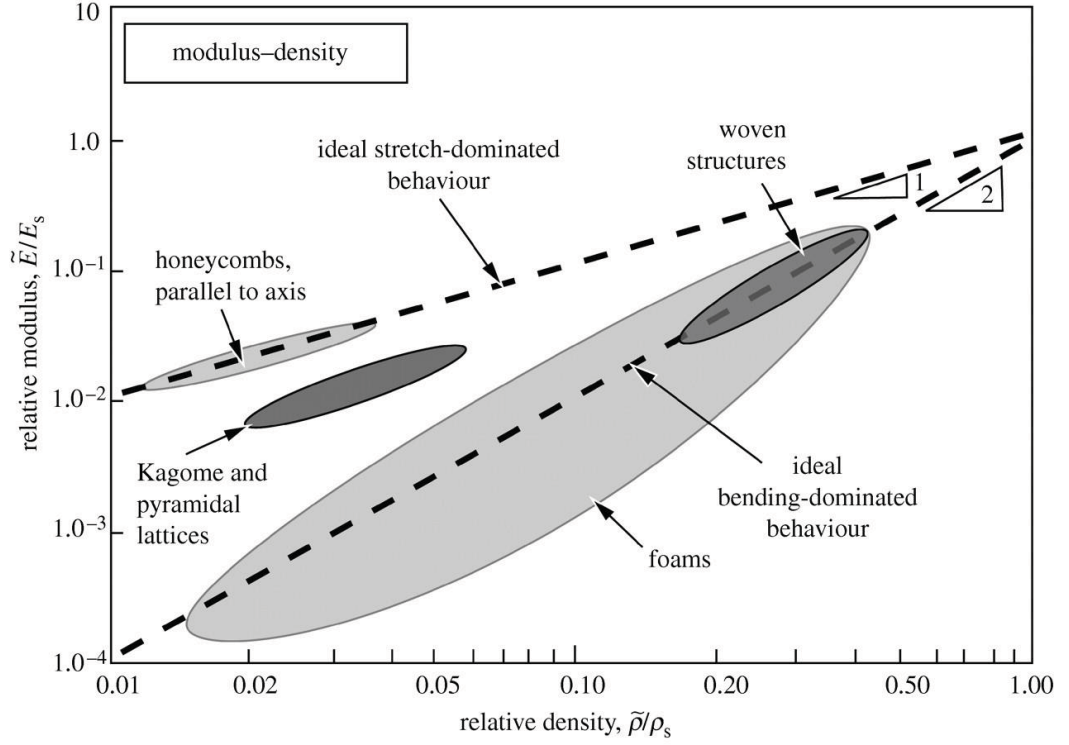


Figure 1.28: Variation of relative modulus with relative density for various cellular materials. The line of slope 1 represents stretch-dominated structures, while slope 2 corresponds to bending-dominated materials [19].

Stretch-dominated structures have a modulus that scales linearly with relative density, as illustrated in Equation 1.7 and this is represented by slope 1 in Figure 1.28. Bending-dominated structures have a modulus that scales with the square of relative density, as shown in Equation 1.2 and the dashed line, slope 2, in the same figure. Foam materials represent an excellent example of bending-dominated structures. They generally fall below the ideal dashed line of slope 2 due to the heterogeneous nature of their structures. The current generation woven lattice structures achieve the optimal values and lie directly on the ideal line for the bending-dominated behavior structure. Hexagonal or square

honeycombs, when loaded in the out-of-plane direction, achieve the optimal values for Young's modulus and lay on the ideal stretch line. The through-thickness Young's modulus for a square or hexagonal honeycomb is given by [29],

$$\bar{E} = \bar{\rho}_c E \quad (1.9)$$

On the other hand, pyramidal, tetrahedral and triangular lattice cores have \bar{E} reduced by a factor α that scales with the inclination angle ω the struts make with the face-sheet as [29]:

$$\alpha = \sin^4 \omega \quad (1.10)$$

They exhibit stretch-dominated properties and lie below the ideal line by a factor that is proportional to the inclination angle of their struts according to Equation 1.10.

For strength, the same general trend is observed in Figure 1.29 with some variations. Stretch-dominated materials have strengths that scale linearly with relative density, as shown in Equation 1.8, represented by the dashed line of slope 1. Bending-dominated structures scale as $(\rho^*/\rho_s)^{3/2}$ with a line of slope 1.5.

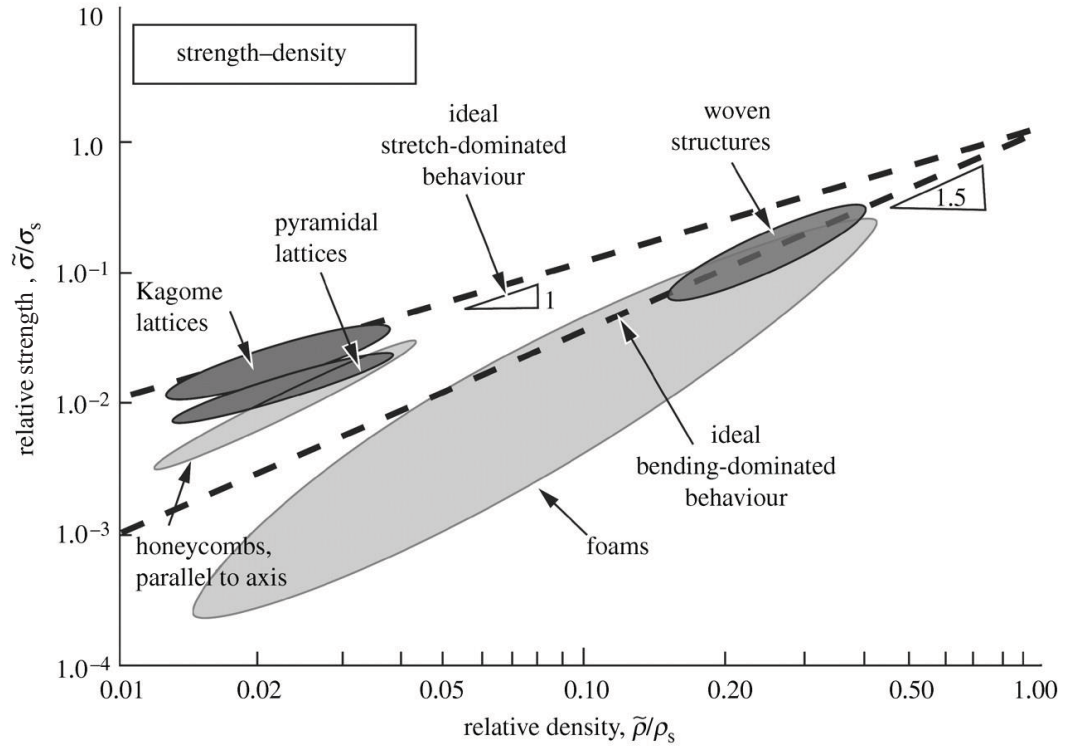


Figure 1.29: Variation of relative strength with relative density for various cellular materials. Stretch dominated structures lie along a trajectory of slope 1; bending dominated structures along line of slope 2 [19].

Lattice structures, such as the pyramidal and Kagome' topologies, offer near-ideal stretch-dominated performance. Honeycombs when compressed in the out-of-plane direction fall below the ideal line because the thin cell walls are prone to buckling. Woven structures lie on the bending-dominated ideal, while foam structures underperform, due to the micro-defects arising from the stochastic nature of manufacturing.

Given the many difficulties associated with manufacturing composite lattice structures, defects and other forms of stress concentration are likely to occur. Chen *et al* [38] investigated the effect of defects on the compressive properties of carbon fiber pyramidal

lattice structures and showed that, compared to open cell foams and honeycombs, pyramidal cores offer a superior defect tolerance.

In addition to through thickness compressive loads, sandwich panel structures are used in applications where they are subjected to various significant loading conditions. One particular area that is attracting significant interest relates to the design and manufacture of lightweight wind turbine blades for use in the energy-generation sector. Clearly, when in operation, wind turbine blades are likely to be subjected to a complex loading history involving coupled deformation modes. The long-term reliability of such blades requires a detailed understanding of the loading patterns within the component, as well the resulting failure modes and their dependence on external parameters such as local temperature, relative humidity and strain-rate.

Leong *et al* [39] investigated the effect of defects on the failure modes in sandwich structures based on thick GFRP face sheets and a balsa core. The samples contained a defect in the form of a wrinkle and were loaded in compression and the strain fields monitored using digital image correlation techniques. The authors showed that the sequence of events leading to failure can be divided into three failure modes, debonding between the core and the face sheets, failure of the face sheet containing the wrinkle and finally complete specimen failure. Skin-core debonding is a common and potentially catastrophic failure mode that is frequently observed in statically and dynamically-loaded sandwich structures.

Hirose *et al* [40, 41] developed a splice-type crack arrester to suppress Mode I failure in sandwich panels based on a foam core. Experimental testing under conditions of Mode I loading showed that the carbon fiber fabric crack arrester resulted in an order of magnitude

increase in the measured fracture toughness. A subsequent finite element analysis of the region immediate to the arrestor indicated that the local strain energy release rate was greatly decreased leading to potential arrest of the propagating crack. A number of researchers have investigated the use of peel stoppers to arrest or modify crack propagation in sandwich structures [42, 43]. Grenestedt [42] developed a peel stopper for potential use in the design of high speed ships. The author noted two specific advantages of the design, these being its ease of manufacture and an absence of connections through the core. Quasi-static tests showed that the peel stoppers performed the desired function and, if correctly designed, did not adversely affect the strength of the structure. Bozhevolnaya *et al* [43] developed a polymer-based peel stopper which could be used as a core insert or as an edge stiffener in a sandwich structure in order to prevent debonding between the skin and core of a sandwich structure. They showed that whilst the peel stoppers did not greatly influence the fatigue life of the sandwich beams, they were highly effective in forcing the crack away from the critical skin-core interface. A number of researchers have investigated the possibility of stitching sandwich panels to reduce debonding and delamination [44–46]. Lascoup *et al* [44] investigated the compressive and shear properties of angle-stitched sandwich structures based on a glass fiber reinforced polyester resin and concluded that the density of the stitches is the most critical parameter in determining the mechanical properties of the sandwich structure. Potluri *et al* [45] conducted quasi-static indentation tests on sandwich panels based on glass fiber reinforced polyester skins and a PVC polymer foam core. The skins were stitched together using a Kevlar 129 yarn. The authors showed that through-thickness stitching significantly reduced the measured debonding area in the

sandwich panels. The energy required to perforate the lower skin initially decreased with increasing stitching density, before increasing monotonically at higher stitch densities.

Based on the above discussions, one can conclude the following, the sandwich panel construction offers excellent mechanical properties at minimal weight. The selection of core type depends on the requirement of the application it is used for. For energy absorption and cushioning applications, foam cores characterized as bending-dominated lattice materials, would be suitable. They offer low stiffness and strength but can undergo large strains. On the other hand, the struts within the lattice material can be arranged in a way that so that strut-stretching is the dominant deformation mode rather than bending. Stretch-dominated lattice cores are excellent for application where high strength and stiffness are required at minimal weight. Micro-truss structured materials based on the pyramidal and Kagome' topologies offer near-ideal stretch-dominated performance. The objective is to investigate the performance of well-known topologies of composite micro-truss structured materials using a new manufacturing technique in an attempt to fill the gap within the unattainable materials space. In addition, methods for enhancing the debonding strength between the core and the face sheets will be investigated.

1.6 Manufacture

Generally, composite sandwich structures are manufactured from two thin but stiff sheets with a thick light weight core attached between them. Typically, the face-sheets and core are manufactured separately and the sandwich panel is subsequently fabricated by attaching the skins on each side of the core. The core is bonded to the skins with an adhesive and by brazing or laser welding for sandwich panel of metallic components. Various manufacturing methods have been developed to achieve sandwich panels that are strong and stiff, yet light in weight as previously discussed. A brief review of composite materials manufacturing is included.

The manufacture of structures from traditional materials, such as metals, involves machining, molding, cutting and joining of the solid materials that are in the forms of sheet, rod, beam or block. However, for structures made from composite materials, the material and the component are manufactured simultaneously [47]. The goal in composite manufacturing is to produce the net-shape of the component, having the desired properties, with minimum post-processing machining and trimming. In addition, the process must produce a finished product that is free from significant defects (voids, cracks, and fiber waviness) with uniform properties. The manufacturing process has a great influence on the final properties of the produced part. Due to this notable processing–property dependency, the manufacturing method should be selected concurrently with the raw material selection and structural design in a unified and interactive process [2]. Numerous methods of manufacturing composites have been developed to meet specific design and or manufacturing requirements. They include autoclave molding, filament winding, automated

tape/fiber placement, injection molding, pultrusion, resin transfer molding and vacuum-assisted resin transfer molding. A brief review of some of these methods is given below.

1.6.1 Autoclave molding

The autoclave molding process is used to fabricate aircraft grade composite components. The process uses materials in pre-preg form. Pre-preg materials are sheets of aligned fiber pre-impregnated with matrix precursor in the form of resin containing hardener that has been partially cured. The pre-preg sheets are cut to shape and placed on a rigid mold in the proper position, orientation and sequence to form a layup. The layup process can be performed manually or automated through the use of automated tape layers or automated tow placement machines. A bleeder/breather is used to soak up excess resin and to allow the escape of gases during curing. After the layup process is complete, a vacuum bag is applied to the surface of the layup and sealed to the mold as shown in Figure 1.30.

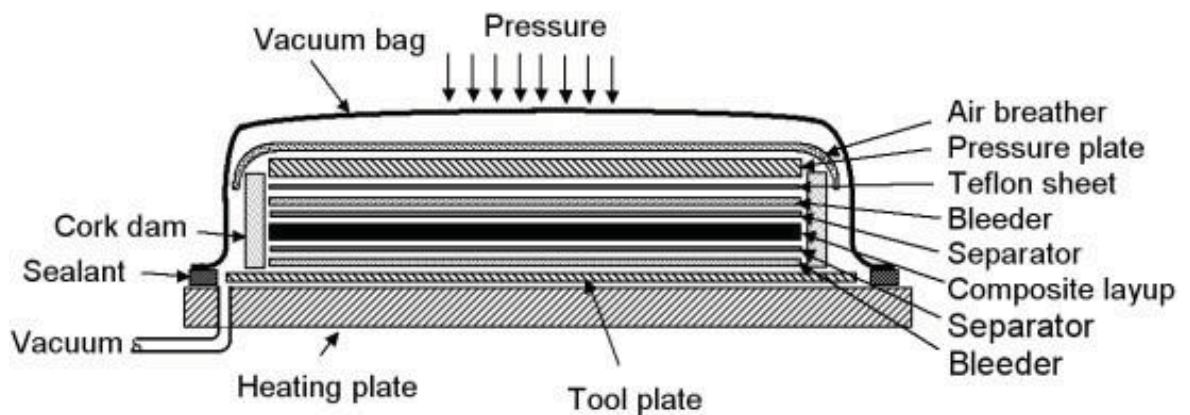


Figure 1.30: layup assembly for autoclave molding of composite laminates [2].

The entire assembly is placed into an internally-heated pressure vessel with internal connections for vacuum hoses (autoclave). The curing process is performed according to the prescribed temperature-pressure-vacuum-time cycle inside the autoclave. The curing process is performed at elevated temperatures and pressure. This allows for a high fiber

volume fraction, low void content and ensures that the service temperature of the composite is sufficiently high.

1.6.2 Filament winding

The process basically involves the winding of continuous fibers under tension, impregnated with resin, over a rotating or stationary mandrel. The fiber tows pass through a resin bath before being wound onto the mandrel as illustrated in Figure 1.31. This process is best suited to components having surfaces of revolution such as pipes, pressure vessels and other circular or oval sectioned components. The desired part thickness, ply layup and fiber volume fraction can be achieved by controlling the winding tension, winding angle and resin content during the laying of the fiber. Once the mandrel is covered to the desired thickness, the resin is cured and the mandrel is removed leaving the hollow finished product.

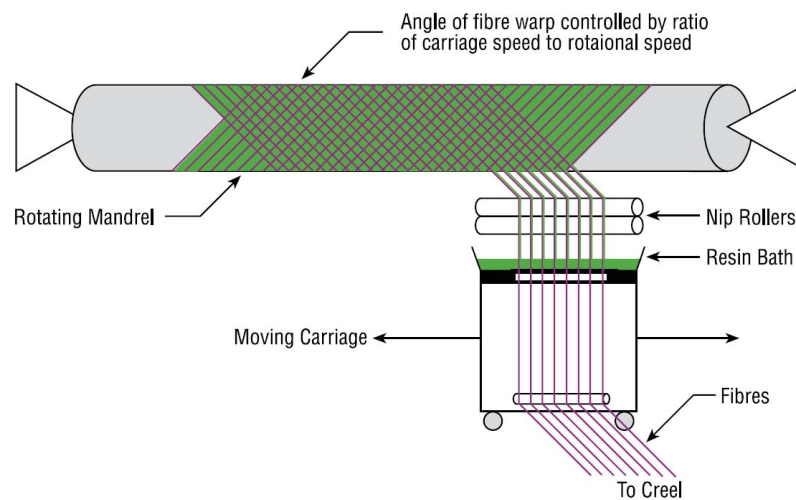


Figure 1.31: Schematic of filament winding process [48].

1.6.3 Resin transfer molding

Resin transfer molding (RTM) is a process that involves placing the dry fabric preform into the cavity of a two-part, matched, closed mold and then filling the mold and hence the preform with liquid resin (Figure 1.32). Pressure is used to inject resin into the mold through injection ports, following predesigned paths through the preform. After injection, the mold temperature is increased to cure the part according to the prescribed time-temperature curing cycle.

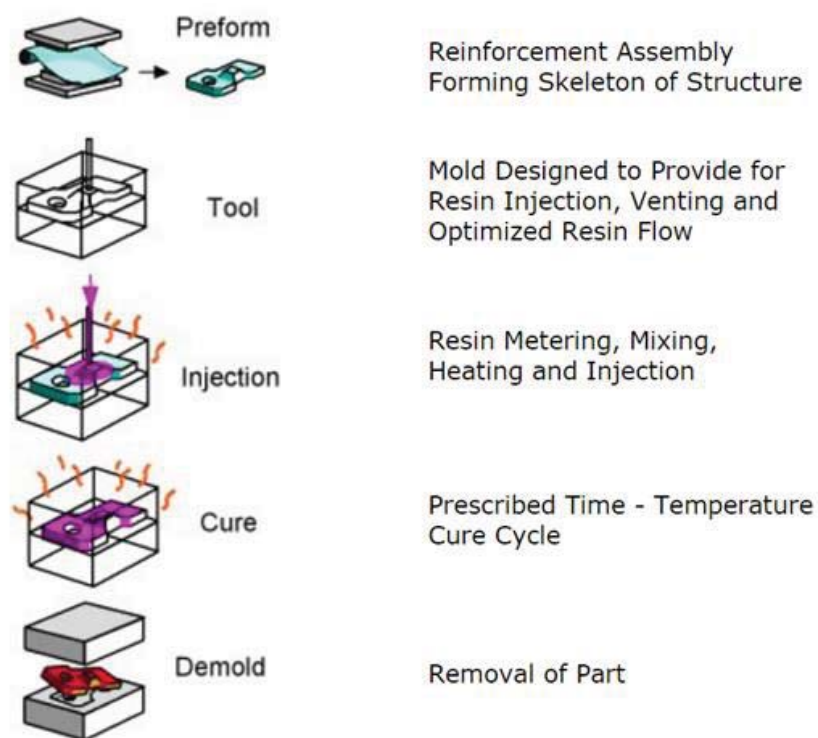


Figure 1.32: Schematic of the RTM process [2].

A variation of the RTM process is the vacuum assisted resin transfer molding (VARTM) process. It involves laying the dry fiber preform over an open mold surface, then placing a peel ply and a permeable membrane to facilitate the flow of resin. The assembly is covered with a vacuum bag and bag leaks are eliminated. Inlet and exit feed tubes are positioned through the bag, and a vacuum is pulled at the exit to infuse the preform (Figure 1.33).

VARTM does not require high temperatures or pressure thus reducing tooling cost and making it suitable for producing large complex components in one shot.

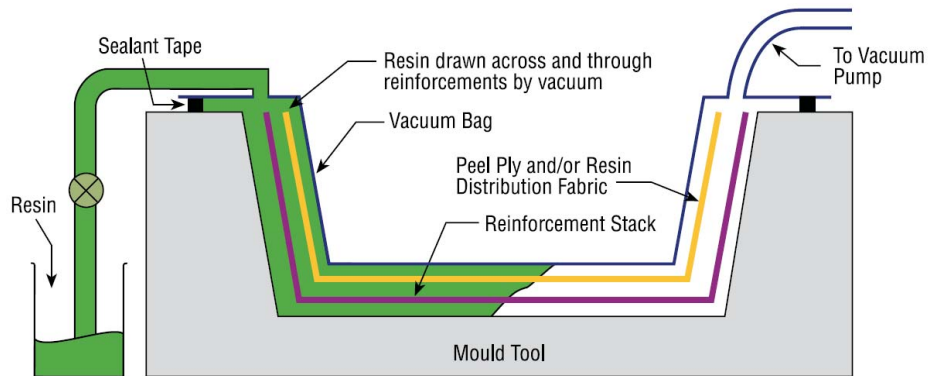


Figure 1.33: Schematic of VARTM process [48].

It is essential to select an appropriate manufacturing process that can be implemented economically with ease while at the same time, maintaining high uniformity and quality. The manufacturing of traditional sandwich structures is labor intensive and a multi-stage process. The core and face-sheets are manufactured separately, subsequently; the face-sheets are then bonded to the core using some form of adhesive. Sandwich panels based on a more complex core configuration such as periodic lattice structures are not obtainable using traditional manufacturing processes. New methods for manufacturing these periodic lattice core sandwich structures were developed as previously described; however, they are considered even more labor intensive when compared to traditional sandwich panels. In most cases, they also require that the core and skins to be shaped to low tolerances to achieve suitable bonding. It is desirable to develop a one-shot process for fabricating periodic lattice sandwich structures, while maintaining quality and uniformity. VARTM process has this merit in which it allows for the core and face-sheets to be formed, cured and bonded together. This has the benefit of eliminating the complicated process of

bonding the face-sheets to the core making the manufacturing process more viable. Traditionally, the VARTM process is not suitable for open cell core materials, as the resin flowing through the preform stack during the infusion process would be drawn to fill all the voids. Resin accumulation in the core is a major challenge in the fabrication of honeycomb sandwich panels using the VARTM process [49]. To enable the manufacture of the micro-lattice core panels using the VARTM process, the Lost-mold technique was developed in this study. The technique is based on the VARTM process and varies by incorporating a removable core within the preform stack. A review of the primary elements of the VARTM process are introduced.

1.7 Vacuum Assisted Resin Transfer Molding (VARTM) process

Liquid composite molding (LCM) encapsulates all the manufacturing process such as Resin Transfer Molding (RTM), Vacuum Assisted Resin Transfer Molding (VARTM), etc. where the matrix in its liquid form is infused into the dry reinforcing fabric. In general, LCM techniques consist of the following production steps [47]:

- Placement of dry reinforcement (preform) stacks in a mold.
- The mold assembly is closed.
- Resin flows through the mold and impregnates the reinforcement.
- The resin is allowed to cure.
- The mold is opened and the product is demolded.

The VARTM procedure is considered a derivative of the RTM process in which the top rigid mold found in the RTM process has been eliminated and replaced by a flexible vacuum bag while a pressure gradient is created by pulling vacuum on the outlet port in order to apply atmospheric pressure to the component.

By eliminating the need for pre-preg materials and autoclave ovens, the VARTM process offers a cost-effective approach for manufacturing composite structures ranging from small components of simple shape to large components with complex shape and high structural performance characteristics [50]. The demand for driving down the cost associated with manufacturing wind turbine blades within the energy generation sector, has generated an increasing interest in LCM techniques, such as VARTM process [51]. Consequently, high-performance components for the wind energy and the marine industries have been successfully manufactured using this process [52]. High process variability, lower achievable fiber volume fractions, dimensional tolerances and mechanical properties

compared to autoclave processing, limited its application within the aerospace industry [52]. More recently, a better understanding of the process physics, the automation of injection equipment and improved materials [50, 53–60] have reduced the barriers for wider usage and enabled the process to be considered for the manufacturing of aerospace grade components. The VARTM process has been successful in manufacturing the C-17 Main landing Gear Door and Forward Pylon of the Chinook that meet the performance requirements (Figure 1.34) [61]. Primary structural components for civil air transportation such as the Airbus A380 flap tracks and Boeing 787 pressure bulk head are currently in production and manufactured by the VARTM process (Figure 1.34) [61].

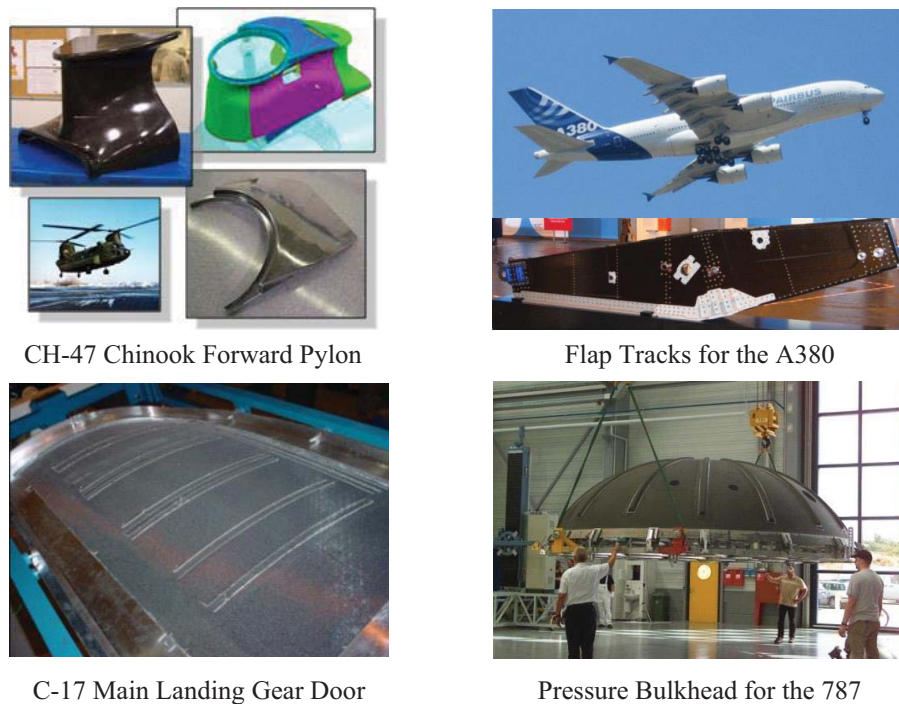


Figure 1.34: Aerospace components manufactured using the VARTM process [61].

1.7.1 Variations of the VARTM process

Several variations of the VARTM process have been patented, all with the same principle of pulling liquid matrix into a sealed dry fiber preform under vacuum only. A non-

exhaustive list of significant infusion technology patents includes 20 processes that span a 45 year time period is illustrated in Table 1.1. The overall objective is to achieve an improved laminate quality by increasing the fiber volume content, decreasing voids and improving surface finish.

Table 1.1: Resin infusion patents overview [62].

Entity	Year	Patent #	Description
Muskat	1950	2,495,640	Marco Method
Smith	1959	2,913,036	Process and apparatus for molding large plastic structures
Geringer	1964	3,137,898	RTM
Muskat	1967	3,342,787	RTM
Group Lotus	1972	(GB) 1,432,333	Vacuum molding patent
Johnson	1979	4,132,755	Process for manufacturing resin-impregnated, reinforced articles without the presence of resin fumes
Rolston	1980	4,238,437	Method for producing fiber reinforced product
Fourcher	1982	4,312,829	Molding method
Palmer	1982	4,311,661	Resin impregnation process
Lecomte	1982	4,359,437	Method and apparatus for producing a thin-walled article of synthetic resin, in particular a large-sized article
Letterman	1986	4,622,091	Resin film infusion process and apparatus
Krauter	1988	4,759,893	Method of making FRP molded parts
Epel	1989	4,873,044	Method and apparatus for reduction of mold cycle time
McGowen	1989	4,886,442	Vacuum bag tooling app. with inflatable seal
Seemann	1990	4,902,215	Plastic transfer molding techniques for the production of fiber reinforced plastic structures
Palmer	1990	4,942,013	Vacuum resin impregnation process
Lindgren	1990	4,975,311	Vacuum lamination station
Bailey	1995	5,588,392	Resin Transfer molding process (for boat hulls)
Seemann	1995	5,439,635	Unitary vacuum bag for forming fiber reinforced composite articles and process for making same
McGuiness	1996	5,526,767	Method of manufacturing a boat hull

Three of the most significant VARTM process variations include: Seemann Composites Resin Infusion Molding Process (SCRIMP), Vacuum-Assisted Process (VAP) and Controlled Atmospheric Pressure Resin Infusion (CAPRI). A brief review of the more widely known and used infusion methods follows.

1.7.1.1 SCRIMP

Seemann Composites Resin Infusion Molding Process (SCRIMP) [63] is one of the earliest patented VARTM variation. It is used in marine and wind blade applications and is licensed by several firms for fabricating aerospace-grade composites. This technique uses a single-sided tool, on which the dry fabric preform is laid and covered with a highly permeable distribution medium before being sealed in a vacuum bag. When vacuum is applied, resin flows preferentially across the surface and simultaneously through the preform thickness. This method allows for the infusion of components with a large surface area where a one sided quality finish is acceptable.

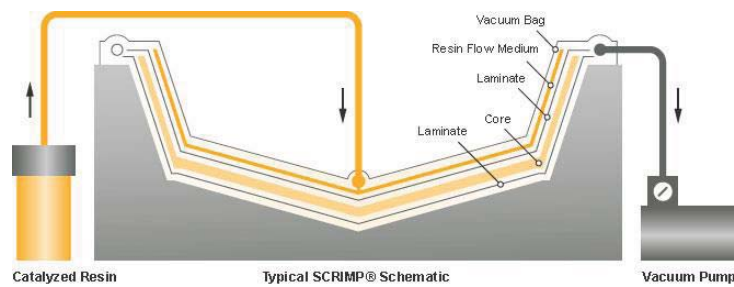


Figure 1.35: Schematic of a typical SCRIMP process [64].

1.7.1.2 VAP

Vacuum-Assisted Process (VAP) is developed and patented by EADS Deutschland [65]. This process features a semi-permeable membrane placed below the vacuum bag separating the vacuum outlet from the surface of the part (Figure 1.36). The membrane is permeable to gas and impermeable to resin which serves to create a uniform vacuum over the surface of the part and provides continuous resin degassing during infusion. This results in a part with a more uniform thickness and reduced void content/dry spots [66]. Examples of components manufactured using the VAP process include the floor structure for the Airbus

350XWB and the cargo door of the Airbus A400M transport aircraft, measuring 7 m x 4 m [67].

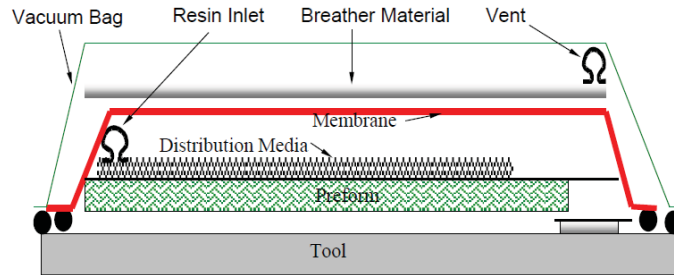


Figure 1.36: Schematic of the VAP setup [61].

1.7.1.3 CAPRI

Controlled Atmospheric Pressure Resin Infusion (CAPRI) was developed by Boeing to improve thickness and fiber volume variability in infused composites [68]. First, the dry preform goes through repeated compression-relaxation cycles, pre-infusion debulking phase, to reduce compressed thickness prior to infusion. During infusion, a partial vacuum is applied to the resin reservoir, effectively reducing the pressure gradient from inlet to vent location. The CAPRI process results in a composite having a smaller thickness gradient, but it can increase the infusion time significantly.

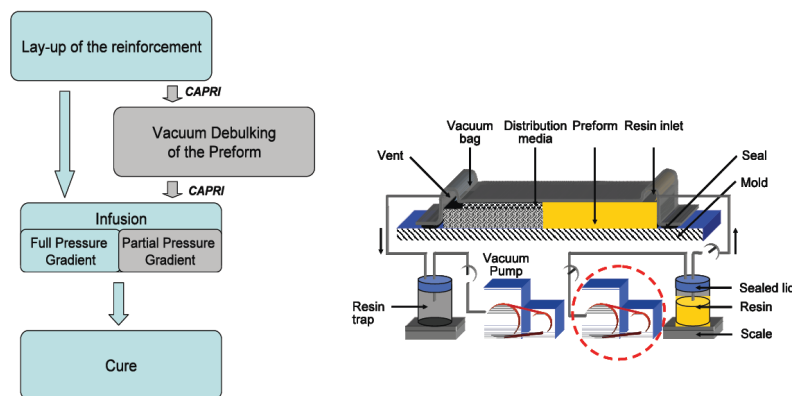


Figure 1.37: Schematic of the CAPRI setup and processing steps [61].

1.7.2 VARTM process and quality of composite

In general, all process variations that fall under the VARTM process umbrella can be divided into a three step procedure, material preparation, infusion, post infusion. Each step of the process has an influence on the quality of the composite, in terms of fiber volume fraction and void content. The following is an overview of the main mechanisms affecting the quality of the final part during each phase of the manufacturing process.

1.7.2.1 Material preparation

During the material preparation phase, the dry fibers, fabric, preforms and other reinforcing materials are cut to dimensions and laid into the mold. Depending on the final part quality requirements, the preform stack has to be dried under vacuum prior to infusion in order to evacuate any trapped moisture. Mixing and degassing of resin prior to infusion ensures that all resin components are blended together with minimum entrapped gases content. The vacuum bag placed over the preform to seal the mold must be properly installed to ensure minimum leak rate. Air leakage during the infusion stage will result in improper flow of resin through the mold, formation of air bubbles and higher-void content parts.

The behavior of a fibrous material when compacted is of great importance during the VARTM process as it influences the infusion process and final part thickness due to nesting of fibers into gaps in the preform structure [59, 60]. This compressive deformation of the preform occurs prior to resin infusion during the debulking phase or during resin impregnation. Once the dry preform is evacuated to a compaction pressure of 1 atm, thickness decreases and fiber volume content is increased. Under atmospheric pressure, the dry fiber content can be maximized by cyclic loading/debulking. Fabric investigated by Gama *et al.* exhibited a hysteresis response to compaction due to increased nesting effect

after each successive loading cycle [69]. The CAPRI process described earlier, utilizes a cyclic debulking phase which changes the permeability and compaction properties to minimize thickness gradients and increase fiber volume fraction [70].

Dry preform, degassed resin, and vacuum bag integrity are essential for a void-free composite, while compaction of the preform serves to increase the fiber volume content of the finished part.

1.7.2.2 Infusion

The purpose of this step is to fully impregnate the dry preform with liquid resin before the resin begins to solidify or gel. Suppression of dry spots and voids improves the composite quality and strength. Modeling of the flow during the infusion stage highlights potential problems prior manufacturing and allows for the optimization of the injection scheme which involves the placement of resin inlet(s) and vent gate(s). Darcy's law is used to model the flow through porous media and has been found successful in modeling the flow of resin through fiber preforms and resin distribution media [54]. The governing equation for Darcy's law is given by:

$$u = \frac{-K}{\mu} \cdot \nabla P \quad (1.11)$$

Where, u is Darcy's velocity, defined as the total flow rate per total flow front area, K is the permeability tensor, which characterizes the ease of flow through the fiber preform, and μ is the viscosity of the resin. This when coupled with mass balance, one can solve for fluid pressure field inside a region permeated by resin. Darcy's law serves as a foundation of several analytical [71] and finite element models [72] that have been developed to predict the flow patterns and the fill time. These helpful tools need the permeability values of the

reinforcement, resin viscosity and process pressure in order to make accurate predictions of fill time and flow patterns.

Bickerton *et al.* [57] presented a numerical and experimental mold-filling case study in which an actively controlled resin injection scheme has been implemented to eliminate dry spots (the same mold-filling case but with a simple injection scheme resulted in dry spots). The SCRIMP process described earlier incorporates a distribution media placed over the preform to enhance resin flow and allow for the infusion of components with a large surface area [64]. The VAP process adds a membrane which allows for continuous venting the surface and continuous flow of resin into the preform fabric, potentially minimizing/eliminating large void areas [66]. In order to enhance resin flow during VARTM manufacture of sandwich panels, holes are sometimes drilled through the core, facilitating the movement of the resin flow front from one skin to the other [73]. Another approach involves elevating the processing temperature; effectively reducing resin viscosity to enhance the flow. Majumdar *et al.* [74] reported an improved wetting of the core and face-sheet of sandwich panels manufactured using elevated temperature VARTM that process higher temperature epoxy resin (88C°).

Numerical models are an excellent tool for predicting the flow pattern, fill time and potential dry spot regions. These tools must be applied in conjunction with accurate material property data to yield accurate predictions. The incorporation of a distribution media or venting membrane, the utilization of an actively controlled injection system, improved material properties, etc. are some of the methods used for enhancing resin flow during the VARTM infusion phase. Through the enhancement of resin flow, dry spots and void content within the composite are minimized to yield a high quality part.

1.7.2.3 Post-infusion

The thickness of the preform stack often changes during the liquid molding process. During the debulking phase, the preform is compacted to effectively reduce its thickness and increase the fiber volume content. With the preform stack being under vacuum pressure, resin flow through the preform is initiated by opening the resin inlet gate. This flow occurs due to a pressure differential between the resin container and vacuum is created by the pump. During the infusion stage, a pressure gradient develops in the area wetted with resin due to flow that causes changes in compaction. Where the flow front develops, the wetted preform pressure is reduced by resin pressure, while the dry preform region remains under atmospheric pressure. A stress balance proposed by Terzaghi is given by [60]:

$$P_{atm} = \sigma_c + P_r \quad (1.12)$$

Here, σ_c is the local compaction, P_{atm} is the atmospheric pressure and P_r is the resin pressure.

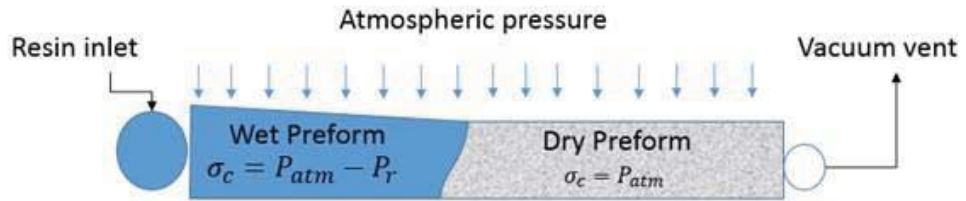


Figure 1.38: Schematic of compaction pressure variation during VARTM infusion [51].

At this stage, the pressure at the inlet gate is atmospheric pressure resulting in a zero compaction stress on the preform (maximum thickness region) while the dry preform on the other end experiences maximum compaction stress (minimum thickness region). The flow front eventually approaches the vent gate and set-up is arranged in a manner to allow for excess resin to bleed through the vent port into a vacuum trap. Upon saturation of the

preform, closing the injection line while leaving the vent gate open enables full and uniform vacuum pressure to be reestablished [61]. If the resin has not gelled during this stage of the process, this can lead to increased compaction and uniformity of the final part thickness and properties. If the resin gels, gradients will be frozen into the part. The properties of the resin dictate the optimum process conditions. The VAP process provides uniform vacuum throughout the process, making it more applicable to a wide range of resin systems [61].

This highlights the importance aspects of resin properties on the post-infusion phase. Fast curing resins will gel before allowing the preform to establish uniform thickness while excessive bleeding may result in dry spots and higher void content.

1.8 Elastic and strength properties of composite materials

The analysis of composite materials requires the knowledge of their elastic properties and strength limits. The properties of the composite system can be obtained using a micromechanics approach or through experimental methods. The micromechanics method can predict elastic properties of the composite that are generally in good agreement with the experimental data. However, the micro-mechanics approach does not provide an accurate prediction of the composite material strength; therefore, experimental work is necessary.

1.8.1 Elastic properties of composite materials

A variety of methods have been used to predict the elastic properties of composite materials, these falling into one of the following general categories, micromechanics, numerical or, experimental testing. The objective of micromechanics methods is to characterize the elastic properties of the composite as a function of the material and geometric properties of its constituents. There are several existing models that permit analytical determination of the effective elastic moduli, such as the rule of mixtures method, the composite cylinder assemblage method [75], bounding methods, semi empirical methods, etc. The rule-of-mixture predictions are adequate for longitudinal properties, such as the elastic modulus and the major Poisson's ratio of a unidirectional composite [2].

1.8.2 Strength properties of composite materials

The longitudinal compressive strength of unidirectional composites depends on the constituent materials' strength and stiffness and their distribution within the structure [76]. The fabrication process and the presence of defects in the form void and/or fiber misalignment, for example, can have a great influence on the compressive strength and

failure mode. Various theories in literature have been proposed in an attempt to explain the mechanisms of failure for an axially-compressed unidirectional composite. Generally, four different failure modes can be observed in such structures, elastic micro-buckling, plastic micro-buckling, matrix cracking or splitting, and fiber crushing. Elastic or Euler buckling is a potential failure mode in sufficiently slender columns (regardless of the material type). A brief review of each failure mode is provided as follows.

1.8.2.1 Matrix failure

Matrix failure occurs when the axial strain of the composite reaches a critical value equal to the failure strain of the matrix [77]. The mechanism of failure is brittle crack propagation within the matrix material. This failure mode is observed in ceramic matrix composites for high temperature applications, such as silicon fibers in a pyroceramic matrix [78]. The failure stress (σ_c) resulting from this failure mode is predicted as follows [79]:

$$\sigma_c = \varepsilon_{my} [V_f E_f + (1 - V_f) E_m] \quad (1.13)$$

where ε_{my} is the ultimate yield strain of the matrix, E_f and E_m are the elastic modulus of the fiber and matrix respectively and V_f is the fiber volume fraction.

Generally, a weak matrix material or poor bonding between fiber and matrix would activate this failure mode. Testing carbon fiber-epoxy composite systems with varying fiber-matrix interfacial strength has shown that systems with the lowest interfacial strength fail by developing longitudinal cracks within the matrix [80]. For systems with intermediate and high interfacial strength, the failure mode was micro-buckling/kinking and fiber compression respectively [80]. Compression testing is strongly influenced by test fixture. Applying a load directly on the composite ends might result in premature failure, in the form of end-crushing (brooming), and/or longitudinal matrix splitting [81].

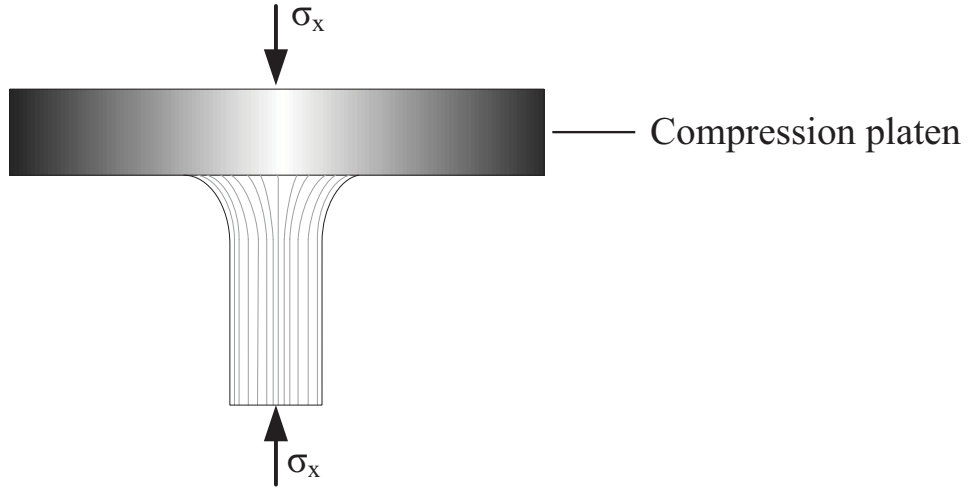


Figure 1.39: Matrix splitting (brooming).

This is considered a weak failure mode with a peak stress dictated by the strength of the matrix alone. To suppress this “artificially low” strength, end caps or clamps are used to laterally constrain the load ends and activate a stronger failure mode [47].

1.8.2.2 Fiber crushing

When the critical uniaxial strain to failure of the composite is equal to the crushing strain of the fiber, fiber crushing is considered the operative mode of failure [77]. It is a failure of the fibers due to pure compression. This failure mode was observed in early fiber-epoxy systems manufactured from fibers having a low crushing strength and an epoxy resin with high yield strength [82]. In order to observe the mechanisms of fiber crushing, fibers are embedded in a clear epoxy cast with a large cross-section relative to the fiber size [76]. For carbon fibers, Kevlar fibers and wood, failure in the form of microscopic micro-buckling or kinking within each fiber was noted [82]. Using the rule of mixtures formula to predict the average axial crushing strength in the composite [82]:

$$\sigma_{crush} = \varepsilon_{fc} [V_f E_f + (1 - V_f) E_m] \quad (1.14)$$

Where ε_{fc} is the fiber crushing strain. Modern carbon-fiber epoxy systems employ fibers with a higher crushing strength and a tougher epoxy matrix with a lower yield strength. Consequently, fiber crushing is generally not an operative failure mode and other failure mechanisms are activated.

1.8.2.3 Elastic micro-buckling

This model is based on the observation that the fibers undergo micro-buckling within the matrix, due to elastic bending of the fibers and elastic shear within the matrix. Once a critical compressive load is reached, the fibers bend due to an instability on the micro-scale and eventually break to form kink bands, Figure 1.40.

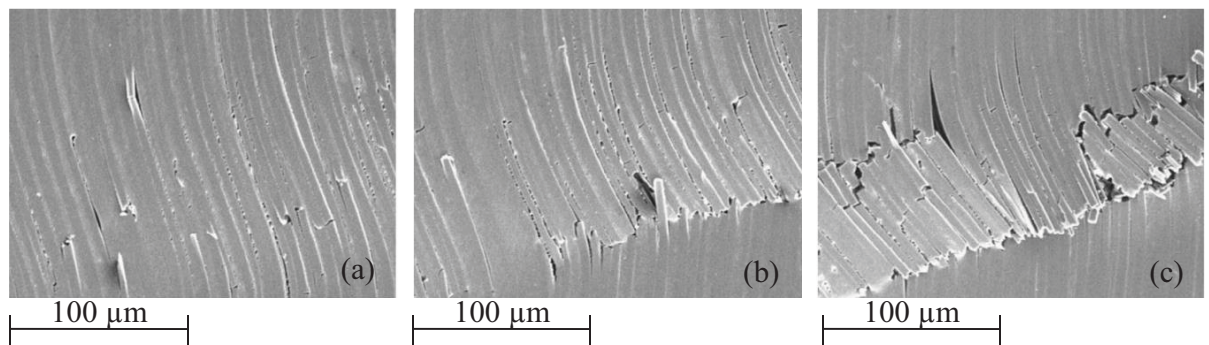


Figure 1.40: a) Initial buckling of fibers, b) development of cracks on the lower edge and c) a fully-formed kink band [83].

Most elastic micro-buckling models are extensions of the theory presented by Rosen, which is based on an idealized two dimensional model with perfectly straight fibers embedded in a linear elastic matrix [84]. Rosen recognized that the composite structure may be short and stiff on the macro-scale, but on the micro-scale, individual fibers have relatively small diameter and undergo buckling as slender columns. Two modes under which failure occurs were assumed, an extensional or out-of-phase mode and a shear or in-phase mode (Figure 1.41).

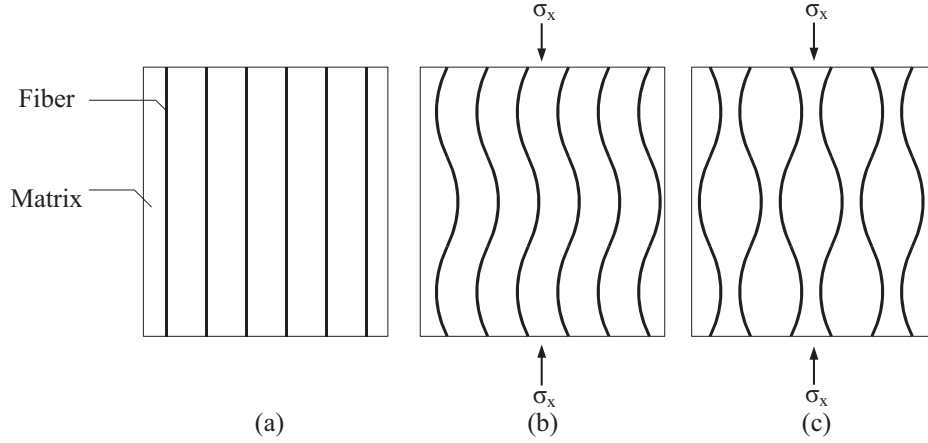


Figure 1.41: Elastic micro-buckling modes: (a) Initial configuration (b) Shear mode and (c) Extensional mode.

For composites based on a low fiber volume fraction (< 0.3), the compressive strength is predicted using the Elastic micro-buckling extensional mode as:

$$\sigma_x = 2V_f \sqrt{\frac{E_f E_m V_f}{3(1 - V_f)}} \quad (1.15)$$

The shear mode is predicted for higher values of V_f , with a corresponding compressive strength,

$$\sigma_x = \frac{G_m}{1 - V_f} + \frac{\pi^2 V_f E_f}{3} \left(\frac{d}{\lambda} \right)^2 \quad (1.16)$$

where G_m is the matrix shear modulus, d the fiber diameter and λ is the buckling wavelength. The first term $\frac{G_m}{1 - V_f}$ is the contribution to the compressive strength from matrix shear and the second term $\frac{\pi^2 V_f E_f}{3} \left(\frac{d}{\lambda} \right)^2$ is the contribution from the finite bending resistance of the fibers [82]. The role of fiber bending is considered negligible, therefore, eliminated from the above equation, and the shear mode compressive stress reduces to (minimum shear mode strength, $\lambda \rightarrow \infty$):

$$\sigma_x \cong \frac{G_m}{1 - V_f} \quad (1.17)$$

Strength predictions for the extensional mode are higher than for the shear mode. The model provided by Rosen is based on idealized system of perfectly aligned fibers and does not account for pre-existing fiber misalignment, which plays a critical role in reducing the strength appreciably. For this reason, the strength predictions are found to be an order of magnitude higher than experimentally-measured values. Later models, based on the analysis of microbuckling, have attempted to improve predictions by accounting for initial fiber waviness or misalignment, matrix nonlinearity and possible debonding [85]. These aspects are incorporated into the model in the form of correction factors based on empirical data to improve the predictions made by the model. Xu and Reifsnider proposed a model based on the analysis of micro-buckling and included a matrix slippage parameter to account for the fiber-matrix bond condition, which can be determined experimentally [86]. The model gave strength predictions that were in good agreement with data from composites based on a high strength carbon fiber, but over-estimated the strength of E-glass composites [85]. The model proposed by Lo and Chim introduced a factor to account for the uncertainty in boundary conditions [87]. Strength predictions have shown good agreement with a variety of published experimental data [85].

1.8.2.4 Plastic micro-buckling (kinking)

This is an imperfection-based model which assumes the presence of initial fiber misalignment within a narrow band in the composite, known as a kink band. Failure is initiated by plastic shear deformation resulting from the rotation of the initially-misaligned fibers within this band. Argon [88] and Budiansky [89] investigated the influence of fiber

misalignment on compressive strength and suggested that the initial fiber misalignment angle ($\bar{\varphi}$) and the shear yield stress of the matrix are the main factors influencing compressive strength.

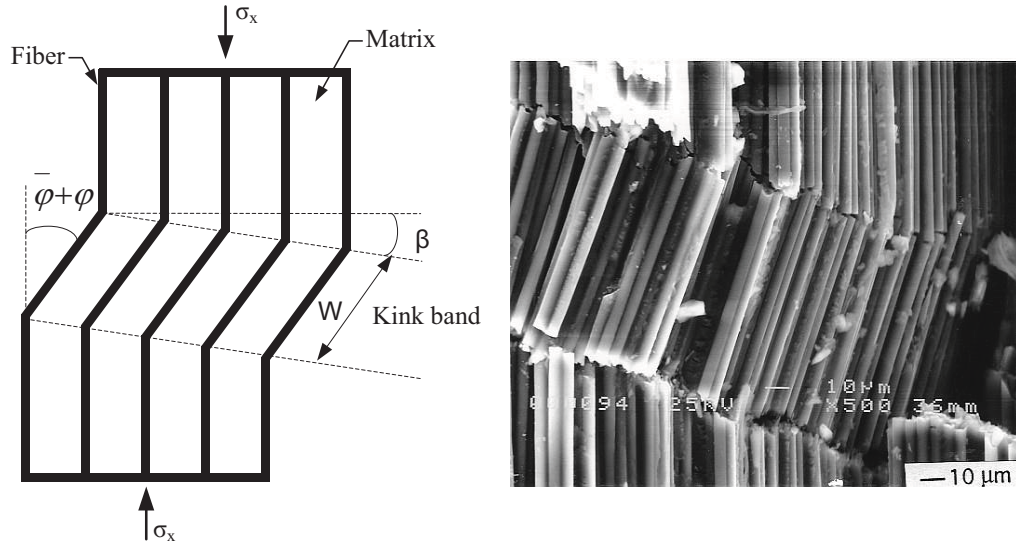


Figure 1.42: a) Kink band geometry and b) kink band failure in unidirectional carbon-epoxy composite [88].

Based on Argon's argument, by considering the maximum initial misalignment of the fibers ($\bar{\varphi}$), in a band with $\beta = 0$ (Figure 1.42) of a rigid-perfectly plastic composite, the compressive strength is given by [88]:

$$\sigma_x = \frac{\tau_y}{\bar{\varphi}} \quad (1.18)$$

where τ_y is the in-plane shear strength of the composite. The above prediction ignores the fact that kink band orientations are generally observed to be inclined to the transverse direction [90].

Budiansky extended Argon's concept and proposed an elastic-perfectly plastic kink band model ($\tau = G\gamma$ for $\gamma < \gamma_y$, $\tau = \tau_y$ for $\gamma > \gamma_y$, where $\gamma_y = \tau_y/G$) for which the compression failure was given as [89]:

$$\sigma_x = \frac{\tau_y}{\gamma_y + \bar{\varphi}} = \frac{G}{1 + \bar{\varphi}/\gamma_y} \quad (1.19)$$

where γ_y is the shear yield strain of the composite and G is the longitudinal shear modulus of the composite. The rotation in the kink band is $(\bar{\varphi} + \varphi)$ where $\varphi = \gamma$ is the additional rotation under remote stress. This result (still for $\beta = 0$) and further analysis of kinking at other angles led to the conclusion that kinks at $\beta = 0$ resulted in the lowest compressive stress. This indicated that kink bands should form at an angle perpendicular to the loading axis, contrary to the experimental evidence. Budiansky and Fleck plotted available experimental values of compressive strength vs. longitudinal shear modulus of the composite for different $\bar{\varphi}/\gamma_y$ values [91]. The data were in agreement with the above equation for a range of $\bar{\varphi}/\gamma_y$ values close to 4. This corresponded to an initial misalignment angle of approximately 2° , which is consistent with reported values of fiber misalignment in carbon fiber-PEEK matrix unidirectional composites. The micro-buckling predictions offered by Argon's model of a rigid-perfectly plastic composite were found to be asymptotically equal to the predictions of Budiansky's model of an elastic-perfectly plastic composite [85, 92].

1.8.2.5 Elastic Buckling

A sufficiently slender column subjected to an axial compressive load would laterally deflect and fail by bending, resulting in sudden collapse. Gross column buckling occurs at stress

levels below the material's inherent ultimate compressive stress. This is a geometric instability failure mode observed in slender structural members. It is possible to estimate the buckling stress using Euler's buckling equation:

$$\sigma_x = \frac{\pi^2 E_x}{SR^2} \quad (1.20)$$

Where E_x is the axial stiffness in the direction of compressive loading and SR is the slenderness ratio calculated as:

$$SR = kL(I/A)^{-0.5} \quad (1.21)$$

where k is an end constraint factor (ranging between 0.5 and 2), L is the specimen length, I and A are the moment of inertia and cross-sectional area respectively. However, the general Euler buckling formula is developed for isotropic materials and subsequently modified to account for the influence of material orthotropy as follows [93]:

$$\sigma_x = \frac{\pi^2 E_x}{SR^2 + 1.2\pi^2 \left(\frac{E_x}{G_{xz}} \right)} \quad (1.22)$$

Where G_{xz} is the shear stiffness in the through-the-thickness direction ($G_{xz} = G_{xy}$ for transversely-isotropic material). The influence of material orthotropy is represented in the second term in the denominator of the Euler buckling equation.

Based on the previous discussion, an axially-loaded unidirectional composite will exhibit compressive failure in a number of competing failure modes. The operative failure mode is particularly sensitive to the degree of imperfection, usually in the form of fiber misalignment, and the shear properties of the matrix. Experimental data in the literature strongly suggest that the most likely failure mode in carbon-epoxy composites designed for strength-critical applications is micro-buckling involving fiber kinking [76, 77, 82, 85, 91, 93, 94]. There are two main, sometimes competing models for predicting the compressive

strength of composites, namely, the elastic micro-buckling model and the plastic micro-buckling (kink band) model. Both models are based on different assumptions relating to the mechanisms under which failure occurs. Elastic micro-buckling assumes failure due to local instability of the fibers while the kink band model is based on the plastic shear deformation of initially misaligned fibers within a certain band. Although the two models are derived based on different failure mechanisms, they predict the compressive strength quite accurately with little variations between them once the parameters representative of the material are known [92, 95]. These parameters are not readily available for the materials used in this study. Therefore it is necessary to carry out experimental work to determine the strength properties of the parent material.

References

- [1] C.T. Sun, *Mechanics of Aircraft Structures*, Wiley-Interscience, 1998.
- [2] I. M. Daniel and O. Ishau, *Engineering Mechanics of Composite Materials*, 1994.
- [3] J. Wang, A.G. Evans, K. Dharmasena and H.N.G. Wadley, “On the performance of truss panels with Kagome’ cores”, *Int. J. Solids and Struct.*, vol. 40, pp. 6981–6988, 2003.
- [4] R. Biagi and H. Bart-Smith, “Imperfection sensitivity of pyramidal core sandwich structures”, *Int. J. Solids Struct.*, vol. 44, pp. 4690–4706, 2007.
- [5] V. S. Deshpande, N. A. Fleck and M. F. Ashby, “Effective properties of the octet-truss lattice material”, *J. Mech. Phys. Solids*, vol. 49, pp. 1747–1769, 2001.
- [6] D. T. Queheillalt and H. N. G. Wadley, “Pyramidal lattice truss structures with hollow trusses”, *Mater. Sci. Eng. A*, vol. 397, pp. 132–137, 2005.
- [7] S. Chiras, D. R. Mumm, A. G. Evans, N. Wicks, J. W. Hutchinson, K. Dharmasena, H. N. G. Wadley and S. Fichter, “The structural performance of near-optimized truss core panels”, *Int. J. Solids Struct.*, vol. 39, pp. 4093–4115, 2002.
- [8] Y. Shen, S. McKown, S. Tsopanos, C. J. Sutcliffe, R. A. W. Mines and W. J. Cantwell, “The mechanical properties of sandwich structures based on metal lattice architectures”, *J. Sandw. Struct. Mater.*, 2009.
- [9] M. Smith, Z. Guan and W. J. Cantwell, “Finite element modelling of the compressive response of lattice structures manufactured using the selective laser melting technique”, *Int. J. Mech. Sci.*, vol. 67, pp. 28–41, 2013.
- [10] Wadley Research Group. *Ultra-light Cellular Materials*, [Online]. Available: <http://www.virginia.edu/ms/research/wadley/cellular-materials.html>.

- [11] F. W. Zok, H. J. Rathbun, Z. Wei and A. G. Evans, “Design of metallic textile core sandwich panels”, *Int. J. Solids Struct.*, vol. 40, pp. 5707–5722, 2003.
- [12] M. Santorinaios, W. Brooks, C. J. Sutcliffe and R. A. W. Mines, “Crush behavior of open cellular lattice structures manufactured using selective laser melting”, *WIT Trans. Built Environ.*, vol. 85, pp. 481–490, 2006.
- [13] L. J. Gibson and M. F. Ashby, *Cellular Solids: Structure and Properties*, Cambridge University Press, Cambridge, 2009.
- [14] P. Fratzl and R. Weinkamer, “Nature’s hierarchical materials”, *Prog. Mater. Sci.*, vol. 52, pp. 1263–1334, 2007.
- [15] D. J. Sypeck, “Cellular truss core sandwich structures”, *Appl. Compos. Mater.*, vol. 12, pp. 229–246, 2005.
- [16] H. N. G. Wadley, “Cellular metals manufacturing”, *Adv. Eng. Mater.*, vol. 4, pp. 726–733, 2002.
- [17] V. Kumar and N. P. Suh, “A process for making microcellular thermoplastic parts”, *Polym. Eng. Sci.*, vol. 30, pp. 1323–1329, 1990.
- [18] M. Scheffler and P. Colombo, “Cellular Ceramics: Structure”, *Manufacturing, Properties and Applications*, John Wiley & Sons, 2006.
- [19] M. F. Ashby, The properties of foams and lattices, *Philos. Trans. A. Math. Phys. Eng. Sci.*, vol. 364, pp. 15–30, 2006.
- [20] V. S. Deshpande, M. F. Ashby and N. A. Fleck, “Foam topology: Bending versus stretching dominated architectures”, *Acta Mater.*, vol. 49, pp. 1035–1040, 2001.
- [21] J. C. Maxwell, “On the calculation of the equilibrium and stiffness of frames”, *London, Edinburgh and Dublin Philos. Mag. J. Sci.*, vol. 27, pp. 294–299, 1864.

- [22] C. R. Calladine, *Theory of Shell Structures*, Cambridge University Press, 1989.
- [23] A. G. Evans, J. W. Hutchinson, N. A. Fleck, M. F. Ashby and H. N. G. Wadley, “The topological design of multifunctional cellular metals”, *Prog. Mater. Sci.*, vol. 46, pp. 309–327, 2001.
- [24] H. N. G. Wadley, “Multifunctional periodic cellular metals.”, *Philos. Trans. A. Math. Phys. Eng. Sci.*, vol. 364, pp. 31–68, 2006.
- [25] F. Côté, V. S. Deshpande, N. A. Fleck and A. G. Evans, “The out-of-plane compressive behavior of metallic honeycombs”, *Mater. Sci. Eng. A*, vol. 380, pp. 272–280, 2004.
- [26] F. Côté, V. S. Deshpande, N. A. Fleck and A. G. Evans, “The compressive and shear responses of corrugated and diamond lattice materials”, *Int. J. Solids Struct.*, vol. 43, pp. 6220–6242, 2006.
- [27] M. R. M. Rejab and W. J. Cantwell, “The mechanical behavior of corrugated-core sandwich panels”, *Compos. Part B Eng.*, vol. 47, pp. 267–277, 2013.
- [28] S. Yin, L. Wu and S. Nutt, “Stretch-bend-hybrid hierarchical composite pyramidal lattice cores”, *Compos. Struct.*, vol. 98, pp. 153–159, 2013.
- [29] H. N. G. Wadley, N. A. Fleck and A. G. Evans, “Fabrication and structural performance of periodic cellular metal sandwich structures”, *Compos. Sci. Technol.*, vol. 63, pp. 2331–2343, 2003.
- [30] J. Xiong, L. Ma, L. Wu, B. Wang and A. Vaziri, “Fabrication and crushing behavior of low density carbon fiber composite pyramidal truss structures”, *Compos. Struct.*, vol. 92, pp. 2695–2702, 2010.

- [31] K. Finnegan, G. Kooistra, H. N. G. Wadley and V. S. Deshpande, “The compressive response of carbon fiber composite pyramidal truss sandwich cores”, *Int. J. Mater. Res.*, vol. 98, pp. 1264–1272, 2007.
- [32] C. Schneider, M. N. Velea, S. Kazemahvazi and D. Zenkert, “Compression properties of novel thermoplastic carbon fibre and poly-ethylene terephthalate fibre composite lattice structures”, *Mater. Des.*, vol. 65, pp. 1110–1120, 2015.
- [33] B. Wang, L. Wu, L. Ma, Y. Sun and S. Du, “Mechanical behavior of the sandwich structures with carbon fiber-reinforced pyramidal lattice truss core”, *Mater. Des.*, vol. 31, pp. 2659–2663, 2010.
- [34] J. Xiong, B. Wang, L. Ma, J. Papadopoulos, A. Vaziri and L. Wu, “Three-dimensional Composite Lattice Structures Fabricated by Electrical Discharge Machining”, *Exp. Mech.*, vol. 54, pp. 405–412, 2013.
- [35] S. Yin, L. Wu and S. R. Nutt, “Compressive efficiency of stretch-stretch-hybrid hierarchical composite lattice cores”, *Mater. Des.*, vol. 56, pp. 731–739, 2014.
- [36] B. C. Lee, K. W. Lee, J. H. Byun and K. J. Kang, “The compressive response of new composite truss cores”, *Compos. Part B Eng.*, vol. 43, pp. 317–324, 2012.
- [37] T. George, V. S. Deshpande, K. Sharp and H. N. G. Wadley, “Hybrid core carbon fiber composite sandwich panels: Fabrication and mechanical response”, *Compos. Struct.*, vol. 108, pp. 696–710, 2014.
- [38] M. Chen, X. Zhu, H. Lei, H. Chen and D. Fang, “Effect of Defect on the Compressive Response of Sandwich Structures with Carbon Fiber Pyramidal Truss Cores”, *Int. J. Appl. Mech.*, vol. 7, p. 1550004, 2015.

- [39] M. Leong, L. C. T. Overgaard, O. T. Thomsen, E. Lund and I. M. Daniel, “Investigation of failure mechanisms in GFRP sandwich structures with face sheet wrinkle defects used for wind turbine blades”, *Compos. Struct.*, vol. 94, pp. 768–778, 2012.
- [40] Y. Hirose, H. Matsuda, G. Matsubara, M. Hojo, K. Yoshida and F. Inamura, “Numerical analysis of splice-type crack arrester with a filler under mode-I type loading”, *Compos. Struct.*, vol. 100, pp. 127–134, 2013.
- [41] Y. Hirose, H. Matsuda, G. Matsubara, M. Hojo, K. Yoshida and F. Inamura, Experimental evaluation of splice-type crack arrester with a filler under mode-I type loading, *Compos. Struct.*, vol. 100, pp. 300–306, 2013.
- [42] J. L. Grenestedt, “Development of a new peel-stopper for sandwich structures, *Compos. Sci. Technol.*”, vol. 61, pp. 1555–1559, 2001.
- [43] E. Bozhevolnaya, J. Jakobsen and O. T. Thomsen, “Fatigue performance of sandwich beams with peel stoppers”, *Int. J. Exp. Mech.*, vol. 45, pp. 349–357, 2009.
- [44] B. Lascoup, Z. Aboura, K. Khellil and M. Benzeggagh, “On the mechanical effect of stitch addition in sandwich panel”, *Compos. Sci. Technol.*, vol. 66, pp. 1385–1398, 2006.
- [45] P. Potluri, E. Kusak and T. Y. Reddy, “Novel stitch-bonded sandwich composite structures”, *Compos. Struct.*, vol. 59, pp. 251–259, 2003.
- [46] K. T. Tan, A. Yoshimura, N. Watanabe, Y. Iwahori and T. Ishikawa, “Effect of stitch density and stitch thread thickness on damage progression and failure characteristics of stitched composites under out-of-plane loading”, *Compos. Sci. Technol.*, vol. 74, pp. 194–204, 2013.

- [47] D. B. Miracle, S. L. Donaldson, S. D. Henry, C. Moosbrugger, G. J. Anton, B. R. Sanders, N. Hrivnak, C. Terman, J. Kinson, K. Muldoon and others, *ASM handbook*, vol. 21, ASM International Materials Park, OH, USA, 2001.
- [48] *Guide to Composites*. [Online]. Available: URL <http://www.netcomposites.com>.
- [49] V. G. K. Menta, R. B. R. Vuppalapati, K. Chandrashekhara, D. Pfitzinger and N. Phan, “Evaluation of honeycomb composite sandwich structures manufactured using VARTM process”, *Int. SAMPE Symposium and Exhibition*, Jan. 2010.
- [50] R. S. Parnas, J. G. Howard, T. L. Luce and S. G. Advani, “Permeability characterization. Part 1: A proposed standard reference fabric for permeability”, *Polym. Compos.*, vol. 16, pp. 429–445, 1995.
- [51] S. Sharma and K. K. Wetzel, “Process Development Issues of Glass--Carbon Hybrid-reinforced Polymer Composite Wind Turbine Blades”, *J. Compos. Mater.*, vol. 44, pp. 437–456, 2010.
- [52] D. Heider and J. W. Gillespie Jr, *VARTM Variability and Substantiation*, University of Delaware, 2008.
- [53] T. L. Luce, S. C. Advani, J. G. Howard and R. S. Parnas, “Permeability Characterization. Part 2: Flow Behavior in Multiple-Layer Preforms”, *Polymer Composites*. vol. 16, pp. 429-445, 1995.
- [54] C. Shih and L. J. Lee, “Effect of fiber architecture on permeability in LCM”, *Polym. Compos.*, vol. 19, pp. 626–639, 1998.
- [55] S. Bickerton and S. G. Advani, “Characterization and modeling of race-tracking in liquid composite molding processes”, *Compos. Sci. Technol.*, vol. 59, pp. 2215–2229, 1999.

- [56] T. S. Lundström, R. Stenberg, R. Bergström, H. Partanen and P. A. Birkeland, “In-plane permeability measurements: a nordic round-robin study”, *Compos. Part A Appl. Sci. Manuf.*, vol. 31, pp. 29–43, 2000.
- [57] S. Bickerton, H. C. Stadtfeld, K. V. Steiner and S. G. Advani, “Design and application of actively controlled injection schemes for resin-transfer molding”, *Compos. Sci. Technol.*, vol. 61, pp. 1625–1637, 2001.
- [58] K. Hoes, D. Dinescu, H. Sol, M. Vanheule, R. S. Parnas, Y. Luo and I. Verpoest, “New set-up for measurement of permeability properties of fibrous reinforcements for RTM”, *Compos. - Part A Appl. Sci. Manuf.*, vol. 33, pp. 959–969, 2002.
- [59] S. Bickerton, M. J. Buntain and A. A. Somashekar, “The viscoelastic compression behavior of liquid composite molding preforms”, *Compos. Part A Appl. Sci. Manuf.*, vol. 34, pp. 431–444, 2003.
- [60] P. A. Kelly, R. Umer and S. Bickerton, “Viscoelastic response of dry and wet fibrous materials during infusion processes”, *Compos. Part A Appl. Sci. Manuf.*, vol. 37, pp. 868–873, 2006.
- [61] Federal Aviation Administration, *Overview of Vacuum-Assisted Resin Transfer Molding Processing*, 2013. [Online]. Available: <http://www.tc.faa.gov/its/worldpac/techrpt/tc12-35.pdf>.
- [62] *The VIP Primer*. [Online]. Available: URL <http://www.grpguru.com/vipupdate.asp>.
- [63] W. H. Seemann III, *Plastic transfer molding techniques for the production of fiber reinforced plastic structures*. U.S. patent no. 4902215, issued 1990.

- [64] B. Seemann, *An Overview of the SCRIMP™ Technology*, 2000. [Online]. Available: URL http://www.tpicomposites.com/media/5997/scrimp_overview_2005.pdf.
- [65] J. Filsinger, T. Lorenz, F. Stadler and S. Utecht, *Method and device for producing fiber-reinforced components using an injection method*. U.S. patent no. 6843953, issued 2005.
- [66] A. Hänsch, *VAP® Vacuum Assisted Process*, 2013. [Online]. Available: URL <http://www.vap-info.com/en/download/VAP-vacuum-assisted-process.pdf>.
- [67] EADS, *VAP® Center of Excellence for aviation applications*. [Online]. Available: URL <http://www.vap-info.com/en/aerospace.html>.
- [68] J. A. Woods, A. E. Modin, R. D. Hawkins and D. J. Hanks, *Controlled atmospheric pressure resin infusion process*. U.S. patent no. 7334782, issued 2008.
- [69] B. Gama, H. Li, W. Li, A. Paesano, D. Heider and J. Gillespie Jr, “Improvement of dimensional tolerances during VARTM processing”, *33 rd Int. SAMPE Tech. Conf.*, pp. 1415–1427, 2001.
- [70] C. Niggemann, Y. S. Song, J. W. Gillespie and D. Heider, “Experimental investigation of the controlled atmospheric pressure resin infusion (CAPRI) process”, *J. Compos. Mater.*, vol. 42, pp. 1049–1061, 2008.
- [71] R. Mathuw, S. G. Advani, D. Heider, C. Hoffmann, J. W. Gillespie and B. K. Fink, “Flow front measurements and model validation in the vacuum assisted resin transfer molding process”, *Polym. Compos.*, vol. 22, pp. 477–490, 2001.
- [72] R. Brault, M. Niquet and S. Mistou, “Experimental and numerical modelling of LRI process”, *Key Engineering Materials*, vol. 446, pp. 121–130, 2010.

- [73] A. May-Pat, F. Aviles and J. Aguilar, “Mechanical properties of sandwich panels with perforated foam cores”, *J. Sandw. Struct. Mater.*, vol. 13, pp. 427–444, 2011.
- [74] P. Majumdar, D. Srinivasagupta, H. Mahfuz, B. Joseph, M. M. Thomas and S. Christensen, “Effect of processing conditions and material properties on the debond fracture toughness of foam-core sandwich composites: experimental optimization”, *Compos. Part A Appl. Sci. Manuf.*, vol. 34, pp. 1097–1104, 2003.
- [75] Z. Hashin, “On elastic behavior of fibre reinforced materials of arbitrary transverse phase geometry”, *J. Mech. Phys. Solids*, vol. 13, pp. 119–134, 1965.
- [76] H. T. Hahn and J.G. Williams, “Compression failure mechanisms in unidirectional composites”, *Composite materials: testing and design (seventh conference)*, ASTM International, 1986.
- [77] P. M. Jelf and Fleck N. A., “Compression failure mechanisms in unidirectional composites”, *J. Compos. Mater.*, vol. 26, pp. 2706–2726, 1992.
- [78] J. Lankford, “Dynamic compressive fracture in fiber-reinforced ceramic matrix composites”, *Mater. Sci. Eng. A*, vol. 107, pp. 261–268, 1989.
- [79] T. Hayashi and K. Koyama, “Theory and experiments of compressive strength of unidirectionally fiber-reinforced composite materials”, *Mechanical Behavior of Materials: Proceedings of the First International Conference*, pp. 104–112, 1972.
- [80] M. S. Madhukar and L. T. Drzal, “Fiber-matrix adhesion and its effect on composite mechanical properties. III. Longitudinal (0) compressive properties of graphite/epoxy composites”, *J. Compos. Mater.*, vol. 26, pp. 310–333, 1992.

- [81] US Department of Defense, *Composite Materials Handbook Volume 1: Polymer Matrix Composites - Guidelines for Characterisation of Structural Materials*, vol. 1, pp. 1–586, 2002.
- [82] N. A. Fleck, “Compressive failure of fiber composites”, *Adv. Appl. Mech.*, vol. 33, pp. 43–117, 1997.
- [83] R. Gutkin, S. T. Pinho, P. Robinson and P. T. Curtis, “On the transition from shear-driven fibre compressive failure to fibre kinking in notched CFRP laminates under longitudinal compression”, *Compos. Sci. Technol.*, vol. 70, pp. 1223–1231, 2010.
- [84] B. W. Rosen, *Mechanics of composite strengthening*, 1965.
- [85] C. R. Schultheisz and A. M. Waas, “Compressive failure of composites, Part I: Testing and micromechanical theories”, *Prog. Aerosp. Sci.*, vol. 32, pp. 1–42, 1996.
- [86] Y. L. Xu and K. L. Reifsnider, “Micromechanical modeling of composite compressive strength”, *J. Compos. Mater.*, vol. 27, pp. 572–588, 1993.
- [87] K. H. Lo and E.-M. Chim, “Compressive strength of unidirectional composites”, *J. Reinf. Plast. Compos.*, vol. 11, pp. 838–896, 1992.
- [88] A. S. Argon, “Fracture of composites”, *Treatise Mater. Sci. Technol*, vol.1, pp.79-114, 2013.
- [89] B. Budiansky, “Micromechanics”, *Comput. Struct.*, vol. 16, pp. 3–12, 1983.
- [90] B. Budiansky and N. A. Fleck, “Compressive kinking of fiber composites: A topical review”, *Appl. Mech. Rev.*, vol. 47, pp. S246–S250, 1994.
- [91] B. Budiansky and N. A. Fleck, “Compressive failure of fibre composites”, *J. Mech. Phys. Solids*, vol. 41, pp. 183–211, 1993.

- [92] N. K. Naik and R. S. Kumar, “Compressive strength of unidirectional composites: evaluation and comparison of prediction models”, *Compos. Struct.*, vol. 46, pp. 299–308, 1999.
- [93] E. M. Odom and D. F. Adams, “Failure modes of unidirectional carbon/epoxy composite compression specimens”, *Composites*, vol. 21, pp. 289–296, 1990.
- [94] C. Soutis, “Compression testing of pultruded carbon fibre-epoxy cylindrical rods”, *J. Mater. Sci.*, vol. 35, pp. 3441–3446, 2000.
- [95] C. T. Sun and J. L. Tsai, “Comparison of microbuckling model and kink band model in predicting compressive strengths of composites”, *13th International Conference on Composite Materials*, 2001.

Chapter 2: Experimental procedures

2.1 Introduction

This chapter provides an overview of the procedure used in measuring the mechanical properties range of all-composite lattice structures. All tests were limited to quasi-static loading conditions. Lattice structures were manufactured and mechanical tests were carried on glass fiber reinforced plastic (GFRP), natural fiber reinforced plastic (NFRP) and carbon fiber reinforced plastic (CFRP) lattice core structures.

The study started by looking at drilling PET foams with a view to introducing a ‘simple through-thickness lattice’ structure that could both enhance resin flow and improve both compression strength and skin-core adhesion. Prior to manufacture, holes were drilled into a PET foam core to create the simple through-thickness lattice. Glass fibers were then inserted into the perforations in an attempt to improve the mechanical properties of the sandwich structure. Initial tests focused on measuring the fracture toughness and through-thickness strength using the three-point-bend test and axial compression test respectively. The results from these tests were compared to data generated from similar tests on a plain PET core, as well as on samples in which no fiber reinforcement was incorporated into the vertical holes.

The work was then extended by looking at the possibility of removing the ‘core’ by adopting a lost mold technique that would leave a free-standing lattice structure. Here, core structures for potential use in sandwich panels were prepared by drilling holes in a well-defined pattern through either a high quality wax block or a machined salt slab. Continuous

carbon fiber strands were then inserted through each of the holes in the perforated array, ensuring that one continuous tow extended through all of the elements within a given core structure. The study investigated this technique for producing a range of lattice structures of varying complexity, based on a carbon fiber reinforced epoxy composite and natural fiber reinforced epoxy composite. Initially, two threading techniques were used to prepare the composite lattice. Subsequent testing focused on assessing the effect of fiber volume fraction, strut diameter and threading technique on the compression properties of vertical truss structures and their individual reinforcing members. Pyramidal truss and complex octet truss structures were also considered. The final portion of this study investigated the mechanical properties of well-defined carbon fiber reinforced lattice structures based on what are termed BCC, BCCz, FCC and F₂BCC designs. All the lattices were produced using the lost mold technique and have been evaluated at in compression under quasi-static rates of strain.

2.2 Lattice fabrication

The following provides a detailed overview of the VARTM process and the lost mold technique developed in this study. The function of each of the consumable products and constituent materials used during the process is illustrated followed with a description of the preparation process. Finally, the infusion and post-infusion procedures are considered.

2.2.1 Consumable materials

Provided here is a list of consumable materials used in the VARTM process and the lost mold procedure, with the exception of the “Removable core” which is used during the lost mold procedure only.

- **Release wax**

Release wax is used for coating the mold surface prior to the stacking process. Allows for the release of the cured component from the mold surface.

- **Peel plies**

Woven fabric generally applied as the last material in the preform stack sequence. They are peeled from the surface of the cured component to leave a clean and contaminant free surface.

- **Distribution mesh**

Placed onto the peel ply covered preform stack. The distribution media facilitates the flow of resin and allow for the complete infusion of the component.

- **Vacuum Bagging Films**

Used to seal the entire assembly to the tool surface to create an air tight enclosure.

- **Sealant Tape**

Sealant tape is used seal the vacuum bagging film to the tool surface to create an airtight seal.

- **Vacuum Fittings**

Used to connect the bagged assembly to the vacuum pump and the resin reservoir.

2.2.2 Constituent materials

Constituent materials making up the final component include the following listed materials. All materials are applicable to both manufacturing procedures, with the exception the core which is not lost during the VARTM process.

- **Reinforcing fibers**

These can be of different types, based on the required needs and specifications and include carbon, glass, natural fibers, etc. In this study, unidirectional fabric / carbon - UT-C300 and E-glass fabric both supplied by Gurit Ltd., were used. Natural jute fiber were also examined. Two forms of the reinforcing material were used, fabric sheets and fiber tows. The fabric sheets were used to produce the facings in the resulting sandwich structure, whereas the fiber tows are used to reinforce the structure in the through-thickness direction. The tows can be cut from a reel of continuous fiber tow or removed from the fabric by carefully extracting individual strands.

- **Epoxy/resin mix**

Prime 20LVTM Epoxy Infusion System supplied by Gurit Ltd. was utilized along with a fast hardener. The precise type of hardener to be selected is based on the amount of time needed for the part to be infused before the resin/hardener mix begins to gel. The current hardener has a gel time of 30 minutes at 25°C, which is deemed sufficient for the purpose of achieving full infusion of the parts being manufactured in this study.

- **Core (VARTM) or removable core (lost mold)**

The hybrid sandwich panels were manufactured using the VARTM process in which the core material used was a closed cell PET foam.

A high quality wax block or a dissolvable material, such as rock salt was used in the lost mold procedure only. The wax block was obtained from Ferris File-A-Wax, a provider of carving and milling waxes. Different wax block formulae, with varying mechanical properties are available. The purple wax block used in this study is characterized as being a

high speed machinable wax with superior hardness properties. They came in blocks that measure 146.1 x 88.9 x 38.1 mm.

An advantage of using a rock salt is ease of removal. Once the panel has been cured and post cured the salt core can be simply removed by placing it under a continuous stream of warm water. However, rock salt is more difficult to drill as it is more brittle in comparison to wax, making it prone to breaking and chipping often resulting in the undesired countersunk holes rather than the desired straight ones. In addition, salt powder resulting from the drilling process must be removed to prevent rusting of lab equipment. Wax on the other hand, is much easier to drill resulting in near perfect straight holes. However, they require higher temperatures to melt and remove. This may have an influence on the mechanical properties of the finished structure.

2.2.3 Preparation Process

The core is prepared by drilling an array of holes reflecting the final configuration of the lattice structure. A CNC machine or a vertical drill is utilized while controlling the orientation of the mold to obtain the desired final core configuration. Different diameters of holes were introduced into the core by using appropriate drill bit sizes.

In the case for the lost mold procedure, the joints in the lattices were formed by feeding the fibers through adjacent channels or holes within the lost mold. It was important, therefore, to ensure that the holes in the complex geometries are accurately co-located at the surface of the mold to ensure that an individual fiber extends out of one hole and directly into another.

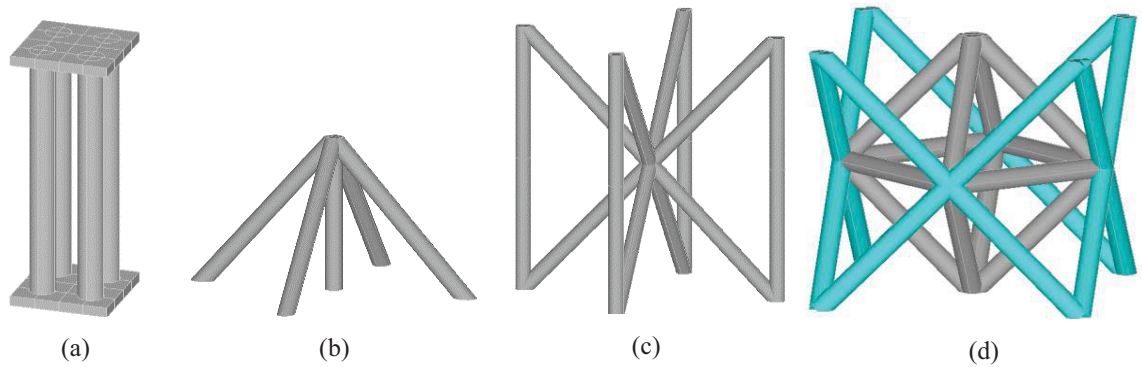


Figure 2.1: Four lattice structures (progressing from simple to complex) that have been manufactured. (a) Vertical column, (b) modified pyramidal truss, (c) BCCz lattice and (d) an octet structure.

The number of fabric sheets, the stacking sequence and orientation will clearly influence the mechanical properties and final thickness of the skins in the sandwich panel. Generally, a balanced, symmetric sequence of four fabric sheets was used for each $(0/90)_s$ face-sheet. The fabric sheets were cut to the dimensions that fully cover the surface of the core. For ease of handling, the face-sheet stack was held together and to the core surface using a minimum amount of 3M 77 Super Multipurpose Adhesive Aerosol.

Fibers were then fed through the array of holes (this can be via either a manual or an automated process). During the manual process, a sewing needle with an eye, or an opening, sufficiently large for the fiber tows, was utilized for threading. A double threading approach was utilized, by pulling the fiber tow through the eye and doubling it up. The end that is threaded through the eye will meet up with the thread from the spool. The length of the fiber threaded in the needle should be sufficiently long to ensure that the fiber can extend throughout the sandwich structure.

2.2.3.1 Weave pattern

Several weaving patterns were adopted to determine which will yield superior mechanical properties. The first procedure involved threading the fibers through the array of holes and then across the top of the core prior placing the face-sheets, as shown in threaded samples in Figure 2.2.

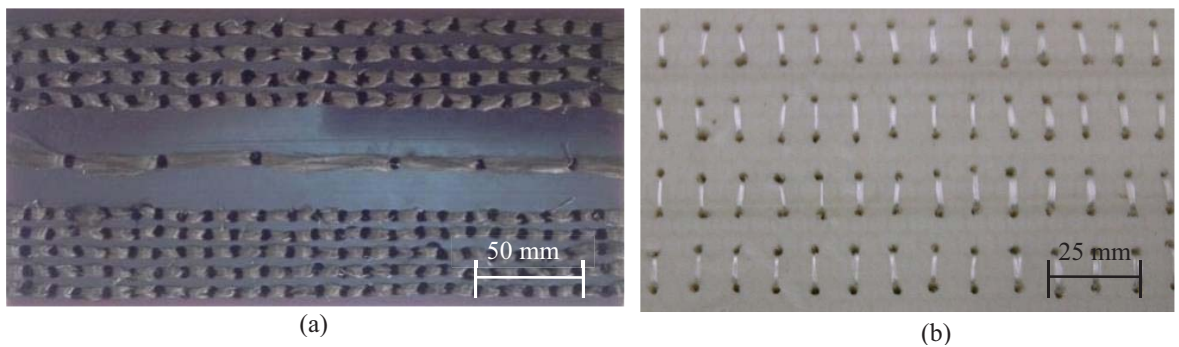


Figure 2.2: (a) Wax block showing threading pattern of carbon fiber (b) Perforated PET foam core with holes reinforced with glass fibers.

Another weave pattern involved threading the fibers through the fabric used to produce the facings in the resulting sandwich structures. A prepared sample showing this threading pattern is shown in Figure 2.3. To ensure that there are no fiber breaks within the through-thickness reinforcement, a continuous fiber tow was used to link adjacent holes in both weaving patterns.

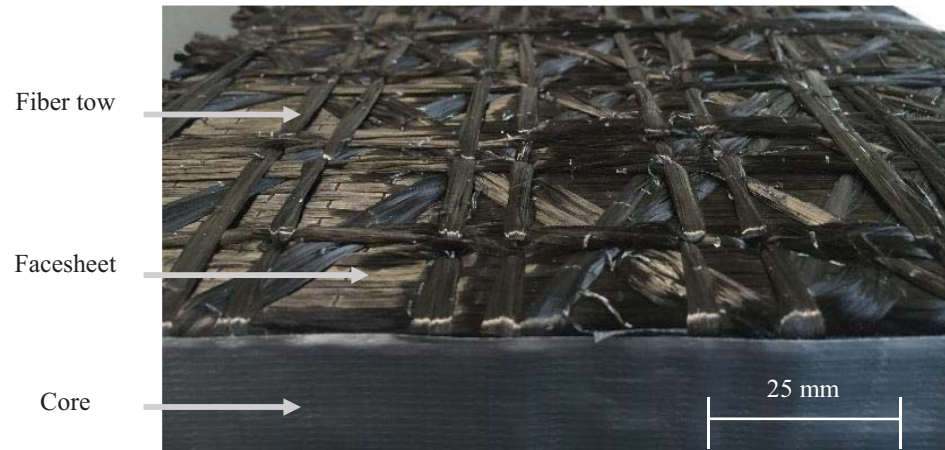


Figure 2.3: Threaded samples showing fibers extending over the skins through the holes.

In the last pattern, fiber strands with a length equal to twice the thickness of the core were inserted through the holes. The protruding fibers at each end of the strand were then spread over the top and bottoms surfaces of the foam core in a circular fashion, as shown in Figure 2.4.

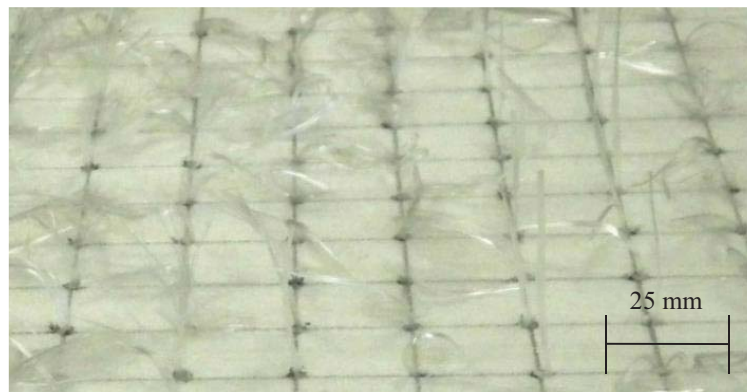


Figure 2.4: Perforated foam core with holes reinforced with glass fiber tows.

In all weaving methods, the fiber volume fraction within an individual hole was varied by controlling the number of fiber tows during the threading process.

2.2.4 Infusion Process

Following the threading process, the reinforced core blocks were infused with resin using the VARTM manufacturing technique. The laboratory set-up for the infusion process is illustrated in Figure 2.5.

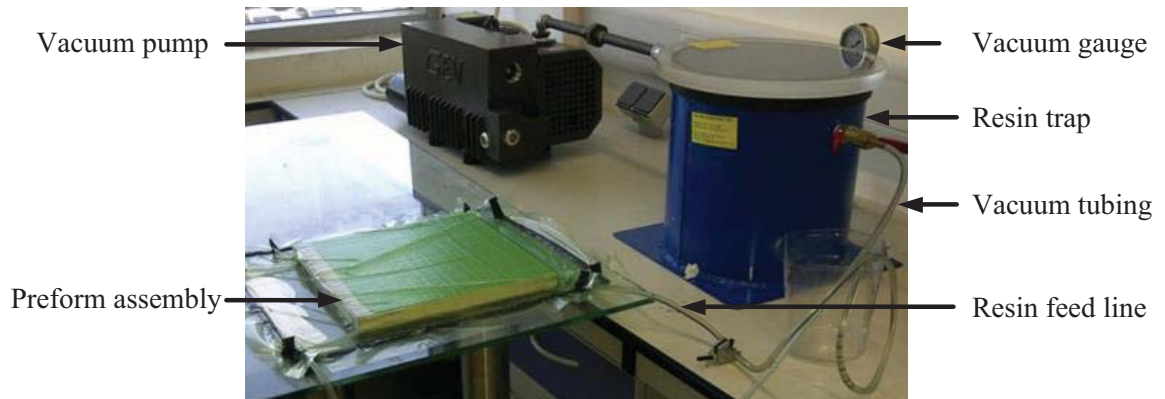


Figure 2.5: Photograph illustrating laboratory set-up of the VARTM infusion process.

Here, a distribution or flow medium, Gurit Knitflow40[®], was used to facilitate the flow of resin throughout the structure. A glass mold, with line injection and a line vent was used to fabricate the sandwich panels. The glass mold permitted the observation of the resin flow process in the lower skin during the infusion process. A schematic of the lay-up arrangement for the VARTM process is shown in Figure 2.6. The skins in the sandwich structures were typically based on four layers of fabric on each side. The edges of the mold were sealed using a vacuum bagging material and a sealant tape. The sandwich panels were infused with resin under vacuum and then allowed to cure at room temperature for 12 hours.

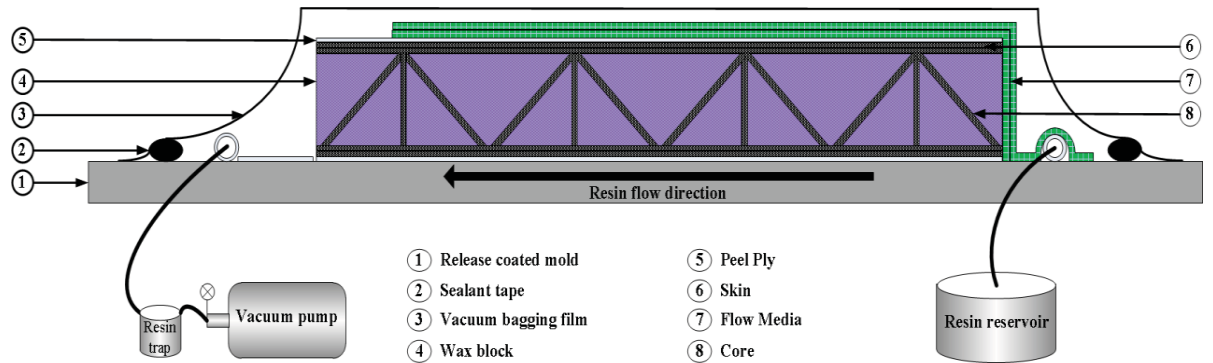


Figure 2.6: Schematic of the VARTM process used to infuse the skins and core.

2.2.5 Post infusion process

Once cured, the panels were removed from the bagging material and then post-cured for 7 hours at 65 °C. Finally, the wax mold was removed by placing the panels in an oven heated to 120 °C for four hours or by dissolving in warm water if it was salt based. A schematic diagram of the entire process is given Figure 2.7.

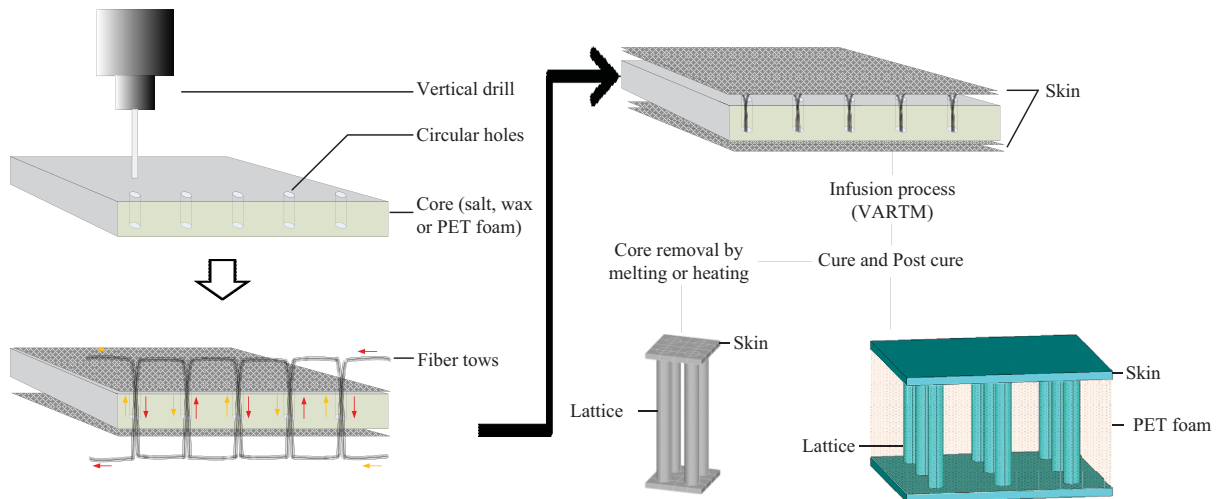


Figure 2.7: Summary of the step-by-step procedures used in the VARTM process and lost mold technique.

2.3 Hybrid core sandwich panel studies

2.3.1 Overview

In this section, the use of a unidirectional glass fiber reinforced plastic (GFRP) vertical column lattice structures that reinforce closed cell polymer foam in a hybrid composite truss/foam core sandwich panel is explored (Figure 2.8).

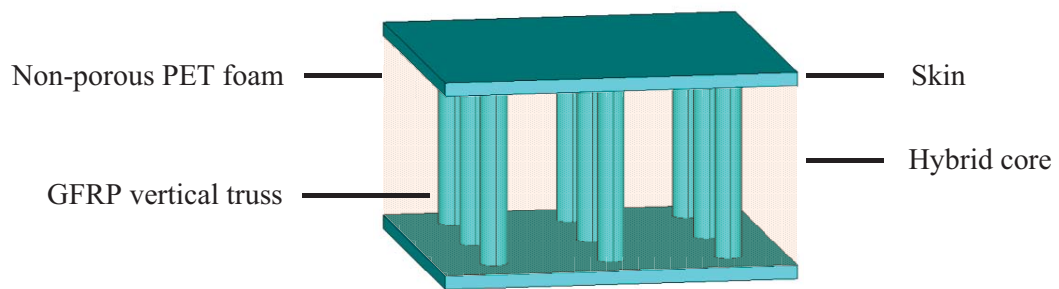


Figure 2.8: Hybrid composite core structure consisting of a unidirectional GRFP lattice with PET foam configured as the core of a sandwich panel with glass fiber composite face sheets.

The non-porous polymer foam serves multiple purposes. It provides a medium for creating holes that reflect the truss cross-sectional shape and configuration, prevent the movement of the face-sheets relative to each and maintain a uniform separation between them, increase the adhesively bonded contact area with the face-sheets and provide thermal and acoustic insulation, core strengthening and energy absorption during impact. The unidirectional vertical trusses are non-laminated materials making them, in principle, immune to delamination failure. Having the reinforcing fibers aligned with the column axis may serve to increase the axial compressive strength of the strut and the skin-core interfacial fracture toughness properties.

This section investigates the fabrication of a vertical truss structure within a PET foam core and the effect of varying the truss arrangement and fiber volume content within the truss on the mechanical response of the sandwich panel in compression. Another objective is to investigate the effect the vertical truss have on the interfacial fracture properties of sandwich structures based on a brittle PET foam hybrid core. The fracture properties of these hybrid cores are compared to those offered by a plain PET foam as well as cores containing resin-filled perforations.

2.3.2 Materials and Manufacturing

Tests were undertaken on the six types of sandwich structure designs summarized in Figure 2.10 a. The core material was a non-porous (closed-cell) PET foam, with a nominal density 130 kg/m^3 and a thicknesses 20 mm. Material A was based on the plain PET foam and did not contain any perforations. Prior to the manufacture of Materials B to F, circular perforations, with an average diameter of 3.0 mm, were drilled in the PET foam. Material B contained perforations arranged in a 25.4 mm square pattern, whereas Material C had perforations positioned in a 12.7 mm square pattern as illustrated in Figure 2.9.

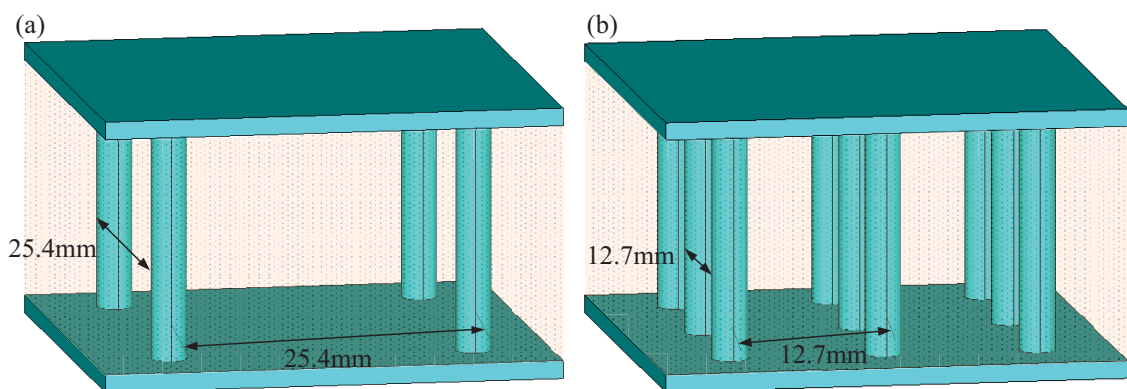


Figure 2.9: (a) Materials B and D unit cell with vertical truss arranged in a 25.4mm square pattern (b) Materials C and E with truss positioned in a 12.7mm square pattern.

Materials D and E had similar hole patterns to Materials B and C respectively; through which continuous glass fiber strands were inserted that went in and out of adjacent holes, as shown schematically in Figure 2.10 bi. Here, an initial batch of samples was produced using a single E-glass fiber strand (Materials D-S and E-S) and a subsequent batch using two (double) strands (Materials D-D and E-D). The approximate fiber volume fraction in those perforations reinforced with a single strand was 1.5%, whereas those containing two strands had a nominal fiber volume fraction of 3%. Material F had a similar pattern of holes to that of Material B, through which 40 mm long glass fiber strands were inserted. The protruding fibers at each end of the strand were then spread over the top and bottoms surfaces of the foam core in a circular fashion, as shown schematically in Figure 2.10bii. Once again both single (Material F-S) and double (Material F-D) glass fiber strands were used. Table 2.1 summarizes the values for the hole separation, fiber volume fraction in the holes as well as the overall panel density.

Table 2.1: Summary of hole separation, fiber volume fraction in the perforations and overall core density for the various materials.

Material	Hole separation d (mm)	Hole fiber volume fraction %	Core density (kg/m ³)
A	n/a	n/a	130
B	25.4	0	153
C	12.7	0	203
D-S	12.7	1.5	205
D-D	12.7	3.0	207
E-S	25.4	1.5	157
E-D	25.4	3.0	159
F-S	25.4	1.5	163
F-D	25.4	3.0	167

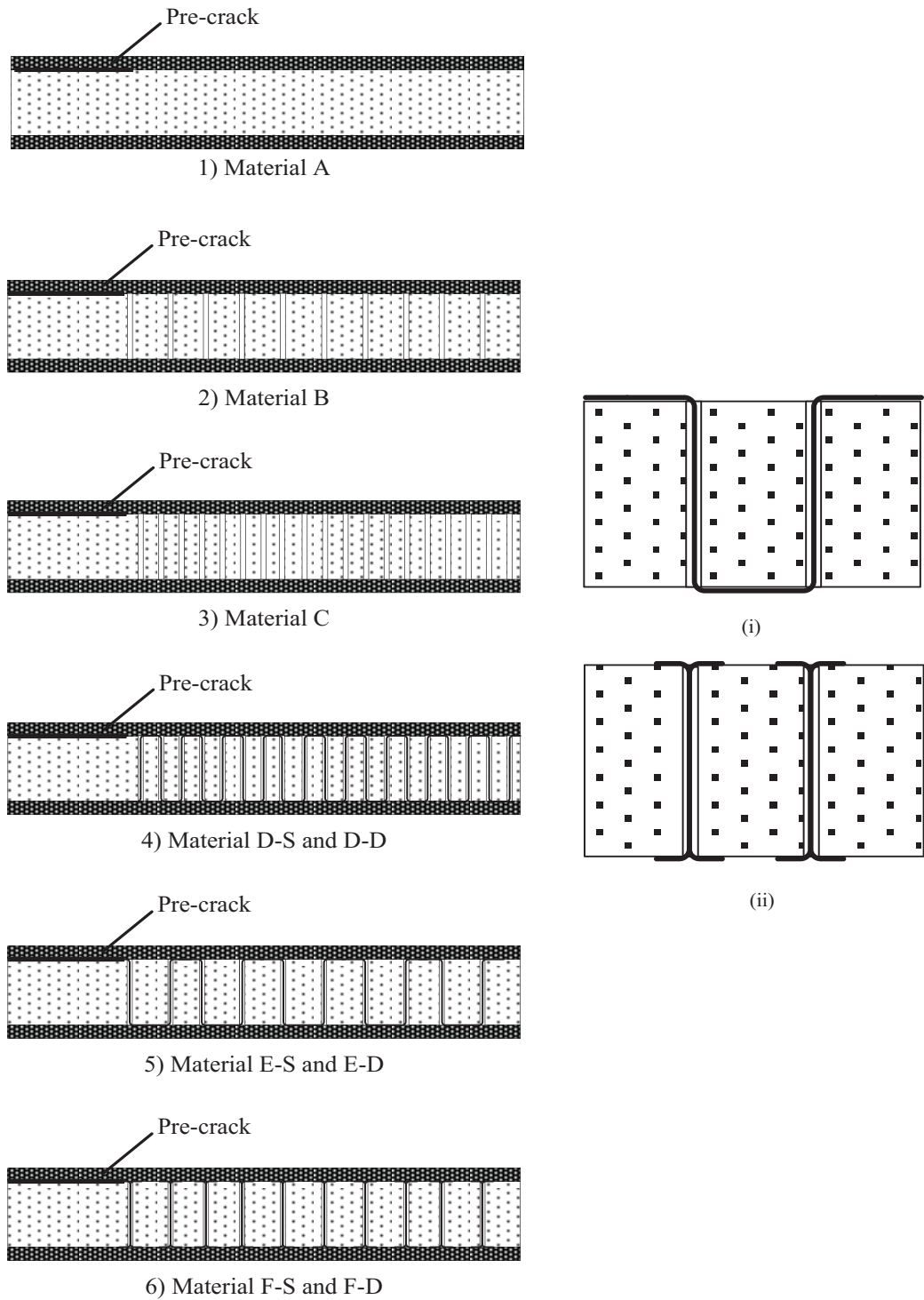


Figure 2.10: (a) Schematic of the configuration of sandwich panels investigated in this study. (b) Schematic of the patterns for the through-thickness fiber reinforcement in (i) Materials D and E and (ii) Material F.

The reinforcement used to manufacture the face-sheets was a unidirectional E-glass fabric with an areal density 600 g/m^2 . During lamination, a 60 mm long folded aluminum foil was placed along the width of the top face of the foam in order to act as a pre-crack during subsequent mechanical testing. It should be noted the core immediately under the aluminum foil in all samples was free of perforations, as shown in the sketches in Figure 2.10a.

All of the sandwich panels were fabricated using the VARTM manufacturing technique as described in Section 2.2.4. A schematic of the lay-up arrangement for the VARTM process is shown in Figure 2.11.

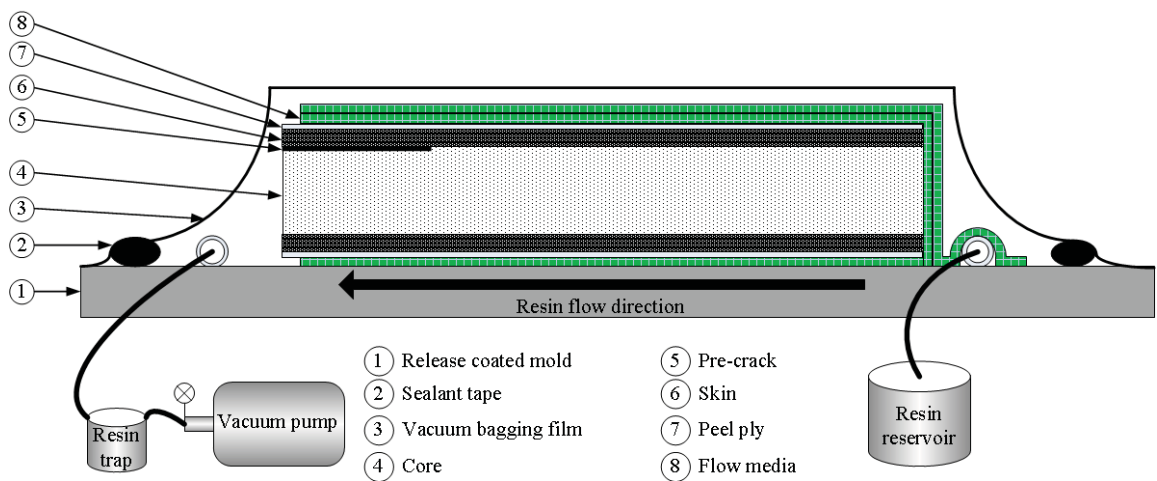


Figure 2.11: Schematic of the VARTM manufacturing set-up.

The skins in the sandwich structures were based on four layers of glass fabric. In order to facilitate and balance the flow of resin through the sandwich panel, two layers of a resin distribution medium were placed on the uppermost fibers and one layer was placed under the lower skin. This procedure was found to yield high quality panels with good reproducibility. Once the stacking procedure was completed (Figure 2.12), the edges of the mold were sealed using a vacuum bag and a sealant tape. The mold was then infused with

resin under vacuum at a pressure of 1 atm. The resin flow fronts were monitored and recorded. The resin-infused panels were cured at room temperature for approximately 12 hours and then post-cured at 65 °C for 7 hours as previously mentioned.



Figure 2.12: Stacking procedure completed in preparation for vacuum bagging and infusion.

2.3.3 Compression tests

The through-thickness compression strength of the sandwich structures was determined using an Instron 5969 testing machine. Square specimens with an edge length of 50 mm based on Materials A, B, C, D-S, E-S and F-S, the descriptions of which are summarized in Table 2.1. Each sample was compressed between the two circular steel platens of the Instron machine, as shown in Figure 2.13, at a crosshead displacement rate of 5 mm/min. Typically, four repeats of each core configuration were tested.

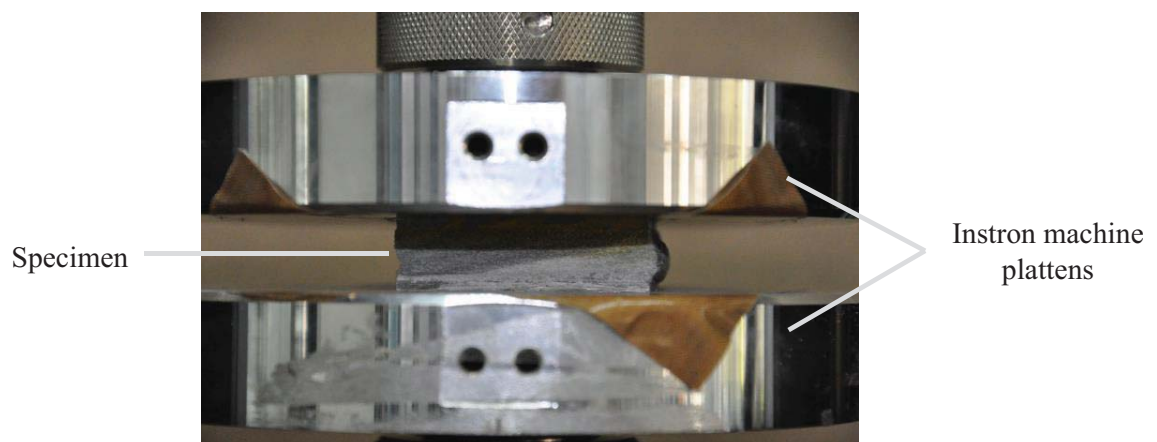


Figure 2.13: The hybrid core under compression loading.

2.3.4 Interfacial fracture tests

The skin-core interfacial fracture properties of the six types of sandwich structure were characterized using the three-point-bend sandwich specimen shown in Figure 2.14. This test consists of loading a protruding tongue at one end of the test sample via a three point bending fixture. Prior to testing, the core and the lower skin directly under the pre-crack were removed using a band saw to leave the upper skin extending at one end. Any residual foam on the protruding composite tongue was removed manually. Here, beams with length and width dimensions of 280 mm x 50 mm were loaded in flexure on an Instron 4505 universal testing machine. Prior to testing the samples were pre-cracked manually to extend the initial crack by approximately 10 mm. The specimens were placed on supports with a diameter of 10 mm, positioned 250 mm apart and loaded centrally, as shown in Figure 2.14. The diameter of the central loading bar was 10 mm. The crosshead displacement rate was set at 2 mm/min. for all tests. Crack propagation was monitored with the aid of a painted grid applied to the skin-core interfacial region. The specimens were loaded until the crack approached the central loading point and then unloaded.

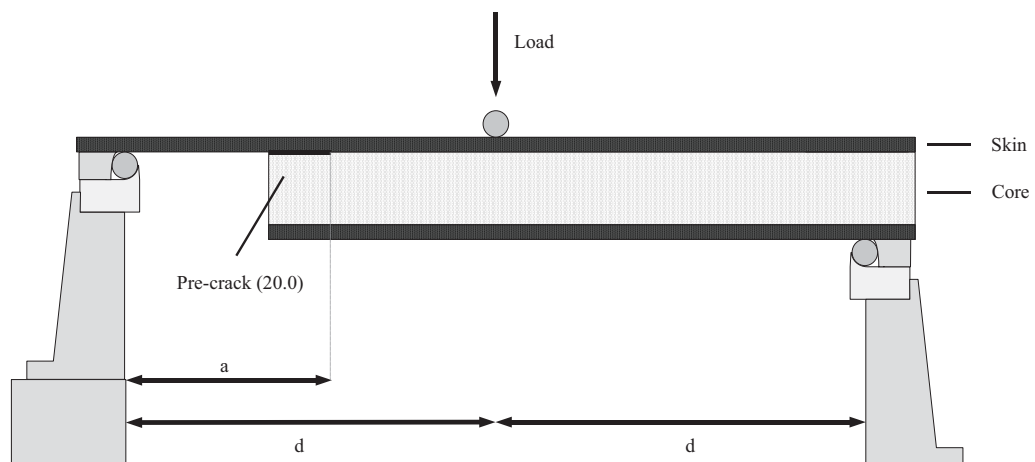


Figure 2.14: Schematic of the three point bend test used to characterize the interfacial fracture toughness of the sandwich structures.

The interfacial fracture energy was determined using the compliance calibration technique.

Here the interfacial fracture toughness, G_C , is given by:

$$G_C = \frac{P^2}{2B} \frac{dC}{da} \quad (2.1)$$

Where P is the applied load, C is the specimen compliance, a , is the crack length and B is the specimen width. In an earlier study [1], it was shown that the compliance of the three point sandwich specimen exhibits a cubic dependency on the crack length, a . Indeed, plots of compliance against a^3 yielded a straight line, whose slope depended on the stiffness of the test sample.

In this study, it was therefore assumed that the compliance depended on crack length according to:

$$C = C_o + ka^3 \quad (2.2)$$

Giving the interfacial fracture energy as:

$$G_C = \frac{3kP^2a^2}{2B} \quad (2.3)$$

The value of k can be determined from the slope of the plot of compliance against the cube of crack length. Figure 2.15a and Figure 2.15b show plots of specimen compliance against the cube of crack length for Materials B and C respectively.

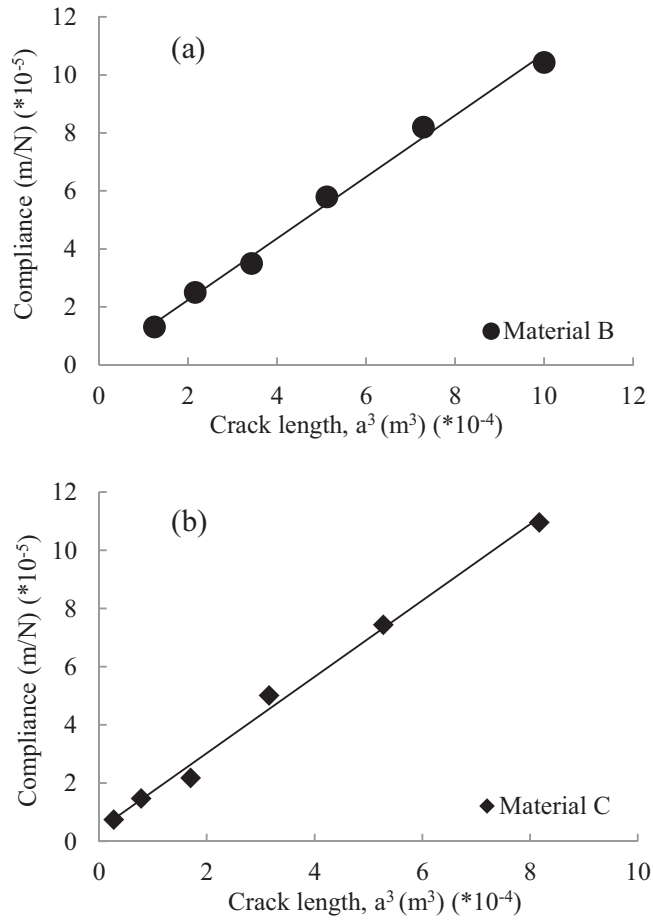


Figure 2.15: Plot of compliance against the cube of crack length of the specimen from (a) Material B, (b) Material C.

Given that crack propagation was highly unstable in many cases, the crack was propagated by hand during this particular test. Here, the precracked sample was loaded within the elastic regime and the compliance measured. The sample was then removed from the test machine and the crack extended by approximately 10 mm by placing it in a bench vice and loading the composite arm manually. The specimen was then re-tested and the new compliance measured. This procedure was repeated several times. From the two traces in Figure 2.15, it is clear that Equation 2.2 accurately captures the compliance-crack length dependency, suggesting that it can be used to characterize the compliance versus crack

length response of these sandwich structures. The mode-mixity at the tip of a crack in a three point bend balsa-based sandwich structure has been analyzed using the virtual crack closure integral in a previous investigation [1]. Here, it was shown that the crack tip in this three point bend specimen is subjected to both Mode I and Mode II loading with the Mode II contribution increasing with crack length. In the present case, the core is clearly a column-reinforced foam. It is believed that the crack tip is loaded predominantly in Mode I, although it is likely that local variations in the overall level of mode-mixity will occur close to the vertical columns.

2.4 Vertical, pyramidal, and octet lattice studies

2.4.1 Overview

In the following, a range of truss structures, based on composite materials have been manufactured using a lost-mold technique. The process included the manufacturing of the vertical, pyramidal, modified pyramidal and octet truss configuration. Further, the process was applied for producing a new range of environmentally-friendly vertical lattice structures based on natural fibers.

The aim here is to assess the quality of a range of truss structures, based on composite materials that have been manufactured using a lost-mold technique. Additionally, the effect of fiber volume fraction, threading technique and strut diameter on the compression properties of vertical truss structures and their individual reinforcing members were examined. The compression response of an all composite pyramidal and octet truss structures is also examined. The properties of the various lattice structures considered here were predicted using analytical and finite element modeling techniques.

2.4.2 Materials and fabrication

The composite column truss cores investigated in this study were manufactured using a lost mold procedure. Here, a series of holes were drilled into wax blocks with length, width and thickness dimensions of 150 x 90 x 36 mm respectively. Four drill diameters were used, these being 2, 2.5, 3 and 4 mm as illustrated in Figure 2.16. The 2 mm and 2.5 mm diameter holes were drilled in six by six arrays to form a unit cell, the 3 mm holes in five by six arrays and the 4 mm holes in four by five arrays, yielding cores with relative densities of 16.3, 26.7, 30.4 and 34.9% respectively.

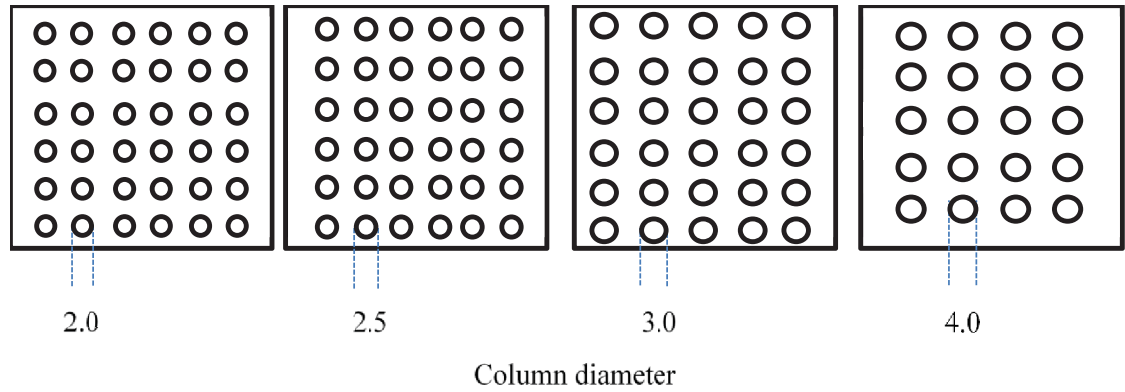


Figure 2.16: Schematic diagram showing the locations of the 2, 2.5, 3, and 4 mm diameter holes in the test samples. The edge lengths of the squares is nominally 30 mm. All dimensions are in mm.

Carbon fiber tows were then threaded through the holes in order to reinforce the structure in the through-thickness direction. Two weaving patterns were adopted and these are shown schematically in Figure 2.17. The first procedure involved threading the fibers through the array of holes and then across the top of the lost mold, as shown schematically in Figure 2.17a. It is worth noting that the same fiber tow is used to link all of the holes in a unit cell, thereby ensuring that there are no fiber breaks in the entire structure. The fiber volume fraction within an individual hole was varied by using increasing numbers of fiber tows during the threading process.

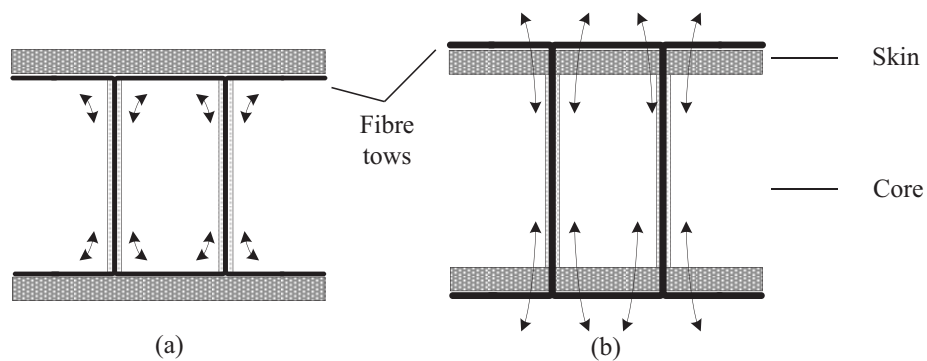


Figure 2.17: Schematic drawings of the two procedures used to thread the samples.

The second weaving pattern involved threading the fibers through the carbon fiber fabric that formed the facings in the resulting sandwich structures. This is shown schematically in Figure 2.17b. Anchoring the through-thickness fibers to the facings has the effect of reducing lateral movement of the composite columns during compression loading.

Following the threading process, the reinforced core blocks were infused with resin using the VARTM manufacturing technique as described in Section 2.2.4. A schematic of the lay-up arrangement for the VARTM process is shown in Figure 2.18. The skins in the sandwich structures were based on four layers of carbon fiber fabric. The panels were allowed to cure at room temperature as described in Section 2.2.5.

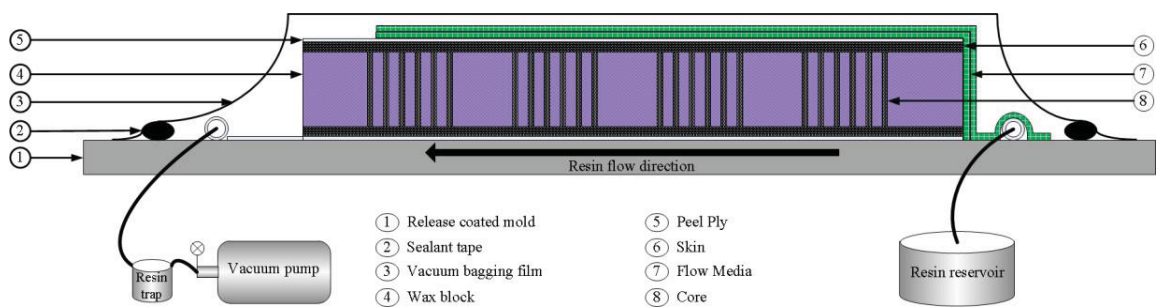


Figure 2.18: Schematic of the VARTM process used to infuse the skins and core.

A second set of lattice structure based on vertical natural fiber struts have been manufactured using the lost mold technique. Using the same drilling configuration shown in Figure 2.16, Jute fiber tows were then threaded through the holes in order to reinforce the structure in the through-thickness direction. The fiber volume fraction within an individual hole was varied by using increasing numbers of fiber tows during the threading process. Initially, 3 and 4 mm diameter columns with fiber volume fractions between zero (i.e. pure resin) and 12% were manufactured. The weaving pattern involved threading the fiber tows through the jute fiber fabric used to produce the facings in the resulting sandwich structures

(Configuration B). Following resin infusion, the wax was melted in an oven leaving a free standing lattice structure.

Tests were also undertaken on sandwich panels based on a pyramidal core, Figure 2.19a, and a modified pyramidal core, in which the unit cell included a central vertical member through its apex, Figure 2.19b. These structures were manufactured using lost molds based on 200 mm square, 28 mm thick salt blocks. Here, the carbon fibers were woven through holes with diameters of 3 mm, according to Configuration A. Following resin infusion, the salt mold was dissolved using a continuous stream of water.

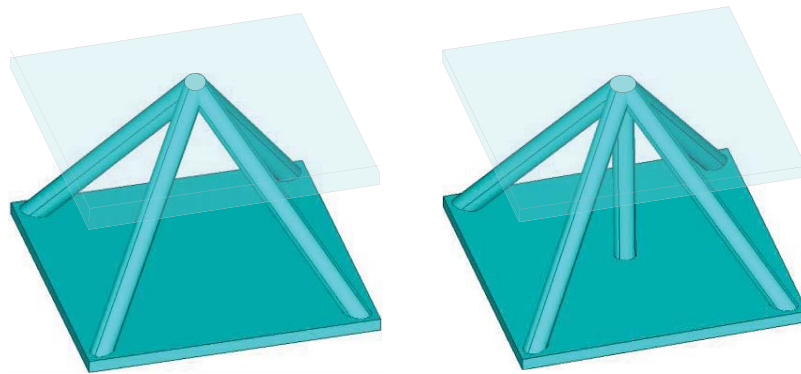


Figure 2.19: Idealized images of (a) a pyramidal structure and (b) a modified pyramidal structure, reinforced with a central vertical member.

Finally, octet truss structures with strut diameters of 4 mm were prepared by drilling an array of holes through 56 mm thick salt blocks. Following resin infusion, the salt mold was dissolved using a continuous stream of water exposing the octet truss core as shown in Figure 2.20.

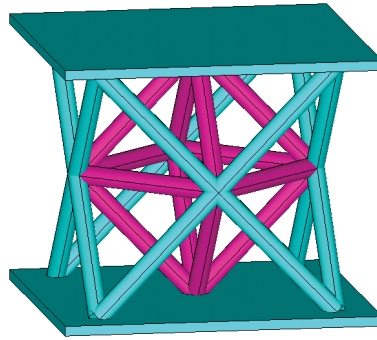


Figure 2.20: Computer generated image of an octet truss structure.

2.4.3 Compression tests

The quasi-static properties of the lattice structures were evaluated by loading the specimens between circular steel platens of an Instron 5969 at a crosshead displacement rate of 2 mm/min as illustrated in Figure 2.22. The strain in the cores was estimated from the crosshead displacement of the test machine. Typically, three to four repeat tests were conducted on each lattice structure. The failure modes during compression loading were elucidated by photographing the samples at regular intervals. Following testing, the specimens were photographed and examined under a low power microscope.

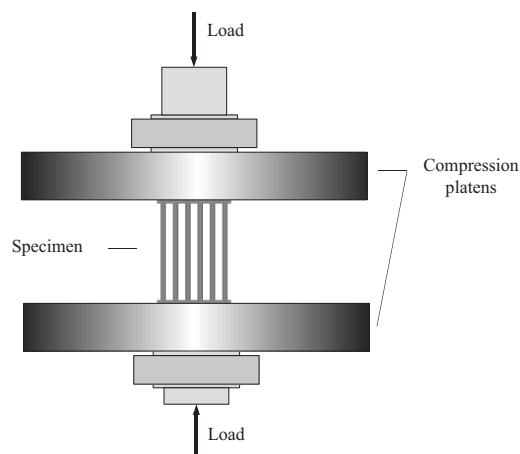


Figure 2.21: Schematic of the compression test used to characterize the axial strength of the manufactured core structure.

2.5 BCC, BCCz, FCC and F₂BCC lattice studies

2.5.1 Overview

The aim of the work outlined here is to investigate the mechanical properties of a range of lattice structures based on a carbon fiber reinforced epoxy composite. The work here examined the potential offered by the lost-mold technique for manufacturing more complex all-composite structures that have hitherto proved extremely challenging to manufacture. Here, the lost mold technique is used to produce a number of relatively complex structures based on what are termed BCC, BCCz, FCC and F₂BCC designs. In the following chapters, analytical models and finite element analyses are used to predict the mechanical response of these lattices. The strength and energy-absorbing characteristics of these structures are then investigated experimentally and the data compared to the aforementioned predictions.

2.5.2 Materials and fabrication

Four, all-composite lattice designs, were considered in this study, these being the BCC, BCCz, FCC and F₂BCC designs shown schematically in Figure 2.22. The BCC structure has a central node, from which eight struts extend to the corners of the unit cell. The BCCz structure is similar to the BCC lattice, but with four additional vertical struts along the four vertical edges of the cell. The FCC structure has two crossed struts on each of the vertical faces and finally the F₂BCC design combines the struts in the FCC and BCC geometries into a single cell.

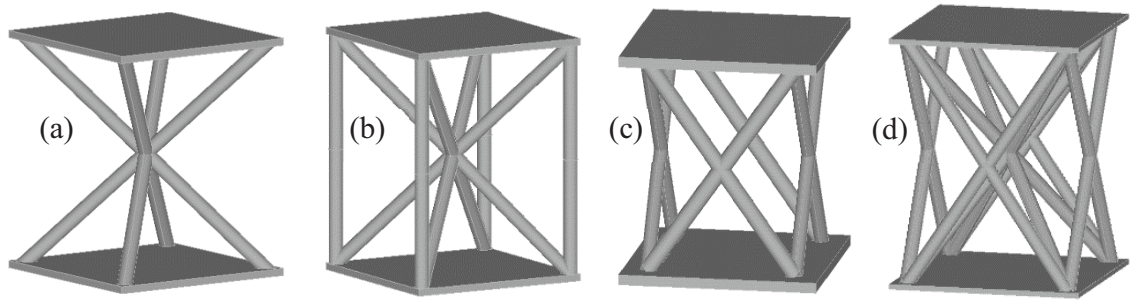


Figure 2.22: Schematic of the unit cell topologies: (a) the BCC unit cell and (b) the BCCz unit cell (c) the FCC unit cell and (d) the F₂BCC lattice.

The lattices were prepared using a lost-mold procedure that has previously been used to manufacture the previous set of truss cores for energy-absorbing applications. Here, 3 mm diameter holes were drilled into wax blocks with a thickness of 37 mm. The non-vertical holes were introduced by placing the wax blocks on a wooden support inclined at 45 degrees. Following the drilling procedure, carbon fiber tows were inserted through the holes with the aid of a large steel needle. The findings of testing the previously described set of lattice structures will show that superior compression strengths can be achieved by anchoring the carbon fibers to the woven carbon fabrics used to produce the composite skins. In order to achieve this, the tows were fed back and forth through the fabrics used to produce the composite skins, as shown schematically in Figure 2.23a and in the photograph in Figure 2.23.b. This threading procedure ensured that the same fiber tow extended through all of the struts within an individual cell, as well as into the upper and lower skins. These facings were based on four layers of plain woven carbon fiber fabric. The fiber volume fraction within a unit cell can be varied by using increasing numbers of fiber tows during the threading process. In this study, the nominal fiber volume fraction, V_f , was maintained at approximately 25%.

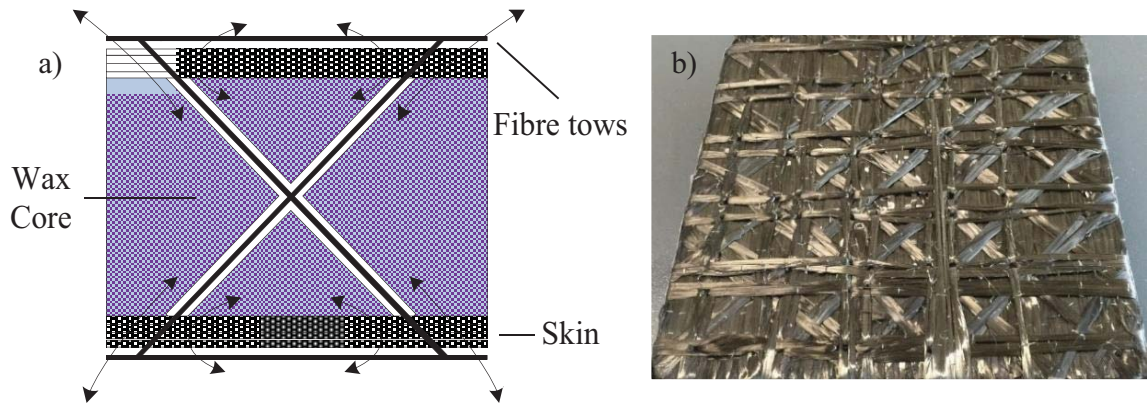


Figure 2.23: (a) Schematic drawings of the procedure used to thread the samples. The fibers extend through the holes and then between the wax core and the skins. (b) Threaded samples showing fibers extending over the skins through the holes.

Once the threading procedure was complete, the wax block was vacuum-bagged and infused with a toughened epoxy, PrimeTM 20LV (Gurit Ltd.), using the VARTM technique as outlined in Section 2.2.4. Here, a distribution medium, Gurit Knitflow40[®], was placed on the upper skins to ensure the effective flow of resin through the lattice block. The experimental set-up for the VARTM process is shown schematically in Figure 2.24. The sandwich panel was infused with resin under vacuum and then allowed to cure at room temperature for 12 hours. Once cured the panels were removed from the bagging material and then post-cured for 7 hours at 65 °C. Finally, the wax mold was removed by placing the panels in an oven heated to 120 °C for four hours.

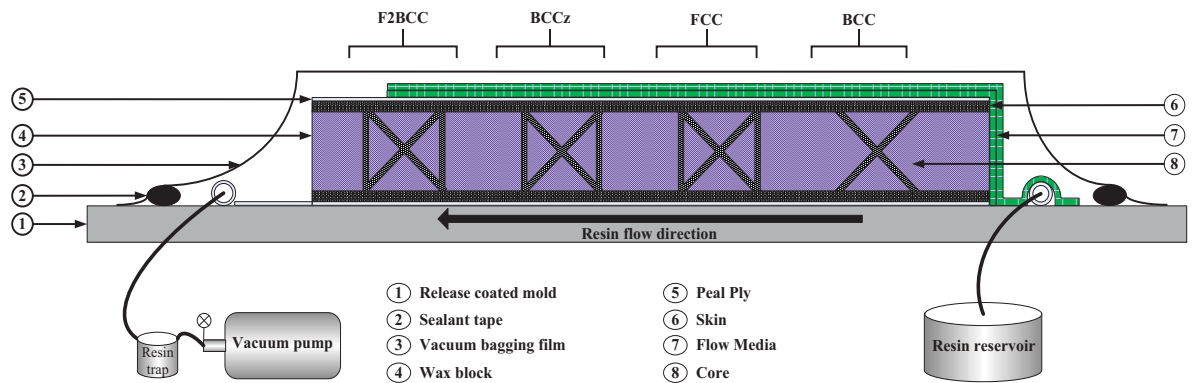


Figure 2.24. Schematic of the VARTM process used to infuse the lattice structures.

2.5.3 Compression tests

The quasi-static properties of the lattice structures were evaluated by loading the specimens in an Instron 5969 at a crosshead displacement rate of 2 mm/min as illustrated in Figure 2.21. Typically, four repeat tests were conducted on each lattice structure. Following testing, the specimens were photographed and examined under a low power microscope.

2.6 Other lattice structures

Finally, the lost-mold technique has been used to manufacture an airfoil cross-section based on a vertical lattice geometry in addition to a single skin sandwich panel and lattice wheel structures. The resulting structures are illustrated in in Appendix B. Here, it has been shown that this simple approach can be used to manufacture relatively complex load-bearing structures in a simple one-shot manufacturing procedure. Summary of the airfoil fabrication process is included in Appendix C.

References

- [1] W. J. Cantwell, R. Scudamore, J. Ratcliffe, and P. Davies, “Interfacial fracture in sandwich laminates”, *Compos. Sci. Technol.*, vol. 59, pp. 2079–2085, 1999.

Chapter 3: Analytical Modeling

3.1 Introduction

The goal in this chapter is to derive the analytical expressions for predicting the elastic properties and the through-thickness compression collapse strength of composite based lattice structures manufactured using the lost mold technique. The analytical calculations are then compared with experimental data from the quasi-static tests and finite element model predictions.

3.2 Elastic properties of parent material

All of the struts manufactured using the lost mold technique were based on a unidirectional fiber composite made from aligned continuous fibers that are embedded in a matrix as shown in Figure 3.1. The reinforcing fiber is carbon, specifically, strands or tows extracted from UT-C300 unidirectional fabric supplied by Gurit Ltd. Natural jute fiber was also considered in this study. The matrix is an epoxy resin supplied under the commercial name PRIME™ 20LV from Gurit Ltd. The effective mechanical properties of the manufactured composite are a function of both the fiber and matrix properties, their respective volume fractions and of the fiber distribution within the matrix. The effective elastic properties are considered here. Other physical properties, such as the thermal expansion coefficients, moisture swelling coefficients, static and dynamic viscoelastic properties, conductivity, and moisture diffusivity are beyond the scope of this work.

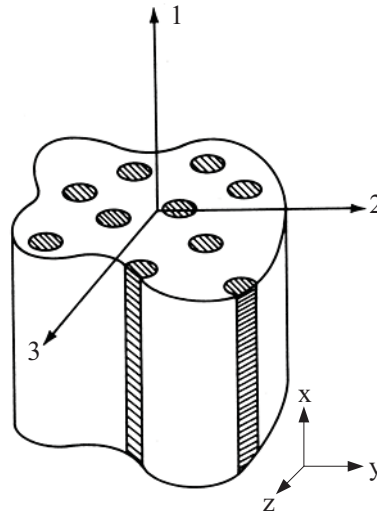


Figure 3.1: Unidirectional fiber-reinforced composite [1]

An analytical micromechanics model, based on the rule of mixtures, is employed to predict the elastic properties of the composite material making up the truss within the core. Typical values of basic properties of the constituent materials (fibers and matrix) were used in the micromechanics model and these are summarized in Table 3.1 for the carbon based composite [2, 3].

Table 3.1: Constituent materials elastic properties

Property	Carbon fiber (UT-C300)	Epoxy-Resin (PRIME™ 20LV)
Density (ρ)	0.0018 g/mm ³	0.00115 g/mm ³
Weight per unit length	0.0008 g/mm	-
Longitudinal elastic modulus (E_x)	210-230 GPa	3-6 GPa
Transverse elastic modulus (E_y, E_z)	10-20 GPa	3-6 GPa
Longitudinal shear modulus (G_{xy})	27 GPa	1-2 GPa
Transverse shear modulus (G_{yz})	7 GPa	1-2 GPa
Longitudinal Poisson's ration (ν_{xy})	0.20	0.36
Transverse Poisson's ration (ν_{yz})	0.30	0.36

The fiber volume fraction is a necessary parameter for estimating the elastic properties and this was derived as follows:

$$V_f = \frac{\text{Volume of fibers}}{\text{Volume of composite}} = \frac{\text{Mass of fiber} / \text{Fiber density}}{\text{Volume of composite}} \quad (3.2)$$

$$= \frac{\text{Mass of fiber}}{\pi r^2 l \rho_f}$$

where ρ_f is the density of the carbon fiber, l and r are the strut length and radius respectively. The fiber volume fraction within the strut was controlled by the number of identical fiber strands passing through it. Fiber tows measuring one meter in length, weighing 0.8 g, according to the manufacturer's catalogue. The latter was also confirmed in laboratory measurements. The mass of fibers in each vertical column is estimated as follows:

$$\text{Mass of fibers} = \text{No. of strands} \times \text{Fiber mass per unit length} \times l$$

Finally, the fiber volume fraction reduces to,

$$V_f = \frac{\text{No. of strands} \times \text{Fiber mass per unit length}}{\pi r^2 \rho_f} \quad (3.3)$$

The matrix volume fraction is simply:

$$V_m = 1 - V_f \quad (3.4)$$

A unidirectional fiber reinforced composite is considered an orthotropic material with one plane of symmetry perpendicular to the fiber direction with the other two being parallel to the fiber direction and orthogonal. The 3-D Hooke's law, which relates stress and strain for an orthotropic material, in terms of compliance is given by:

$$\begin{Bmatrix} \epsilon_1 \\ \epsilon_2 \\ \epsilon_3 \\ \gamma_1 \\ \gamma_2 \\ \gamma_3 \end{Bmatrix} = \begin{bmatrix} S_{11} & S_{12} & S_{13} & 0 & 0 & 0 \\ S_{12} & S_{22} & S_{23} & 0 & 0 & 0 \\ S_{13} & S_{23} & S_{33} & 0 & 0 & 0 \\ 0 & 0 & 0 & S_{44} & 0 & 0 \\ 0 & 0 & 0 & 0 & S_{55} & 0 \\ 0 & 0 & 0 & 0 & 0 & S_{66} \end{bmatrix} \begin{Bmatrix} \sigma_1 \\ \sigma_2 \\ \sigma_3 \\ \sigma_4 \\ \sigma_5 \\ \sigma_6 \end{Bmatrix} \quad (3.5)$$

It is noted that nine constants are required to describe this material. All fibers passing through the vertical columns making up the composite core are aligned in one direction and their distribution through the cross-section is random, Figure 3.2.

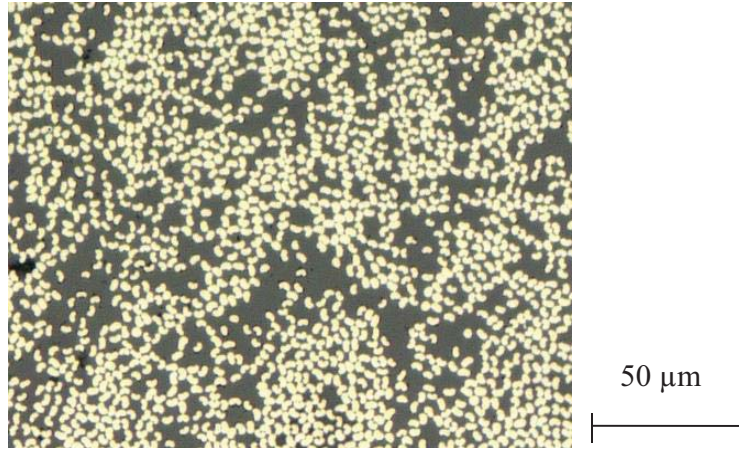


Figure 3.2: Randomly distributed fibers in the cross-section of a strut with $V_f=51\%$.

Therefore, the fiber direction can be considered an axis of symmetry and consequently the vertical columns are considered transversely isotropic material through the cross-section. A transversely-isotropic material is described by five independent material constants. The five most commonly used independent engineering constants are listed below,

$$E_1, E_2, \nu_{12}, \nu_{23}, G_{23}$$

Where the symbols, E, ν, G are the elastic modulus, Poisson's ratio and shear modulus respectively, and the numbered subscripts refer to composite coordinates in Figure 3.1. The generalized 3-D Hooke's law in terms of compliance reduces to,

$$\begin{Bmatrix} \epsilon_1 \\ \epsilon_2 \\ \epsilon_3 \\ \gamma_1 \\ \gamma_2 \\ \gamma_3 \end{Bmatrix} = \begin{bmatrix} S_{11} & S_{12} & S_{12} & 0 & 0 & 0 \\ S_{12} & S_{22} & S_{23} & 0 & 0 & 0 \\ S_{12} & S_{23} & S_{22} & 0 & 0 & 0 \\ 0 & 0 & 0 & 2(S_{22} - S_{23}) & 0 & 0 \\ 0 & 0 & 0 & 0 & S_{66} & 0 \\ 0 & 0 & 0 & 0 & 0 & S_{66} \end{bmatrix} \begin{Bmatrix} \sigma_1 \\ \sigma_2 \\ \sigma_3 \\ \sigma_4 \\ \sigma_5 \\ \sigma_6 \end{Bmatrix} \quad (3.6)$$

The Voigt model, known as the rule of mixtures model, is used to obtain the longitudinal elastic properties. On the other hand, the Reuss model, also known as the inverse rule of mixtures, is used to obtain the elastic properties along the transverse direction of the fibers. The fibers are considered anisotropic with different properties in the axial and transverse directions, while the matrix is isotropic. Assuming a perfect bond between fibers and matrix, the elastic properties are extracted using both models. For longitudinal loading parallel to the unidirectional aligned fibers, the elastic modulus (E_1) is:

$$E_1 = V_f E_{1f} + V_m E_m \quad (3.7)$$

where V_f and V_m are the volume fractions of fiber and matrix respectively, E_{1f} is the longitudinal elastic modulus of the fiber and E_m is the elastic modulus of the matrix. Similarly, the major Poisson's ratio ν_{12} can be predicted from the values of the fiber and the matrix as follows,

$$\nu_{12} = V_f \nu_{12f} + V_m \nu_m \quad (3.8)$$

In the case of transverse loading in the 2-direction, the transverse modulus of the composite (E_2) is obtained as:

$$E_2 = \frac{E_{2f} E_m}{V_f E_m + V_m E_{2f}} \quad (3.9)$$

where E_{2f} is the transverse modulus of fibers. Similarly, the shear modulus of the composite (G_{12}), can be determined from the shear moduli of the fibers (G_{12f}) and matrix (G_m):

$$G_{12} = \frac{G_{12f}G_m}{V_fG_m + V_mG_{12f}} \quad (3.10)$$

The Poisson's ration in the 2-3 plane is related to transverse Poisson's ratio of the fibers (v_{23f}) and matrix (v_m) as follows [4]:

$$v_{23} = \frac{v_{23f}v_m}{V_mv_{23f} + V_fv_m} \quad (3.11)$$

Any two perpendicular directions on the 2-3 plane can be taken as axes due to the random distribution of fibers on that plane. In other words, the 2-3 plane is isotropic. Therefore, the following holds in the 2-3 plane:

$$G_{23} = \frac{E_2}{2(1 + v_{23})} \quad (3.12)$$

Considering transverse isotropy of the material by taking into account that the directions 2 and 3 (cross-section plane) are indistinguishable, the following relations are applied:

$$E_2 = E_3 \quad (3.13)$$

$$v_{12} = v_{13} \quad (6.14)$$

$$G_{12} = G_{13} \quad (3.15)$$

From the symmetry of the compliance matrix [S] and the above, we can conclude that:

$$\frac{v_{12}}{E_1} = \frac{v_{21}}{E_2} \quad (3.16)$$

$$\frac{v_{13}}{E_1} = \frac{v_{31}}{E_3} \quad (3.17)$$

$$\frac{v_{23}}{E_2} = \frac{v_{32}}{E_3} \quad (3.18)$$

As previously mentioned, for a transversely isotropic material, only five material constants are independent and because the [S] matrix must be symmetric, the compliance matrix in terms of elastics properties is as follows:

$$[S] = \begin{bmatrix} \frac{1}{E_1} & -\frac{\nu_{12}}{E_1} & -\frac{\nu_{12}}{E_1} & 0 & 0 & 0 \\ -\frac{\nu_{12}}{E_1} & \frac{1}{E_2} & -\frac{\nu_{23}}{E_2} & 0 & 0 & 0 \\ -\frac{\nu_{12}}{E_1} & -\frac{\nu_{23}}{E_2} & \frac{1}{E_2} & 0 & 0 & 0 \\ 0 & 0 & 0 & 2\left(\frac{1+\nu_{23}}{E_2}\right) & 0 & 0 \\ 0 & 0 & 0 & 0 & \frac{1}{G_{12}} & 0 \\ 0 & 0 & 0 & 0 & 0 & \frac{1}{G_{12}} \end{bmatrix} \quad (3.19)$$

During the weaving process, fiber tows are passed through the holes at a slight angle with respect to the strut's axial direction (x-axis), as shown in Figure 3.3. The degree of the inclination depends on the geometry of the column (diameter and height) and varies between 3° to 6° approximately for columns with diameters of 2 mm to 4 mm respectively.

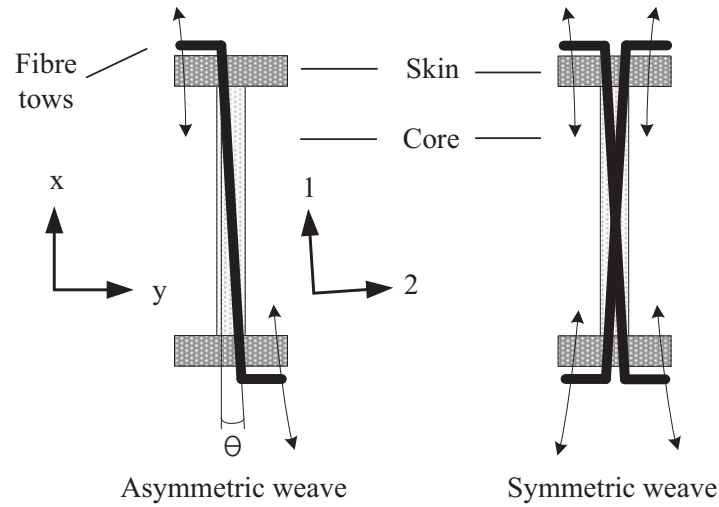


Figure 3.3: Fiber tows through the core oriented at an angle.

The core columns were reinforced with fibers using a symmetric weave pattern, consequently yielding a balanced and symmetric composite about the reference x-axis. The compliance matrix $[S]$ is transformed into the global coordinated system as follows:

$$[S'] = [T]^T [S] [T] \quad (3.20)$$

where $[T]$ is the transformation matrix. The stiffness matrix $[C']$ in the global coordinate system per fiber weave is obtained by:

$$[C'] = [S']^{-1} \quad (3.21)$$

Assuming that the fiber tows were distributed equally over the four quadrants of the cylinder, the stiffness matrix of the column is built by averaging the stiffness matrices for each quadrant (k) in the global coordinate system resulting from each weave direction as follows:

$$[C'] = \sum_{k=1}^4 \frac{1}{4} [C'_k] \quad (3.22)$$

The properties of the composite column are obtained by inverting the average to obtain the compliance and using the following:

$$[S'] = \begin{bmatrix} S'_{11} & S'_{12} & S'_{12} & 0 & 0 & 0 \\ S'_{12} & S'_{22} & S'_{23} & 0 & 0 & 0 \\ S'_{12} & S'_{23} & S'_{22} & 0 & 0 & 0 \\ 0 & 0 & 0 & S'_{44} & 0 & 0 \\ 0 & 0 & 0 & 0 & S'_{66} & 0 \\ 0 & 0 & 0 & 0 & 0 & S'_{66} \end{bmatrix}$$

$$= \begin{bmatrix} \frac{1}{E_x} & -\frac{\nu_{yx}}{E_y} & -\frac{\nu_{zx}}{E_z} & 0 & 0 & 0 \\ -\frac{\nu_{xy}}{E_x} & \frac{1}{E_y} & -\frac{\nu_{zy}}{E_z} & 0 & 0 & 0 \\ -\frac{\nu_{xz}}{E_x} & -\frac{\nu_{yz}}{E_y} & \frac{1}{E_z} & 0 & 0 & 0 \\ 0 & 0 & 0 & \frac{1}{G_{yz}} & 0 & 0 \\ 0 & 0 & 0 & 0 & \frac{1}{G_{xz}} & 0 \\ 0 & 0 & 0 & 0 & 0 & \frac{1}{G_{xy}} \end{bmatrix} \quad (3.23)$$

Therefore, it is possible to obtain the apparent properties of the composite column in terms of compliance as follows:

$$\begin{aligned}
E_x &= 1/S'_{11} & G_{yz} &= 1/S'_{44} & v_{xy} &= -S'_{21}/S'_{11} \\
E_y &= 1/S'_{22} & G_{xz} &= 1/S'_{55} & v_{xz} &= -S'_{31}/S'_{11} \\
E_z &= 1/S'_{33} & G_{xy} &= 1/S'_{66} & v_{yz} &= -S'_{32}/S'_{22}
\end{aligned} \tag{6.24}$$

The slight tilt of the fibers in the columns does not significantly influence the axial elastic modulus of the structure. Results from calculations demonstrate that the maximum value for the ratio E_1/E_x was equal to 1.03. A similar pattern is observed for the remaining elastic properties. The apparent elastic properties of the composite struts that take into account the fiber tilt are used throughout this work.

3.3 Elastic values

Based on the micromechanics approach, the elastic properties of the truss material were determined. Table 3.2 summarizes the elastic properties predictions for various materials.

Table 3.2: Elastic properties for materials having three different fiber content.

Symbol	V _f = 21%	V _f = 35%	V _f = 50%	Property
E ₁	46 GPa	75 GPa	104 GPa	Elastic modulus in the longitudinal direction
E ₂	4 GPa	5 GPa	6 GPa	Elastic modulus in the transverse direction
E ₃	4 GPa	5 GPa	6 GPa	Elastic modulus in the transverse direction
G ₁₂ , G ₁₃	1.7 GPa	2.0 GPa	2.5 GPa	Axial shear modulus
G ₂₃	1.5 GPa	1.8 GPa	2 GPa	Through-thickness shear modulus
ν ₁₂ , ν ₁₃	0.35	0.32	0.28	Axial Poisson's ratio
ν ₂₃	0.34	0.33	0.33	Through-thickness Poisson's ratio

The elastic modulus in the longitudinal direction (E_1) of several circular rods (various diameters and fiber volume content) were characterized using the three-point-bend test. The flexural modulus was calculated according to the following:

$$E_1 = \frac{mL^3}{48I} \quad (3.25)$$

Where m is the gradient of the initial straight-line portion of the load deflection curve, L is the support span and I the cross-sectional area moment of inertia. The results from the 3-point bend tests and the micromechanics approach are summarized in Figure 3.4 which shows good agreement between predicted and measured values.

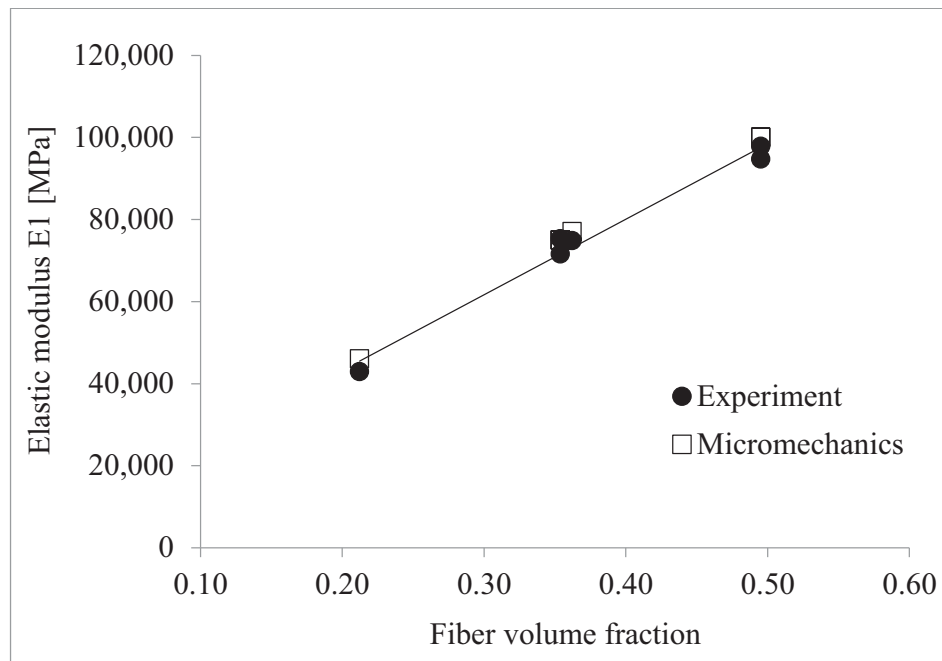


Figure 3.4: Estimated longitudinal modulus for materials having various fiber volume fractions. Experimental results are based on the 3-point bend test performed on rods having circular cross-sections.

3.4 Strength values

The strength properties of the composite material are necessary for predicting the lattice structure response using analytical calculations and FE modeling. The compression strength of composite materials manufactured using the lost mold technique were determined experimentally through a series quasi-static compression tests the results of which are presented in detail in Chapter 5. Here, a summary of the measured and assumed strength values are presented in Table 3.3.

Table 3.3: Summary of the strength characteristics for materials having 28% and 42% fiber volume fraction.

Symbol	$V_f = 28\%$	$V_f = 42\%$	Property
X^T	250 MPa*	350 MPa*	Longitudinal tensile strength
X^C	210 MPa	315 MPa	Longitudinal compressive strength
Y^T	65 MPa*	80 MPa*	Transverse tensile strength
Y^C	65 MPa*	80 MPa*	Transverse compressive strength
S^L	6 MPa*	7 MPa*	Transverse shear strength
S^T	12 MPa*	14 MPa*	Longitudinal shear strength

* Assumption

Summary of the mechanical properties, including elastic and strength characteristics, for all materials examined in this study are listed in Appendix A. The influence of varying the assumed values (with the exception of the longitudinal tensile strength, X^T) on the FE simulation results was found to be relatively insignificant. The assumed values were doubled in one FE simulation case and reduced by half in another case and it was found that they both predict very similar stiffness and collapse strength properties. The FE simulation strength predictions were most sensitive to the longitudinal compressive and tensile strengths X^C and X^T respectively.

3.5 Analytical model of the compressive response

The goal of this section is to obtain the elastic properties and collapse strength of the various truss core configurations as a function of the apparent composite material properties and the core geometry. Extensive work has been carried out in developing relations between the parent material properties and the elastic response and the strength prediction of the various lattice core structures [5–11]. The pyramidal core equations included in this chapter serve as an introduction to the topic of deriving elastic and strength response of lattice structures in terms of the parent material properties and geometric properties of the core. This work is further extended to derive similar relations for the vertical column core and the modified pyramidal core.

3.5.1 Analytical predictions for the response of composite pyramidal truss core

3.5.1.1 Relative density

The geometric configuration of a unit cell of a 4-legged pyramidal truss core is shown in Figure 3.5. The critical parameters describing the geometry include the truss length, l , the diameter, d and the truss inclination angle w with respect to the horizontal.

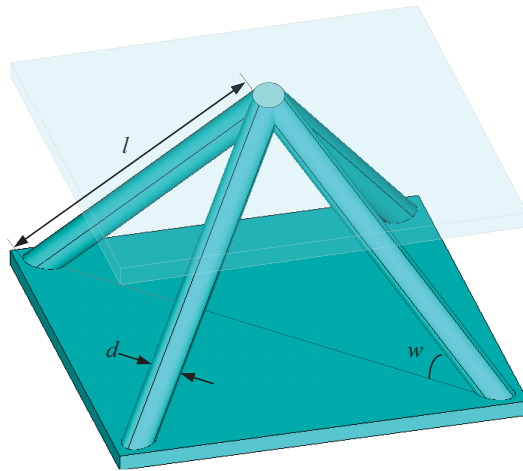


Figure 3.5: Schematic of a unit cell of the 4-legged pyramidal core.

Here, the inclination angle of the trusses with respect to the lower face-sheet of the unit cell $w = 45^\circ$ with a truss length $l = 36mm$ and a diameter $d = 3mm$. The relative density of the 4-legged pyramidal cell structure can be determined by calculating the volume of the truss within a unit cell and dividing it by the volume of the unit cell. The volume of a unit cell is simply given by:

$$Unit\ cell\ volume = 2l^3 \sin(w) \cos^2(w) \quad (3.26)$$

The volume within the unit cell occupied by the cylindrical truss is:

$$Truss\ volume = 4\pi r^2 l \quad (3.27)$$

Thus, the relative density is given by:

$$\bar{\rho}_{pyr} = \frac{4\pi}{\bar{l}^2 \sin 2w \cos w} \quad (3.28)$$

where the non-dimensional lengths $\bar{l} = l/r$ (r is the truss radius).

3.5.1.2 Elastic modulus

The following procedure involves deriving the analytical expressions for the through-thickness compressive stiffness and strength of the composite pyramidal core sandwiched between two rigid face-sheets. The pyramidal trusses are made from a unidirectional composite with the fibers aligned along the axial direction of the struts of the pyramidal truss. A local coordinate system (e_1 - e_2) is defined, with the e_1 axis parallel to the axial direction of the truss and aligned with the reinforcing fibers. The elastic modulus and the compressive strengths in the e_1 direction are E_s and σ_c respectively, while τ_y is the longitudinal shear strength of the composite truss. Using the approach developed by Finnegan [5], the analytical expression for the compressive elastic modulus of a pyramidal core unit cell is obtained in terms of the core geometry and the elastic properties of the

parent material. The elastic deformation of a single truss is initially examined, for which the results are extended to evaluate the effective properties of the pyramidal core.

Considering a pyramidal unit cell, as shown in Figure 3.6a, with an applied axial compressive force F applied in the x -direction of the global Cartesian coordinate system resulting in displacement δ , as shown in Figure 3.6b. A free-body diagram for a single rigid-jointed truss is shown in Figure 3.6c, in which the axial, F_a , and shear, F_s forces are created in each of the trusses.

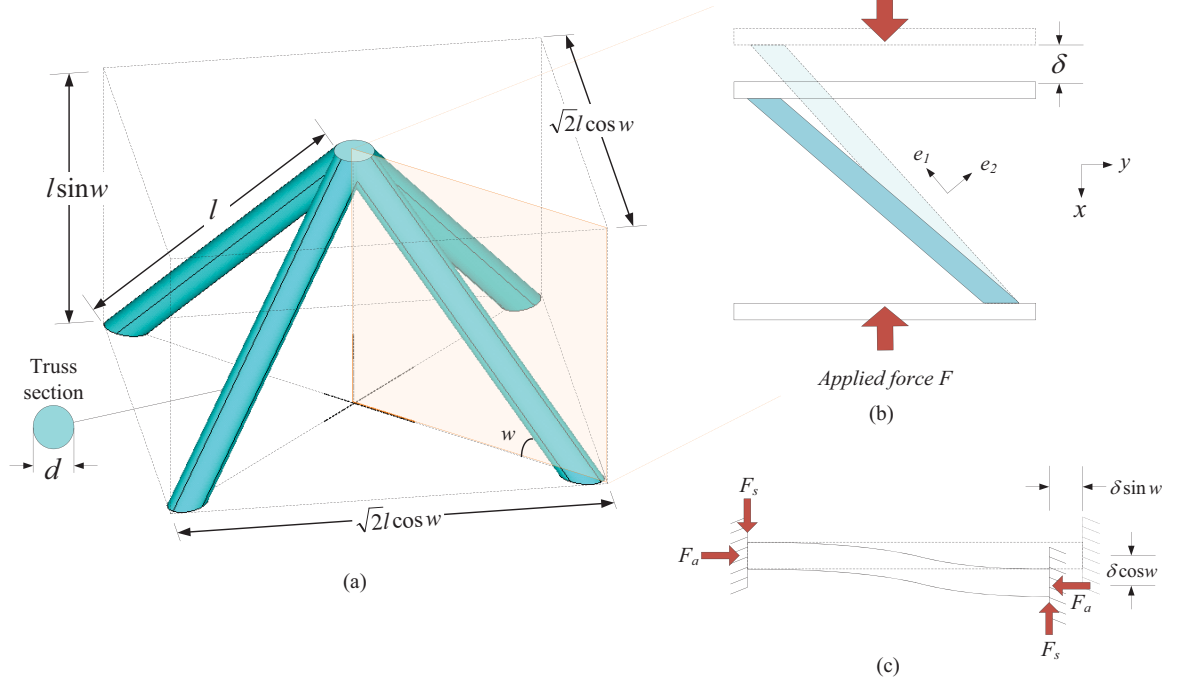


Figure 3.6: Schematic of (a) unit cell (b) deflection of a single truss of the pyramidal core upon application of a uniaxial compressive load (c) the free-body diagram of a truss subjected to compression and shear.

By resolving the resulting displacement δ into two perpendicular components in the local coordinate system we obtain:

$$\delta_a = \delta \sin w \quad (3.29)$$

and

$$\delta_s = \delta \cos w \quad (3.30)$$

Using beam theory, the axial and shear forces in the strut are given by:

$$F_a = \frac{E_s \pi r^2 \delta \sin w}{l} \quad (3.31)$$

and

$$F_s = \frac{12 E_s I \delta \cos w}{l^3} \quad (3.32)$$

respectively, where $I = \pi r^4/4$ is the second moment of area of the truss circular cross-section. The net applied force, F is the sum of the axial and shear-force components in the x-direction:

$$F = F_a \sin w + F_s \cos w = \frac{E_s \pi r^2 \delta}{l} \left[\sin^2 w + 3 \left(\frac{r}{l} \right)^2 \cos^2 w \right] \quad (3.33)$$

Realizing that each of the 4 trusses in the pyramidal core supports the applied force F as in Equation 3.33 and knowing the planar area A of the unit cell, the through-thickness stress, σ_{pyr} , supported by the unit cell is,

$$\sigma_{pyr} = \frac{F_{total}}{A} = \frac{8F}{(2 l \cos w)^2} \quad (3.34)$$

The axial strain in the unit cell in the x-direction ε_{pyr} by definition is:

$$\varepsilon_{pyr} = \frac{\delta}{l \sin w} \quad (3.35)$$

Based on the expressions for stress, σ_{pyr} and strain, ε_{pyr} of the unit cell in Equations 3.34 and 3.35; the elastic modulus defined by $E_{pyr} = \sigma_{pyr}/\varepsilon_{pyr}$ for the pyramidal core is given by:

$$\frac{E_{pyr}}{E_s} = \frac{2\pi \sin w}{\bar{l}^2 \cos^2 w} \left[\sin^2 w + \frac{3 \cos^2 w}{\bar{l}^2} \right] \quad (3.36)$$

The elastic modulus is related to the relative density $\bar{\rho}_{pyr}$ of the core via:

$$\frac{E_{pyr}}{E_s} = \bar{\rho}_{pyr} \sin^4 w + \frac{3 \bar{\rho}_{pyr}^2 \sin^3 w \cos^4 w}{2\pi} \quad (3.37)$$

The first term represents the contribution to stiffness of the core, due to stretching of the struts, while the second term represents the contribution from bending of the struts [5].

By considering a pin-jointed strut, a first order approximation for the elastic modulus of the core can be obtained. In the absence of shear forces on a pin-jointed strut, the net applied force F in the x-direction becomes:

$$F = F_a \sin w = \frac{E_s \pi r^2 \delta \sin^2 w}{l} \quad (3.38)$$

Using Equations 3.34 and 3.35 the elastic modulus E_{pyr} for the pyramidal core is given by:

$$\frac{E_{pyr}}{E_s} = \frac{2\pi \sin^3 w}{\bar{l}^2 \cos^2 w} \quad (3.39)$$

In terms of relative density, the above expression reduces to:

$$\frac{E_{pyr}}{E_s} = \bar{\rho}_{pyr} \sin^4 w \quad (3.40)$$

Deshpande *et al.* provided a first order approximation of the axial modulus for a pyramidal core, which is found to be in agreement with the above equation [6].

3.5.1.3 Collapse strength

3.5.1.3.1 Plastic micro-buckling

Prior micro-buckling, the rigid-jointed strut is elastic and the previous analysis in Section 3.5.1.2 is applicable. The net applied fore, F per strut follows from Equation 3.33 as:

$$F = \sigma_c \pi r^2 \sin w \left[1 + \frac{3 \cot^2 w}{\bar{l}^2} \right] \quad (3.41)$$

Within the elastic region, the axial stress σ_c is given by $\sigma_c = E_s \delta \sin w / l$. At the onset of failure, σ_c represents the axial stress required to initiate failure in the strut. Using Equation 3.34, the nominal compressive strength of a pyramidal core composed of four struts can be written as follows:

$$\frac{\sigma_{pyr}}{\sigma_c} = \frac{2\pi \sin w (\bar{l}^2 + 3 \cot^2 w)}{\bar{l}^2 (\bar{l} \cos w)^2} \quad (3.42)$$

In terms of the unit cell relative density $\bar{\rho}_{pyr}$ the above expression reduces to:

$$\frac{\sigma_{pyr}}{\sigma_c} = \bar{\rho} \sin^2 w \left[1 + \frac{3 \bar{\rho} \cos^4 w}{2\pi \sin w} \right] \quad (3.43)$$

It is generally accepted that plastic micro-buckling is an imperfection-sensitive event that is dependent on the initial misalignment of the fiber and the non-linear longitudinal shear of the composite within a narrow kink band. Argon suggested that the initial misalignment angle ($\bar{\varphi}$) of the fibers and the shear yield stress of the matrix are the main factors influencing compressive strength, σ_{max} as given in the following expression:

$$\sigma_{max} = \frac{\tau_y}{\bar{\varphi}} \quad (3.44)$$

For a rigid perfectly-plastic composite of shear strength τ_y . It is assumed that the kink band is normal to the axial fiber direction, with a vanishing inclination angle β . For the truss in the pyramidal core, the case of remote stress involving combined axial compression and in-plane shear stress, τ^∞ must be considered. Budiansky and Fleck [12] have shown that the

presence of a remote shear results in a knockdown effect on the micro-buckling strength and can be approximated by:

$$\sigma_c = \frac{\tau_y - \tau^\infty}{\bar{\varphi}} \quad (3.45)$$

Prior microbuckling, the truss is elastic and the expressions for the in-plane shear stress τ^∞ given as $\tau^\infty = F_s/\pi r^2$ is expressed as follows:

$$\frac{\tau^\infty}{\sigma_c} = 3 \left(\frac{r}{l} \right)^2 \cot w \quad (3.46)$$

Thus, from Equations 3.45 and 3.46 the critical strength under combined axial compression and in-plane shear in the inclined truss can be expressed as:

$$\sigma_c = \frac{\tau_y}{\bar{\varphi} + 3 \left(\frac{r}{l} \right)^2 \cot w} = \frac{\sigma_{max}}{\left[1 + \frac{3 \cot w}{\bar{\varphi}} \left(\frac{r}{l} \right)^2 \right]} \quad (3.47)$$

Combining Equations 3.47 and 3.43, the strength of the pyramidal core in terms of the micro-buckling strength σ_{max} of the rigid-jointed pyramidal truss is obtained. The fiber misalignment angle of the unidirectional fibers is taken to be 2° as previously described.

For pin-jointed struts it is possible to derive an expression for the compressive strength of the pyramidal core. The resulting calculation gives an upper bound of the strength of the pyramidal core in terms of the failure stress σ_{max} of the composite parent material. The net applied force, F per pin-jointed strut in the absence of shear follows from Equation 3.33 as:

$$F = \sigma_c \pi r^2 \sin w \quad (3.48)$$

Using Equation 3.34, the compressive strength of a pyramidal core composed of four pin-jointed struts can be written as:

$$\frac{\sigma_{pyr}}{\sigma_c} = \frac{2\pi \sin w}{\bar{l}^2 \cos^2 w} \quad (3.49)$$

In terms of relative density, the expression simplifies to:

$$\frac{\sigma_{pyr}}{\sigma_c} = \bar{\rho}_{pyr} \sin^2 w \quad (3.50)$$

In the case of remote stress involving axial compression stress only, the micro-buckling strength σ_c is simply:

$$\sigma_c = \sigma_{max} \quad (3.51)$$

3.5.1.3.2 Euler buckling

Under an axial compressive load, the pyramidal core may collapse by elastic buckling of the constituent trusses. For a rigid-jointed strut subjected to an axial load, the Euler buckling load P_E is given by:

$$P_E = \frac{4\pi^2 E_s I}{l^2} \quad (3.52)$$

Thus the compressive collapse strength of a composite strut due to elastic buckling is given by:

$$\sigma_c = \frac{\pi^2 E_s}{\bar{l}^2 + 1.2\pi^2 (E_s/G_s)} \quad (3.53)$$

Where G_s is the strut shear modulus. The calculated value is then substituted for σ_c in Equation 3.42 to arrive at the elastic buckling strength of the pyramidal unit cell.

For pin-jointed strut subjected to an axial load, the Euler buckling load P_E is given by:

$$P_E = \frac{\pi^2 E_s I}{l^2} \quad (3.54)$$

Thus the compressive collapse strength of a pin-jointed composite strut due to elastic buckling is given by:

$$\sigma_c = \frac{\pi^2 E_s}{4\bar{l}^2 + 1.2\pi^2(E_s/G_s)} \quad (3.55)$$

The calculated value is then substituted for σ_c in Equation 3.49 to arrive at the elastic buckling strength of a pin-jointed pyramidal unit cell.

3.5.1.3.3 Summary

The following summarizes the above results for the case of pin-jointed pyramidal struts and for the rigid-jointed strut case.

Table 3.4: Pyramidal lattice elastic and strength properties

Relative density	$\bar{\rho}_{pyr} = \frac{4\pi}{\bar{l}^2 \sin 2w \cos w}$ Equation 3.28	
Elastic modulus (rigid-jointed)	$\frac{E_{pyr}}{E_s} = \bar{\rho}_{pyr} \sin^4 w + \frac{3\bar{\rho}_{pyr}^2 \sin^3 w \cos^4 w}{2\pi}$ Equation 3.37	
Elastic modulus (pin-jointed)	$\frac{E_{pyr}}{E_s} = \bar{\rho}_{pyr} \sin^4 w$ Equation 3.40	
Collapse strength (rigid-jointed)	$\frac{\sigma_{pyr}}{\sigma_c} = \bar{\rho} \sin^2 w \left[1 + \frac{3\bar{\rho} \cos^4 w}{2\pi \sin w} \right]$ Equation 3.43	
	Plastic micro-buckling $\sigma_c = \frac{\sigma_{max}}{\left[1 + \frac{3 \cot w}{\bar{\phi}} \left(\frac{r}{\bar{l}} \right)^2 \right]}$ Equation 3.47	Elastic buckling $\sigma_c = \frac{\pi^2 E_s}{\bar{l}^2 + 1.2\pi^2(E_s/G_s)}$ Equation 3.53
Collapse strength (pin-jointed)	$\frac{\sigma_p}{\sigma_c} = \bar{\rho} \sin^2 w$ Equation 3.50	
	Plastic micro-buckling $\sigma_c = \sigma_{max}$ Equation 3.51	Elastic buckling $\sigma_c = \frac{\pi^2 E_s}{4\bar{l}^2 + 1.2\pi^2(E_s/G_s)}$ Equation 3.55

3.5.2 Analytical predictions of the vertical column core response

3.5.2.1 Relative density

A schematic diagram showing a unit cell of a vertical column core is shown in Figure 3.7. The parameters describing the geometry include the vertical truss height, h , with a circular cross-section of diameter, d , along with the length, l , and width, w , of the core base. In all geometric variations of the column core configuration, the columns were equally spaced within the core base.

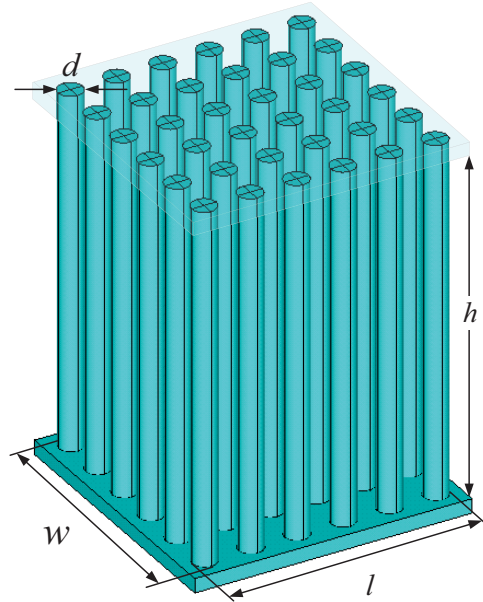


Figure 3.7: Schematic diagram of a vertical column core

The effective relative density of the vertical column core, defined as the ratio of the density of the vertical column core to the density of the solid material from which it is made and is given by:

$$\bar{\rho}_{vert} = \frac{n\pi r^2}{A} \quad (3.56)$$

where n is the number of columns comprising the core, r is the individual column cross-sectional radius and A the unit cell planar area.

3.5.2.2 Elastic modulus

The analytical expressions for the axial compressive modulus and strength of the composite vertical column core sandwiched between two rigid face-sheets are derived. The vertical columns are made from a unidirectional composite, with fibers aligned in the axial direction, parallel to the x-axis of the global coordinate system. The elastic modulus and the compressive strengths in the x-direction are E_s and σ_c respectively. The analytical expression for the compressive elastic modulus of a vertical column core unit cell is obtained in terms of the core geometry and the elastic properties of the parent material. The elastic deformation of a single column is initially examined for which the results are extended to evaluate the effective properties of the entire core.

Considering a vertical column core unit cell, as shown in Figure 3.8a, with an applied compressive force F in the x-direction of the global Cartesian coordinate system resulting in displacement δ as shown in Figure 3.8(b). Using beam theory, the axial force in the strut are given by:

$$F_a = \frac{E_s \pi r^2 \delta}{h} \quad (3.57)$$

Each columns within the core supports an applied force F_a , therefore, the compressive stress, σ_{vert} supported by the unit cell is given by:

$$\sigma_{vert} = \frac{F_{total}}{A} = \frac{nE_s \pi r^2 \delta}{Ah} \quad (3.58)$$

Since the axial strain of the unit cell in the x-direction is given by $\varepsilon = \delta/h$, it follows that the elastic modulus defined by $E = \sigma/\varepsilon$ for the vertical column core is given by:

$$\frac{E_{vert}}{E_s} = \frac{n\pi r^2}{A} \quad (3.59)$$

The elastic modulus is related to the relative density of the core via:

$$E_{vert} = \bar{\rho}_{vert} E_s \quad (3.60)$$

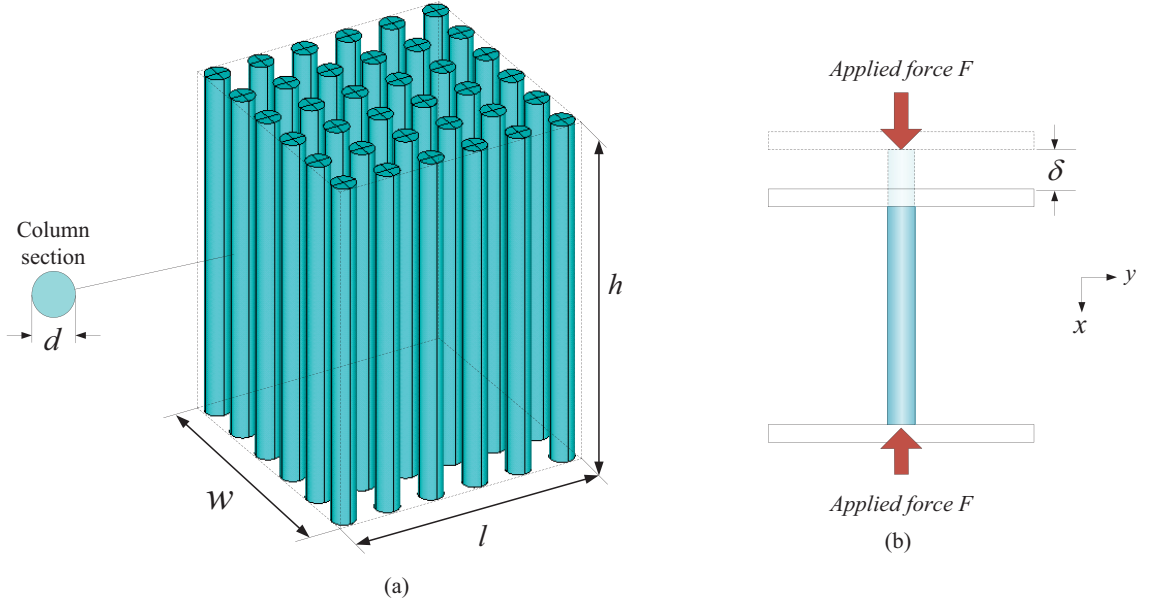


Figure 3.8: Schematic of (a) unit cell (b) deflection of single column within the core upon application of a uniaxial compressive load.

3.5.2.3 Collapse strength

3.5.2.3.1 Plastic micro-buckling

For slender columns, compressive loading of unidirectional fiber reinforced columns in the axial direction results in either Euler elastic buckling or plastic micro-buckling. For the case of plastic micro-buckling failure, compression tests on coupon samples of individual columns will provide reliable strength data for the parent material. Once the strength of the parent material σ_{max} is known, the expression for the compressive strength of the vertical column core can be given as:

$$\frac{\sigma_{vert}}{\sigma_{max}} = \frac{n\pi r^2}{A} \quad (3.61)$$

The compression strength can be related to the unit cell relative density through:

$$\sigma_{vert} = \bar{\rho}_{vert} \sigma_{max} \quad (3.62)$$

3.5.2.3.2 Euler buckling

There are a number of competing failure modes for a unidirectional fiber reinforced column, including plastic micro-buckling, delamination, brooming, and elastic buckling. The composite core and face-sheet were manufactured using the lost mold technique in a continuous nature as a single component, which ensured that delamination and brooming were not operative failure modes. Thus, the compressive strength of the vertical column core is governed by the lowest strength value of either plastic micro-buckling or global elastic buckling. The critical Euler buckling strength for a pin-ended column, σ_c is given by:

$$\sigma_c = \frac{\pi^2 E_s}{4\bar{h}^2 + 1.2\pi^2(E_s/G_s)} \quad (3.63)$$

where the non-dimensional lengths $\bar{h} = h/r$. The peak elastic buckling strength of the core can then be found by substituting σ_c for σ_{max} in Equation 3.62.

$$\sigma_{vert} = \bar{\rho}_{vert} \sigma_c \quad (3.64)$$

3.5.2.4 Summary

Relative density	$\bar{\rho}_{vert} = \frac{n\pi r^2}{A}$ Equation 3.56	
Elastic modulus	$E_{vert} = \bar{\rho}_{vert} E_s$ Equation 3.60	
Collapse strength	$\sigma_{vert} = \bar{\rho}_{vert} \sigma_c$ Equation 3.62	
	Plastic micro-buckling $\sigma_c = \sigma_{max}$	Elastic buckling $\sigma_c = \frac{\pi^2 E_s}{4\bar{h}^2 + 1.2\pi^2 (E_s/G_s)}$ Equation 3.63

3.5.3 Analytical predictions for the response of the modified pyramidal truss core

3.5.3.1 Relative density

A unit cell based on a modified pyramidal truss is shown in Figure 3.9. This unit cell configuration is similar to the pyramidal truss core with the addition of a vertical truss located at the center of the core. The critical parameters describing the geometry include the outer truss length, l , with a circular cross-section of diameter, d and the truss inclination angle w . The outer struts are inclined with respect to the horizontal plane at an angle w , while the central strut is perpendicular to the base of the cell.

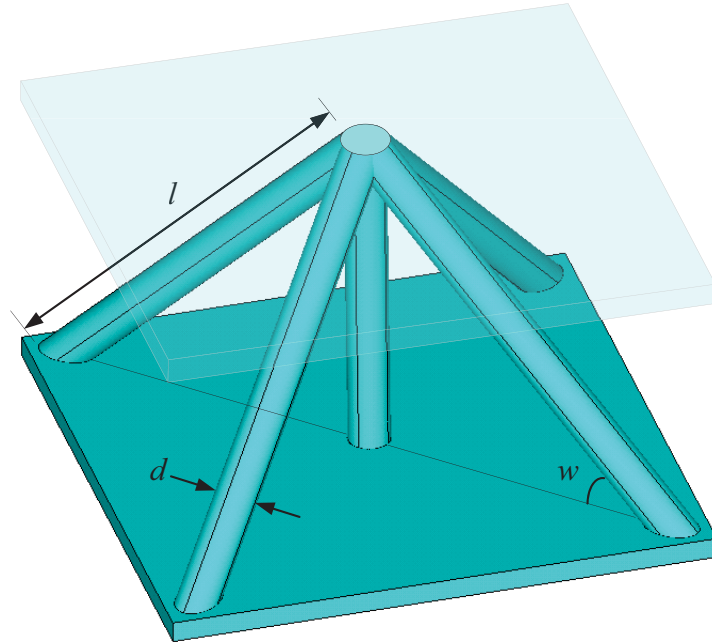


Figure 3.9: Sketch of a unit cell of the 4-legged pyramidal core.

The modified pyramidal cores that were manufactured and tested for this study had a strut angle $w=45^\circ$ with respect to the horizontal plane, in addition to a central vertical truss, all having a cross-sectional diameter $d = 3\text{mm}$. Geometric considerations dictate that the relative density of the core (calculated as the ratio of the truss volume to that of the unit cell) is given by:

$$\bar{\rho}_{mp} = \frac{4\pi(1 + \sin w/4)}{\bar{l}^2 \sin 2w \cos w} \quad (3.65)$$

3.5.3.2 Elastic modulus

Analytical expressions for the through-thickness elastic modulus of the modified pyramidal core is obtained in terms of the core geometry and the elastic properties of the parent material. This is done by analyzing the elastic deformations of a single inclined strut and the vertical strut of the core and then extending the results to evaluate the effective elastic properties of the core. Consider the unit cell sketched in Figure 3.10a with an applied through-thickness compressive force F (Figure 3.10 b). Axial, F_a , and shear, F_s forces are created in each of the inclined trusses, while an axial force, F_{av} is created on the central vertical truss, as shown in Figure 3.10a and Figure 3.10b respectively. Using beam theory, the force components acting on the inclined trusses are given as:

$$F_a = \frac{E_s \pi r^2 \delta \sin w}{l} \quad \text{and} \quad (3.66)$$

$$F_s = \frac{12E_s I \delta \cos w}{l^3}$$

Similarly, the compressive force acting on the vertical truss is given as:

$$F_{av} = \frac{E_s \pi r^2 \delta}{l \sin w} \quad (3.67)$$

Taking in to account the four inclined trusses, in addition to the vertical strut, the total through-thickness force, F_{total} acting on a unit cell is given by:

$$F_{total} = 4F_a \sin w + 4F_s \cos w + F_{av} \quad (3.68)$$

By considering the unit cell of the modified pyramidal core sketched in Figure 3.10(a). The through-thickness nominal stress σ_{mp} is related to the force F_{total} via:

$$\sigma_{mp} = \frac{F_{total}}{A} = \frac{F_{total}}{(\sqrt{2} l \cos w)^2} \quad (3.69)$$

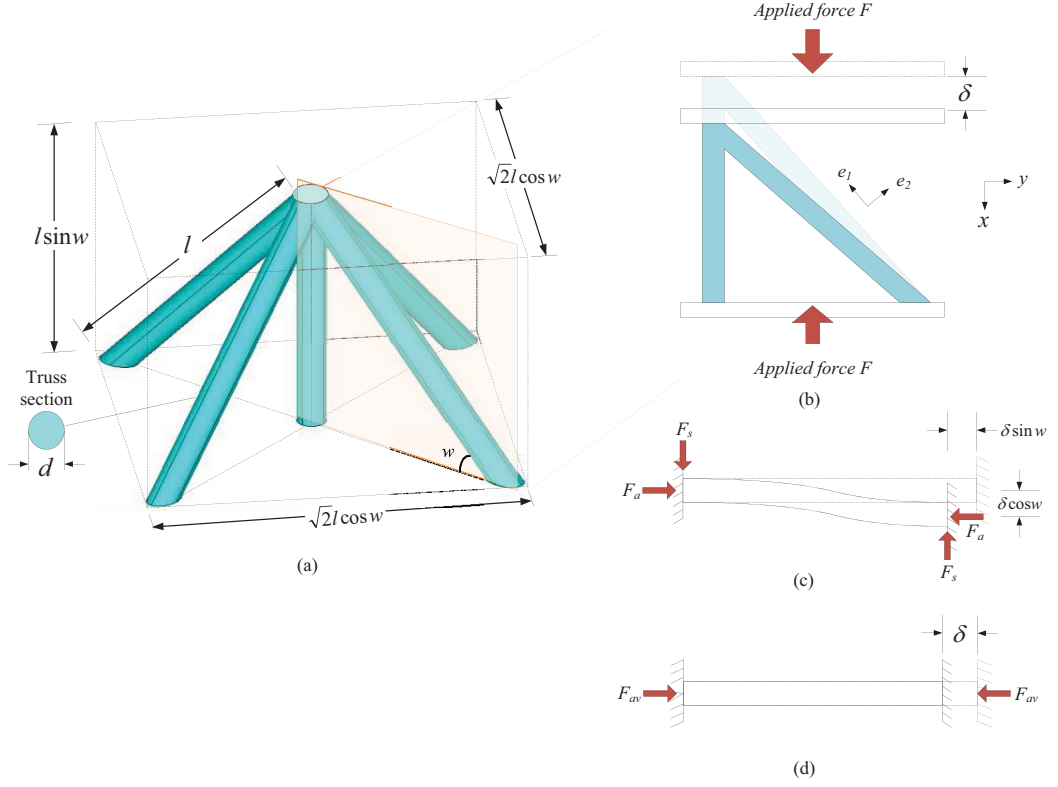


Figure 3.10: Schematic of (a) unit cell (b) deflection of a single inclined truss and the vertical truss of the pyramidal core upon application of a uniaxial compressive load (c) the free-body diagram of a truss subjected compression and shear.

The through-thickness nominal strain ε_{mp} for a given displacement δ is:

$$\varepsilon_{mp} = \frac{\delta}{l \sin w} \quad (3.70)$$

The effective elastic modulus of the modified pyramidal core E_{mp} follows from the above as:

$$\frac{E_{mp}}{E_s} = \frac{2\pi \sin w}{\bar{l}^2 \cos^2 w} \left[\sin^2 w + \frac{3 \cos^2 w}{\bar{l}^2} + \frac{1}{4 \sin w} \right] \quad (3.71)$$

In terms of relative density, the expression is given by:

$$\frac{E_{mp}}{E_s} = \frac{\bar{\rho}_{mp} \sin^4 w}{(1 + \sin w/4)} + \frac{3\bar{\rho}_{mp}^2 \sin^3 w \cos^4 w}{2\pi(1 + \sin w/4)^2} + \frac{\bar{\rho}_{mp} \sin w}{4(1 + \sin w/4)} \quad (3.72)$$

The first and third terms represents the contribution to stiffness of the core due to stretching of all the struts while the second term represents the contribution from bending of the inclined struts.

By considering a modified pyramidal constructed from pin-jointed struts, a first order approximation for the elastic modulus of the core can be obtained. In the absence of shear force on pin-jointed struts, the net applied through thickness force F_{total} reduces to:

$$F_{total} = 4F_a \sin w + F_{av} = \frac{E_s \pi r^2 \delta}{l} \left[4 \sin^2 w + \frac{1}{\sin w} \right] \quad (3.73)$$

Using Equations 3.69 and 3.70 the elastic modulus E_{mp} of the core becomes:

$$\frac{E_{mp}}{E_s} = \frac{2\pi (\sin^2 w + 1/4 \sin w)}{\bar{l}^2 \cos^2 w} \quad (3.74)$$

In terms of relative density, the above expression reduces to:

$$\frac{E_{mp}}{E_s} = \bar{\rho}_{mp} \left[\frac{4 \sin^4 w + \sin w}{4 + \sin w} \right] \quad (3.75)$$

3.5.3.3 Collapse strength

3.5.3.3.1 Plastic micro-buckling

Prior micro-buckling, a modified pyramidal core composed of rigid-jointed struts is elastic.

Therefore, net applied force, F_{total} acting on a unit cell follows from Equation 3.68 as:

$$F_{total} = \sigma_c \pi r^2 \sin w \left[4 + 12 \cot^2 w \left(\frac{r}{l} \right)^2 \right] + \pi r^2 \sigma_{cv} \quad (3.76)$$

Within the elastic region, the axial stress σ_c is given by $\sigma_c = E_s \delta \sin w / l$ and σ_{cv} given by $\sigma_{cv} = E_s \delta / l \sin w$. At the onset of failure, σ_c and σ_{cv} represent the axial stresses required to initiate failure in the inclined strut and vertical strut respectively. Using

Equation 3.69, the nominal compressive strength of a modified pyramidal core can be written as:

$$\sigma_{mp} = \frac{2\pi \sin w (\bar{l}^2 + 3\cot^2 w)}{\bar{l}^2 (\bar{l} \cos w)^2} \sigma_c + \frac{\pi}{2(\bar{l} \cos w)^2} \sigma_{cv} \quad (3.77)$$

The first term represents the contribution to compression strength from the angled struts while the second terms from the vertical strut. Recall that the critical strength under combined axial compression and in-plane shear in the inclined truss is given as:

$$\sigma_c = \frac{\sigma_{max}}{\left[1 + \frac{3\cot w}{\bar{\phi} \bar{l}^2}\right]} \quad (3.78)$$

By assuming that the modified pyramidal core fails when the inclined trusses reach their strength limit σ_c , and knowing that $\sigma_{cv} = \sigma_c / \sin^2 w$, the compressive strength of the core can be expressed as:

$$\sigma_{mp}^{upper} = \frac{2\pi \sin w \left[(\bar{l}^2 + 3\cot^2 w) \sigma_c + \left(\frac{\bar{l}^2}{4\sin^3 w} \right) \sigma_c \right]}{\bar{l}^2 (\bar{l} \cos w)^2} \quad (3.79)$$

This yields an upper bound approximation of the compression strength of the modified pyramidal core. A lower bound prediction is obtained by assuming that the core fails when the vertical strut reaches its strength limit σ_{cv} ($\sigma_c = \sigma_{cv} \sin^2 w$) as:

$$\sigma_{mp}^{lower} = \frac{2\pi \sin^3 w \left[(\bar{l}^2 + 3\cot^2 w) \sigma_{cv} + \left(\frac{\bar{l}^2}{4\sin^3 w} \right) \sigma_{cv} \right]}{\bar{l}^2 (\bar{l} \cos w)^2} \quad (3.80)$$

Where $\sigma_{cv} = \sigma_{max}$ due to the absence of shear loading on the vertical strut. Finally, by assuming that the inclined and the vertical struts fail simultaneously, an approximate average of the above two predictions for the compression strength of the core is obtained from Equation 3.77 as:

$$\sigma_{mp}^{avg} = \frac{2\pi \sin w \left[(\bar{l}^2 + 3\cot^2 w) \sigma_c + \left(\frac{\bar{l}^2}{4 \sin w} \right) \sigma_{cv} \right]}{\bar{l}^2 (\bar{l} \cos w)^2} \quad (3.81)$$

Predictions from Equation 3.81 were found to be in good agreement with FE model results as described in the following chapter.

The compression strength of a modified pyramidal core composed of pin-jointed struts is derived as follows. The net applied force, F_{total} on a pin-jointed core follows from Equation 3.76 as:

$$F_{total} = 4\pi r^2 \sin w \sigma_c + \pi r^2 \sigma_{cv} \quad (3.82)$$

Using Equation 3.69, the compressive strength of the core can be written as:

$$\sigma_{mp} = \frac{2\pi \sin w}{(\bar{l} \cos w)^2} \sigma_c + \frac{\pi}{2(\bar{l} \cos w)^2} \sigma_{cv} \quad (3.83)$$

Using the same approach, an upper, lower and an average prediction can be made using the following:

$$\sigma_{mp}^{upper} = \frac{2\pi \sin w}{(\bar{l} \cos w)^2} \left(\sigma_c + \frac{\sigma_c}{4 \sin^3 w} \right) \quad (3.84)$$

$$\sigma_{mp}^{lower} = \frac{2\pi \sin^3 w}{(\bar{l} \cos w)^2} \left(\sigma_{cv} + \frac{\sigma_{cv}}{4 \sin^3 w} \right) \quad (3.85)$$

$$\sigma_{mp}^{avg} = \frac{2\pi \sin w}{(\bar{l} \cos w)^2} \left(\sigma_c + \frac{\sigma_{cv}}{4 \sin w} \right) \quad (3.86)$$

respectively. In the absence of shear load on the pin-jointed angled struts, $\sigma_c = \sigma_{cv} = \sigma_{max}$. It is later found that σ_{mp}^{avg} yields values that are in good agreement with FE model predictions.

3.5.3.4 Euler buckling

For a rigid-jointed strut subjected to an axial load, the Euler buckling strength is given by:

$$\sigma_c = \frac{\pi^2 E_s}{\bar{l}^2 + 1.2\pi^2(E_s/G_s)} \text{ and } \sigma_{cv} = \frac{\pi^2 E_s}{\bar{h}^2 + 1.2\pi^2(E_s/G_s)} \quad (3.87)$$

For a pin-jointed strut subjected to an axial load, the Euler buckling strength is given by:

$$\sigma_c = \frac{\pi^2 E_s}{4\bar{l}^2 + 1.2\pi^2(E_s/G_s)} \text{ and } \sigma_{cv} = \frac{\pi^2 E_s}{4\bar{h}^2 + 1.2\pi^2(E_s/G_s)} \quad (3.88)$$

σ_c and σ_{cv} correspond to the Euler buckling strength of the angled and vertical strut respectively. The values are then substituted into their corresponding Equations (Equation 3.81 or 3.86).

3.5.4 Summary

The following summarizes the derived expressions for the rigid-jointed and pin-jointed modified pyramidal lattice.

Relative density	$\bar{\rho}_{mp} = \frac{4\pi(1+\sin w/4)}{\bar{l}^2 \sin 2w \cos w}$ Equation 3.65	
Elastic modulus (rigid-jointed)	$\frac{E_{mp}}{E_s} = \frac{\bar{\rho}_{mp} \sin^4 w}{(1+\sin w/4)} + \frac{3\bar{\rho}_{mp}^2 \sin^3 w \cos^4 w}{2\pi(1+\sin w/4)^2} + \frac{\bar{\rho}_{mp} \sin w}{4(1+\sin w/4)}$ Equation 3.72	
Elastic modulus (pin-jointed)	$\frac{E_{mp}}{E_s} = \bar{\rho}_{mp} \left[\frac{4\sin^4 w + \sin w}{4 + \sin w} \right]$ Equation 3.75	
Collapse strength (rigid-jointed)	$\sigma_{mp}^{avg} = \frac{2\pi \sin w \left[(\bar{l}^2 + 3\cot^2 w)\sigma_c + \left(\frac{\bar{l}^2}{4 \sin w} \right) \sigma_{cv} \right]}{\bar{l}^2 (\bar{l} \cos w)^2}$ Equation 3.81	
	Plastic micro-buckling $\sigma_c = \frac{\sigma_{max}}{\left[1 + \frac{3\cot w}{\bar{\varphi} \bar{l}^2} \right]}$ Equation 3.78 $\sigma_{cv} = \sigma_{max}$	Elastic buckling $\sigma_c = \frac{\pi^2 E_s}{\bar{l}^2 + 1.2\pi^2 (E_s/G_s)}$ Equation 3.87 $\sigma_{cv} = \frac{\pi^2 E_s}{\bar{h}^2 + 1.2\pi^2 (E_s/G_s)}$ Equation 3.87
	$\sigma_{mp}^{avg} = \frac{2\pi \sin w}{(\bar{l} \cos w)^2} \left(\sigma_c + \frac{\sigma_c^*}{4 \sin w} \right)$ Equation 3.86	
Collapse strength (pin-jointed)	Plastic micro-buckling $\sigma_c = \sigma_{cv} = \sigma_{max}$	Elastic buckling $\sigma_c = \frac{\pi^2 E_s}{4\bar{l}^2 + 1.2\pi^2 (E_s/G_s)}$ Equation 3.88 $\sigma_{cv} = \frac{\pi^2 E_s}{4\bar{h}^2 + 1.2\pi^2 (E_s/G_s)}$ Equation 3.88

3.5.5 Analytical predictions of the response of the octahedral lattice core

3.5.5.1 Relative density

A unit cell of the octahedral lattice structure is shown in Figure 3.11. The cell structure has a face centered cubic (FCC) nature. This cubic symmetry of the core generates near isotropic properties. The octahedral structure can be visually constructed by stacking tetrahedral sub-units on each of the eight faces of the octahedron core. The lattice material is constructed from identical circular cylindrical struts.

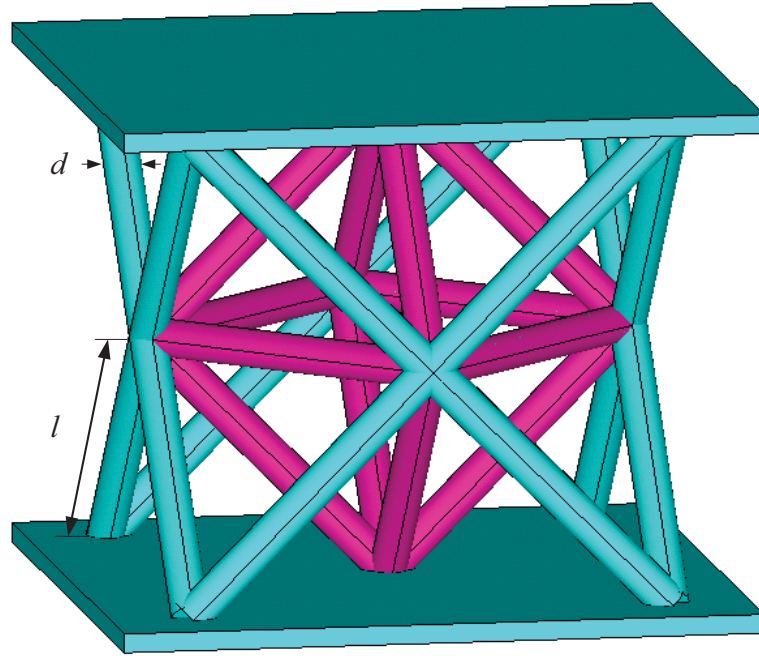


Figure 3.11: Structure of an octahedral lattice core. The red struts represent the octahedron core.

The relative density of the core material can be obtained from the ratio of the truss volume to the volume of the unit cell which can be approximated as [7]:

$$\bar{\rho}_{oct} = 6\pi\sqrt{2} \left(\frac{r}{l}\right)^2 \quad (3.89)$$

where l and d are the length and radius of strut. The above expression is a first order approximation, which gives an upper bound value for the relative density, due to double-counting of the node volumes. For small values of a/l , as in the case for the manufactured octahedral cores in this study, the double-counting of the node volumes is considered insignificant and a first order approximation will suffice.

3.5.5.2 Elastic modulus

Based on the work of Deshpande and Fleck [7] the elastic modulus response of an octahedral lattice core subjected to a transverse compressive load is dependent on the axial elastic modulus E_s of the parent material of the constituent struts along with the relative density $\bar{\rho}$ of the core as follows:

$$\frac{E}{E_s} = \frac{\bar{\rho}_{oct}}{5} \quad (3.90)$$

3.5.5.3 Collapse strength

3.5.5.3.1 Plastic micro-buckling and elastic buckling

An octahedral core subjected to a through thickness compressive load may fail due to plastic micro-buckling or elastic buckling of the constituent trusses. Considering plastic micro-buckling, the compressive strength of the lattice core is given by [7]:

$$\frac{\sigma_{oct}}{\sigma_{max}} = 2\pi\sqrt{2}\left(\frac{r}{l}\right)^2 \quad (3.91)$$

The octahedral lattice core may collapse by elastic buckling of the struts if the Euler buckling strength of the struts is less than their plastic micro-buckling strength. By assuming the presence of pin-jointed struts, the lower bound estimate of the buckling strength of an axially-loaded strut is given by:

$$\sigma_{Euler} = \frac{\pi^2 r^2 E_s}{4l^2} \quad (3.92)$$

The elastic buckling strength of the core is obtained by substituting σ_{Euler} for σ_{max} in Equation 3.91. For the case of the current octahedral lattice based on a truss having a length $l = 36\text{mm}$ and a diameter $d = 4\text{mm}$, with a slenderness ratio $SR = 40$. Therefore, the struts are considered short and elastic buckling is not operative. This is also confirmed from the lower-bound calculations of the elastic buckling strengths which were found to be higher than the calculated plastic micro-buckling loads.

3.5.6 Analytical predictions of the response of the BCC core

3.5.6.1 Relative density

The geometric configuration of a BCC unit cell is illustrated in Figure 3.5. The critical parameters describing the geometry include the truss length, l , diameter, d and inclination angle w with respect to the horizontal plane.

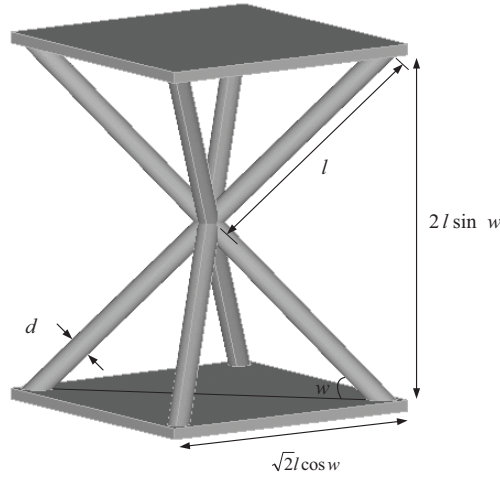


Figure 3.12: Schematic of a BCC unit cell.

Here, the inclination angle of each truss with respect to the face-sheets is $w = 45^\circ$. The truss has a length $l = 26.1mm$ and diameter $d = 3mm$. The BCC unit cell is constructed from 8 struts each having a volume equal to $\pi r^2 l$, therefore, the relative density of a BCC unit cell is given by:

$$\bar{\rho}_{BCC} = \frac{4\pi}{l^2 \sin 2w \cos w} \quad (3.93)$$

Which is found to be identical to the relative density of the pyramidal lattice core.

3.5.6.2 Elastic modulus

Using the same approach as in Section 3.5.1 for the pyramidal lattice, the analytical expression for the compressive elastic modulus of a BCC unit cell is obtained in terms of

the core geometry and the elastic properties of the parent material. The elastic deformation of a single truss is initially examined, for which the results are extended to evaluate the effective properties of the entire BCC cell. Considering a quarter of a BCC unit cell, as shown in Figure 3.13a, with an applied axial compressive force F applied in the x -direction of the global Cartesian coordinate system resulting in displacement 2δ , as shown. A free-body diagram for a single truss is shown in Figure 3.13b, in which the axial, F_A , and shear, F_S forces are created in each of the BCC struts resulting in displacement δ .

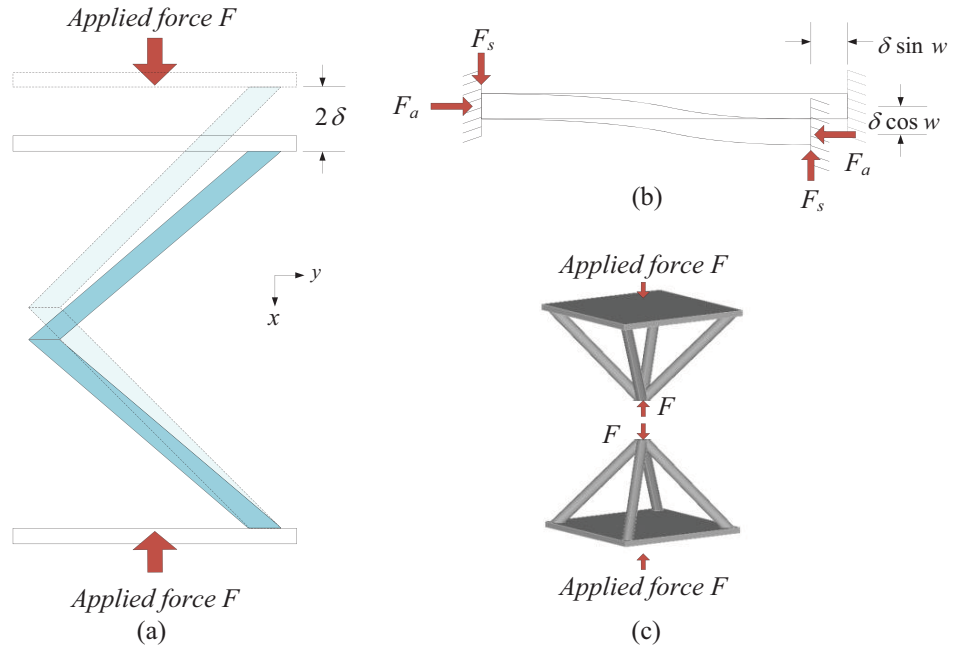


Figure 3.13: Schematic showing (a) deflection of a BCC cell upon application of a uniaxial compressive load (b) the free-body diagram of a strut subjected to compression and shear (c) due to symmetry the BCC resembles the pyramidal lattice unit cell.

Using beam theory, the axial and shear forces in the strut can be determined. The net applied force, F_s is the sum of the axial and shear-force components in the x -direction per strut:

$$F_s = F_a \sin w + F_s \cos w = \frac{E_s \pi r^2 \delta}{l} \left[\sin^2 w + 3 \left(\frac{r}{l} \right)^2 \cos^2 w \right] \quad (3.94)$$

The BCC unit cell has a planar area is given by $(\sqrt{2} l \cos w)^2$, therefore, the through-thickness stress, σ_{BCC} is given by:

$$\sigma_{BCC} = \frac{F_{total}}{A} = \frac{8F_s}{(2 l \cos w)^2} \quad (3.95)$$

The axial strain in the unit cell in the x-direction by definition is:

$$\varepsilon_{BCC} = \frac{2\delta}{2l \sin w} = \frac{\delta}{l \sin w} \quad (3.96)$$

The initial modulus for the BCC unit cell E_{BCC} is obtained by dividing the above expression of stress by strain resulting in the following:

$$\frac{E_{BCC}}{E_s} = \frac{2\pi \sin w}{\bar{l}^2 \cos^2 w} \left[\sin^2 w + \frac{3\cos^2 w}{\bar{l}^2} \right] \quad (3.97)$$

The elastic modulus in terms of relative density is given by:

$$\frac{E_{BCC}}{E_s} = \bar{\rho}_{BCC} \sin^4 w + \frac{3\bar{\rho}_{BCC}^2 \sin^3 w \cos^4 w}{2\pi} \quad (3.98)$$

This is identical to the analytical expression for the elastic modulus of the pyramidal lattice.

By considering a pin-jointed strut, the elastic modulus E_{BCC} for the BCC core is given by:

$$\frac{E_{BCC}}{E_s} = \frac{2\pi \sin^3 w}{\bar{l}^2 \cos^2 w} \quad (3.99)$$

In terms of relative density, the above expression reduces to:

$$\frac{E_{BCC}}{E_s} = \bar{\rho}_{BCC} \sin^4 w \quad (3.100)$$

3.5.6.3 Collapse strength

3.5.6.3.1 Plastic micro-buckling

Prior failure, the rigid-jointed truss is elastic and the net applied force, F_s per strut follows from Equation 3.94 as:

$$F_s = \sigma_c \pi r^2 \sin w \left[1 + \frac{3 \cot^2 w}{\bar{l}^2} \right] \quad (3.101)$$

where σ_c is the axial stress required to initiate failure in the inclined strut. Within the elastic region, the axial stress σ_c is given by $\sigma_c = E_s \delta \sin w / l$. Using Equation 3.95, the nominal compressive strength of a pyramidal core composed of four struts can be written as follows:

$$\frac{\sigma_{BCC}}{\sigma_c} = \frac{2\pi \sin w (\bar{l}^2 + 3 \cot^2 w)}{\bar{l}^2 (\bar{l} \cos w)^2} \quad (3.102)$$

In terms of the unit cell relative density $\bar{\rho}_{pyr}$ the above expression reduces to:

$$\frac{\sigma_{BCC}}{\sigma_c} = \bar{\rho}_{BCC} \sin^2 w \left[1 + \frac{3 \bar{\rho}_{BCC} \cos^4 w}{2\pi \sin w} \right] \quad (3.103)$$

For pin-jointed struts, the compressive strength of the BCC core can be written as:

$$\frac{\sigma_{BCC}}{\sigma_c} = \frac{2\pi \sin w}{\bar{l}^2 \cos^2 w} \quad (3.104)$$

In terms of relative density, the expression simplifies to:

$$\frac{\sigma_{BCC}}{\sigma_c} = \bar{\rho}_{BCC} \sin^2 w \quad (3.105)$$

3.5.6.3.2 Elastic buckling

The elastic buckling strength of a BCC unit cell (rigid-jointed or pin-jointed struts) can be calculated using the expressions developed for the pyramidal lattice.

3.5.6.4 Summary

The BCC formulations are found to be identical to the pyramidal lattice analytical expressions. Formulas in Table 3.4 can be directly applied to predict the elastic and strength properties of a BCC unit cell lattice.

3.5.7 Analytical predictions of the response of the FCC core

3.5.7.1 Relative density, elastic modulus and collapse strength

The geometric configuration of a FCC unit cell is illustrated in Figure 3.14. The critical parameters describing the geometry include the truss length, d , radius, r and inclination angle α with respect to the horizontal plane. Here, the inclination angle of each truss with respect to the face-sheets is $\alpha = 55^\circ$. The truss has a length $d = 22.1\text{mm}$ and radius $r = 1.5\text{mm}$.

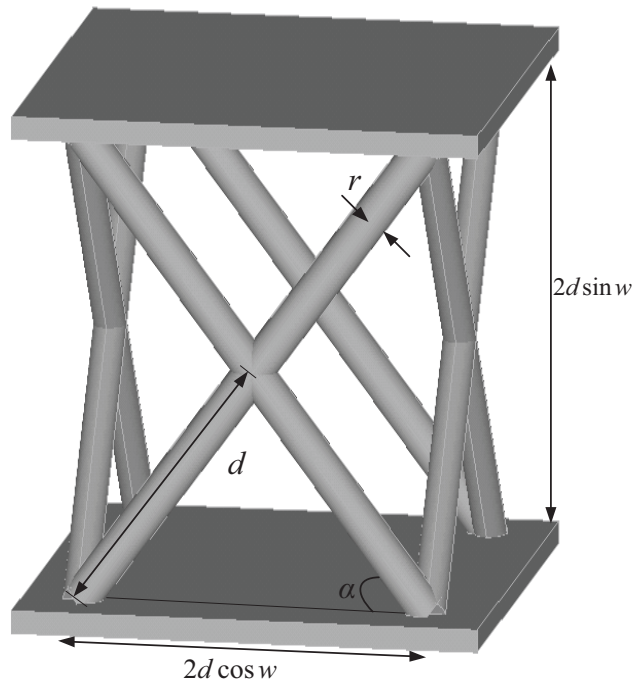


Figure 3.14: Schematic of a FCC unit cell.

Using the same approach used in deriving the analytical expressions for the pyramidal and BCC lattice, one can arrive at the formulas describing the relative density, elastic modulus and strength as follows.

- Relative density:

$$\bar{\rho}_{FCC} = \frac{4\pi}{d^2 \sin 2\alpha \cos \alpha} \quad (3.106)$$

- Elastic modulus:

The elastic modulus in terms of relative density for FCC with rigid-jointed struts is given by:

$$\frac{E_{FCC}}{E_s} = \bar{\rho}_{FCC} \sin^4 \alpha + \frac{3\bar{\rho}_{FCC}^2 \sin^3 \alpha \cos^4 \alpha}{2\pi} \quad (3.107)$$

For an FCC composed of pin-jointed struts:

$$\frac{E_{FCC}}{E_s} = \bar{\rho}_{FCC} \sin^4 \alpha \quad (3.108)$$

- Collapse strength

A. Plastic micro-buckling

The nominal compressive strength of an FCC core composed of rigid-jointed struts is given by:

$$\frac{\sigma_{FCC}}{\sigma_c} = \bar{\rho}_{FCC} \sin^2 \alpha \left[1 + \frac{3\bar{\rho}_{FCC} \cos^4 \alpha}{2\pi \sin \alpha} \right] \quad (3.109)$$

where $\sigma_c = \sigma_{max} / \left[1 + \frac{3 \cot \alpha}{\bar{\varphi}} \left(\frac{r}{d} \right)^2 \right]$.

For pin-jointed struts, the FCC compressive strength is simplified to:

$$\frac{\sigma_{FCC}}{\sigma_c} = \bar{\rho}_{FCC} \sin^2 \alpha \quad (3.110)$$

where $\sigma_c = \sigma_{max}$.

B. Elastic buckling

Thus the compressive collapse strength of rigid-jointed strut due to elastic buckling is given by:

$$\sigma_c = \frac{\pi^2 E_s}{4\bar{d}^2 + 1.2\pi^2(E_s/G_s)} \quad (3.111)$$

The elastic buckling strength for rigid-jointed strut is calculated using Equation 3.111 and the value is substituted in for σ_c in Equation 3.109 to yield the elastic buckling strength of the FCC cell. The compressive strength of a pin-jointed composite strut due to elastic buckling is given by:

$$\sigma_c = \frac{\pi^2 E_s}{16\bar{d}^2 + 1.2\pi^2(E_s/G_s)} \quad (3.112)$$

The calculated value is substituted for σ_c in Equation 3.110.

3.5.8 Analytical predictions of the response of the BCCz core

This section presents analytical solutions for the initial modulus and strength properties (due to plastic microbuckling and elastic buckling) of the lattices.

3.5.8.1 Relative density

The geometric configuration of a BCCz unit cell is illustrated in Figure 3.15. Similar to the BCC structure, here, the inclination angle of each truss with respect to the face-sheets is $w = 45^\circ$. The angled struts have a length $l = 26.1\text{mm}$ and diameter $d = 3\text{mm}$. The BCCz unit cell is constructed from 10 struts of equal radius, four of which are vertical.

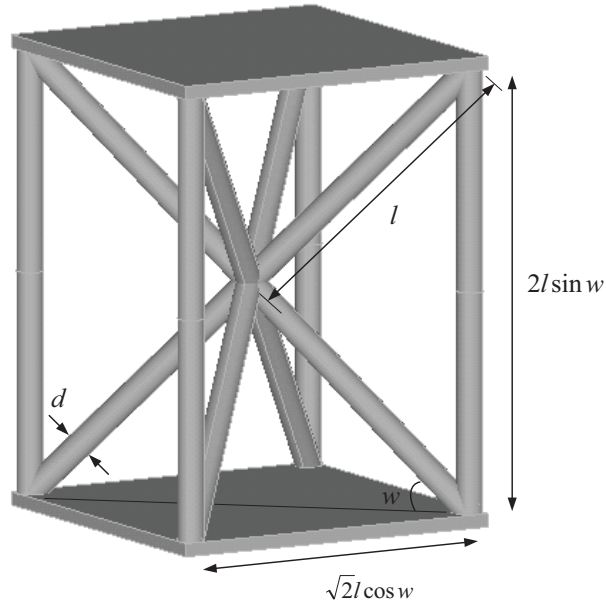


Figure 3.15: Schematic of a BCC-z unit cell.

The effective relative density of the vertical column core, defined as the ratio of the density of the vertical column core to the density of the solid material from which it is made and is given by:

$$\bar{\rho}_{BCCz} = \frac{8l\pi r^2 + 8l\pi r^2 \sin w}{2l \sin w (\sqrt{2} l \cos w)^2} \equiv \frac{4\pi(1 + \sin w)}{\bar{l}^2 \sin 2w \cos w} \quad (3.113)$$

where the non-dimensional length $\bar{l} = l/r$.

3.5.8.2 Elastic modulus

Consider a quarter of a BCCz unit cell, as shown in Figure 3.16a, with an axial compressive force F applied in the through thickness x -direction. The resulting displacement associated with the application of this force is 2δ . A free-body diagram for a rigid-jointed angled strut is shown in Figure 3.16b, in which the axial; F_A , and shear, F_S forces occur in each of the struts. A compressive force F_{av} is applied on the vertical column shown in Figure 3.16c.

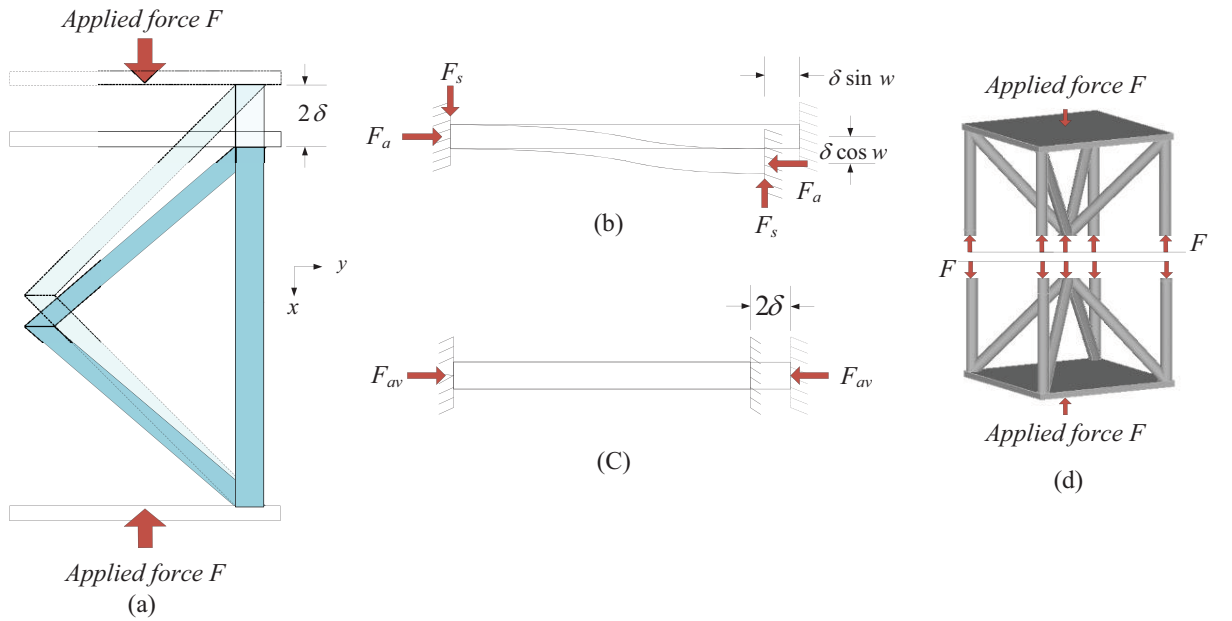


Figure 3.16: Schematic showing (a) deflection of a BCCz core upon application of a uniaxial compressive load (b) the free-body diagram of a strut subjected to compression and shear (c) the free-body diagram of half a vertical strut subjected.

For an imposed compression displacement δ , the axial and shear forces in each of the struts are given using beam theory by:

$$F_a = \frac{E_s \pi r^2 \delta \sin w}{l} \quad (3.114)$$

and

$$F_s = \frac{12E_s I \delta \cos w}{l^3} \quad (3.115)$$

The vertical strut experiences compression force, F_{av} :

$$F_{av} = \frac{E_s \pi r^2 \delta}{l \sin w} \quad (3.116)$$

The total applied compression force on the BCCz unit cell follows as:

$$\begin{aligned} F_{BCCz} &= 4(F_a \sin w + F_s \cos w + F_{av}) \\ &= \frac{4E_s \pi r^2 \delta}{l} \left[\sin^2 w + 3 \left(\frac{r}{l} \right)^2 \cos^2 w + \frac{1}{\sin w} \right] \end{aligned} \quad (3.117)$$

The applied through-thickness stress, σ_{BCCz} and strain ε_{BCCz} of the unit cell are then correlated to the force and displacement δ by:

$$\sigma_{BCC} = \frac{F_{BCCz}}{(\sqrt{2} l \cos w)^2} \quad (3.118)$$

and

$$\varepsilon_{BCCz} = \frac{\delta}{l \sin w} \quad (3.119)$$

respectively. The initial modulus for the BCCz unit cell $E_{BCCz} = \sigma_{BCCz} / \varepsilon_{BCCz}$ follows from Equations 3.118 and 3.119 as:

$$\frac{E_{BCCz}}{E_s} = \frac{2\pi \sin w}{\bar{l}^2 \cos^2 w} \left[\sin^2 w + \frac{3\cos^2 w}{\bar{l}^2} + \frac{1}{\sin w} \right] \quad (3.120)$$

The elastic modulus in terms of relative density is given by:

$$\frac{E_{BCCz}}{E_s} = \frac{\bar{\rho} \sin^4 w}{(1 + \sin w)} + \frac{3\bar{\rho}^2 \sin^3 w \cos^4 w}{2\pi(1 + \sin w)^2} + \frac{\bar{\rho} \sin w}{(1 + \sin w)} \quad (3.121)$$

The first and third terms represent the contribution to stiffness due to stretching of the angled and vertical struts while the second term represents the contribution from bending of the angled struts.

In the absence of shear force on pin-jointed struts, the net applied through thickness force, F_{BCCz} reduces to:

$$F_{BCCz} = 4(F_a \sin w + F_{av}) = \frac{4E_s \pi r^2 \delta}{l} \left[\sin^2 w + \frac{1}{\sin w} \right] \quad (3.122)$$

Using Equations 3.118, 3.119 and 3.122 the elastic modulus E_{BCCz} of the core is given by:

$$\frac{E_{BCCz}}{E_s} = \frac{2\pi (\sin^2 w + 1/\sin w)}{\bar{l}^2 \cos^2 w} \quad (3.123)$$

In terms of the unit cell relative density $\bar{\rho}_{BCCz}$ the initial modulus is expressed as:

$$\frac{E_{BCCz}}{E_s} = \bar{\rho}_{BCCz} \left[\frac{\sin^4 w + \sin w}{1 + \sin w} \right] \quad (3.124)$$

3.5.8.3 Collapse strength

3.5.8.3.1 Plastic micro-buckling

Within the elastic region, the axial stress σ_c in the angled strut is given by $\sigma_c = E_s \delta \sin w / l$ and the axial stress in the vertical strut σ_{cv} is given by $\sigma_{cv} = E_s \delta / l \sin w$.

Prior to failure the strut is elastic and the net force F_{BCCz} acting on a unit cell follows from Equation 3.117 as:

$$F_{total} = \frac{\pi d^2}{4} \sin w \left[4 + 3 \cot^2 w \left(\frac{d}{l} \right)^2 \right] \underbrace{\left(\frac{E_s \delta \sin w}{l} \right)}_{\sigma_c} + \pi d^2 \underbrace{\left(\frac{E_s \delta}{l \sin w} \right)}_{\sigma_{cv}} \quad (3.125)$$

At the onset of failure, σ_c and σ_{cv} represent the axial stresses required to initiate failure in the inclined strut and vertical strut, respectively. Using Equation 3.118, the total force

F_{total} is normalized to obtain the compressive strength of the BCCz core which can be written as:

$$\sigma_{BCCz} = \frac{2\pi \sin w (\bar{l}^2 + 3\cot^2 w)}{\bar{l}^2 (\bar{l} \cos w)^2} \left(\frac{E_s \delta \sin w}{l} \right) + \frac{2\pi}{(\bar{l} \cos w)^2} \left(\frac{E_s \delta}{l \sin w} \right) \quad (3.126)$$

The first term represents the contribution to strength from the inclined struts, while the second terms represents the contribution from the vertical struts. Assuming that the BCCz unit cell fails when the angled struts reach their strength limit, for which the critical displacement is given by:

$$\delta = \delta_{angled}^{crit} = \frac{\sigma_c l}{E_s \sin w} \quad (3.127)$$

hen, an upper bound approximation of the unit cell strength σ_{BCCz}^{upper} is obtained by substituting Equation 3.127 into Equation 3.126 as follows:

$$\sigma_{BCCz}^{upper} = \frac{2\pi \sin w \left[(\bar{l}^2 + 3\cot^2 w) \sigma_c + \left(\frac{\bar{l}^2}{\sin^3 w} \right) \sigma_c \right]}{\bar{l}^2 (\bar{l} \cos w)^2} \quad (3.128)$$

The inclined struts experience a combined axial compression and in-plane shear, which results in a knockdown effect on the material critical strength σ_{max} . Finnegan *et al* [7] demonstrated that the critical strength under combined axial compression and in-plane shear in the inclined fixed-end struts can be expressed as:

$$\sigma_c = \frac{\sigma_{max}}{\left[1 + \frac{3\cot w}{\bar{\varphi} \bar{l}^2} \right]} \quad (3.129)$$

Where $\bar{\varphi}$ represents the fiber misalignment angle. By substituting the values of σ_c from Equation 3.129 into Equation 3.128, one can arrive at the unit cell collapse strength. A lower bound strength approximation σ_{BCCz}^{lower} is obtained if the unit cell is assumed to fail when the vertical struts reach their strength, for which the critical displacement is given by:

$$\delta = \delta_{vertical}^{crit} = \frac{\sigma_{cv} l \sin w}{E_s} \quad (3.130)$$

Then, a lower bound approximation of the unit cell strength σ_{BCCz}^{lower} is obtained by substituting Equation 3.130 into Equation 3.126 as follows:

$$\delta \sigma_{BCCz}^{lower} = \frac{2\pi \sin^3 w \left[(\bar{l}^2 + 3\cot^2 w) \sigma_{cv} + \left(\frac{\bar{l}^2}{\sin^3 w} \right) \sigma_{cv} \right]}{\bar{l}^2 (\bar{l} \cos w)^2} \quad (3.131)$$

Due to the absence of shear loading on the vertical struts, the collapse strength is given as:

$$\sigma_{cv} = \sigma_{max}. \quad (3.132)$$

The critical strength lies between the stress obtained from σ_{BCCz}^{upper} and stress from σ_{BCCz}^{lower} . Finally, by assuming that the inclined and the vertical struts fail simultaneously, a value between the upper and lower bounds for the compression strength of the lattice is found by substituting Equation 3.127 and Equation 3.130 into the first and second term of Equation 3.126 respectively as follows:

$$\sigma_{BCCz}^{avg} = \frac{2\pi \sin w \left[(\bar{l}^2 + 3\cot^2 w) \sigma_c + \left(\frac{\bar{l}^2}{\sin w} \right) \sigma_{cv} \right]}{\bar{l}^2 (\bar{l} \cos w)^2} \quad (3.133)$$

Predictions from Equation 3.133 were found to be in good agreement with FE model results.

A BCCz core composed of pin-jointed struts will experience a net applied force, F_{BCCz} given as:

$$F_{BCCz} = 4\pi r^2 \sin w \sigma_c + 4\pi r^2 \sigma_{cv} \quad (3.134)$$

Using Equation 3.118, the compressive strength of the core can be written as:

$$\sigma_{BCCz} = \frac{2\pi \sin w}{(\bar{l} \cos w)^2} \sigma_c + \frac{2\pi}{(\bar{l} \cos w)^2} \sigma_{cv} \quad (3.135)$$

Adopting the same approach, an upper, lower and an average prediction can be made using the following expressions:

$$\sigma_{BCCz}^{upper} = \frac{2\pi \sin w}{(\bar{l} \cos w)^2} \left(\sigma_c + \frac{\sigma_c}{\sin^3 w} \right) \quad (3.136)$$

$$\sigma_{BCCz}^{lower} = \frac{2\pi \sin^3 w}{(\bar{l} \cos w)^2} \left(\sigma_{cv} + \frac{\sigma_{cv}}{\sin^3 w} \right) \quad (3.137)$$

$$\sigma_{BCCz}^{avg} = \frac{2\pi \sin w}{(\bar{l} \cos w)^2} \left(\sigma_c + \frac{\sigma_{cv}}{\sin w} \right) \quad (3.138)$$

respectively. Due to the absence of shear load on the pin-jointed struts, $\sigma_c = \sigma_{cv} = \sigma_{max}$. It is later found that σ_{BCCz}^{avg} yields values that are in good agreement with FE model predictions.

3.5.8.4 Euler buckling

For a rigid-jointed strut subjected to an axial load, the elastic buckling strength is given by:

$$\sigma_c = \frac{\pi^2 E_s}{\bar{l}^2 + 1.2\pi^2(E_s/G_s)} \text{ and } \sigma_{cv} = \frac{\pi^2 E_s}{\bar{h}^2 + 1.2\pi^2(E_s/G_s)} \quad (3.139)$$

Here σ_c and σ_{cv} corresponding to the Euler buckling strength of the angled and vertical struts respectively. The resulting values are then substituted into Equation 3.133 to arrive at the elastic buckling strength of the BCCz cell.

For a pin-jointed strut subjected to an axial load, the Euler buckling strength is given by:

$$\sigma_c = \frac{\pi^2 E_s}{4\bar{l}^2 + 1.2\pi^2(E_s/G_s)} \text{ and } \sigma_{cv} = \frac{\pi^2 E_s}{4\bar{h}^2 + 1.2\pi^2(E_s/G_s)} \quad (3.140)$$

The values are then substituted into Equation 3.138.

3.5.9 Analytical predictions of the response of the F₂BCC core

3.5.9.1 Relative density, elastic modulus and collapse strength

The F₂BCC structure is a combination of a BCC and a FCC structure in a unit cell. The geometric configuration of a F₂BCC unit cell is illustrated in Figure 3.17.

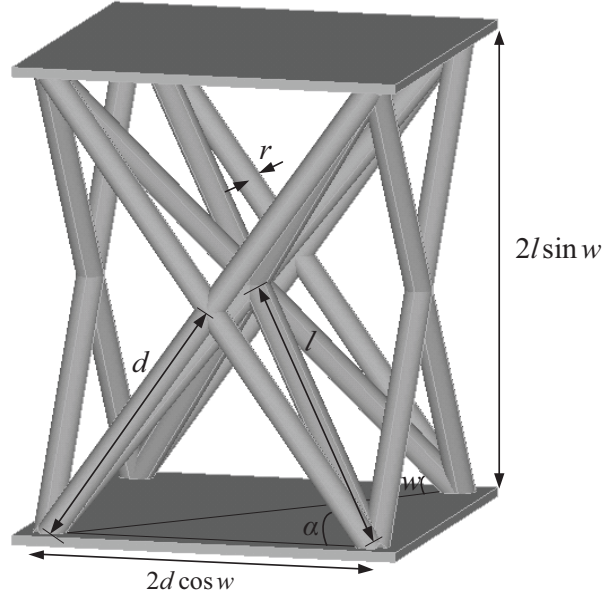


Figure 3.17: Schematic of a F₂BCC unit cell.

The analytical expressions describing the relative density, elastic modulus and strength of the F₂BCC is found as follows:

- **Relative density:**

$$\bar{\rho}_{F_2BCC} = \bar{\rho}_{BCC} + \bar{\rho}_{FCC} = \frac{4\pi}{\bar{l}^2 \sin 2w \cos w} + \frac{4\pi}{\bar{d}^2 \sin 2\alpha \cos \alpha} \quad (3.141)$$

- **Elastic modulus:**

The elastic modulus for a F₂BCC with rigid-jointed struts is given by:

$$\frac{E_{F_2BCC}}{E_s} = \frac{2\pi \sin w}{\bar{l}^2 \cos^2 w} \left(\sin^2 w + \frac{3 \cos^2 w}{\bar{l}^2} \right) + \frac{2\pi \sin \alpha}{\bar{d}^2 \cos^2 \alpha} \left(\sin^2 \alpha + \frac{3 \cos^2 \alpha}{\bar{d}^2} \right) \quad (3.142)$$

Or in terms of relative density:

$$\begin{aligned} \frac{E_{F_2BCC}}{E_s} = & \bar{\rho}_{BCC} \sin^4 w + \frac{3\bar{\rho}_{BCC}^2 \sin^3 w \cos^4 w}{2\pi} + \bar{\rho}_{FCC} \sin^4 \alpha \\ & + \frac{3\bar{\rho}_{FCC}^2 \sin^3 \alpha \cos^4 \alpha}{2\pi} \end{aligned} \quad (3.143)$$

For an F₂BCC composed of pin-jointed struts, the expression for the initial stiffness is given by:

$$\frac{E_{F_2BCC}}{E_s} = 2\pi \left[\frac{\sin w}{\bar{l}^2 \cos^2 w} + \frac{\sin \alpha}{\bar{d}^2 \cos^2 \alpha} \right] = \bar{\rho}_{BCC} \sin^4 w + \bar{\rho}_{FCC} \sin^4 \alpha \quad (3.144)$$

- **Collapse strength**

- A. Plastic micro-buckling

The analytical expression for the collapse strength of the F₂BCC unit cell can be obtained by assuming that the cell fails when the struts in the BCC lattice reach their critical strength limit, or, when the struts in the FCC lattice reach their critical strength. Alternatively, assuming that all struts experience the same stress level for a given displacement, the collapse strength is found to be in fair agreement with FE models. The expression for the nominal compressive strength of an F₂BCC core composed of rigid-jointed struts is given by:

$$\begin{aligned} \sigma_{F_2BCC}^{avg} = & \bar{\rho}_{BCC} \sin^2 w \left[1 + \frac{3\bar{\rho}_{BCC} \cos^4 w}{2\pi \sin w} \right] \sigma_c^{BCC} \\ & + \bar{\rho}_{FCC} \sin^2 \alpha \left[1 + \frac{3\bar{\rho}_{FCC} \cos^4 \alpha}{2\pi \sin \alpha} \right] \sigma_c^{FCC} \end{aligned} \quad (3.145)$$

where $\sigma_c^{BCC} = \sigma_{max} / \left[1 + \frac{3\cot w}{\bar{\varphi}} \left(\frac{r}{l} \right)^2 \right]$ and $\sigma_c^{FCC} = \sigma_{max} / \left[1 + \frac{3\cot \alpha}{\bar{\varphi}} \left(\frac{r}{d} \right)^2 \right]$.

For pin-jointed struts, the F₂BCC compressive strength is simplified to:

$$\sigma_{F_2BCC}^{avg} = \sigma_c^{BCC} \bar{\rho}_{BCC} \sin^2 w + \sigma_c^{FCC} \bar{\rho}_{FCC} \sin^2 \alpha \quad (3.146)$$

where $\sigma_c^{BCC} = \sigma_c^{FCC} = \sigma_{max}$.

B. Elastic buckling

The elastic buckling strength for rigid-jointed strut in the BCC and FCC portion of the F₂BCC cell are calculated using Equation 3.53 and 3.111 respectively and the values for σ_c^{BCC} and σ_c^{FCC} are substituted in Equation 3.145 to yield the elastic buckling strength of the F₂BCC cell.

The elastic buckling strength of a F₂BCC cell constructed from pin-jointed struts are calculated using Equation 3.55 and 3.112 and the values for σ_c^{BCC} and σ_c^{FCC} are substituted in Equation 3.146 to yield the elastic buckling strength of the F₂BCC cell.

References

- [1] D. B. Miracle, S. L. Donaldson, S. D. Henry, C. Moosbrugger, G. J. Anton, B. R. Sanders, N. Hrivnak, C. Terman, J. Kinson, K. Muldoon and others, *ASM handbook*, vol. 21, ASM International Materials Park, OH, USA, 2001.
- [2] I. M. Daniel and O. Ishau, *Engineering Mechanics of Composite Materials*, 1994.
- [3] Guide to Composites. [Online]. Available: URL <http://www.netcomposites.com>.
- [4] V. Šmilauer, C. G. Hoover, Z. P. Bažant, F. C. Caner, A. M. Waas and K. W. Shahwan, “Multiscale simulation of fracture of braided composites via repetitive unit cells”, *Eng. Fract. Mech.*, vol. 78, pp. 901–918, 2011.
- [5] K. Finnegan, G. Kooistra, H. N. G. Wadley and V. S. Deshpande, “The compressive response of carbon fiber composite pyramidal truss sandwich cores”, *Int. J. Mater. Res.*, vol. 98, pp. 1264–1272, 2007.
- [6] V. S. Deshpande and N. A. Fleck, “Collapse of truss core sandwich beams in 3-point bending”, *Int. J. Solids Struct.*, vol. 38, pp. 6275–6305, 2001.
- [7] V. S. Deshpande, N. A. Fleck and M. F. Ashby, “Effective properties of the octet-truss lattice material”, *J. Mech. Phys. Solids*, vol. 49, pp. 1747–1769, 2001.
- [8] T. George, V. S. Deshpande and H.N.G. Wadley, “Hybrid carbon fiber composite lattice truss structures”, *Compos. Part A Appl. Sci. Manuf.*, vol. 65, pp. 135–147, 2014.
- [9] T. George, V. S. Deshpande, K. Sharp and H. N. G. Wadley, “Hybrid core carbon fiber composite sandwich panels: Fabrication and mechanical response”, *Compos. Struct.*, vol. 108, pp. 696–710, 2014.

- [10] B. C. Lee, K. W. Lee, J. H. Byun and K. J. Kang, “The compressive response of new composite truss cores”, *Compos. Part B Eng.*, vol. 43, pp. 317–324, 2012.
- [11] L. Dong, V. Deshpande and H. Wadley, “Mechanical response of Ti–6Al–4V octet-truss lattice structures”, *Int. J. Solids Struct.*, vol. 60–61, pp. 107–124, 2015.
- [12] B. Budiansky, “Micromechanics”, *Comput. Struct.*, vol. 16, pp. 3–12, 1983

Chapter 4: Finite Element Analysis

4.1 Introduction

A numerical investigation of the proposed lattice core structures was performed using the ANSYS FE package to predict their response under quasi-static compression loading conditions. Numerical modeling theory and techniques used to model the response of the lattice core specimens are presented. The accuracy of the analytical expressions previously presented was checked against a series of finite element models. Finally, these numerical predictions are compared with experimental results in the following chapter.

4.2 ANSYS FE package

ANSYS Mechanical Parametric Design Language (MAPDL) Version 15.0 was used for generating the model, obtaining the solution and reviewing the results. In general, ANSYS is a comprehensive finite element analysis (FEA) product for simulating structural, vibration, fluid dynamics, heat transfer and electromagnetic interactions. In addition, the software has coupled-physics capabilities involving acoustic, piezoelectric, thermal–structural and thermo-electric analysis [1]. The structural analysis capability in ANSYS MAPDL includes linear, nonlinear and dynamic simulation studies. The ANSYS library includes a number of element types, material models and equation solvers for many mechanical design problems. Using matrix notation, the analysis implicitly solves a system of equations that can be cast into,

$$Ku = F \quad (4.1)$$

where K is the system stiffness matrix, u is the vector of unknowns (i.e. displacement vector in a structural analysis), and F is the force vector [2]. Under the structural analysis discipline, the analysis type must be specified in the solution phase. ANSYS contains several analysis types, such as static, modal, harmonic, eigenvalue buckling, etc. For the case in hand, the boundary conditions do not change as a function of time and the applied loads do not induce significant inertia and damping effects (quasi-static). Therefore, a static structural analysis is deemed fit to determine the displacements, stresses, strains, and forces in the structures. In addition, eigenvalue buckling analysis was carried out to determine the buckling behavior of the structure.

4.3 Constitutive models for the composite material

Here, the constitutive models governing the behavior of the composite materials are presented. The materials making up the struts in the various lattice core configurations are based on unidirectional fiber composites. Therefore, their elastic response will be predicted on the basis of a transversely isotropic material model. ANSYS has built in failure criteria to assess the possibility of failure of the elastic-brittle orthotropic materials based on models proposed by Hashin and Rotem [3], and Hashin [4]. Once the onset of the different damage mechanisms occurring in composites has been established, predicting post-damage degradation based on the amount of dissipated energies [5] was carried using ANSYS built-in capabilities.

4.3.1 Elastic response

All lattice core configurations were constructed from struts with reinforcing fibers aligned along the strut axis in the e_1 -direction as illustrated in Figure 4.1. The e_2 - e_3 principle plane is a plane of isotropic material property.

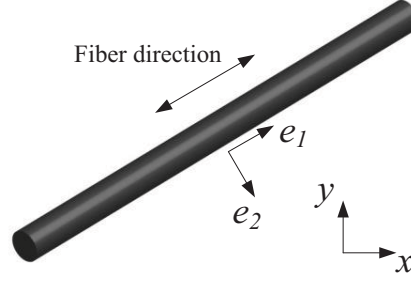


Figure 4.1: Single strut illustrating fiber orientation.

As a result, this transversely-isotropic material is described by five independent material constants that include the Young's modulus E_1 and $E_2 = E_3$, the Poisson's ratio $\nu_{12} = \nu_{13}$ and ν_{23} and the shear modulus $G_{12} = G_{13}$. The subscript 1 represents the longitudinal e_1 -direction and subscripts 2 and 3 represent the transverse e_2 and e_3 -directions. With the e_1 -direction perpendicular to the plane of isotropy, the stress-strain relationship within the elastic regime is given by,

$$\begin{Bmatrix} \epsilon_{11} \\ \epsilon_{22} \\ \epsilon_{33} \\ \gamma_{23} \\ \gamma_{13} \\ \gamma_{12} \end{Bmatrix} = \begin{bmatrix} \frac{1}{E_1} & -\frac{\nu_{12}}{E_1} & -\frac{\nu_{12}}{E_1} & 0 & 0 & 0 \\ -\frac{\nu_{12}}{E_1} & \frac{1}{E_2} & -\frac{\nu_{23}}{E_2} & 0 & 0 & 0 \\ -\frac{\nu_{12}}{E_1} & -\frac{\nu_{23}}{E_2} & \frac{1}{E_2} & 0 & 0 & 0 \\ 0 & 0 & 0 & 2(\frac{1+\nu_{23}}{E_2}) & 0 & 0 \\ 0 & 0 & 0 & 0 & \frac{1}{G_{12}} & 0 \\ 0 & 0 & 0 & 0 & 0 & \frac{1}{G_{12}} \end{bmatrix} \begin{Bmatrix} \sigma_{11} \\ \sigma_{22} \\ \sigma_{33} \\ \sigma_{23} \\ \sigma_{13} \\ \sigma_{12} \end{Bmatrix} \quad (4.2)$$

The above compliance matrix reduces the required elastic constants needed to describe the material response from nine to five. The elastic constants for the strut material were determined using the rule of mixtures model as described in Chapter 3. Table 4.1 gives a summary of the elastic properties for the CFRP rods of three different fiber volume fractions.

Table 4.1: Summary of elastic properties of CFRP materials manufactured at three different fiber volume fractions.

Symbol	$V_f = 14\%$	$V_f = 28\%$	$V_f = 42\%$	Property
E_1	30 GPa	60 GPa	88 GPa	Elastic modulus in the longitudinal direction (e_1)
E_2	4 GPa	4 GPa	5 GPa	Elastic modulus in the transverse direction (e_2)
E_3	4 GPa	4 GPa	5 GPa	Elastic modulus in the transverse direction (e_3)
G_{12}, G_{13}	1.4 GPa	1.7 GPa	2.1 GPa	Axial shear modulus
G_{23}	1.4 GPa	1.6 GPa	1.9 GPa	Through-thickness shear modulus
ν_{12}, ν_{13}	0.34	0.32	0.30	Axial Poisson's ratio
ν_{23}	0.35	0.34	0.34	Through-thickness Poisson's ratio

4.3.2 Damage initiation & progression model for the fiber reinforced composites

Damage initiation and propagation in fiber-reinforced composites are based on a combination of models in which the damage onset is triggered by meeting the requirements of at least one of the four damage initiation mechanisms [3, 4]. Once damage is triggered, material stiffness reduction occurs immediately by degradation of the stiffness matrix coefficients [5]. This is followed by a damage progression phase that is based on the amount of dissipated energies to account for different damage modes (fiber rupture and kinking, matrix cracking and crushing) [6].

Hashin's damage model was considered in the analysis. The model includes four damage initiation mechanisms that are determined according to the following criteria [2],

Fiber tension ($\sigma_{11} > 0$)

$$F_f^T = \left(\frac{\sigma_{11}}{X^T}\right)^2 + \frac{\sigma_{12}^2 + \sigma_{13}^2}{(S^L)^2} \quad (4.3)$$

Fiber compression ($\sigma_{11} \leq 0$)

$$F_f^C = \left(\frac{\sigma_{11}}{X^C}\right)^2 \quad (4.4)$$

Matrix tension ($\sigma_{22} > 0$)

$$F_m^T = \left(\frac{\sigma_{22}}{Y^T}\right)^2 + \left(\frac{\sigma_{12}}{S^L}\right)^2 \quad (4.5)$$

Matrix compression ($\sigma_{22} \leq 0$)

$$F_m^C = \frac{\sigma_{22}}{Y^C} \left[\left(\frac{Y^C}{2S^T}\right)^2 - 1 \right] + \left(\frac{\sigma_{22}}{2S^T}\right)^2 + \left(\frac{\sigma_{12}}{2S^L}\right)^2 \quad (4.6)$$

Where, X^T and X^C are the longitudinal tensile and compressive strength loads. Y^T and Y^C are the transverse tensile and compressive strength loads. S^L and S^T are the in-plane (axial) and out -of-plane shear strength respectively. Table 4.2 presents the damage initiation data for the CFRP material used in the lattice-core specimens.

Table 4.2: Summary of strength characteristic data for the CFRP materials (*Assumption)

Symbol	V _f = 14%	V _f = 28%	V _f = 42%	Property
X^T	200 MPa*	250 MPa*	350 MPa*	Longitudinal tensile strength
X^C	155 MPa	210 MPa	315 MPa	Longitudinal compressive strength
Y^T	50 MPa*	65 MPa*	80 MPa*	Transverse tensile strength
Y^C	50 MPa*	65 MPa*	80 MPa*	Transverse compressive strength
S^L	5 MPa*	6 MPa*	7 MPa*	Transverse shear strength
S^T	10 MPa*	12 MPa*	14 MPa*	Longitudinal shear strength

The response of the material after damage initiation (which describes the rate of degradation of the material stiffness once the initiation criterion is satisfied) is defined by the following equation;

$$[\sigma] = [D]_d \varepsilon \quad (4.7)$$

where σ is the effective stress averaged over the entire domain, ε is the total elastic strain and $[D]_d$ is the damaged elasticity matrix which has the following form for a transversely isotropic material with axial stress state,

$$[D]_d = \frac{1}{A} \begin{bmatrix} (1-d_f)E_1 & (1-d_f)(1-d_m)v_{21}E_1 & 0 \\ (1-d_f)(1-d_m)v_{12}E_1 & (1-d_m)E_2 & 0 \\ 0 & 0 & A(1-d_s)G_{12} \end{bmatrix} \quad (4.8)$$

Where $A = 1 - v_{12}v_{21}(1-d_f)(1-d_m)$, E_1 and E_2 are the undamaged longitudinal (fiber direction) and transverse (radial direction) elastic modulus respectively, the damage variables d_f , d_m and d_s reflect the current state of fiber damage, matrix damage and shear damage respectively. The damage variable assumes values between 0 and 1, where 0 = no damage and 1 = complete loss of stiffness. Further loading of the damaged specimen will cause degradation of the material stiffness coefficients as indicated by the increasing damage variable for the mode. The damage variable d for a given mode is given as follows:

$$d = \frac{\|u\|^f (\|u\| - \|u\|^0)}{\|u\| (\|u\|^f - \|u\|^0)} \quad (4.9)$$

Where $\|u\|^0$ is the equivalent displacement at the damage onset and $\|u\|^f$ is the equivalent displacement when the material reaches its ultimate strength. Damage variables increase gradually based on the energy amounts dissipated for the various damage modes. The fracture energy and viscous regularization values were input for completing the numerical

analysis. Table 4.3 gives the fracture energies viscous damping values for the various failure modes [7].

Table 4.3: Summary of the fracture energy data for the truss material (lower bound and upper bound values correspond to materials having $V_f = 0.14$ and $V_f = 0.48$ respectively)

Symbol	Value	Property
G_c^{ft}	25-100 N/mm	Energy dissipated per unit area from tensile fiber damage
v^{ft}	0.005-0.01 N-s/mm	Viscous damping coefficient for tensile fiber damage
G_c^{fc}	25-100 N/mm	Energy dissipated per unit area from compressive fiber damage
v^{fc}	0.005-0.01 N-s/mm	Viscous damping coefficient for compressive fiber damage
G_c^{mt}	25-100 N/mm	Energy dissipated per unit area from tensile matrix damage
v^{mt}	0.005-0.01 N-s/mm	Viscous damping coefficient for tensile matrix damage
G_c^{mc}	25-100 N/mm	Energy dissipated per unit area from compressive matrix damage
v^{mc}	0.005-0.01 N-s/mm	Viscous damping coefficient for compressive matrix damage

4.4 Quasi-static Finite element modelling

Presented here are details of the numerical modeling procedures for the lattice core structures under quasi-static compression loading. The lattice core structures that were examined include the vertical, pyramidal, modified pyramidal, octet, BCC, BCCz, FCC and F₂BCC lattice structures. Three-dimensional analysis with six degrees of freedom was performed for each core structure type using ANSYS Mechanical APDL 15.0.

4.4.1 Modelling of lattice core sandwich structures

This section details the FE modeling procedure of the various lattice core configurations. The numerical results are then compared to the analytical predictions derived in Chapter 3.

4.4.1.1 Selection of Parts and Elements

The geometry was simplified so that each strut was represented by a straight beam having a circular cross-section. The response of the lattice core under compression loading was modelled using the Timoshenko beam element. This element is suitable for analyzing the behavior of composite structures having a slender to moderately stubby/thick beam structures [8]. The BEAM188 is a three-dimensional beam element defined by two nodal points. The nodes define the spatial position of the element. A third node defines the orientation of the beam element. Figure 4.2 illustrates the geometry, node locations and coordinate system for the BEAM188 element.

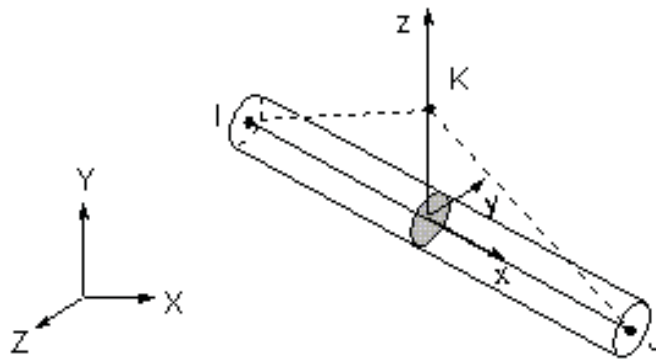


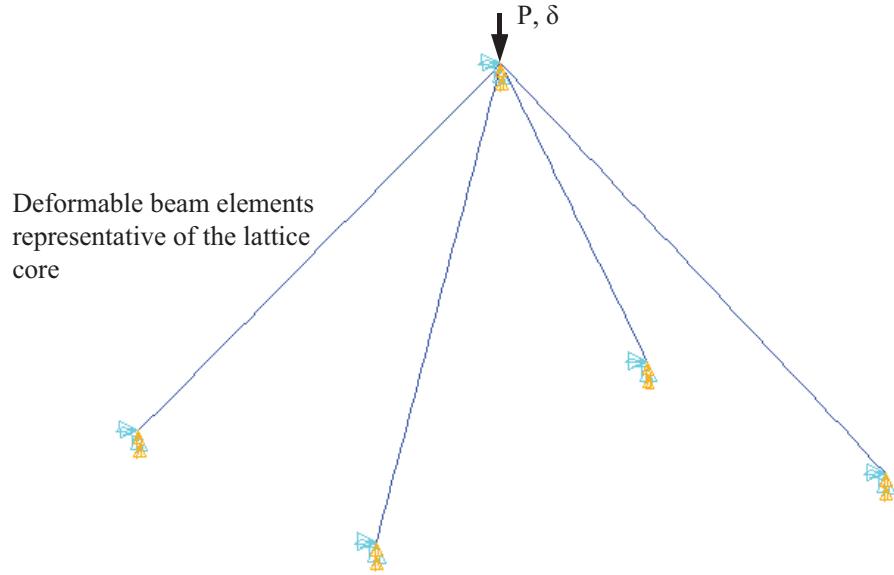
Figure 4.2: BEAM188 element geometry [8]

The lattice core model was created by specifying the location of all points representing the extremity of each strut making up the lattice and then connecting each pair with a geometric line. The cross sectional properties, such as shape and size, are defined in the mesh generation phase. During experimental testing, the facesheets simply transfer the through-thickness loads to the lattice core and do not carry any significant load. Therefore, the lattice core was modeled with appropriate boundary condition without the upper and lower facesheets. Figure 4.3 illustrates a single unit cell of a pyramidal lattice core.

U = Displacement degree of freedom
 ROT = Rotational degree of freedom
 P = Load
 δ = Displacement

Pin-joined: Top surface = $U_x = U_y = ROT_z = 0$; $U_z \neq 0$

Rigid-joined: Top surface = $U_x = U_y = ROT_x = ROT_y = ROT_z = 0$; $U_z \neq 0$



Pin-joined: Bottom surface = Fixed ($U_x = U_y = U_z = ROT_z = 0$)

Rigid-joined: Bottom surface = Fixed ($U_x = U_y = U_z = ROT_x = ROT_y = ROT_z = 0$)

Figure 4.3: Loading direction, boundary conditions and assembly of the pyramidal lattice core.

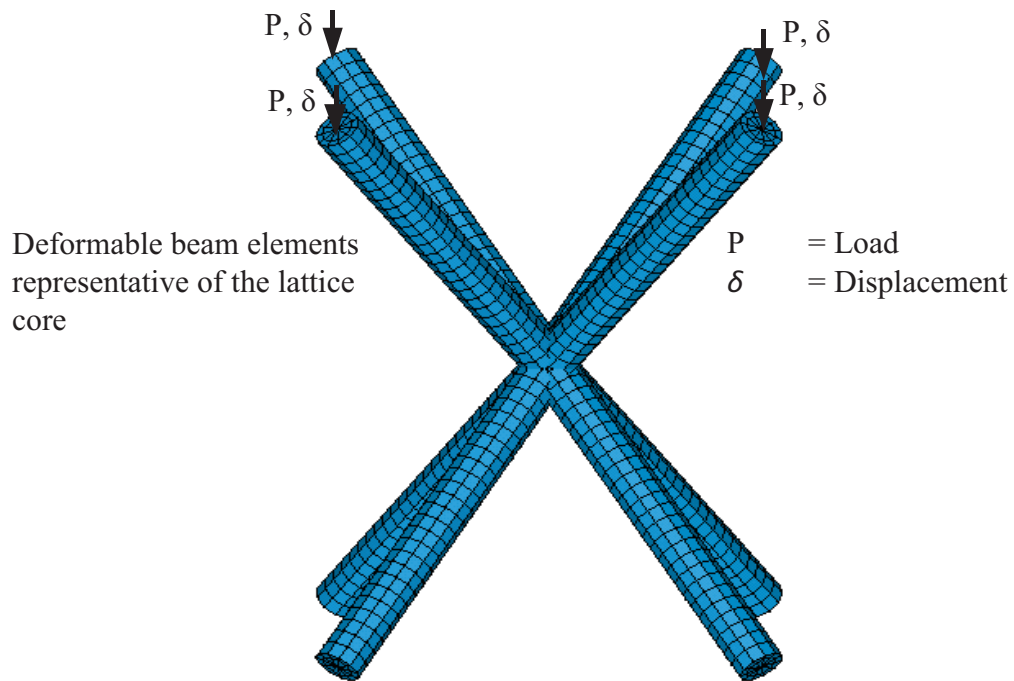
4.4.1.2 Loading and Boundary Conditions

The model needs to be appropriately constrained to capture the behavior of the core under compression loading. In one case, the struts were assumed to be pin-joined at the nodes. In doing so, nodes along the bottom surface were fully constrained in translation and from rotating about the vertical z-axis. On the opposite side, nodes along the top surface were free to move in the z-direction ($U_z \neq 0$) and rotate about x and y-axis ($ROT_x = ROT_y \neq 0$) while being fully constrained in all other degrees of freedom.

In a second case, the struts were assumed to be rigid-jointed. Nodes along the bottom surface were fully constrained in translation and rotation. Nodes along the top surface were free to move along the z-direction ($U_z \neq 0$) while being fully constrained in all other degrees of freedom.

In both cases, with the top surface free to move in the through-thickness direction, the lattice core was compressed by applying a displacement boundary condition. Boundary conditions on a pyramidal lattice is illustrated in Figure 4.3. The displacement boundary conditions were simultaneously applied on all the upper most nodes in the vertical z-direction and at a constant rate. The displacement and reaction loads from the top and bottom surface nodes respectively were recorded to capture the response of the lattice core. Figure 4.4 illustrates the boundary conditions on a BCC unit cell having rigid-jointed struts.

Top surface is fully constrained except in translation in the through-thickness direction



Bottom surface is fully constrained in translation and rotation

Figure 4.4: The FE mesh for the BCC unit cell.

4.4.1.3 Mesh Generation and Control

A mesh was generated on all lines representing the struts making up the lattice core. To completely define the beam elements, the cross-sectional properties and mesh line divisions must be specified. Figure 4.5 illustrates a pyramidal lattice core constructed from 3 mm diameter struts having 13 line divisions around the circumference, two line divisions through the radius and 40 line divisions along the strut length.

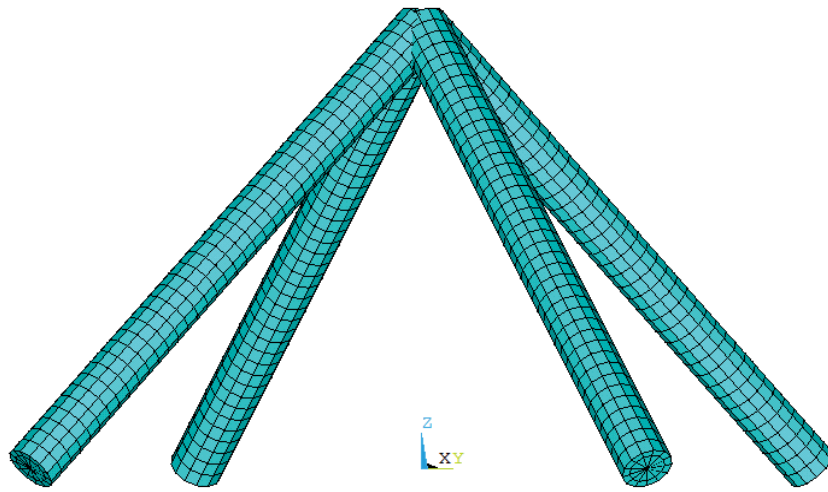


Figure 4.5: Typical mesh generated for the numerical analysis.

4.4.1.4 Model Sensitivity

The numerical model predictions are sensitive to the mesh refinement and geometric imperfections in the form of strut waviness and/or uneven column diameter. Greater accuracy is achieved by using a finer mesh and by introducing small geometric imperfections, similar to those caused by manufacturing of the real lattice.

4.4.1.5 Mesh refinement

A mesh-sensitivity study was carried out by varying the element size starting from large elements, i.e. a coarse mesh, and gradually refining the mesh by decreasing the element

size. This procedure was performed to understand the relationship between element size and material properties. Figure 4.6 summarizes this mesh sensitivity study and illustrates the influence of element size on failure stress and CPU time for the pyramidal lattice core.

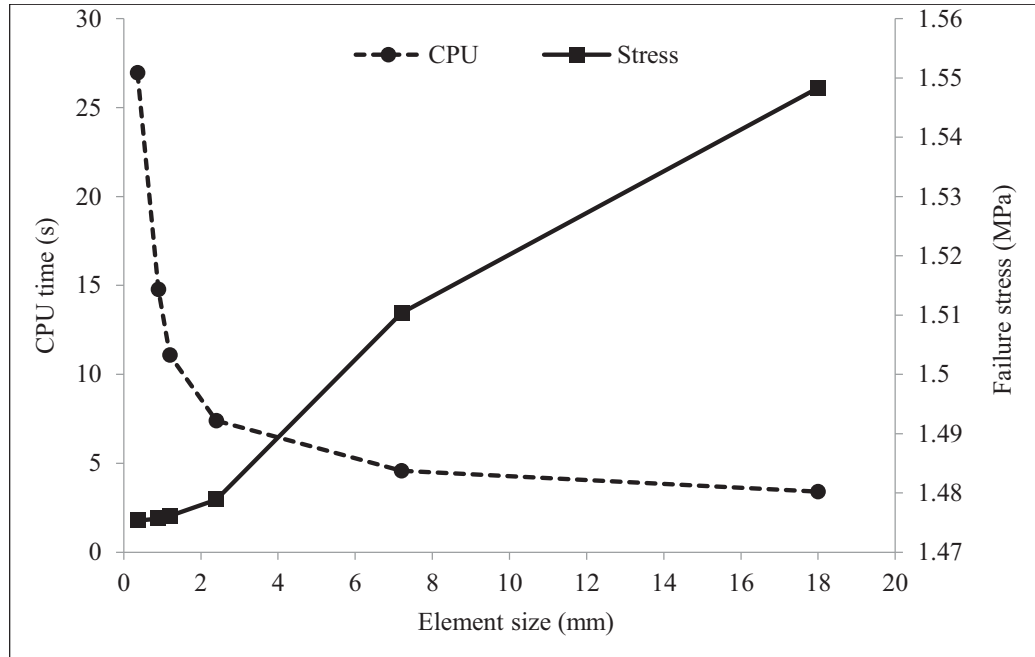


Figure 4.6: Failure stress and CPU time are plotted against element size for the pyramidal pin-jointed lattice core having a strut diameter of 3 mm and a $V_f = 0.06$.

It is evident from Figure 4.6 that the value of the predicted failure stress is dependent on element size. As the element size's decreased below 1.2 mm, the failure stress converges to approximately 1.475 MPa. Reductions in element size below 0.8 mm, results in a slight increase in accuracy, accompanied by rapid increase in CPU time. An element size of 1 mm achieves the optimum balance between CPU time and accuracy. In the FE analysis of the remaining truss core configurations, each cylindrical strut was modelled using between 20 and 40 Timoshenko Beam188 elements depending on the struts' length to achieve a 1 mm element size consistency. A mesh refinement analysis on BCC, BCCz, FCC and F₂BCC

lattice structures illustrate that a mesh size of 1 mm achieves a balance between CPU time and accuracy as illustrated for the F₂BCC lattice case in Figure 4.7.

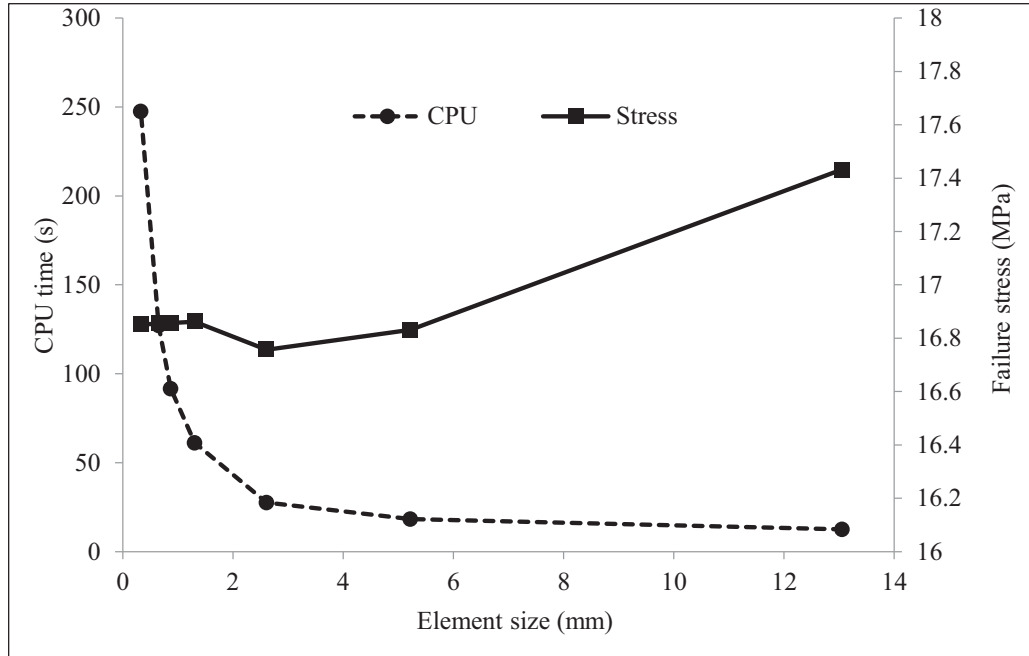


Figure 4.7: Failure stress and CPU time are plotted against element size for the F₂BCC lattice.

4.4.1.6 Load application

In order to make an accurate prediction of the peak stresses, the load must be applied in steps or sub-steps in the specified amount of time. At every specified sub-step within a load step, the solutions are calculated. Gradually applying the loads, by increasing the number of sub-steps, results in longer solution times, but helps the program to overcome convergence difficulties and produce more accurate results. The goal here was to obtain the minimum number of sub-steps to produce an optimally efficient solution. A load application sensitivity study was carried out by varying the number of sub-steps starting from five (1/5th of the total load every sub-step) and systematically increasing the number to help identify when failure initiates and how it progresses as the load increases. The total

displacement load was set at 0.5 mm. Figure 4.8 summarizes the step size sensitivity study and illustrates the influence of the number of steps in which the load is applied on failure stress and CPU time for the end-clamped pyramidal lattice structure.

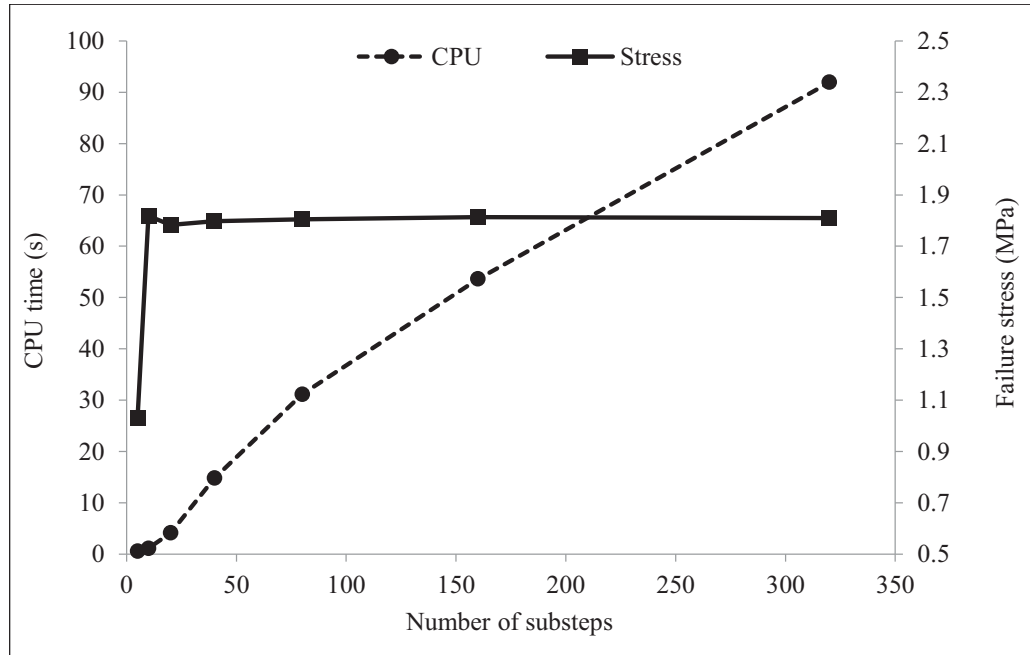


Figure 4.8: Failure stress and CPU time are plotted against step size for the end-clamped pyramidal lattice core.

It is evident from Figure 4.8 that selecting a number of steps between 100 and 150 results is an optimal choice between CPU time and accuracy. Therefore, the displacement load was applied in increments of 0.005 mm to achieve an acceptable level of accuracy and help the program to overcome convergence difficulties. The same observations apply to other lattice structures examined in this study. Figure 4.12 summarizes the step size sensitivity study for the F_2BCC structures.

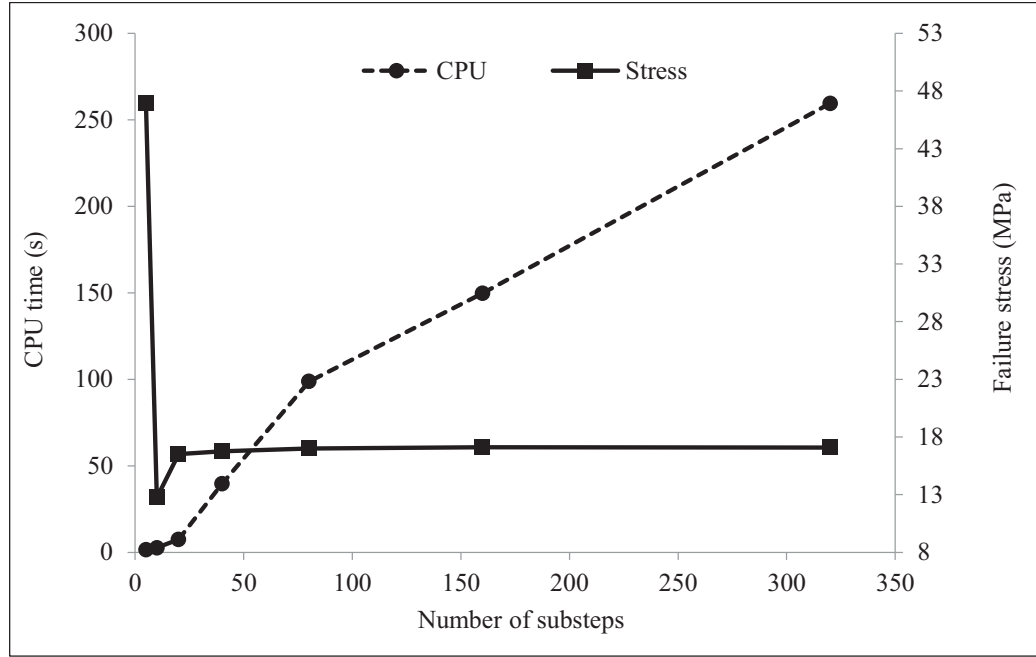


Figure 4.9: The failure stress and CPU time are plotted against step size for the F₂BCC lattice.

4.4.1.7 Geometry imperfection

Defects are inadvertently introduced into composite materials during the manufacturing process. In general, typical defects in composites include the erroneous stacking of plies, fiber waviness and porosity. For the current fabricated lattice cores, flaws in the form of geometric imperfections, fiber volume fraction variations and trapped air voids introduced during the infusion process may exist. These imperfections have a knock-down effect on the mechanical properties of the structure. FE models based on an ideal structure will, therefore, overestimate these properties, resulting in higher stiffness and peak load predictions. Deshpande *et al* [9] numerically investigated the response of the octet lattice under compression loading in which the numerical models of the octet lattice included geometric imperfections in order to make accurate predictions of their collapse stresses. In this study, an imperfection in the shape of the buckling mode was imposed on each strut.

The geometric imperfection is defined by an initial transverse deflection (s), according to the following:

$$s(x) = \frac{\xi r}{2} \left[1 - \cos\left(\frac{2\pi x}{l}\right) \right] \quad (4.10)$$

where ξ is a dimensionless imperfection parameter, x the axial distance along the strut measures from one end, r and l are the strut radius and length respectively.

In ANSYS APDL, a linear (eigenvalue) buckling analysis was initially carried out. This static analysis predicts the theoretical buckling loads for a linear elastic lattice structure, along with the buckled mode shapes of the lattice core. From this preliminary FE analysis, a mode shape resembling the experimental buckling behavior is selected and used in the next step to generate the strut imperfections. In this study, imperfections of the same shape as the first buckling mode (Mode 1) were used. An imperfection factor is applied when updating the geometry with a mode shape as noted in the ANSYS command (UPGEOM, FACTOR). A sensitivity analysis was carried out by systematically varying the imperfection factor ξ from 0 (perfect strut geometry) to 0.1 while examining the corresponding collapse load.

A nonlinear analysis is carried out after updating the geometry. This is a static analysis with large deflection effects activated via ANSYS command line (NLGEOM, ON). The load is increased gradually using small time increments so that the critical load is accurately captured. To overcome solution convergence difficulty at or after buckling, the arc-length method is activated via ANSYS command (ARCLEN, ON). The arc-length-method [10] is employed to track the nonlinear stress strain curve of a structure exhibiting unstable collapse and to speed convergence in static problems involving snapping and buckling behavior.

Figures 4.10 and 4.11 illustrate the results of four sensitivity simulations on the pyramidal lattice and BCCz lattice respectively. It is evident that a perfect model will over-estimate the peak load. Introducing imperfections results in a more conservative estimate, where the predicted peak load decreases as the imperfection factor is increased.

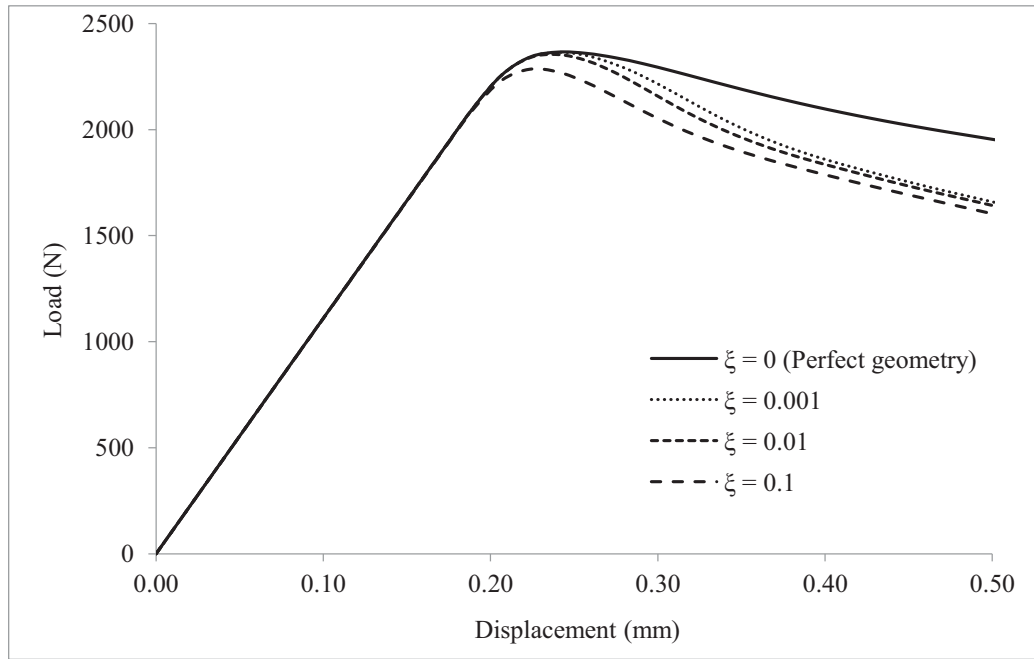


Figure 4.10: An imperfection sensitivity analysis study for the pyramidal lattice model.

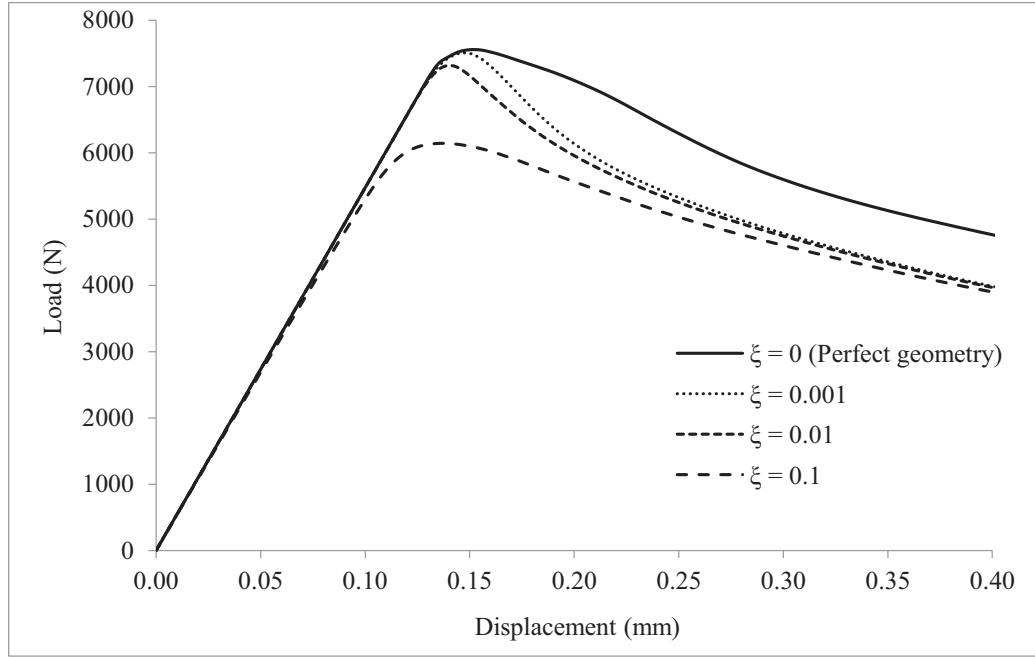


Figure 4.11: An imperfection sensitivity analysis study for the BCCz lattice model.

4.5 Numerical analysis results

In the following sections, the initial elastic modulus and peak stress values are predicted using the numerical models and analytical expressions previously that were previously described. The failure modes are also identified.

4.5.1 Vertical lattice

All of the vertical column lattice cores that were analyzed were composed of four 40 mm height vertical columns arranged in a square pattern. The strut elastic and strength properties were that of a material having a 28% fiber volume fraction. Five relative densities were investigated, with the relative density of the core being controlled by varying the strut diameter, whilst keeping the strut height and unit cell volume constant (7,840 mm³). The predicted through-thickness modulus (E) of the vertical column cores are plotted in Figure 4.12, while the predicted peak stresses are included in Figure 4.13.

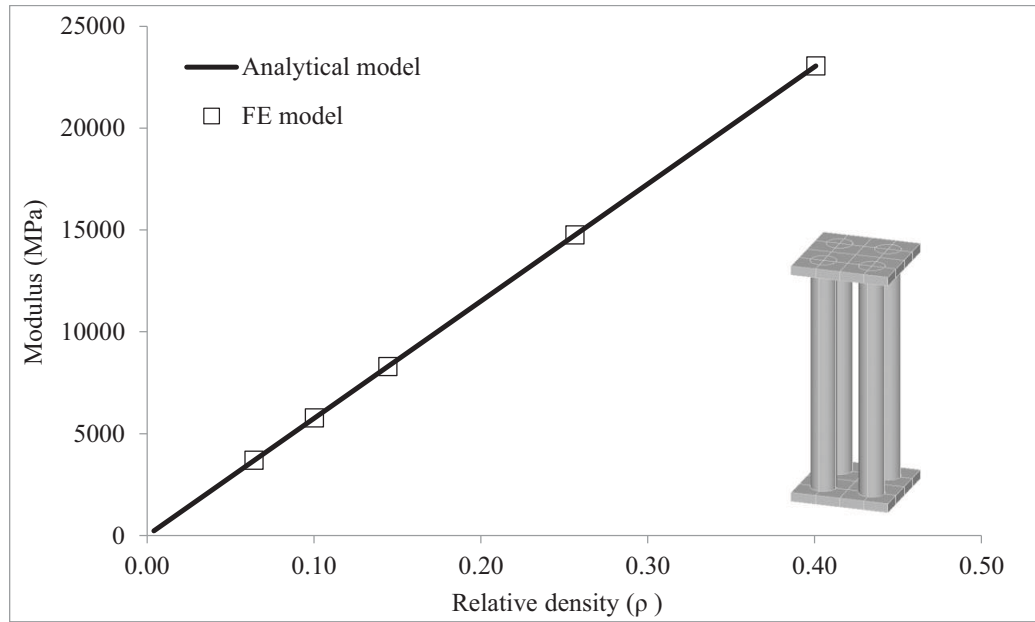


Figure 4.12: Numerical and micro-mechanical predictions of the elastic modulus of the vertical lattice core.

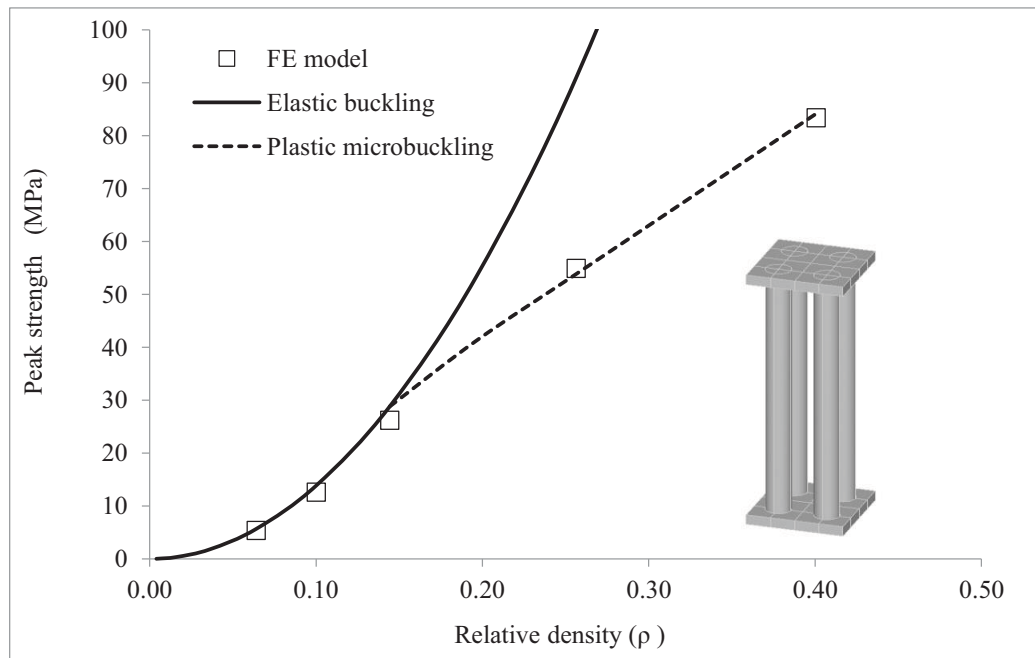


Figure 4.13: Strength predictions based on Euler buckling and plastic micro-buckling failure modes and FE models.

Figures 4.10 and 4.13 indicate good agreement between the different prediction methods. The initial elastic modulus and peak strength values increase with increasing relative density. The modulus increases in a linear fashion as a function of relative density. For cores having a relative density below 0.14 (3 mm column diameter) the struts are predicted to fail due to Euler buckling, while at higher relative density values, plastic microbuckling is expected to be the operative failure mode.

4.5.2 Pyramidal lattice

In this configuration, the struts had an angle of $\omega = 45^\circ$. Strut elastic and strength properties were examined for a material having a 12% fiber volume fraction. The relative density of the core was controlled by varying the strut diameter (d) while keeping all other geometric parameters constant. The predicted initial modulus for the end-clamped and pin-jointed pyramidal truss is shown in Figure 4.14. Both cases predict very similar modulus values for the range of relative densities examined.

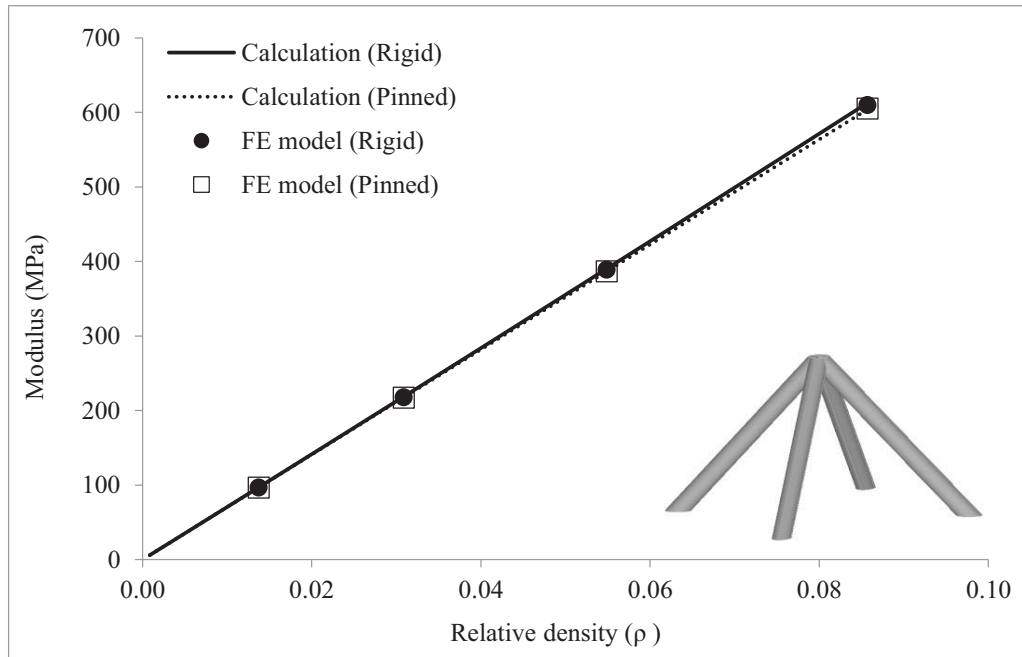


Figure 4.14: Initial elastic modulus of the pyramidal lattice based on numerical and analytical models. The modulus increases linearly with increasing relative density.

The predicted collapse strength for the pin-jointed and end-clamped pyramidal truss are shown in Figures 4.15 and 4.16 respectively. In the case of pin-jointed struts, the failure mode shifts from buckling to plastic microbuckling for cores having a relative density above 0.04%. In contrast, rigid-jointed struts experience elastic buckling at relative densities below 0.008, which corresponds to a strut diameter of 1.5 mm. For relative densities above 0.008, the core fails due to plastic microbuckling. It is worth noting that the predictions indicate that the pin-jointed struts exhibit higher compression strengths than rigid-jointed struts for samples with relative densities above 0.04 (samples that fail due to plastic microbuckling)). This is attributed to the presence of a remote shear load on the edge-clamped struts which reduces the microbuckling strength.

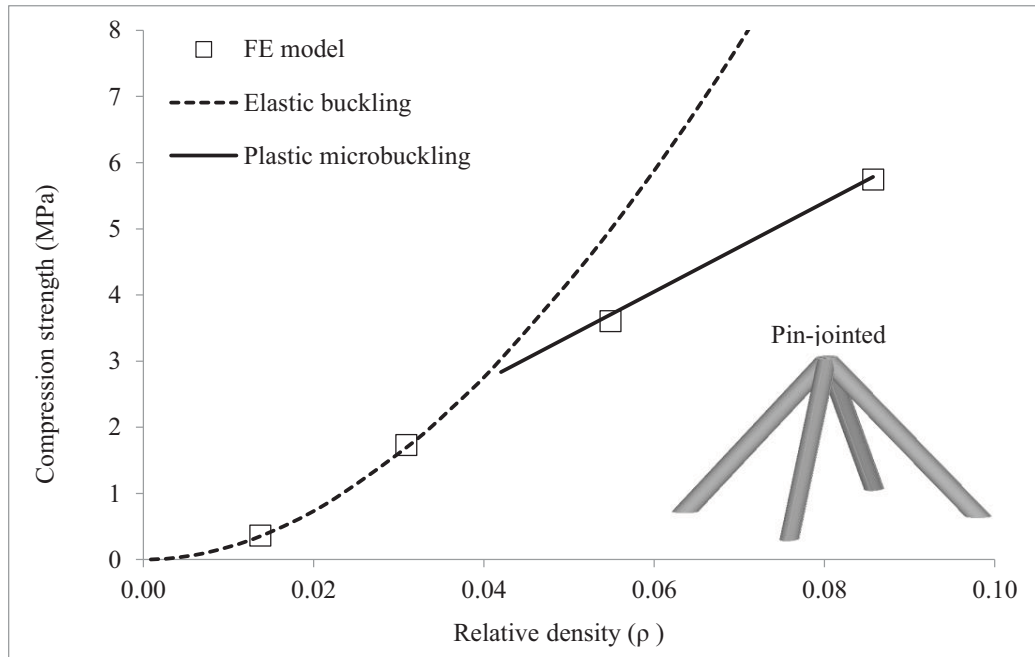


Figure 4.15: Numerical and analytical predictions of the pin-jointed pyramidal lattice compression strength.

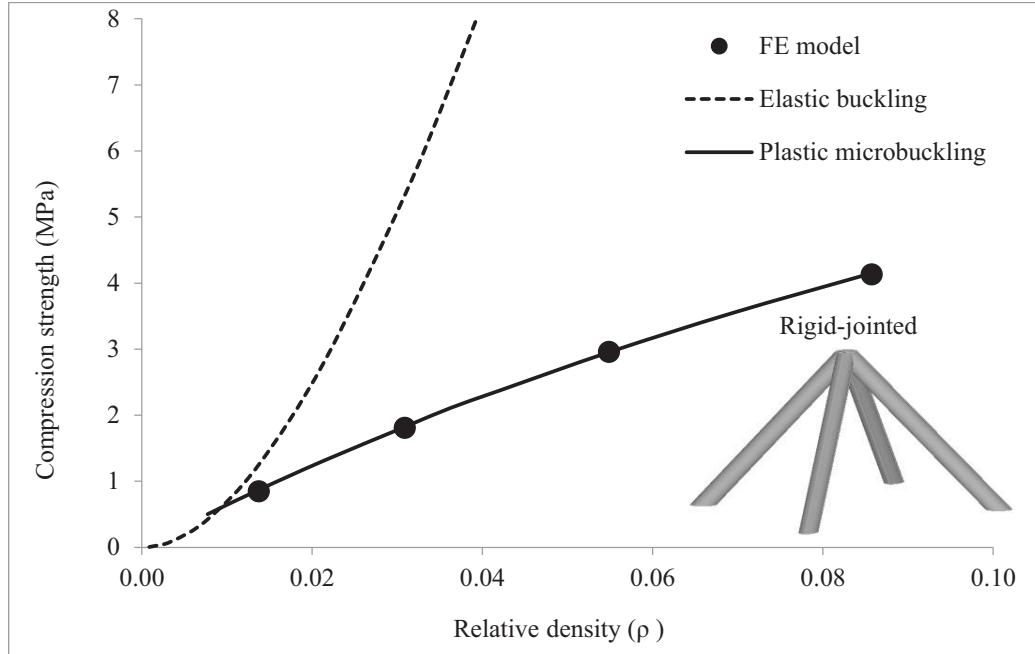


Figure 4.16: FE model and analytical predictions of the rigid-jointed pyramidal lattice compression strength.

4.5.3 Modified pyramidal lattice

In a similar approach to the pyramidal lattice core, the pin-jointed and rigid-jointed strut conditions were examined. The relative density was varied by adjusting the strut diameter while keeping all other parameters constant. The material examined had a 12% fiber volume content. The results for the initial modulus predictions based on FE model and the developed analytical models are illustrated in Figure 4.17. The modified pyramidal lattice stiffness predictions based on edge-clamped or pin-jointed struts models are approximately equal. This is expected from a stretch-dominated structure, where the contribution to stiffness from strut bending (in the rigid-jointed scenario) is relatively small.

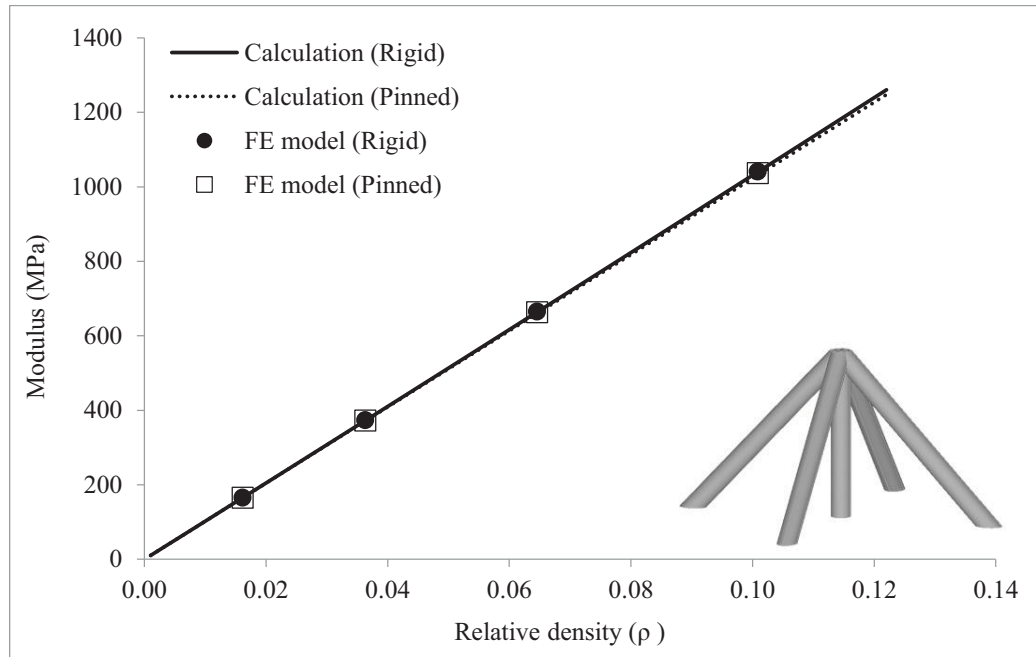


Figure 4.17: FE model and analytical predictions for the initial stiffness of a modified pyramidal lattice core.

Strength predictions for a pin-jointed and rigid-jointed truss cores are shown in Figures 4.18 and 4.19 respectively. The analytical calculations are based on Equations 3.80 and 3.85 that predict average compression strength for the pin-jointed and rigid-jointed cases respectively. Calculated values show good agreement with FE models.

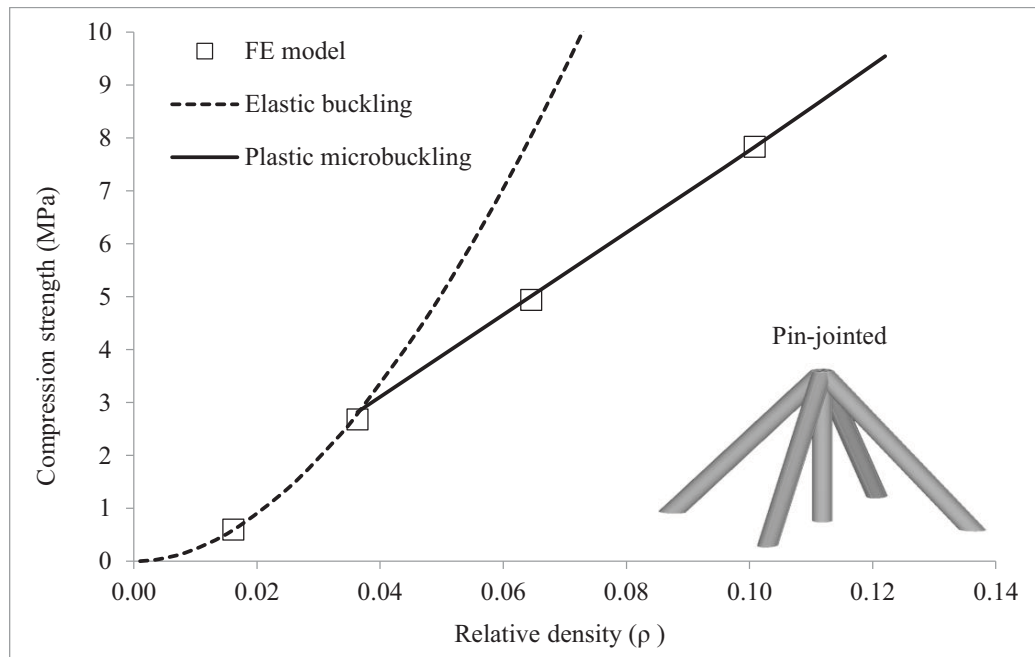


Figure 4.18: Strength predictions for the pin-jointed modified pyramidal core. The failure mode shifts from elastic buckling to plastic microbuckling for cores having a relative density above 0.04%

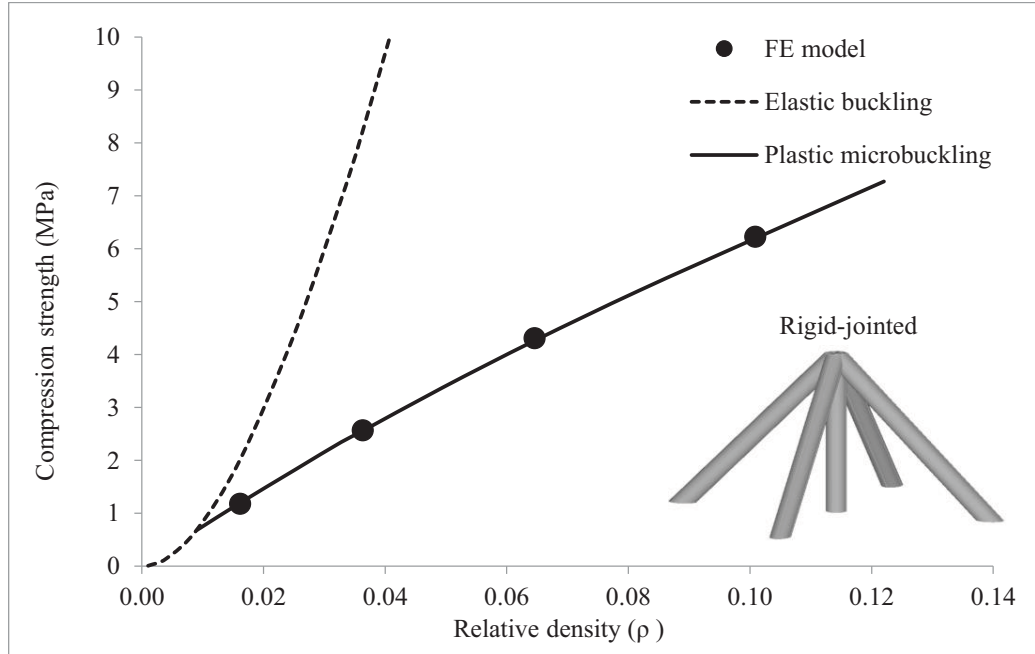


Figure 4.19: Strength predictions based of edge-clamped modified pyramidal model. For relative densities above 0.009 the core fails due to plastic micro-buckling.

4.5.4 BCC lattice

The elastic and strength properties of BCC lattice made of struts having 25% fiber volume fraction was examined. The relative density of the core was controlled by varying the strut radius (r) while keeping the inclination angle and length fixed at $\omega = 45^\circ$ and $l = 26.1$ respectively. The initial stiffness predictions for the pin-jointed or rigid-jointed struts are nearly identical for a given relative density, as illustrated in Figure 4.20. At relative densities above 0.10, bending of the rigid-jointed struts provides a relatively small contribution to stiffness, resulting in it being higher than the stiffness of the pin-jointed BCC struts.

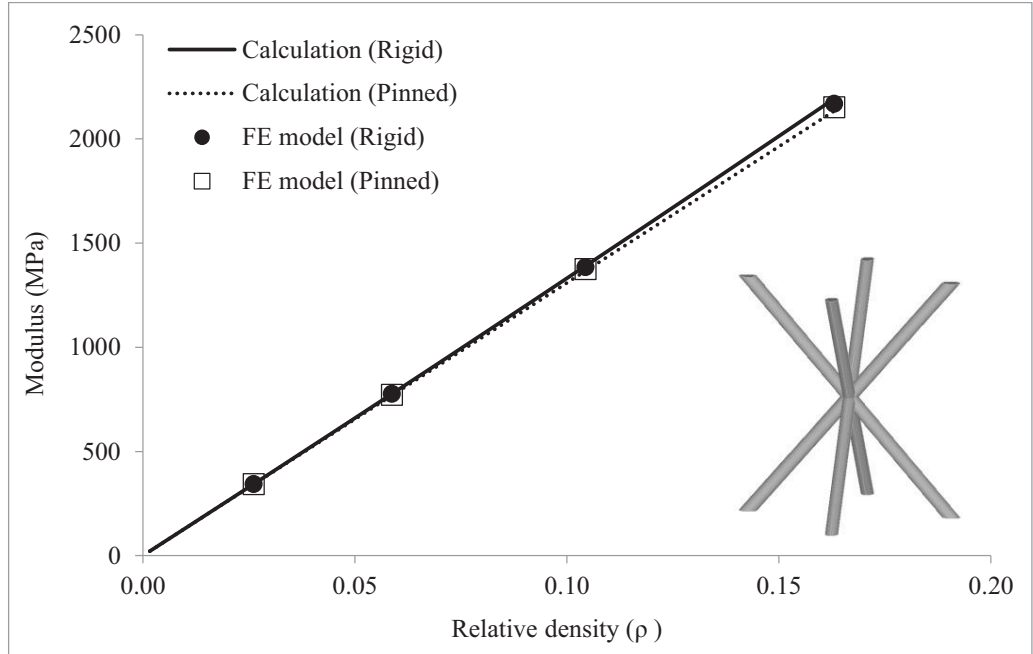


Figure 4.20: Initial stiffness predictions based for a BCC lattice constructed from pin-jointed and rigid-jointed struts.

The predicted collapse strength for the rigid-jointed and pin-jointed cases are shown in Figures 4.21 and 4.22 respectively. The predicted failure mode for samples having a relative density above 0.026 (corresponding to struts with a diameter of 2 mm and above) is plastic microbuckling.

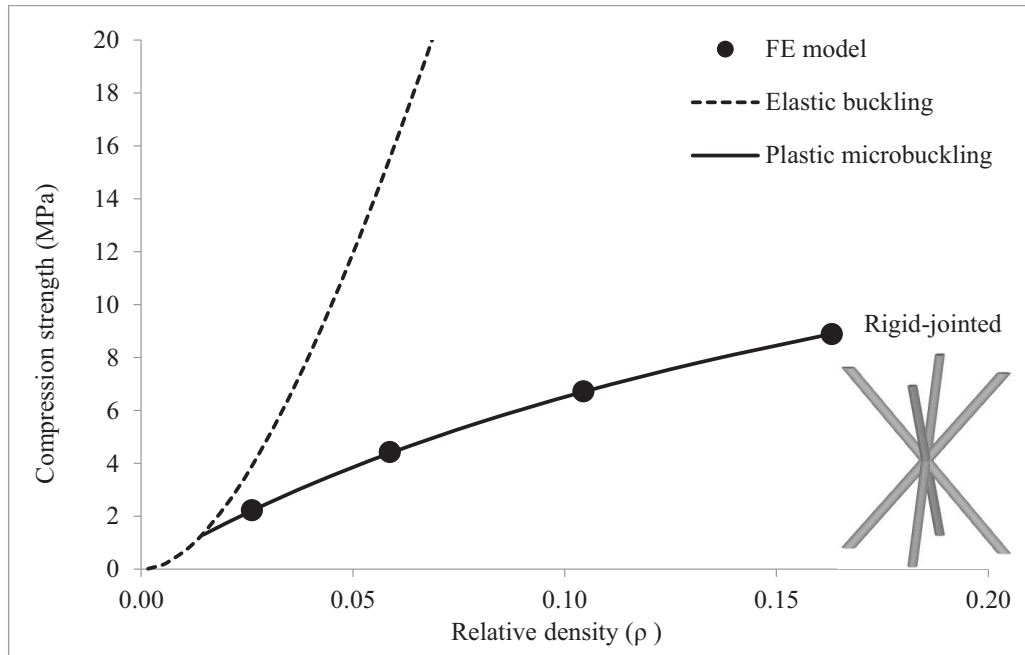


Figure 4.21: Compression strength of a BCC lattice with rigid-jointed struts.

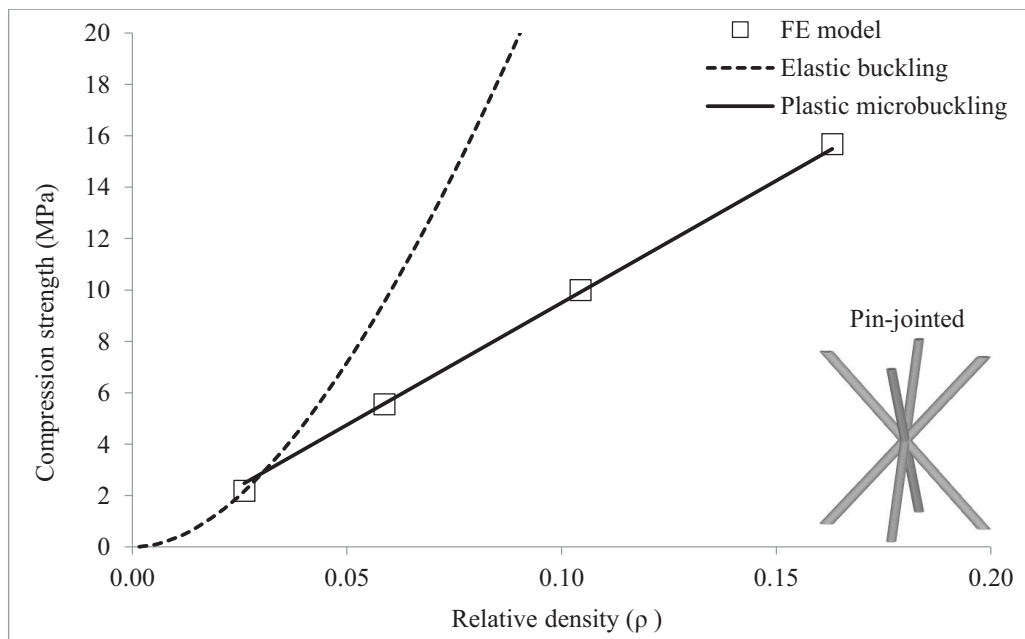


Figure 4.22: Compression strength of a BCC lattice with pin-jointed struts.

As was the case with the pyramidal lattice structures, the pin-jointed struts in the BCC lattice exhibit higher compression strengths than rigid-jointed struts for samples with

relative densities above 0.026. This is attributed to the presence of a remote shear load on the rigid-jointed struts which results in a knockdown effect on the micro-buckling strength, as approximated by Equation 3.46.

4.5.5 BCCz lattice

The pin-jointed and rigid-jointed strut conditions for the BCCz lattice were examined. The relative density was varied by adjusting the strut diameter whilst keeping all other parameters constant. The initial stiffness predictions are shown in Figure 4.23. The BCCz lattice exhibits a stiffness that is approximately four times higher than their BCC counterpart, for a given strut diameter. However, this comes at the cost of an increased relative density.

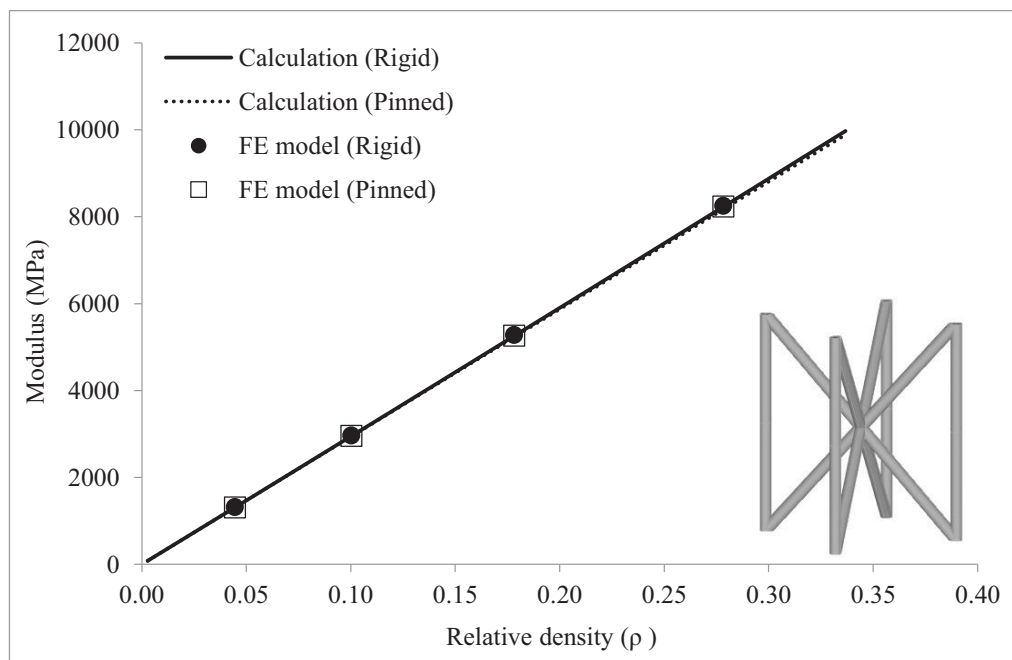


Figure 4.23: FE model and analytical predictions for the initial stiffness of the BCCz lattice structure.

The strength predictions based on a pin-jointed and rigid-jointed truss cores are shown in Figure 4.24 and Figure 4.25 respectively.

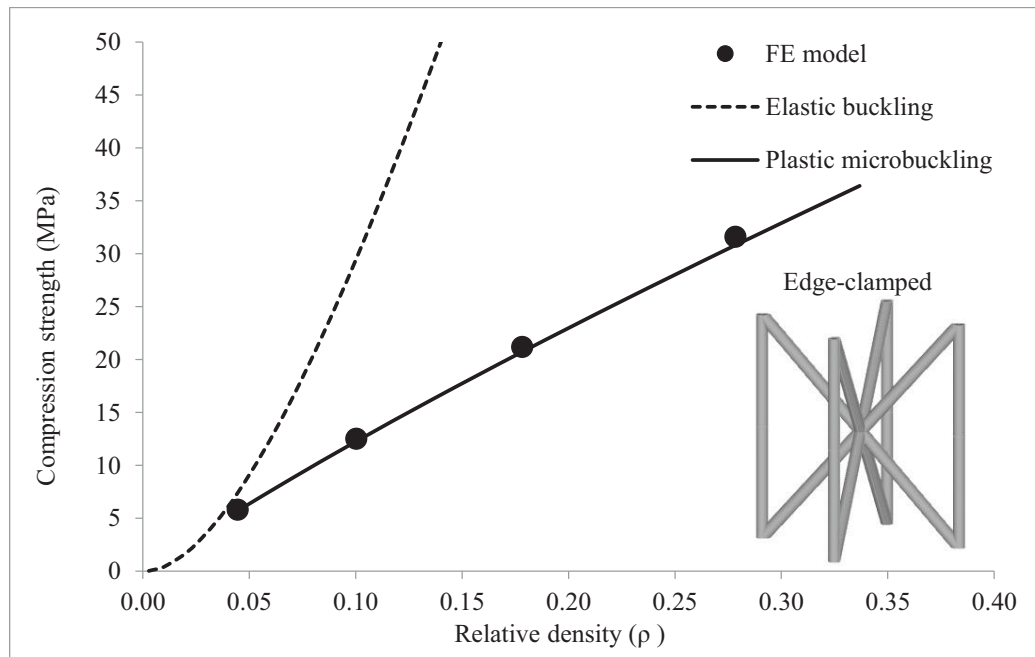


Figure 4.24: Strength predictions for the pin-jointed BCCz core. The failure mode shifts from elastic buckling to plastic microbuckling for cores having a relative density above 0.045%

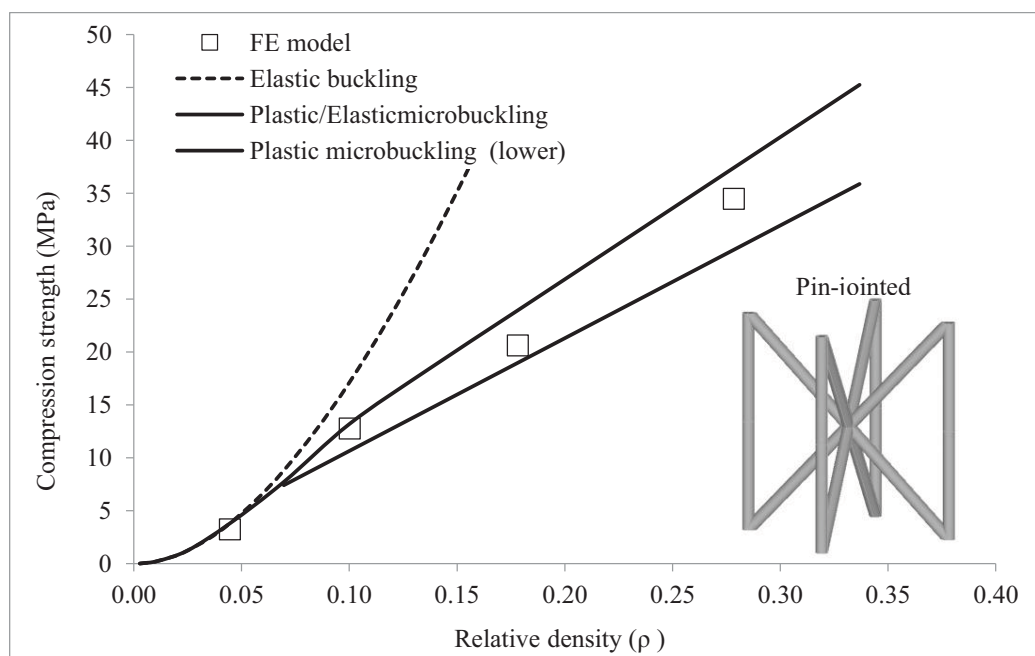


Figure 4.25: Strength predictions based on the rigid-jointed BCCz lattice model.

For the case for BCCz lattice composed of rigid-jointed struts, as shown in Figure 4.25, the analytical predictions are based on Equations 3.130 and 3.132 for the approximated lower and average strength predictions respectively. The FE model shows good agreement with the average calculations for relative densities under 0.10. For relative densities between 0.05 and 0.01, the models predict that the vertical struts fail due to elastic buckling, while the angled struts experience failure due to plastic microbuckling.

4.5.6 FCC lattice

Using the same procedure, the initial stiffness and strength predictions for a rigid-jointed and pin-jointed FCC are summarized in Figure 4.26, Figure 4.27 and Figure 4.28 respectively. The results exhibit good agreement between the analytical calculations and the FE model.

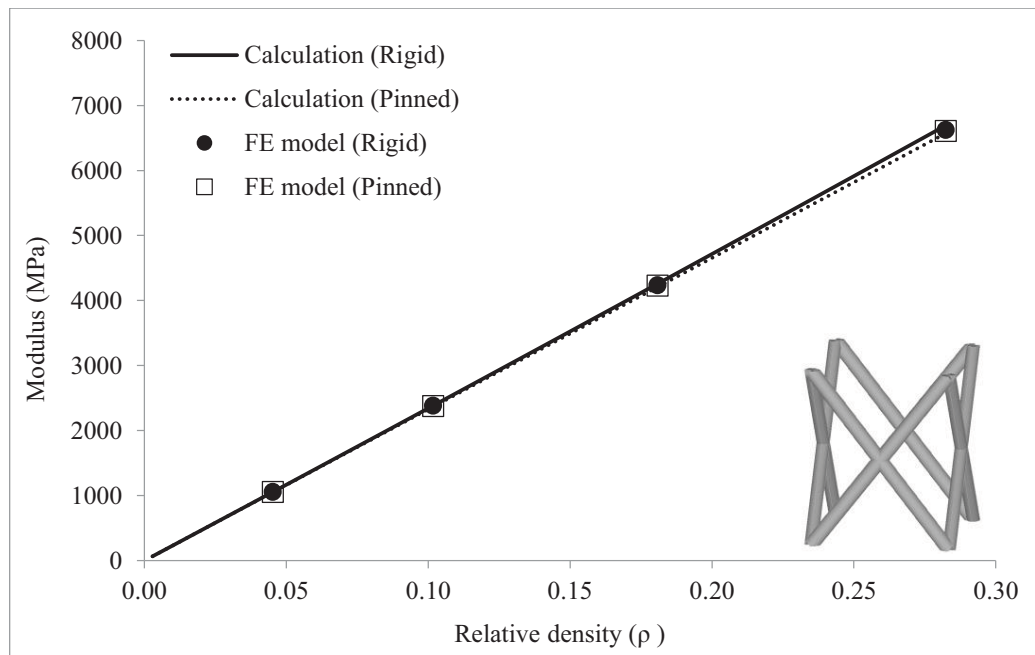


Figure 4.26: Numerical and micro-mechanical predictions of the elastic modulus for an FCC lattice. The initial modulus increases linearly with increasing relative density.

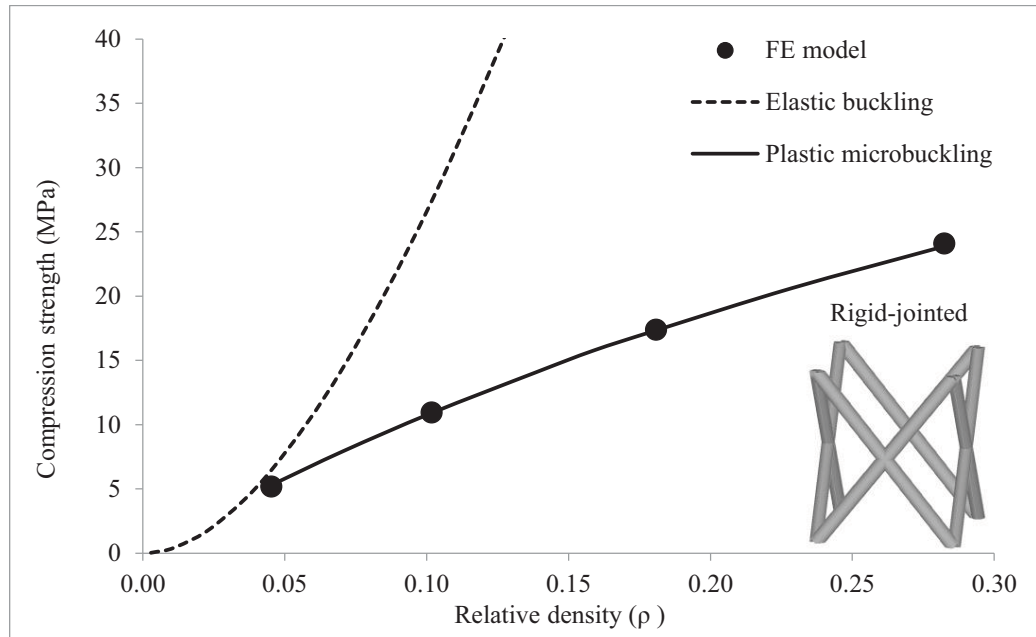


Figure 4.27: Strength predictions based on a rigid-jointed FCC lattice model. The failure mode shifts from elastic buckling to plastic micro buckling for cores having a relative density above 0.045%

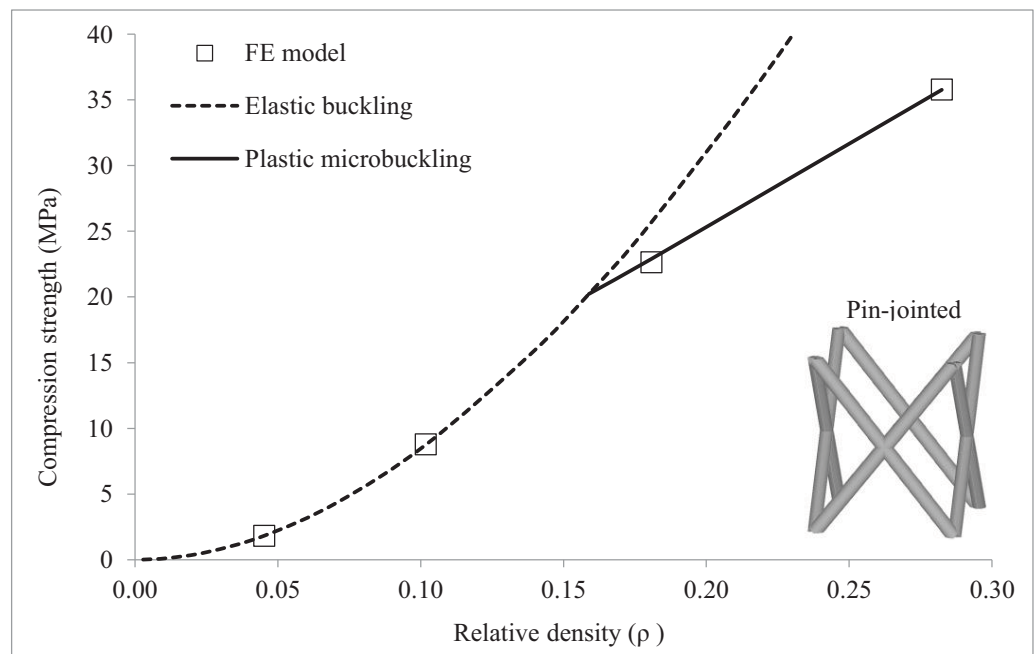


Figure 4.28: Strength predictions for the pin-jointed FCC core. At relative densities over 0.16%, the core fails due to plastic microbuckling.

4.5.7 F₂BCC lattice

Finally, the FE model and analytical predictions of the elastic modulus and strength of the F₂BCC lattice structure are presented here. The initial stiffness predictions are shown in Figure 4.29. The F₂BCC structure is a combination of a BCC and a FCC structure in a single unit cell. This is reflected in the results for the initial modulus, which can also be arrived at by simply adding the previously-predicted stiffness values for the BCC and FCC lattice of a given relative density.

Figure 4.30 illustrates the strength predictions for an F₂BCC lattice based on rigid-jointed truss. It is shown that only samples with relative densities under 0.07 experience elastic buckling failure. The analytical calculations are based on the average strength predictions from Equations 144 and 145 for a rigid-jointed and pin-jointed struts respectively.

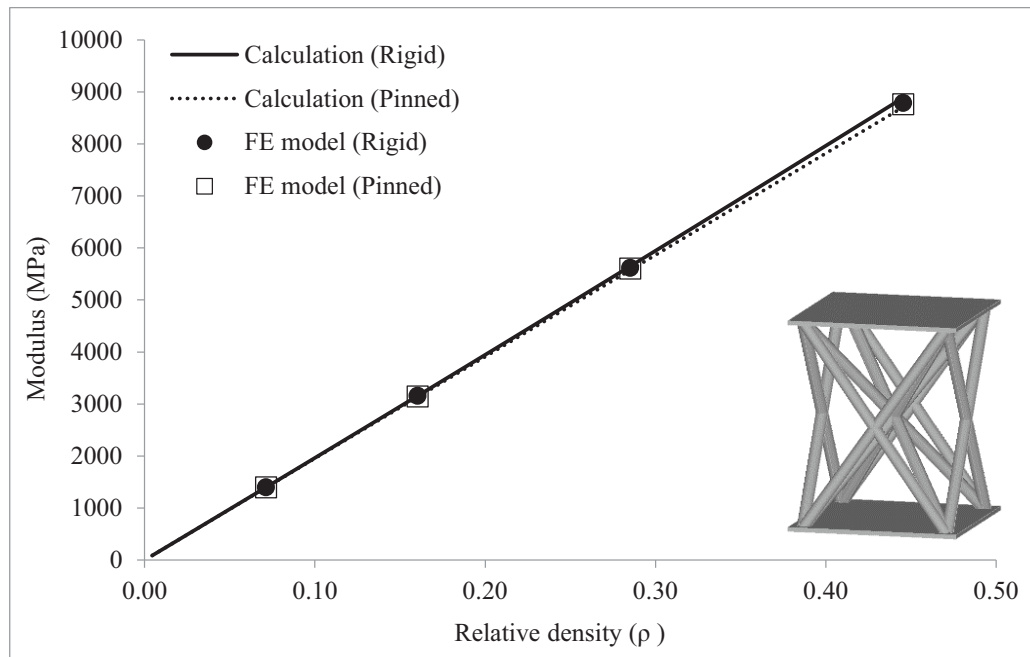


Figure 4.29: Numerical and micro-mechanical predictions of the Elastic modulus.

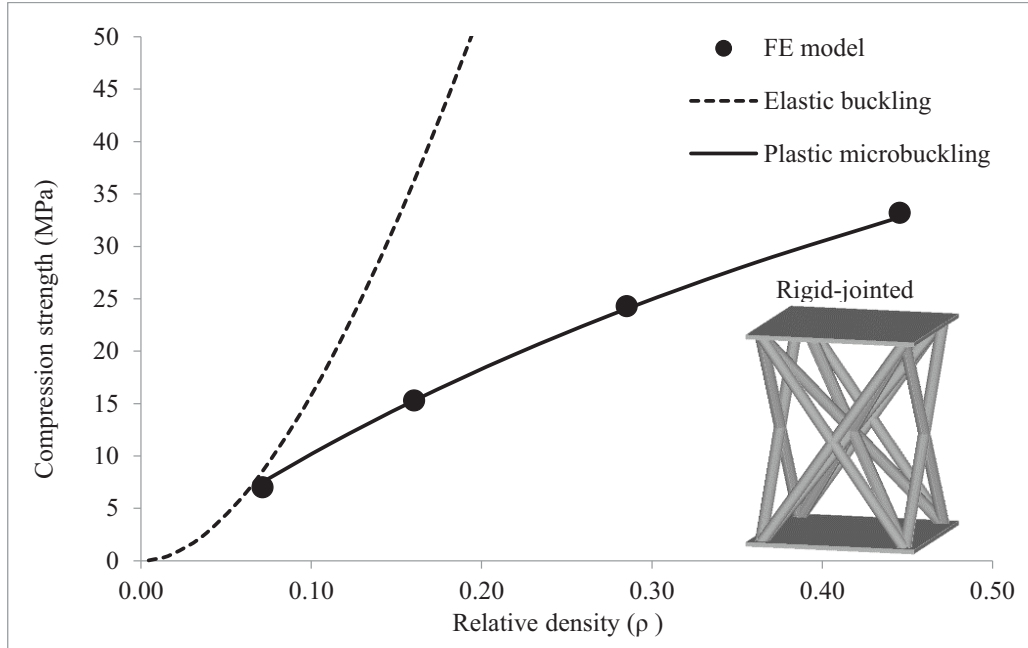


Figure 4.30: Strength predictions based on Euler buckling and plastic micro-buckling failure modes compared to FE model results.

The case for a pin-jointed F_2 BCC lattice is presented in Figure 4.31. At relative densities between 0.07 and 0.30 the analytical models predict that the face centered struts (FCC) fail due to elastic buckling, whilst the body centered struts (BCC) experience plastic micro-buckling failure. The results are in good agreement with the FE model predictions.

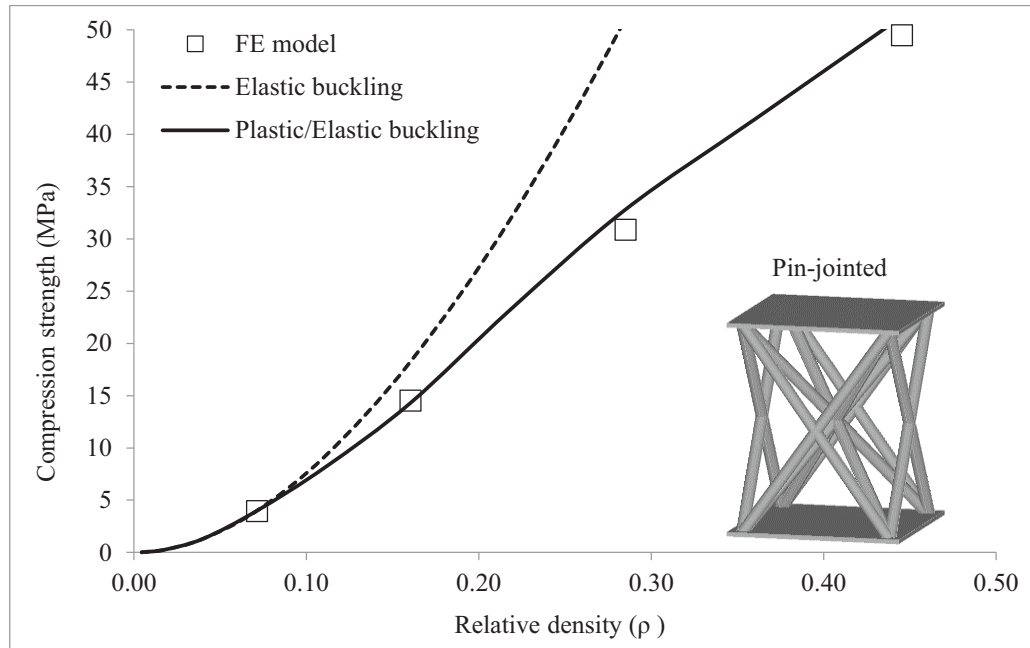


Figure 4.31: Strength predictions based on a rigid-jointed F_2BCC structure. Elastic buckling of the struts is the predicted failure mode for relative densities below 0.07. At relative densities above 0.30, the struts fail due to plastic micro-buckling.

Given that the relative densities of the manufactured lattices differ greatly, a more appropriate comparison can be made by obtaining the specific elastic modulus from the predicted initial stiffness values divided by their respective relative density. The specific initial stiffness values are plotted against the density of the core in Figure 4.32. The same approach is adopted in plotting the specific compression strength vs. core density as illustrated in Figure 4.33. In both plots, lattice configurations made from materials having approximately similar fiber volume fraction are grouped in the same ellipse in the figure.

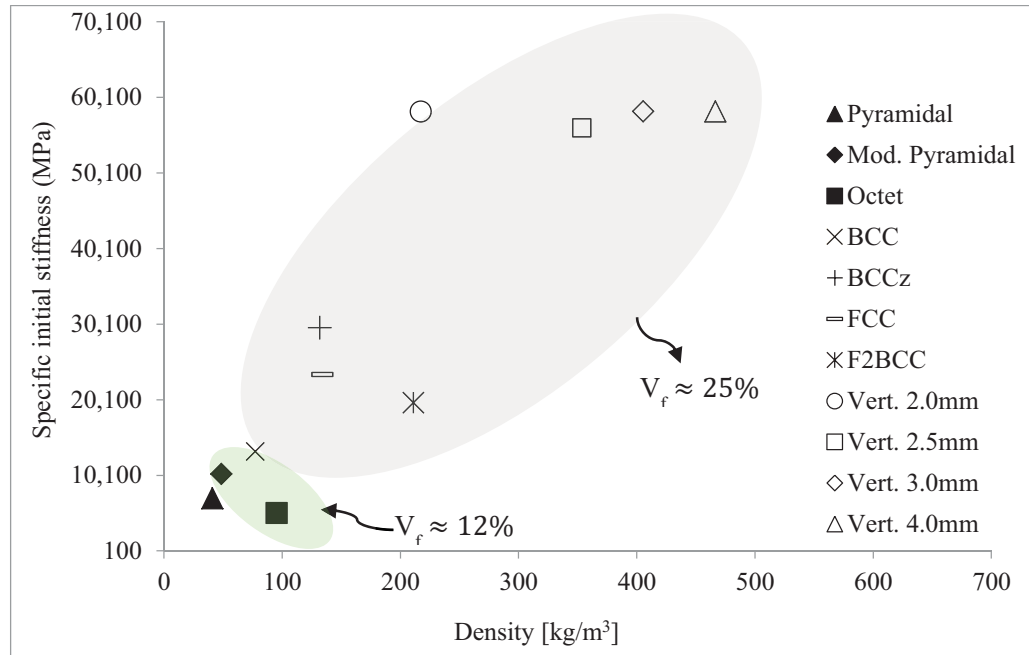


Figure 4.32: Numerical predictions for the specific initial stiffness of the various lattice core configurations.

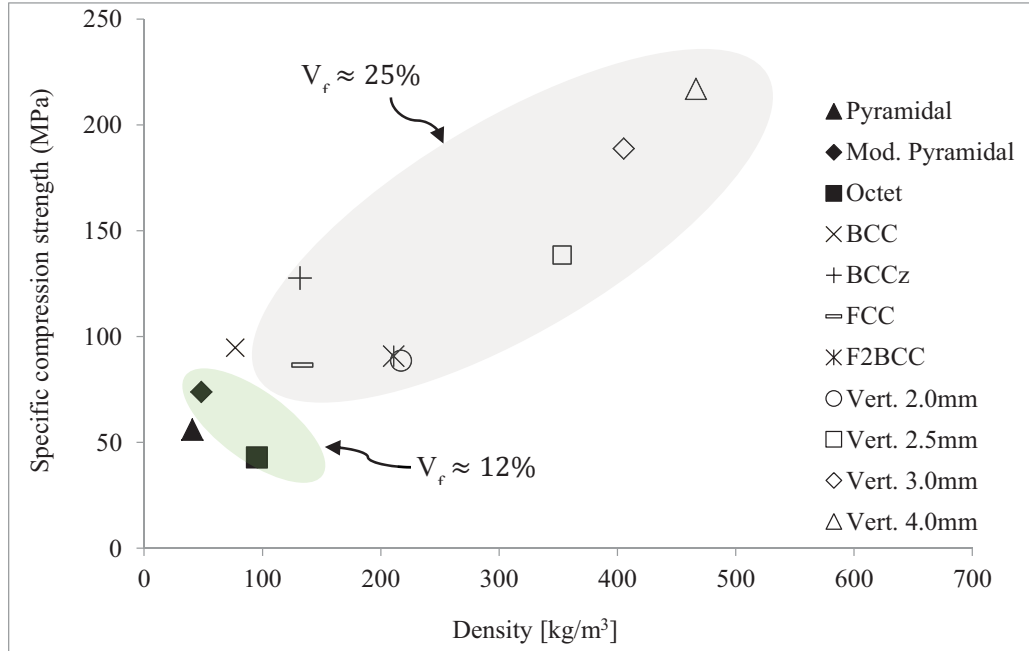


Figure 4.33: Numerical predictions for the specific compression strength of the various lattice core configurations.

It is worth noting that the BCCz lattice potentially offers superior strength properties in comparison to other lattice constructions with greater core densities (F_2 BCC and the 2 mm vertical lattice). Predictions for lattice structures constructed from materials having a fiber volume content of 12% show that the modified pyramidal lattice could offer superior stiffness and strength properties in comparison to pyramidal and octet lattices.

4.6 Conclusions

FE model showed good agreement with analytical predictions. The experimental results will be compared to the predictions and failure modes will be identified and compared in the following chapter.

References

- [1] ANSYS Mechanical. [Online]. Available: URL <http://www.ansys.com/Products/Simulation+Technology/Structural+Analysis/>.
- [2] E. Madenci and I. Guven, *The Finite Element Method and Applications in Engineering Using Ansys*, Springer, 2015.
- [3] Z. Hashin and A. Rotem, “A fatigue failure criterion for fiber reinforced materials”, *J. Compos. Mater.*, vol. 7, 448–464, 1973.
- [4] Z. Hashin, “Failure criteria for unidirectional fiber composites”, *J. Appl. Mech.*, vol. 47, pp. 329–334, 1980.
- [5] A. Matzenmiller, J. Lubliner, and R. L. Taylor, “A constitutive model for anisotropic damage in fiber-composites”, *Mech. Mater.*, vol. 20, pp. 125–152, 1995.
- [6] P. P. Camanho and C. G. Dávila, “Mixed-mode decohesion finite elements for the simulation of delamination in composite materials”, *NASA-Technical Pap.*, vol. 211737, pp. 33, 2002.
- [7] A. Lemaitre, *Sizing and optimization of fiber composite structures*. [Online]. Available: URL [http://www.ansys.com/staticassets/ANSYSFrance/staticassets/Pr%C3%A9sentation s ppt/Seminaire_Composites_ANSYS.pdf](http://www.ansys.com/staticassets/ANSYSFrance/staticassets/Pr%C3%A9sentation%20ppt/Seminaire_Composites_ANSYS.pdf).
- [8] ANSYS® Academic Research, Release 15.0, *Help System*, ANSYS, Inc.
- [9] V. S. Deshpande, N. A. Fleck, and M. F. Ashby, “Effective properties of the octet-truss lattice material”, *J. Mech. Phys. Solids*, vol. 49, pp. 1747–1769, 2001.
- [10] E. Riks, “An incremental approach to the solution of snapping and buckling problems”, *Int. J. Solids Struct.*, vol. 15, pp. 529–551, 1979.

Chapter 5: Results and Discussion

5.1 Introduction

The experimental results with comparison to FE and analytical modeling are presented in this chapter. Here, resin flow patterns and the fill time during the lost mold/VARTM process are reported. The findings of visual assessments of the fabricated lattice structures are included. Subsequently, the results of the quasi-static, through-thickness compression tests on the sandwich structures are presented. Finally, the results of the skin-core interfacial fracture toughness tests are discussed.

5.2 Resin flow and post-manufacture visual assessment

5.2.1 Hybrid GFRP/PET core

Once the lay-up procedure was completed, the infusion processes was initiated and the resin flow patterns in top and bottom face sheets were monitored optically. Since two layers of resin distribution medium were placed on the uppermost surface, this face sheet was impregnated more rapidly than the lower skin. As resin filled the perforations from the top face sheet, two types of flow were observed in the lower skin, one being in-plane and the other being radial through the holes from the top skin to the bottom skin. During the infusion time, the resin impregnated the dry fibers, as illustrated by the wetted regions in Figure 5.1.

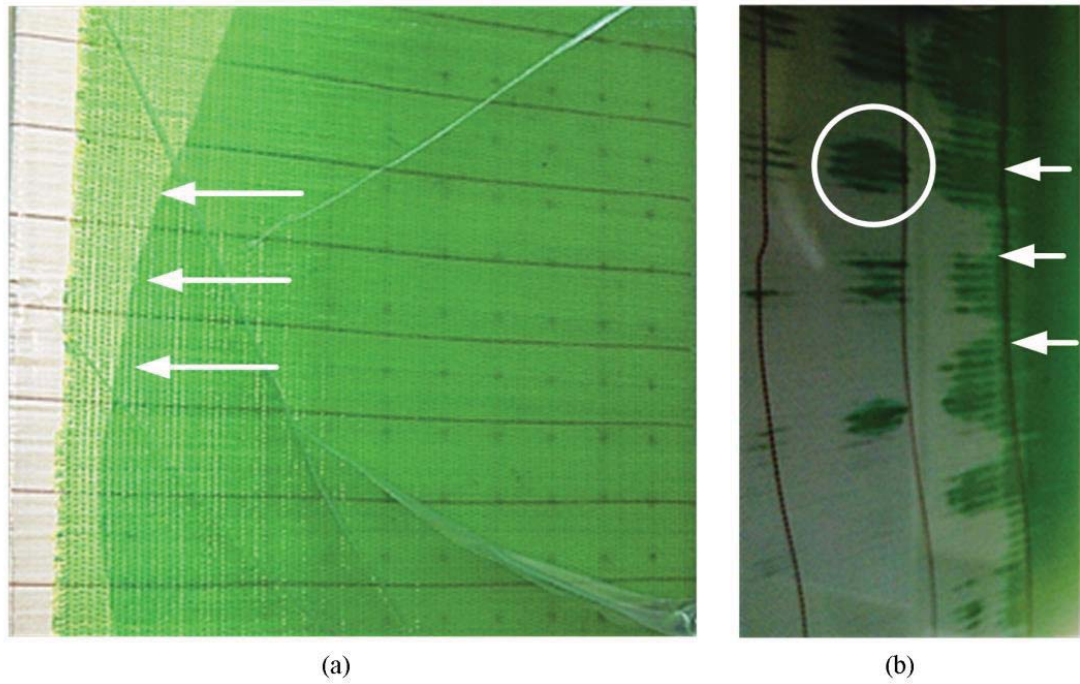


Figure 5.1: (a) Top face sheet with in-plane flow, (b) Bottom face sheet with in-plane and radial flow through the holes from top to bottom.

It was noted that for each material type, that the fill time depended on both the areal density of the drilled holes and the fiber volume fraction in the holes. Materials D-S and D-D were fully impregnated in 15 and 16 minutes perforations using a water-cooled diamond tipped saw. Figure 5.2 shows that all samples with perforations, including those containing fibers, appear to be completely filled with resin.

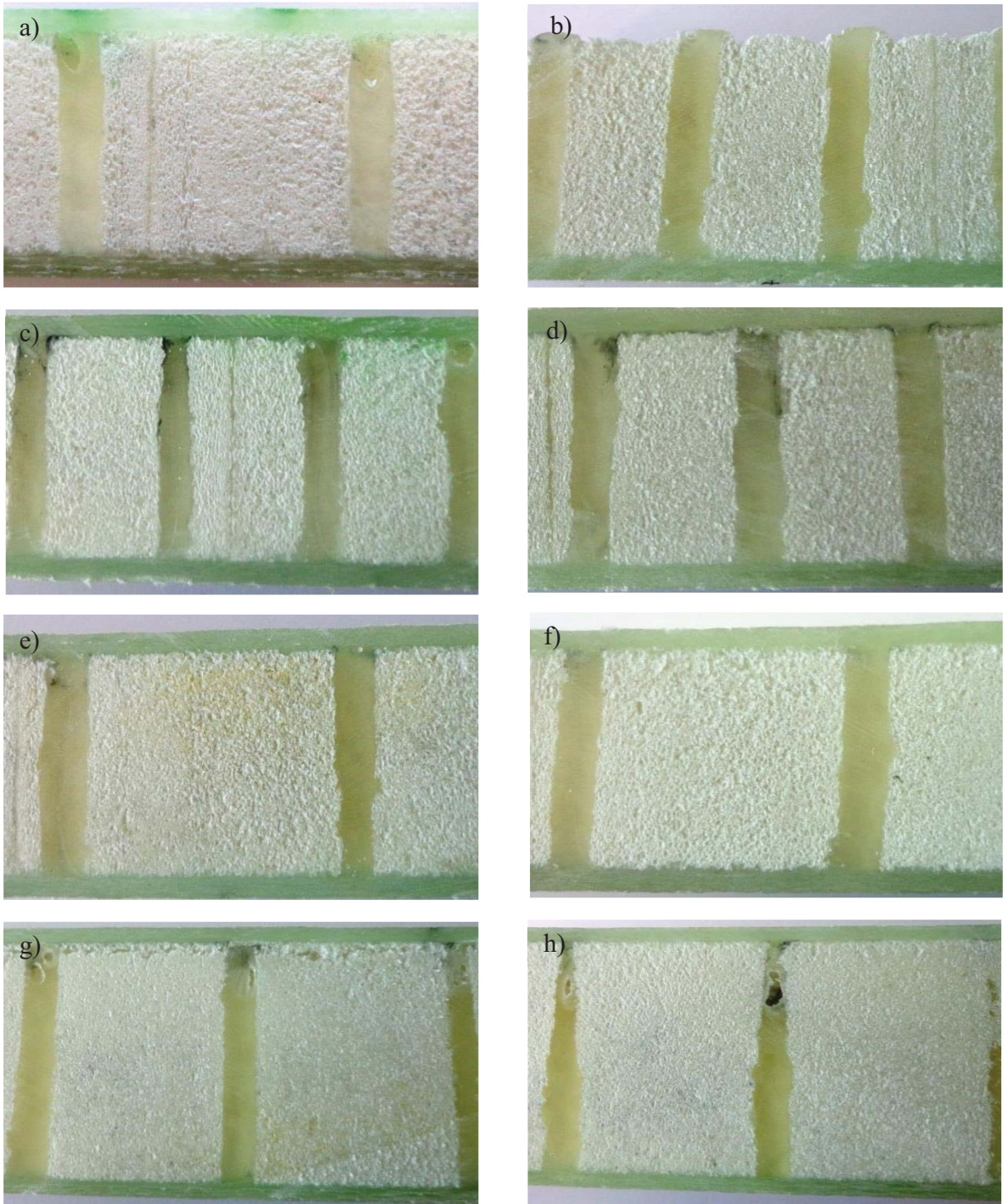


Figure 5.2: Cross-sections of manufactured samples with filled holes. (a) Materials B, (b) Materials C, (c) Material D-D, (d) Material D-S, (e) Material E-D, (f) Material E-S, (g) Material F-D, (h) Material F-S.

5.2.2 Vertical, pyramidal and octet lattice

Figure 5.3 shows a typical truss structure based on 4 mm diameter rods following the VARTM manufacturing process and the removal of the wax core. An examination of the figure indicates that the vertical rods have been successfully infused by the resin during the processing cycle.



Figure 5.3: The unit cell of a column truss core based on an array of 4 mm diameter columns.

Figure 5.4 shows photos of a typical test sample based on 2.5 mm diameter natural fiber based struts. Here, the columns are of a high quality and highly aligned. Closer inspection suggests that one or two columns contained air voids (this can be seen in the left-hand columns). However, most of the samples were relatively defect-free and of a high quality.



Figure 5.4: Photograph of a 6 x 6 column core based on 2.5 mm diameter struts.

Figure 5.5 shows a conventional pyramidal and a modified pyramidal truss structure based on 3 mm diameter rods following the VARTM manufacturing process. Visual inspection indicates successful infusion of all of the columns. A similar scenario is observed in the octet truss, as illustrated in Figure 5.6.

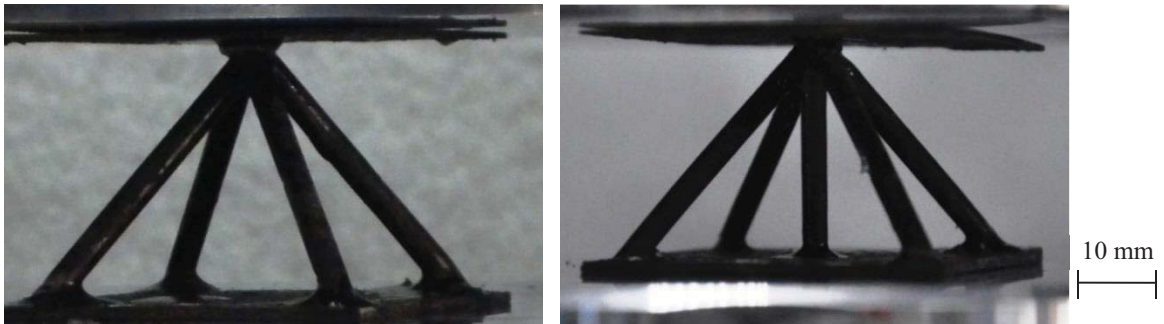


Figure 5.5: Photographs of (a) a pyramidal structure and (b) a modified pyramidal structure, reinforced with a central vertical member.

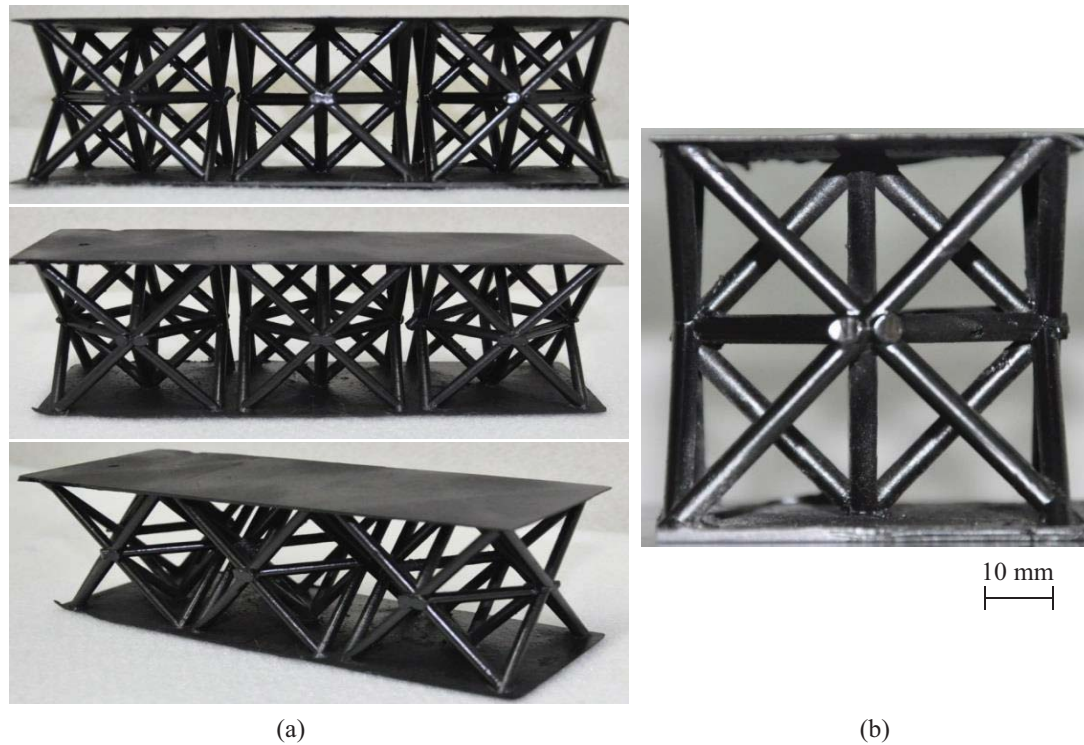


Figure 5.6: (a) Various views of a structure based on three octet unit cells, (b) A photograph of an octet truss unit cell structure

Samples from carbon fiber reinforced columns having different diameters were subsequently sectioned and polished to reveal the distribution of fibers in the cross-section. Sectioning was performed on all samples by cutting across their diameters using a diamond tipped saw to reveal the cross-section. Each sample was then placed in a resin pot and post-cured in preparation for the grinding and polishing process. A Buehler grinding and polishing machine was used according to the recommended four step procedure for preparing polymer-matrix composite samples. An image analysis of each cross-section was undertaken and the fiber volume fraction was calculated using Image J software. Figure 5.7 shows typical cross-sections of individual columns following manufacture.

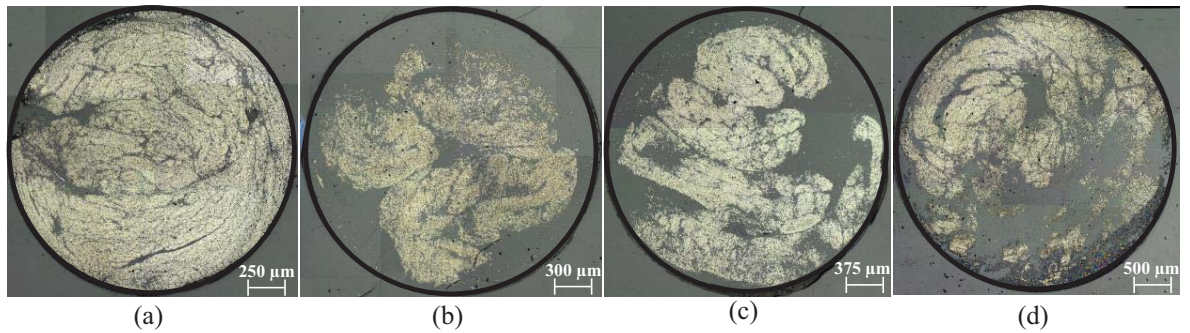


Figure 5.7: Optical micrographs of individual columns (a) 2 mm diameter, $V_f = 0.51$ (b) 2.5 mm diam. $V_f = 0.28$ (c) 3 mm diam. $V_f = 0.28$, (d) 4 mm diam. $V_f = 0.28$.

The 2 mm diameter column offers a fiber volume fraction of 51%, this being the highest value obtained in this study. An examination of the cross-section indicates that the fibers are evenly spread across the sample, although there is a small region of resin enrichment in one region close to the surface of the cylinder. It is also clear that the fibers appear to be fully impregnated by the resin, with there being little or no evidence of any voiding. From the micrograph of the 2.5 mm diameter sample based on a fiber volume fraction of 0.28, it is evident that the fibers are located towards the center of the cross-section, leaving a distinct resin-rich area close to the circumference of the strut. Regions of resin enrichment are also in evidence in the cross-section of the 3 mm specimen, where a number of small voids are also present. Finally, the fiber distribution in the 4 mm diameter sample is reasonably uniform, although resin-rich regions are in evidence.

It is desirable to have an even distribution of fiber through the cross section of the strut. Resin rich regions are relatively weaker than the remaining portions of the strut which will result in an undesirable variation in mechanical properties. The threading process may be automated to achieve a more even fiber distribution within the strut.

5.2.3 BCC, BCCz, FCC and F₂BCC lattice

Figure 5.8 shows photographs of the four lattice structures following the lost-mold manufacturing procedure. An examination of the photographs indicates that the lattices are generally of a high quality, with there no evidence of any significant defects on the surfaces of the samples. The struts all appear to be well anchored to the skins and the central nodes, where several struts meet, appear to be clearly defined. An examination of polished cross-sections removed from the individual struts indicated that the fibers were fully impregnated by the resin, with there being little or no evidence of voids or porosity.



Figure 5.8. Photographs of the BCCz, the F₂BCC, the BCC and FCC lattice structures following manufacture.

5.3 Compression tests

5.3.1 Hybrid GFRP/PET core

In the initial part of the mechanical testing program, the compression response of all core materials summarized in Table 2.1 (with the exception of Materials D-D, E-D and F-D i.e. those with a V_f of 3%). Figure 5.9 shows stress-strain relationships for samples removed from Materials A, B and C.

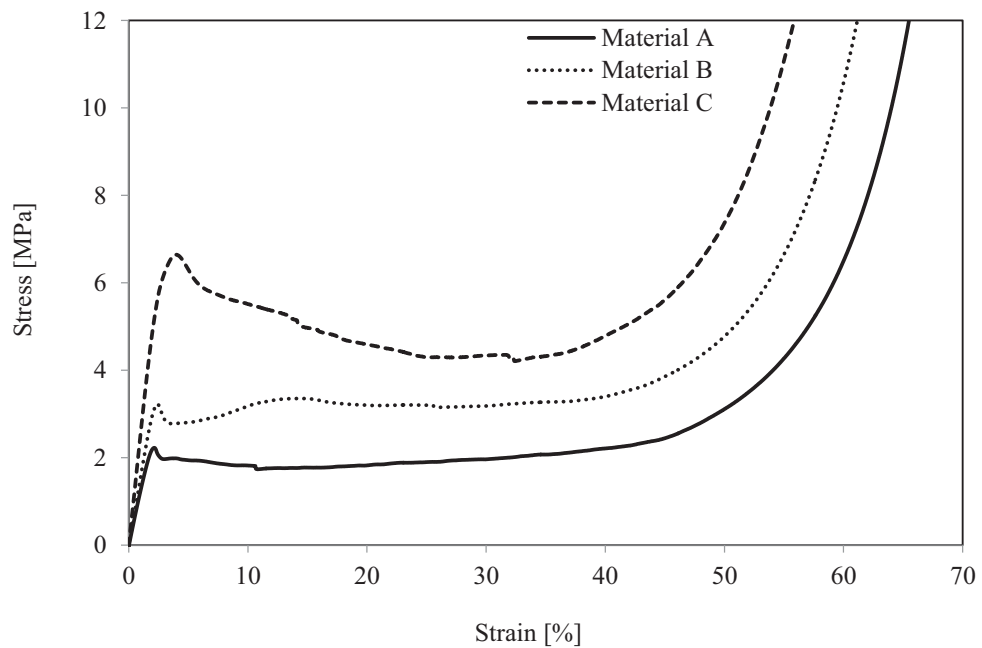


Figure 5.9: Axial compression stress strain-curves for Materials A, B, and C

The trace for the plain PET core is typical of that associated with a compression test on a plain foam. Introducing resin-filled perforations served to increase the compression strength of the foams. For example, the compression strength of Material C, with closely spaced perforations, was approximately three times that of the plain core. The post-yield stress declined gently, as the resin columns started to fracture and fragment, before increasing during the final densification phase. Figure 5.10 shows typical stress-strain

curves for cores containing reinforced perforations (fiber volume fraction = 1.5%). An examination of the figure indicates that the reinforced foams offer compression strengths that are roughly double those of the plain core.

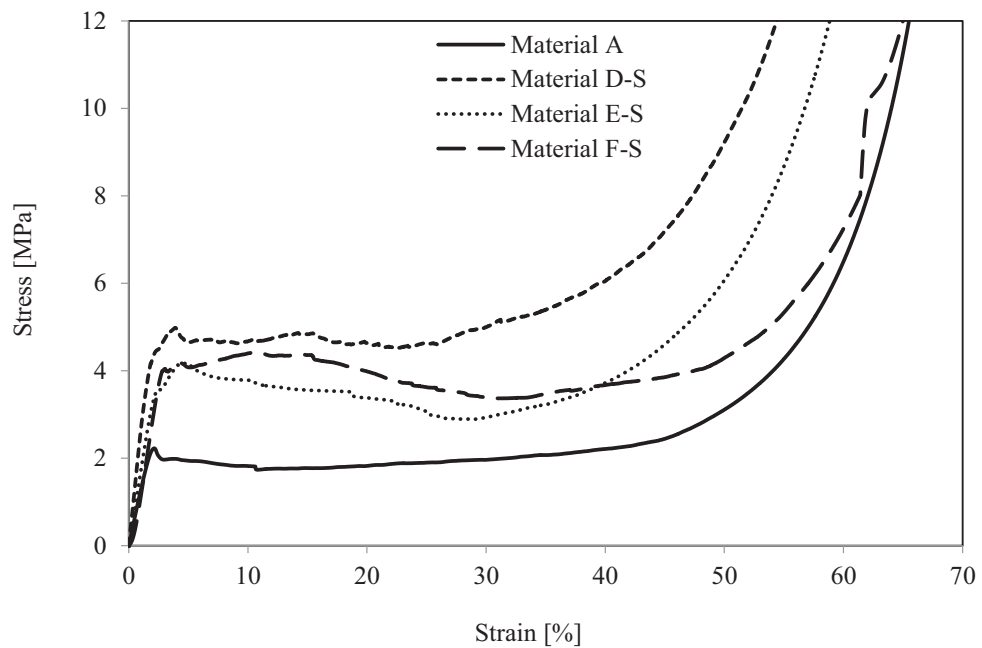


Figure 5.10: Axial compression response of Materials A, D-S, E-S and F-S.

Figure 5.11 summarizes the average compression strength values of the composite cores. The plain core offers a compression strength of approximately 2 MPa, slightly lower than the value of 2.4 MPa quoted in the manufacturer's data sheets. Interestingly, Material C, based on neat resin columns, offers the highest compression strength of all of the systems examined here. In contrast, adding fibers to the resin columns, Material D, resulted in a decrease in compression strength, possibly due to the presence of micro-voids between individual fibers. It should be noted, however, that the average compression strength of the fiber reinforced foams is still fifty percent greater than that of the plain core.

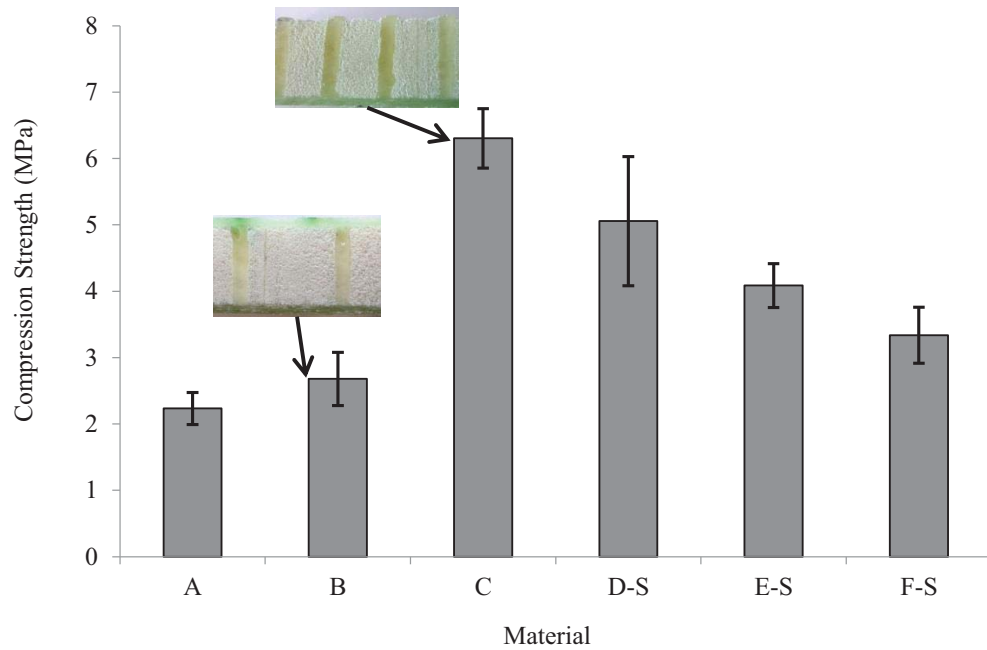


Figure 5.11: Summary of the compression strengths of the core materials.

5.3.2 Vertical, pyramidal and octet lattice

5.3.2.1 Carbon fiber reinforced Individual Columns

Figure 5.13 shows typical stress-strain traces following compression tests on individual struts with diameters of 2.5 and 3.0 mm. Each figure includes a trace following a test in which the fibers were threaded according to Configurations A and B in Figure 5.12.

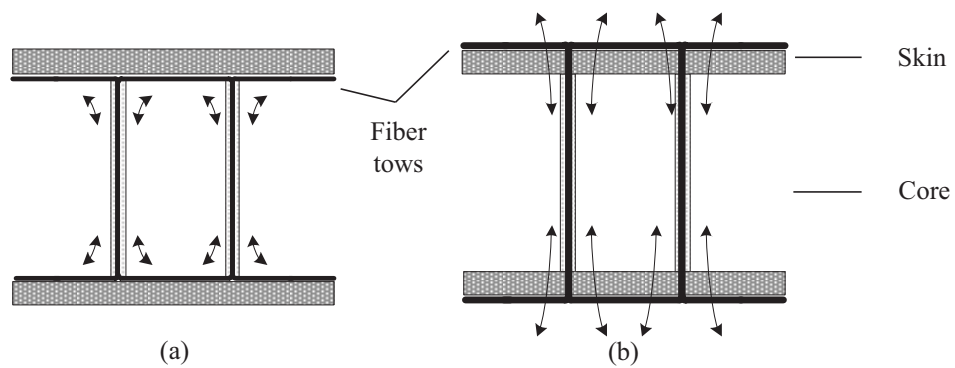


Figure 5.12: Schematic drawings of the two procedures used to thread the samples.

The stress-strain trace for the 2.5 mm diameter sample based on Configuration A increases in a linear fashion to approximately 60 MPa, before dropping and then increasing gently to approximately 95 MPa, prior to ultimate failure, Figure 6a. An examination of the test specimen during testing indicated that failure occurred as a result of interfacial failure between the horizontal tows and the inner skin (i.e. between those fiber tows that link adjacent columns and the facings). Fracture of this interface leads to the lateral movement of the column, as shown in the Photo (i) in Figure 5.13a.

Threading the fibers through the skins (Configuration B) greatly improves the properties of the composite. Here, the compression strength of the strut increases linearly to approximately 180 MPa, at which point the column buckles and the stress drops sharply to approximately 110 MPa. Further loading resulted in the force remaining roughly constant as cracks and splits developed with the region of initial buckling failure. Photograph (ii) in the inset in Figure 5.13a shows the failure process in a typical strut, where it is evident that the column has failed at its mid-point. Figure 5.13b shows the stress-strain traces for the 3 mm diameter columns. The trace for the sample based on Configuration A increases to a maximum of approximately 170 MPa, a point at which the strut begins to tilt sideways. The stress then increases slightly before it begins to drop rapidly as the upper interface failed and the sample tilted to one side, Photograph (i) in Figure 5.13b. Once again, anchoring the fibers to the skins leads to a significant increase in strength and much greater energy absorption, as characterized by the area under the stress-strain curve. Here, initial failure took the form of localized crushing, involving splitting and fiber micro-buckling at one end of the column. These failure processes continued up to a strain approaching 25%, at which point the column tilted and the stress dropped to zero. Photograph (ii) in Figure 5.13b

clearly shows that the composite has splayed out during fracture, absorbing significant levels of energy in the process.

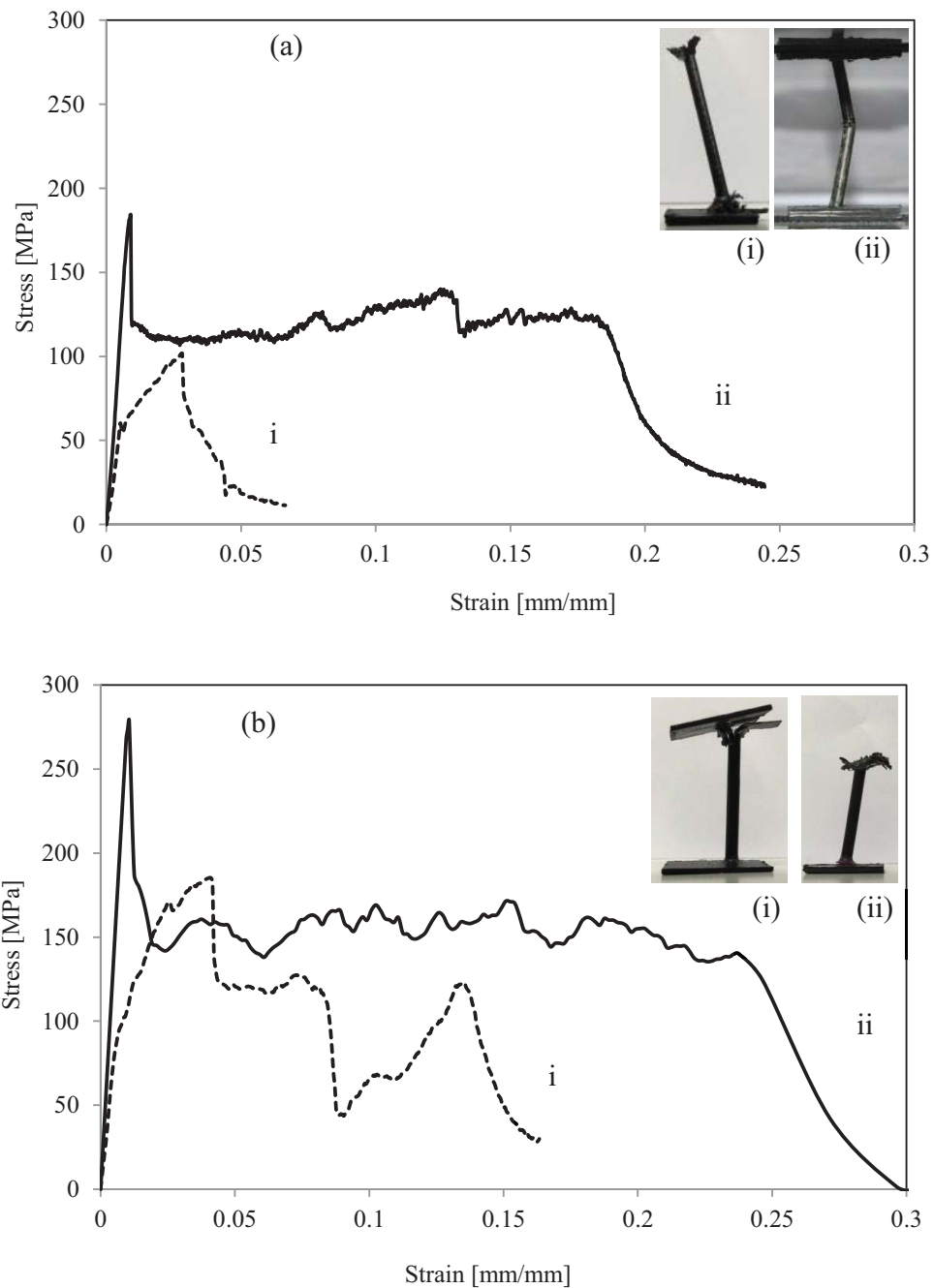


Figure 5.13: Stress-strain traces for individual columns (a) 2.5 mm diameter and (b) 3 mm diameter. $V_f = 0.42$. Dashed line = Configuration A and Solid line = Configuration B.

The influence of weave method on the mechanical properties of the vertical columns is also evident at different fiber volume fractions. Figure 5.14 includes a trace following a compression test on 4 mm sample, in which the fibers were threaded according to Configurations A and B. The fiber volume fraction was maintained at 0.28 for both thread configurations.

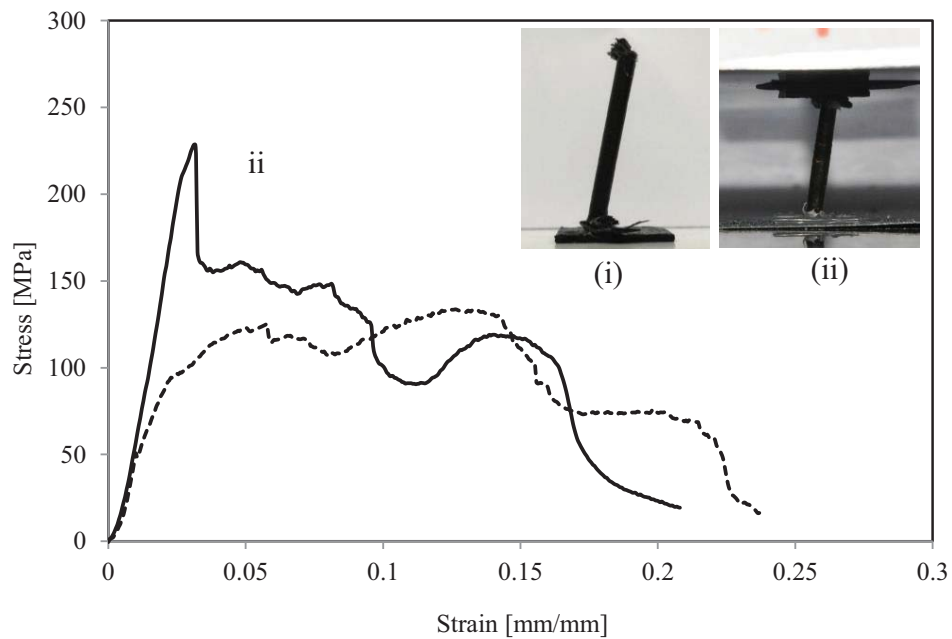


Figure 5.14: Stress-strain traces of individual columns of 4 mm diameter. $V_f = 0.28$.

Dashed line = Configuration A and Solid line = Configuration B

The trace for the sample based on Configuration A increases to a maximum of approximately 90 MPa, a point at which the strut begins to tilt sideways. The stress then increases slightly before it begins to fluctuate and subsequently drop, as upper interface failed and the sample tilted to one side, Photograph (i) in the insert in Figure 5.14. As observed earlier, anchoring the fibers to the skins leads to an improvement in strength. The compression strength of Configuration B strut increases linearly to approximately 225 MPa, at which point the column fails due to localized crushing at one end of the column.

Further loading resulted in a gradually decreasing force up to a strain approaching 20%, at which point the column tilted and the stress dropped to zero. Photograph (ii) in the insert in Figure 5.14 shows the failure process in a typical strut, where it is evident that the composite column has splayed out during fracture.

The influence of fiber volume fraction on the compressive properties of the individual columns is shown in Figure 5.15. Here, the compressive response of samples based on nominal fiber volume fractions of 0.14, 0.28 and 0.42 are presented as a function of the slenderness ratio (length/radius) of the column.

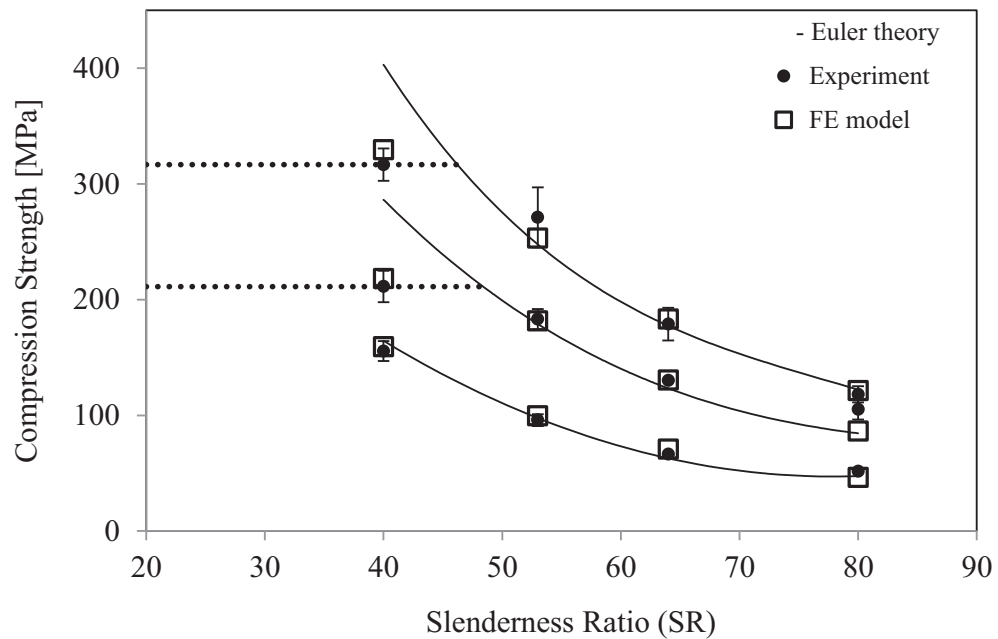


Figure 5.15: Variation of specific compression strength with slenderness ratio for single columns. The samples are based on Configuration B.

Clearly, the compression strength of the individual columns increases with decreasing slenderness ratio. As expected, the fiber volume fraction also plays a significant role, with the compression strength increasing by up to 250% in samples based on small diameters. Included in the figure are the values predicted by Euler buckling theory. Here, the critical

buckling stress for an orthotropic column is given by Equation 3.62. The solid lines in Figure 5.15 show the predictions of Euler theory. An examination of the figure indicates that the simple model accurately predicts the strength of the samples based on intermediate and high values of slenderness ratio. Indeed, for the lowest fiber volume fraction, $V_f = 0.14$, it is evident that Euler buckling theory is accurate over the entire range of configurations considered here. Interestingly, the model breaks down for the 4 mm diameter samples based on fiber volume fractions of 0.28 and 0.42. Here, failure was associated with crushing at one end of the column rather than buckling. Assuming that this is a characteristic property of the material for a given fiber volume fraction, the horizontal dotted lines in the figure have been added to reflect this. Also included in the figure are the predictions of the finite element model. Here agreement between the numerical predictions and the experimental data are extremely good across the range of specimen geometries considered. It is worth noting that the FE model also predicts the change in failure mode from a buckling-type failure in high slenderness columns to one associated with crushing in lower SR samples.

5.3.2.2 Carbon fiber reinforced vertical truss core

Figure 5.16 shows typical stress-strain curves for truss cores based on 3 and 4 mm diameter columns. Given that the applied stress is calculated from the planar area of the truss core rather than the diameter of the column, the maximum stresses in Figure 5.16 are clearly much lower than in the previous figures. As was the case for the simple columns, threading the fibers through the skins serves to greatly enhance the mechanical properties of the core. For example, this stitching technique increases the compressive strength of the 3 mm diameter system by 150% and the 4 mm diameter core by almost 100%.

Figure 5.16a includes photos of the truss cores during the compression process. Loading Configuration A results in skin-core interfacial failure, causing the columns to splay outwards as the crosshead displacement increases. This is reflected in the low values of stress during the intermediate stages of the test. In contrast, many of the columns in Configuration B failed at or close to their mid-points, probably as a result of some initial buckling failure. Failure in the 4 mm diameter samples (Configuration A) was again associated with interfacial failure at the inner skin surfaces, with lateral movement of the columns being clearly evident in Figure 5.16b. In contrast, crushing at the truss extremities was the predominant mode of failure in the 4 mm 'B' samples, a finding that agrees with the earlier observations following tests on the single columns.

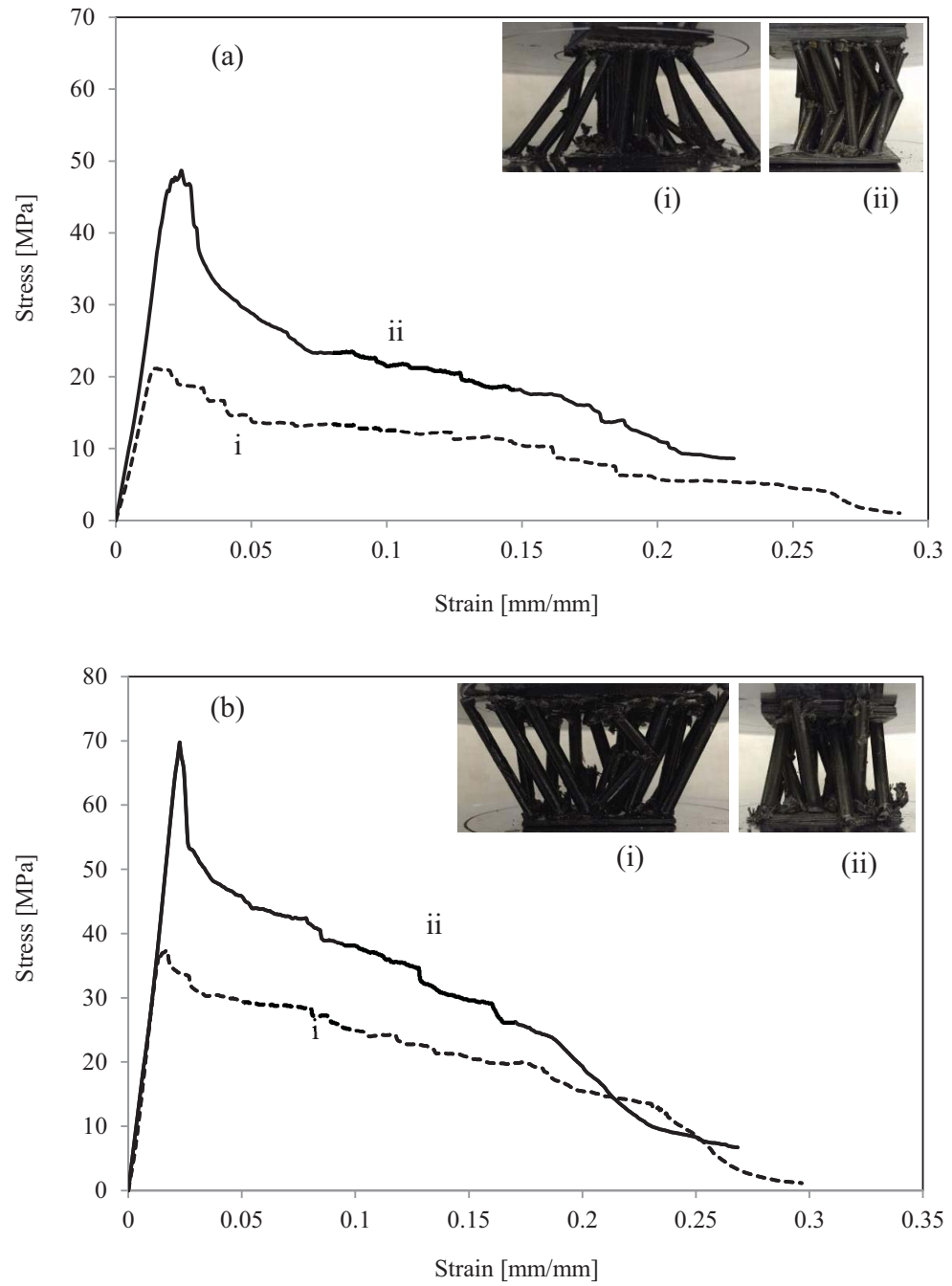


Figure 5.16: Stress-strain traces for multiple columns (a) 3 mm diameter and (b) 4 mm diameter. $V_f = 0.28$. Dashed line = Configuration A and solid line = Configuration B.

Figure 5.17 summarizes the specific compression strengths of the truss cores as a function of slenderness ratio, where the compression data for both configurations are divided by the

relative density, in order to account for differences in the planar arrangement of the truss in the four cores. From the figure, it is again clear that anchoring the columns to the skins has a strongly beneficial effect. Included in the figure are the predictions associated with Euler buckling theory and the finite element analyses.

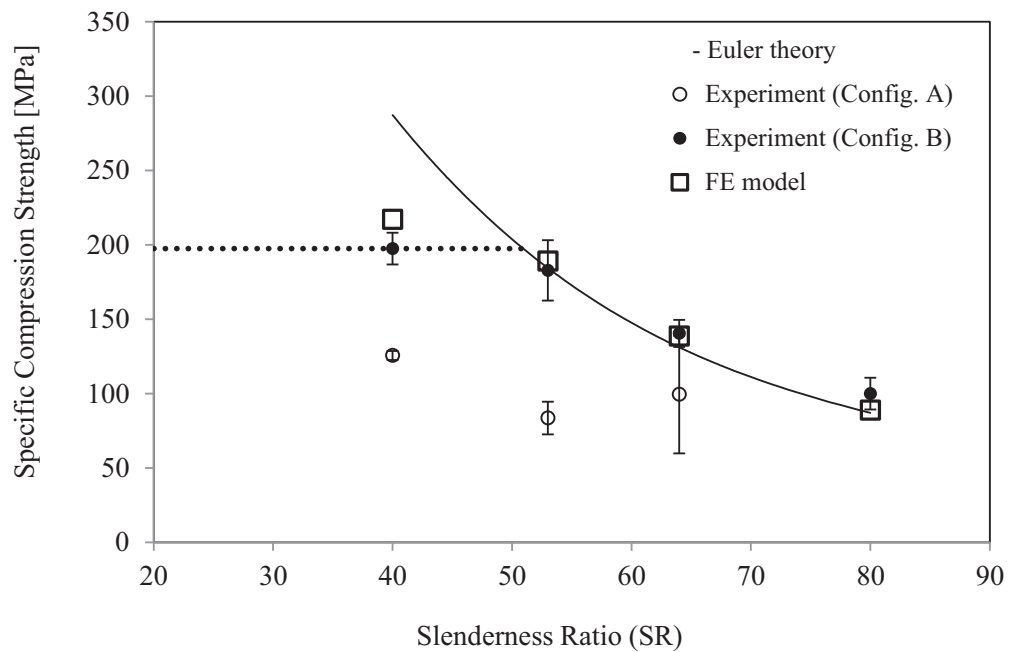


Figure 5.17: The variation of specific compression strength with slenderness ratio for the truss cores. $V_f = 0.28$.

Once again agreement between the predicted values of maximum compression strength and slenderness ratio is very good for intermediate and high values of SR. The Euler model breaks down at lower values of SR, again due to the fact that failure occurs in a crushing mode, rather than buckling, as observed in the remaining samples. The FE model again appears to accurately predict the compression strengths of the cores. As before, a horizontal dashed line is included to reflect crushing at a constant stress at low values of SR. It is interesting to note that the curve for System B virtually collapses onto the trace for the

single columns based on a fiber volume fraction of 0.28, shown in Figure 5.15, suggesting that the response of the core mirrors that of the individual members.

Predictions from FE models show good agreement with test results in terms of stress-strain traces beyond the elastic region as illustrated in Figure 5.18 for the truss core samples. Photographs (i) and (ii) in the insert in Figure 5.18 show the typical failure process based on experiments and FE models. In the photographs it is noted that there is good agreement between the experimentally observed failure mode and the simulated FE models in which the slender columns fail at their mid points due to elastic buckling while at lower SR values failure occurs in a crushing mode.

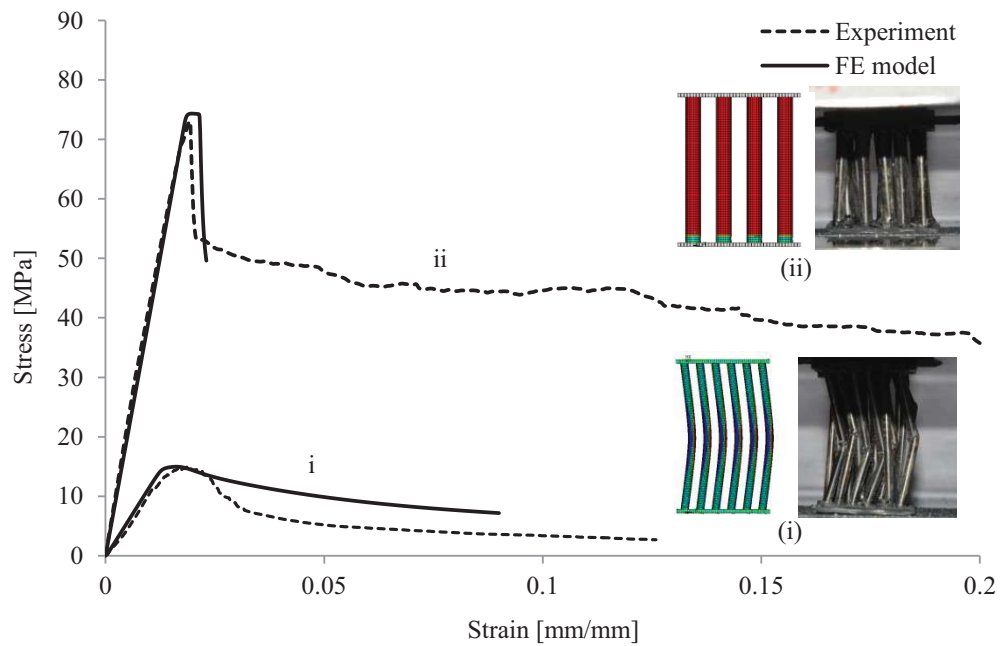


Figure 5.18: Stress-strain traces for multiple columns (i) 2 mm diameter and (ii) 4 mm diameter. $V_f = 0.28$. Dashed line = experiment and solid line = FE model.

Figure 5.19 summarizes the specific energy absorption values of the truss cores. Here, the energy absorbed by the core during the crushing process was normalized by the mass of the core (excluding the skins) to yield SEA values in kJ/kg.

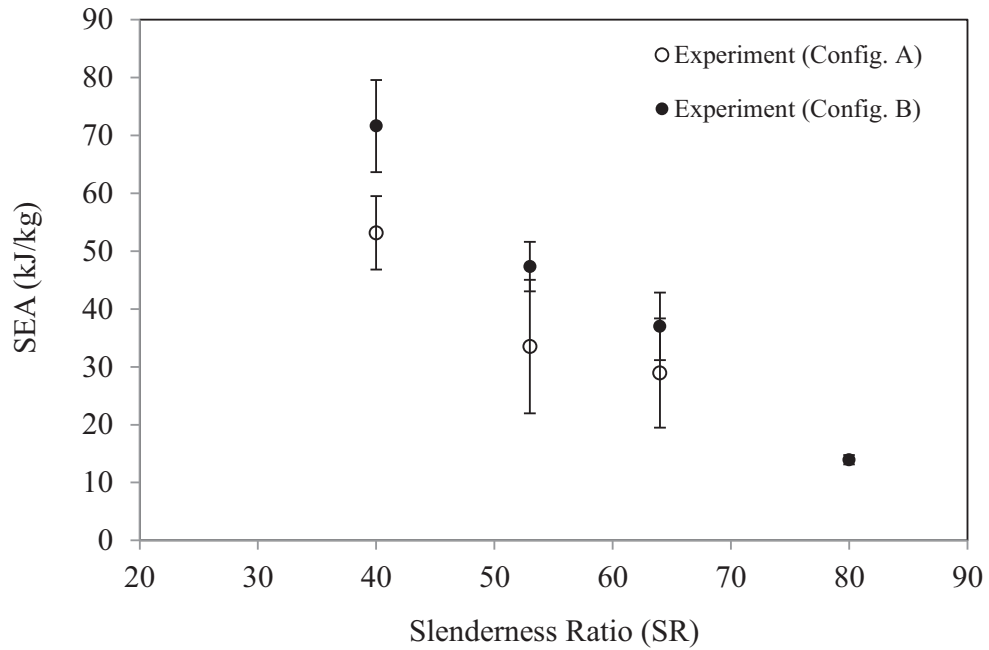


Figure 5.19: The variation of SEA as a function of slenderness ratio for the truss cores.

Decreasing the slenderness ratio clearly has a significant effect on the measured values of energy absorption, with the SEA of samples based on Configuration B increasing from 14 to 72 kJ/kg over the range of truss geometries considered here. The benefits of anchoring the trusses to the skins are clearly apparent, with Configuration B offering values up to 40% higher than Configuration A. It is likely that the value of 72 kJ/kg could be increased significantly by increasing both the relative density of the 4 mm diameter core (the current value is approximately 35%) and the fiber volume fraction within the individual trusses.

5.3.2.3 Natural fiber reinforced Individual Columns

Initial testing focused on understanding the influence of fiber volume fraction on the compression properties of individual struts. Here, 3 and 4 mm diameter columns based on fiber volume fractions between 2 and 12% were tested at a crosshead displacement rate of 2 mm/minute. For comparative purposes, tests were also conducted on pure resin samples, shown as a fiber volume fraction of 0%. Figure 5.20a shows typical stress-strain curves following tests on a 3 mm diameter column. The force for the pure resin sample initially increases in a linear fashion, before the onset of a region of non-linearity, prior to reaching a peak at approximately 19 MPa. Beyond this maximum value, the force starts to drop rapidly as the sample starts to plastically deform and then buckle, as shown in the photograph in Figure 5.21a. Clearly, the initial stiffness of the samples also increases with fiber content.

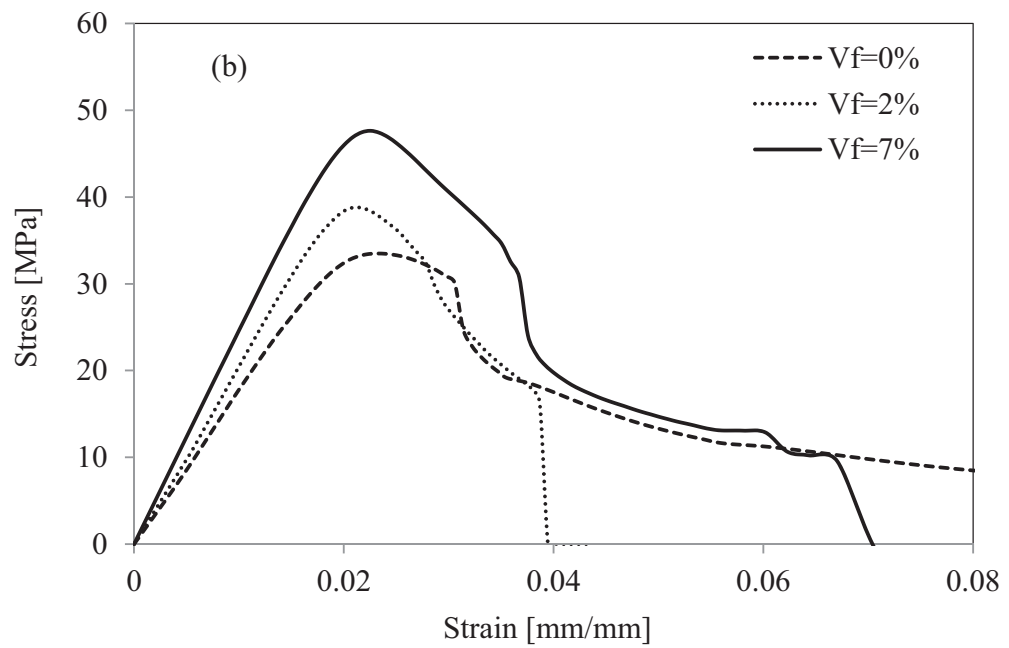
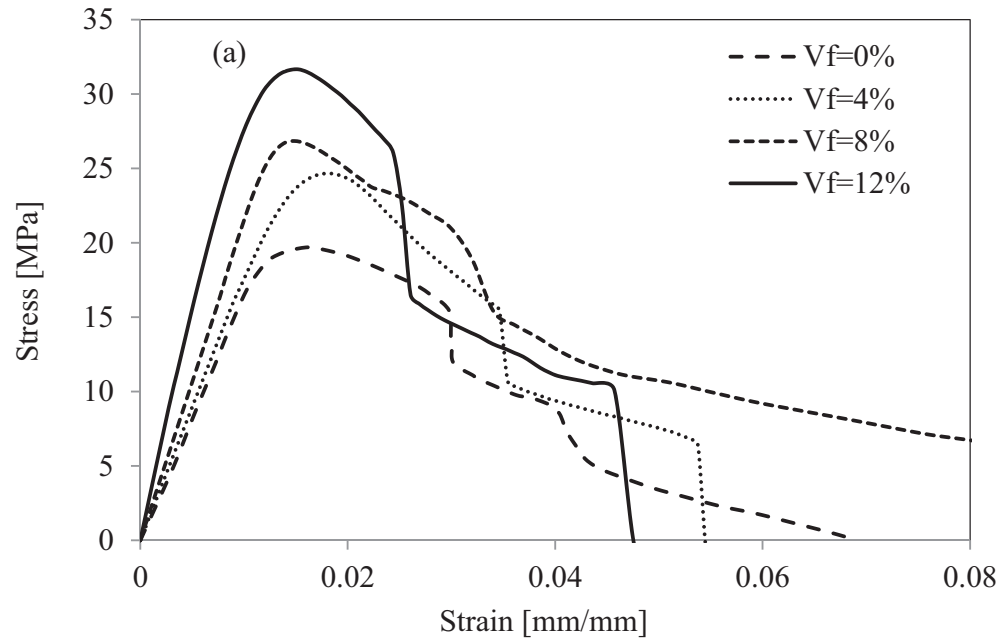


Figure 5.20: Typical stress-strain traces following compression tests on single columns based on different fiber volume fractions (a) 3 mm diameter columns (b) 4 mm diameter columns.

As expected, increasing the volume fraction of fibers within the column serves to increase the load-carrying capability of the sample. For example, adding 4% fibers resulted in a 25% increase in strength, whereas introducing 8% of fibers resulted in a 36% increase in strength relative to the plain resin sample. Previous investigations by the authors have shown that values of fiber volume fraction in excess of 50% can be achieved, suggesting that greater improvements than those apparent in these stress-strain traces can be achieved. The shape of the stress-strain traces are all reasonably similar, with failure being associated with significant out-of-plane deformation and buckling, as shown in the photographs in Figures 5.21b and 5.21c. Increasing the column diameter from 3 to 4 mm results in a 70% increase in the load-carrying capability of the plain resin, Figure 5.20b.

Here again, plastic deformation within the resin and buckling of the strut represented the fundamental failure processes in these samples, Figure 5.22. Again, increasing the fiber volume fraction to 7% served to increase the load-bearing ability of the strut, with an increase of approximately 42% being apparent in Figure 5.20b. Overall, the shape of the stress-strain traces for the 4 mm diameter columns are similar to those of their 3 mm counterparts, with failure involving global buckling and fracture of the column, as shown in Figure 5.22c.

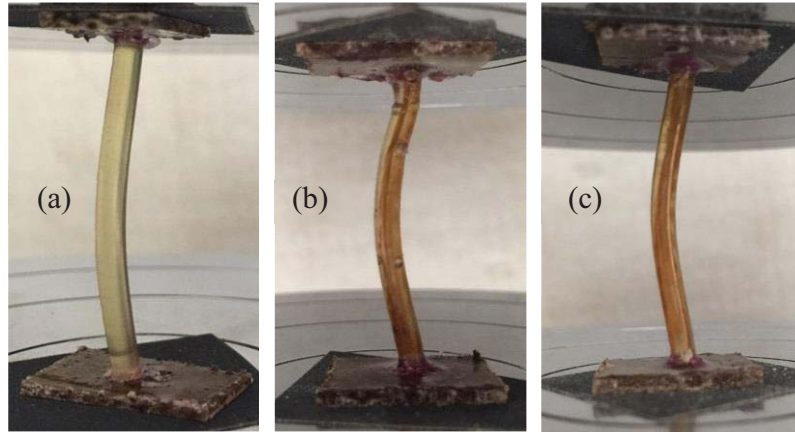


Figure 5.21: Photographs of individual 3 mm diameter columns at various stages of testing:
(i) neat resin, (ii) $V_f = 8\%$ and (iii) $V_f = 12\%$.

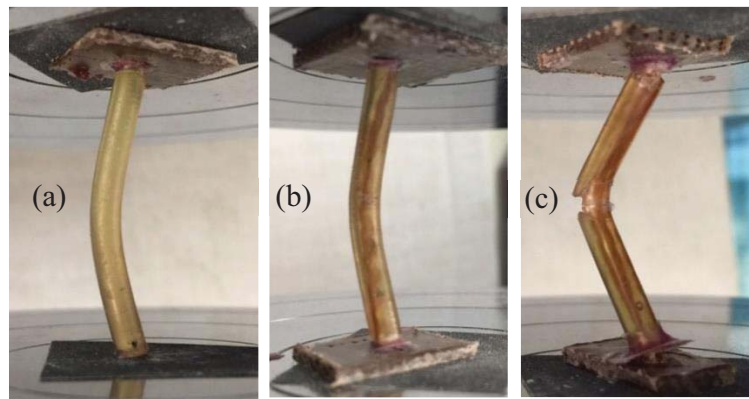


Figure 5.22: Photographs of individual 4 mm diameter columns during testing:
(i) neat resin, (ii) $V_f = 5\%$ and (iii) $V_f = 7\%$.

Figure 5.23 shows the variation of the compression strength of the 3 and 4 mm diameter columns as a function of fiber volume fraction. As noted previously, increasing the fiber content serves to increase the load-carrying capability of the struts.

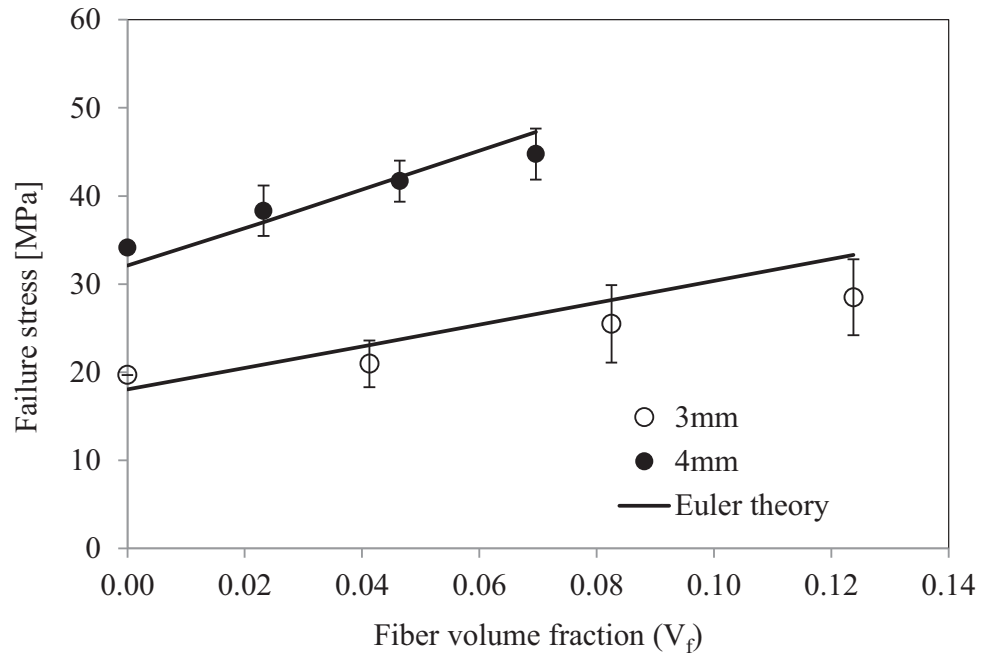


Figure 5.23: The variation of failure stress with fiber volume fraction for the 3 and 4 mm diameter columns. The solid lines correspond to the predictions of Euler buckling theory based on the properties at a given fiber volume fraction.

Given that all of the columns initially fail in a buckling mode, it should be possible to predict their mechanical properties using Euler theory. The value of E_x (modulus in the fiber direction) was predicted using the Rule of Mixtures approach described in Chapter 3 (Equation 3.6). The modulus of the resin E_r was taken as 3.5 GPa. The shear modulus of the jute fiber/epoxy composite was estimated using the same approach (using Equation 3.11). Previous work has shown that the elastic modulus of jute fibers is dependent on the diameter of the fiber bundle and can be up to 28 GPa [1]. In this study, E_f was taken as 28 GPa and the shear modulus of the jute fiber was taken to be 36% of the value of E_f , based on values presented in an earlier study [2]. The shear modulus of the epoxy resin was taken as 1.3 GPa. The predictions yielded by this simple model are included in Figure 5.23,

where it is evident that this simple approach is reasonably successful in predicting the trends in the experimental data.

5.3.2.4 *Natural fiber reinforced truss Cores*

Figure 5.24 shows typical stress-strain traces following compression tests on cores based on truss diameters between 2.5 and 4.0 mm. All three traces exhibit an initial linear region, with the stress increasing to a maximum, followed by a region over which the stress drops as the elements within the core start to deform, buckle and ultimately fracture. As expected, the compression strength increases as the truss diameter is increased.

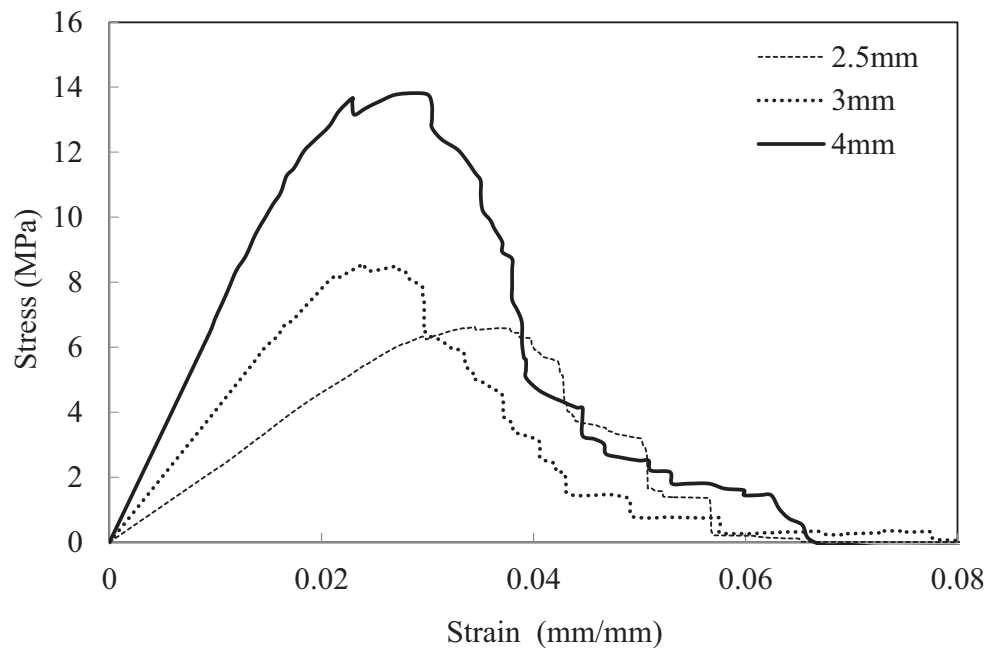


Figure 5.24: Typical stress-strain traces following compression tests on core structures based on arrays of columns with diameters of 2.5, 3 and 4 mm.

Figure 5.25 shows images of the deformation process in the 3 mm diameter samples. Initial loading causes the columns to move laterally, with some elements moving in opposite directions. Continued loading results in buckling of the individual columns and their ultimate fracture at their mid-length locations. Initial inspection of a number of columns

highlighted the regions of fracture at their lower ends, as resin-rich regions along the circumference of the columns fractured at the base.

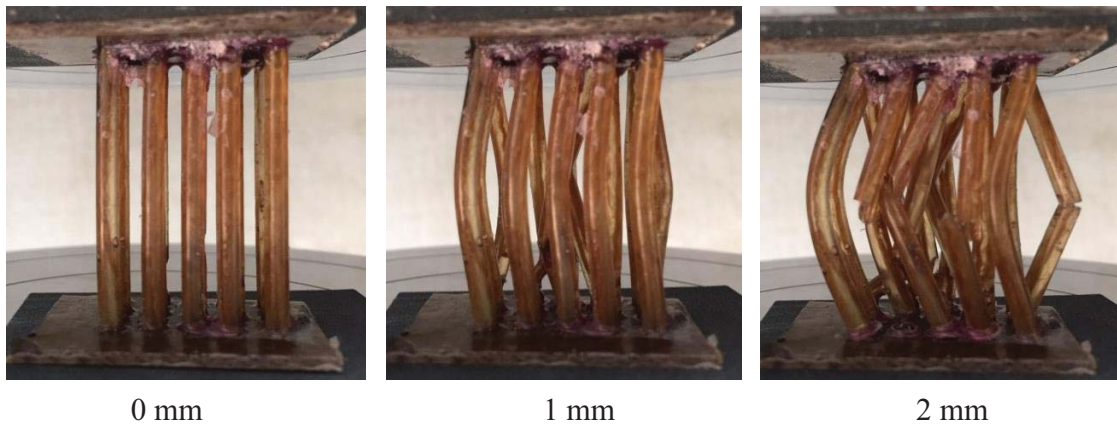


Figure 5.25: Stages of deformation in truss core based on 3 mm diameter columns. The crosshead displacement is shown under each figure.

Similar deformation mechanisms are apparent in the 4 mm diameter columns shown in Figure 5.26. Once again, buckling of the individual struts, followed by their fracture were the failure mechanisms observed during testing.

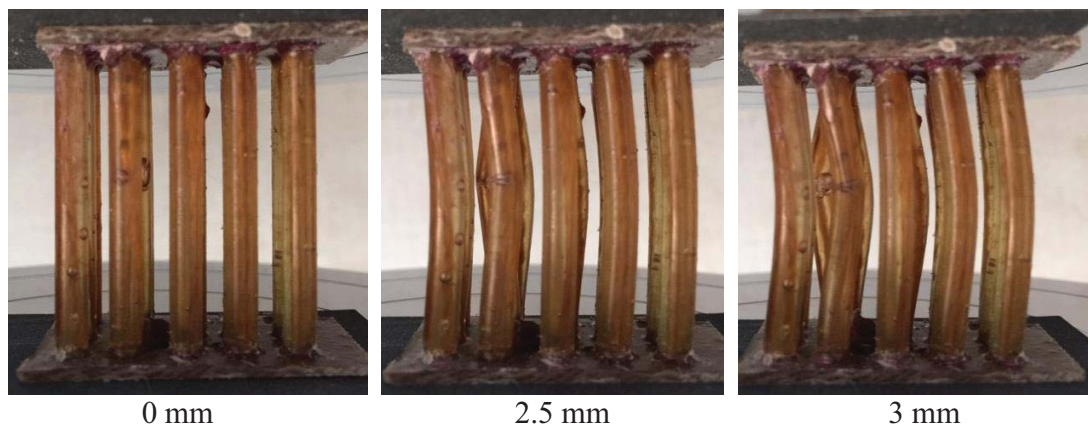


Figure 5.26: Stages of deformation in truss core based on 3mm diameter columns.

The crosshead displacement is shown under each figure.

Figure 5.27 shows the variation of the compression strength of the core materials with column diameter. As before, the compression strength clearly increases rapidly with increasing column diameter. For example, the average strength of the core based on 2 mm diameter columns is approximately 3.6 MPa, whereas that for the 4 mm diameter columns is 15 MPa. Included in the figure is the prediction offered by Euler buckling. As before, this simple approach appears to capture the trends in the experimental data and is useful for predicting the response of these types of truss cores.

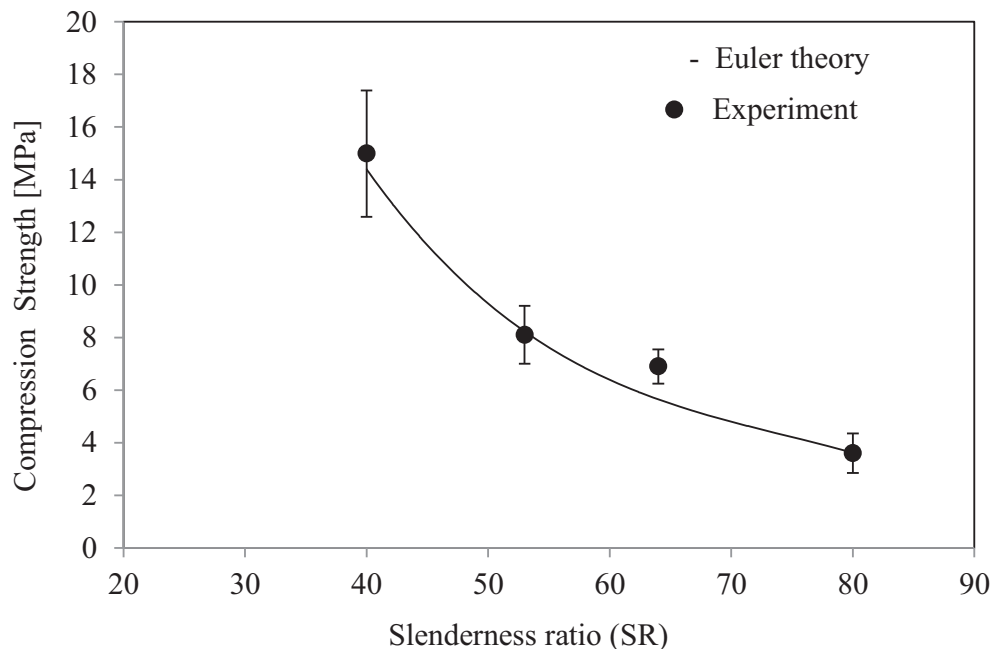


Figure 5.27: The variation of compression strength with slenderness ratio for the truss cores. The solid line corresponds to the prediction offered by Euler theory.

The compressive properties of the truss cores were normalized by their relative densities to yield the specific compressive properties shown in Figure 5.28. Also included in the figure are the data corresponding to tests on individual columns based on equivalent fiber volume fractions. Given that the latter results correspond to tests on individual columns, they were not normalized in any way. It is interesting to note that the core structures appear to loosely

collapse onto the single column data, suggesting that the response of the cores is determined by the behavior of the individual columns. This suggests that the mechanical response of larger core materials can be predicted from the characteristics of the individual elements.

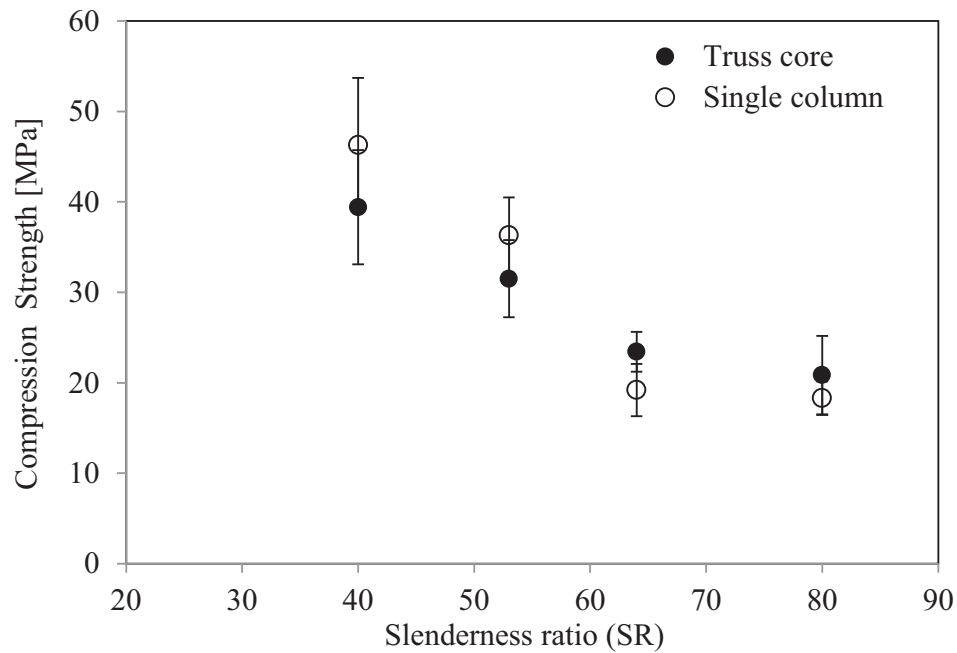


Figure 5.28: The variation of the compression strength of the core structures with column slenderness ratio.

5.3.2.5 *Pyramidal and octet lattice*

The results of testing and modeling the all-composite pyramid-based structures are presented here. During the fabrication process, although the same fiber tows extended through all of the trusses in the structure, they were not anchored to the skins and are therefore likely to offer inferior properties to samples in which the tows were threaded through the skins. Figure 5.29 compares the specific strengths of the plain and modified pyramidal structures with the predictions of the corresponding finite element models. Interestingly, the experimental values of specific strength for the modified structures are

equal to or lower than the standard four-membered structures. The figure shows the typical failure processes in plain and modified specimens based on a fiber volume fraction of 12%. The lateral movement of the bases of the trusses is evident in the plain structure, highlighting the low strength of the interface in this critical location. The vertical truss in the modified sample underwent crushing during the test and slight lateral movement of the trusses is again in evidence.

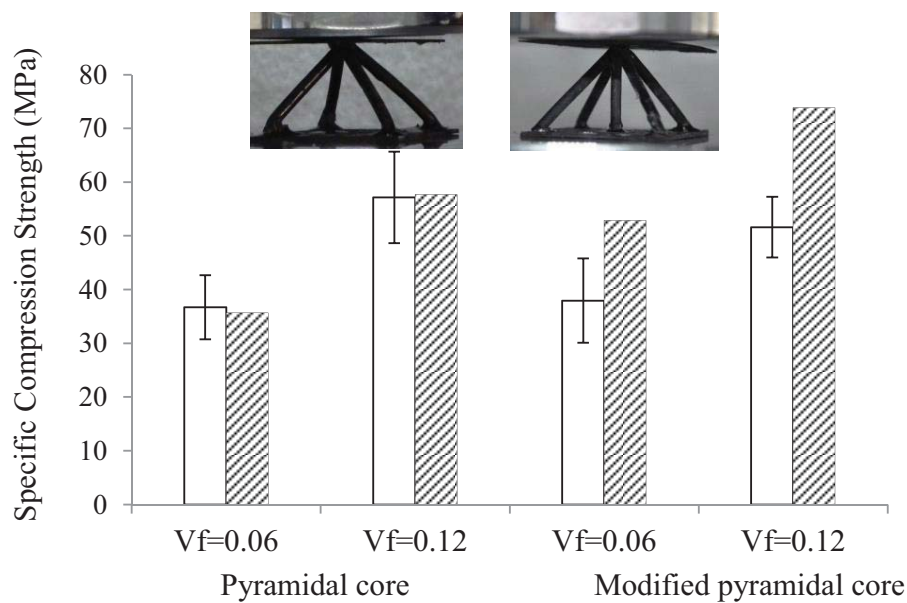


Figure 5.29. Summary of the specific strengths of the pyramidal and modified pyramidal structures. The photos show plain and modified samples during testing. Open columns = experiment and hatched columns = FE modeling.

As expected, increasing the fiber volume fraction serves to increase the load-carrying capability of the structures. Agreement between the FE predictions and the experimental data is relatively poor for the modified pyramids, with the model over-predicting the test results by up to 50%. These errors are likely to be associated with the fact that these pyramidal designs are based on the weaker of the two configurations. However, given the

ability of the FE model to accurately predict the anchored vertical truss cores in Figure 5.17, it is believed that the FE predictions in Figure 5.29 are more representative of the mechanical performance of pyramids based on Configuration B. It is also interesting to note that the FE model predicts that the modified structures offer superior specific properties. There is clearly some distortion to the local fiber architecture at the junction points. For example in the vertical truss structures, the fibers pass from the vertical direction to the horizontal direction as they traverse the skins. In terms of finite element modeling, this is a complex problem and is beyond the scope of this research. In spite of this simplification, agreement between the FE model and experimental data remains good. Figure 5.30a shows an octet truss structure prior to testing. Here, the continuous fiber tows did not connect through the skins and were not inter-twined at the mid nodes. Therefore, upon loading, the relatively weak resin region between the tows fractured, causing the structure to fail at mid-thickness locations, as shown in Figure 5.30b. The resulting specific strengths for structures based on fiber volume fractions of 3.5, 7.0 and 10.6% were 19.1, 25.0 and 25.7 MPa respectively, well below the predicted FE values of 29.2, 35.4 and 41.5 MPa respectively.

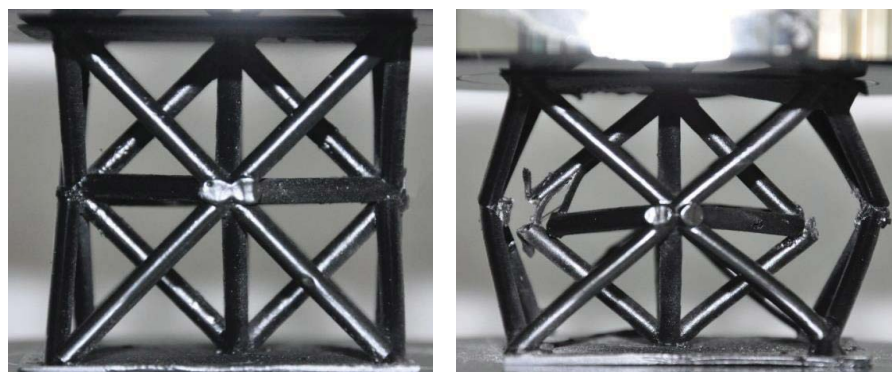
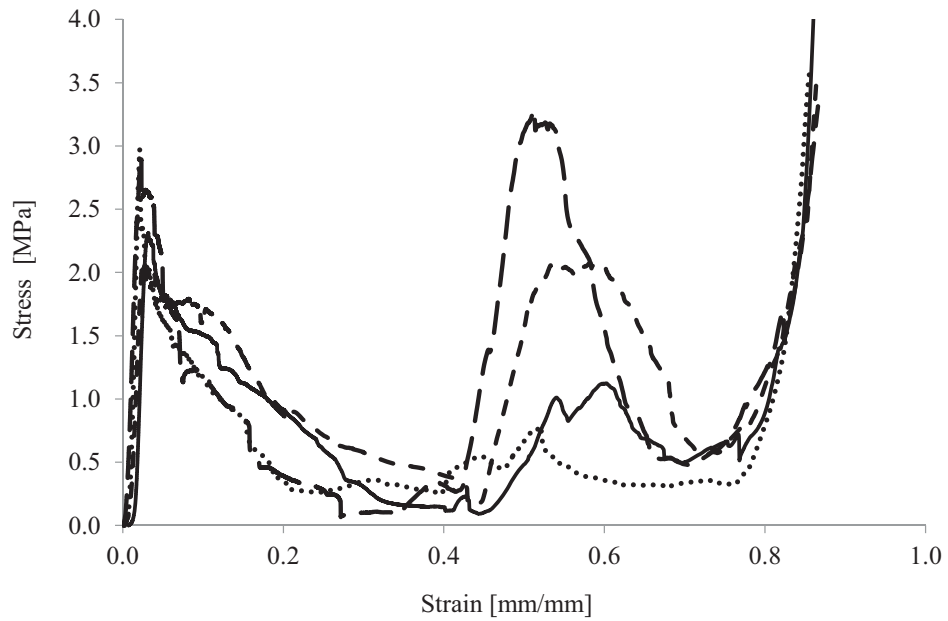


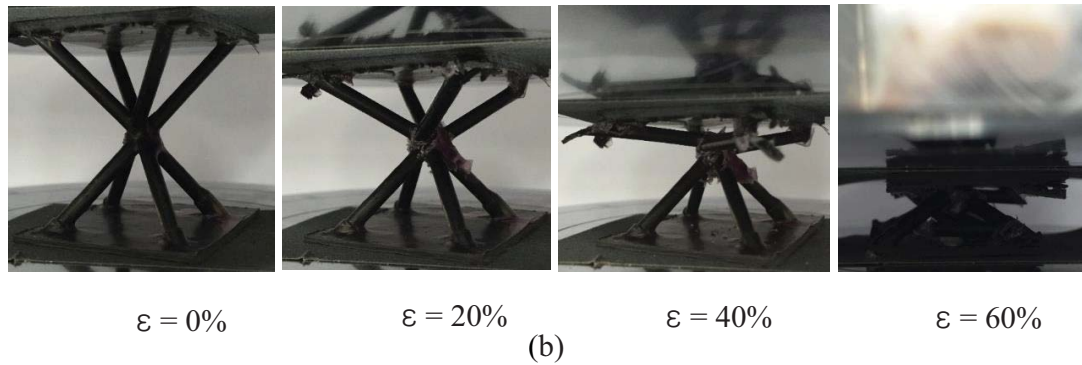
Figure 5.30: Photographs of an octet truss structure (a) prior to testing and (b) following compression testing. The sample height is 56 mm.

5.3.3 BCC, BCCz, FCC and F₂BCC lattice

Figure 5.31 shows the stress-strain traces following tests on the BCC lattice structures, from where it is clear that there is a reasonably high level of repeatability, particularly in the early stages of the test. All traces exhibit an initial linear region prior to reaching a maximum at stress values between 2.2 and 2.9 MPa. The stress then drops steadily as the lattices begin to fail, typically at the uppermost nodes between the core and the skin. The stress reaches a minimum before increasing rapidly to values that can, in certain cases, exceed the initial strength of the structure. This second peak is associated with loading the lower pyramid in the BCC lattice once the crosshead has reached roughly the mid-point of the lattice structure, as shown in the photographs presented in Figure 5.31b. This second loading regime then continues until the lowermost nodes begin to fail, at which point the entire structure collapses. Clearly, there is some scatter in the behavior of the lattices during this second phase of loading, with one structure resisting a stress of over 3.2 MPa and another just 0.75 MPa. The lower value is associated with nodal failures occurring in the upper and lower pyramids during the initial loading cycle. Clearly, when the crosshead reaches the height of the lower pyramid, its properties are already significantly degraded. In the final part of the test, the stress increases very rapidly as the lattice is crushed between the two steel platens of the test machine.



(a)

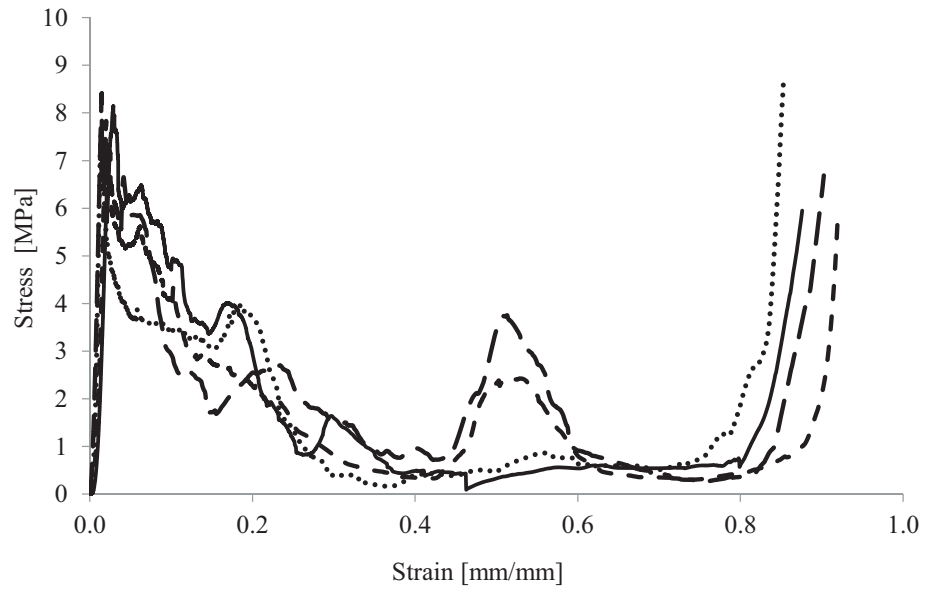


(b)

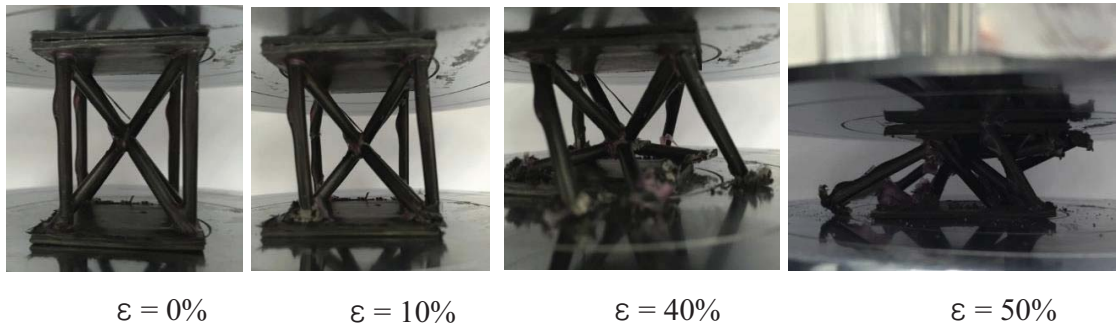
Figure 5.31. (a) Stress-strain traces for the BCC lattice structure (b) photographs showing the deformation modes with increasing strain.

Figure 5.32 shows the stress-strain curves for the BCCz structure, where it is clear that the inclusion of four vertical struts greatly enhances the compression strength of the lattice. Here, the initial stress increases linearly to values exceeding 7.5 MPa, before dropping steadily as the vertical struts and the angled struts fail at the skin-core interface, as observed previously. With continued loading, the stress in some samples begins to increase to values

observed previously in the BCC structure, as in this case, the upper pyramid is loaded and ultimately fails, Figure 5.32b.



(a)

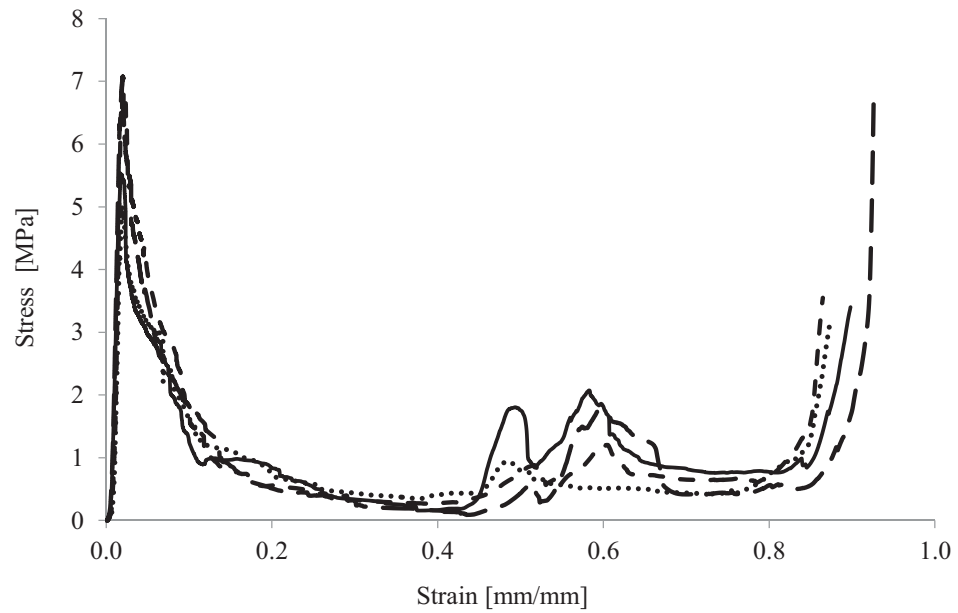


(b)

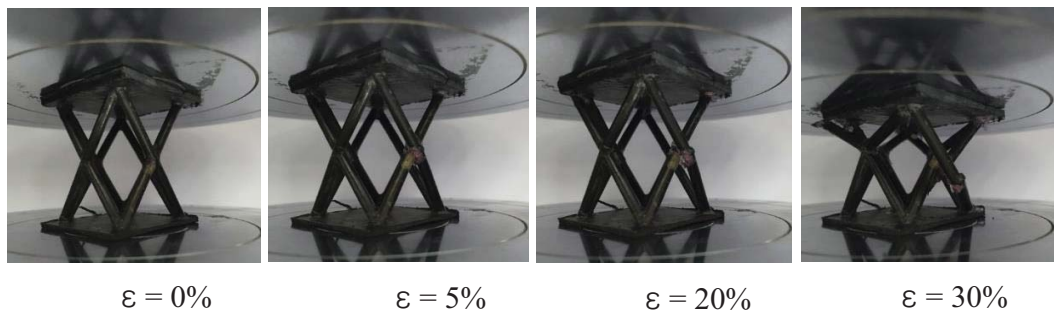
Figure 5.32. (a) Stress-strain traces for the BCCz lattice structure (b) photographs showing the deformation modes with increasing strain.

Figure 5.33 presents the stress-strain traces and associated photographs for the FCC structure, where the initial stress increases to values of up to 7 MPa, i.e. similar to those observed in the BCCz lattice. The stress then drops sharply as the struts fail in a global buckling mode, with some mid-nodes failing, due to the fact that the fibers are not

intertwined at these locations. The remaining portions of the stress-strain traces are similar to those observed in Figure 5.32, with a small peak being evident at a strain of approximately 0.5. This secondary peak is associated with the crosshead loading the lower triangular structures on the four walls of the unit cell.



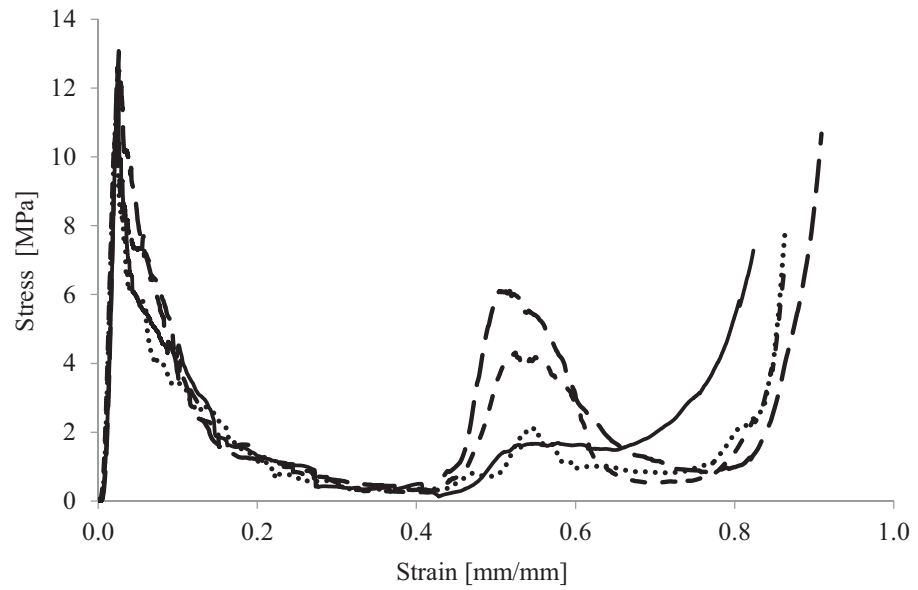
(a)



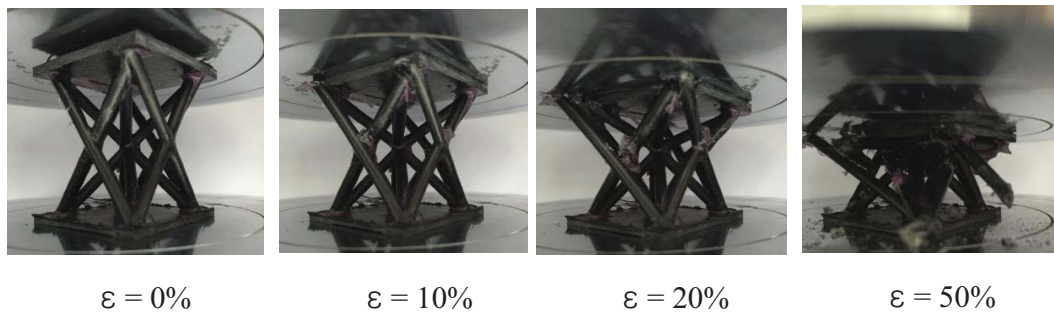
(b)

Figure 5.33. (a) Stress-strain traces for the FCC lattice structure (b) photographs showing the deformation modes with increasing strain.

Finally, the F_2BCC structures, shown in Figure 5.34, offer the highest compression strengths of the four lattices considered in this study. Here, the initial part of the stress-strain trace increases to a peak value of up to 13 MPa before dropping as the struts in the four walls fail in a global buckling with mid-nodes failing. Following this, some of the joints at the skin-core interface begin to fail. The second peak in the traces is associated with loading both the lower pyramid as well as the triangular structures on the vertical faces of the cell. The fact that the maximum stress recorded during this part of the test is greater than that recorded on the other samples, is due to the fact that more sub-structures are loaded during this part of the compression process.



(a)



(b)

Figure 5.34. (a) Stress-strain traces for the F_2BCC lattice structure (b) photographs showing the deformation modes with increasing strain.

Figure 5.35 summarizes the elastic modulus values of the four lattice structures, where it is clear that the F_2BCC lattice structure offers the highest modulus values. Included in the figure are the predictions offered by the finite element model and the analytical models presented above. It is clear that in all cases, the models over-predict the experimental values. It is also evident that there is excellent agreement between the analytical and finite

element models in all four cases. The differences between the measured and predicted modulus values are likely to be due to errors associated with using the crosshead displacement to determine the strain and also discrepancies between the assumed and actual boundary conditions at the strut-skin interface. In spite of these errors, the models correctly predict the general trends in the experimental data (i.e. the BCC is the least stiff and the F₂BCC is the stiffest).

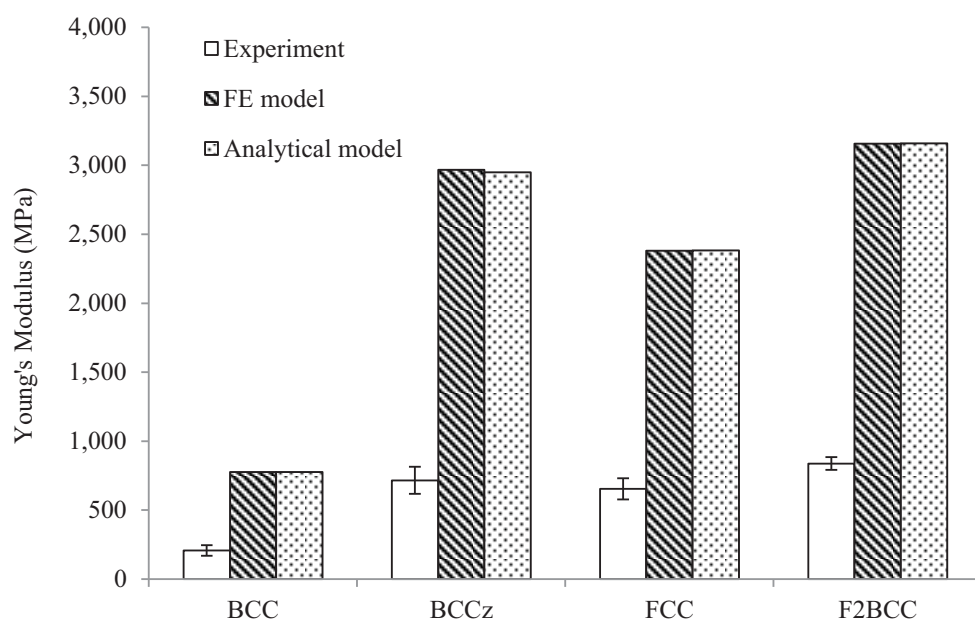
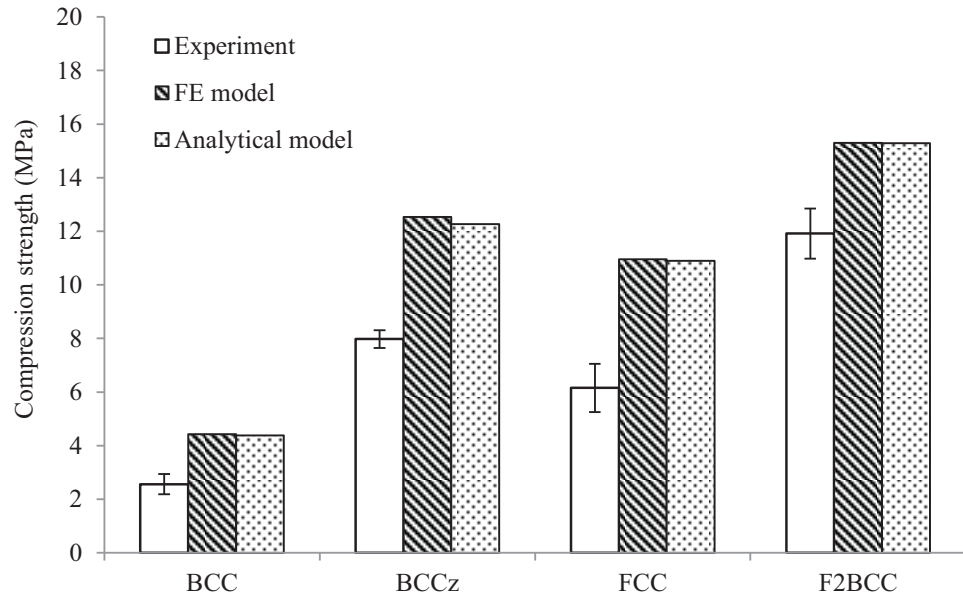


Figure 5.35. Summary of the Young's modulus properties of the four lattice structures. Included in the figure are the experimentally-determined values of modulus as well as those predicted by the analytical and FE models,

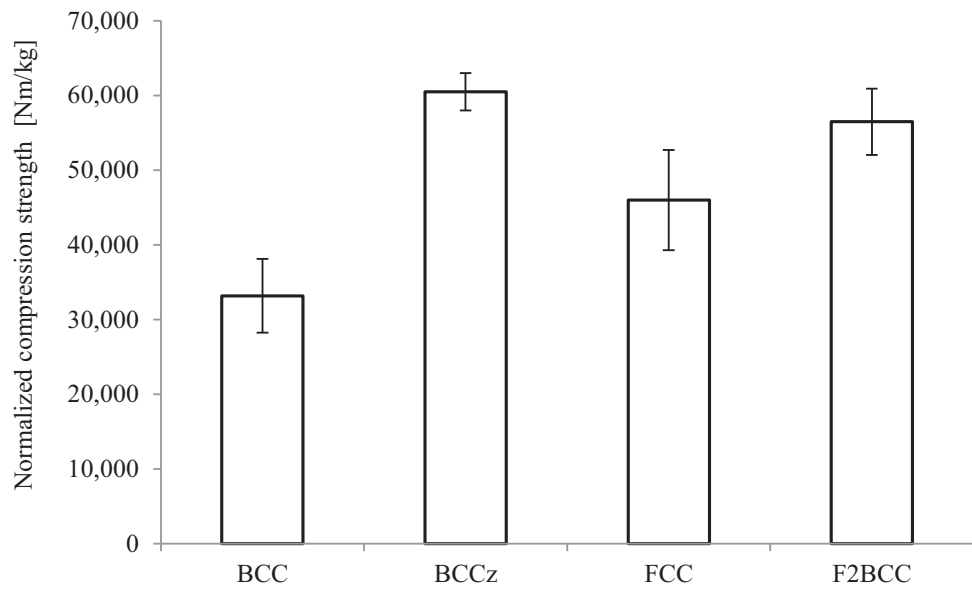
Figure 5.36a compares the experimentally-determined values of the compression strength of the four lattices with the predictions offered by both the analytical analysis and the FE model. The elastic buckling loads for each of the examined structures were higher than the predicted plastic microbuckling loads. Therefore, all of the structures were predicted to fail due to plastic microbuckling and these results are presented in Figure 5.36a. It is evident

that the F₂BCC structure offers the highest strength of the four designs considered in this study, with the average value being 12 MPa. The BCCz structure, with its four vertical members offers the second highest strength, with values averaging 8 MPa. In contrast, the BCC lattice offers a relatively low resistance to compressive loading, with the properties averaging just over 2.5 MPa. An examination of the figure indicates that the analytical and finite element models over-estimate the measured values of compression strength. The disparity between the measured and predicted values are likely to be associated with the presence of defects in the lattices and fiber distortion in the nodal regions. It is interesting to note, however, that the models correctly rank the four lattices in terms of their maximum strength. Agreement between the finite element models and the analytical solutions is very good, with the greatest error being less than four percent.

Given that the relative densities of the four lattices differ greatly, a more appropriate comparison can be made by determining the specific compression strengths by dividing the measured strengths by their respective density. The resulting values, shown in Figure 5.36b, indicate that when normalized with respect to relative density, the overall differences between the lattices are reduced. Here, the BCCz offers the highest specific properties, with the BCC continuing to offer the lowest values. The values for the BCCz and F₂BCC structures compare favorably with published data on a range of core materials. For example, crosslinked PVC foams typically offer values between 11 and 30 kNm/kg [3], aluminum honeycomb structures based on two densities of an A3003 alloy have been shown to exhibit values between 46 and 55 kNm/kg [4] and a Nomex honeycomb, with a density of 48 kg/m³, has been shown to offer a value of approximately 29 kNm/kg [5].



(a)



(b)

Figure 5.36. (a) Comparison of the compression strengths of the four lattice structures and (b) comparison of the specific compression strengths (experimental data) of the lattices.

The specific energy absorption values of the lattices structures were characterised by dividing the area under the load-displacement trace by the mass of the lattice structure

(excluding the skins). Figure 5.37 summarizes the resulting values of SEA for the structures tested in this study. The BCCz structure offers the highest specific energy absorption characteristics of the four lattices, with values averaging 80 kJ/kg. This is an encouraging value, suggesting that these particular structures are effective energy-absorbing systems. The energy-absorbing capability of the F₂BCC is slightly lower than that associated with its BCCz counterpart, with the average value being approximately 75 kJ/kg. The BCC structure offers the lowest values of SEA, with the average being just over 43 kJ/kg.

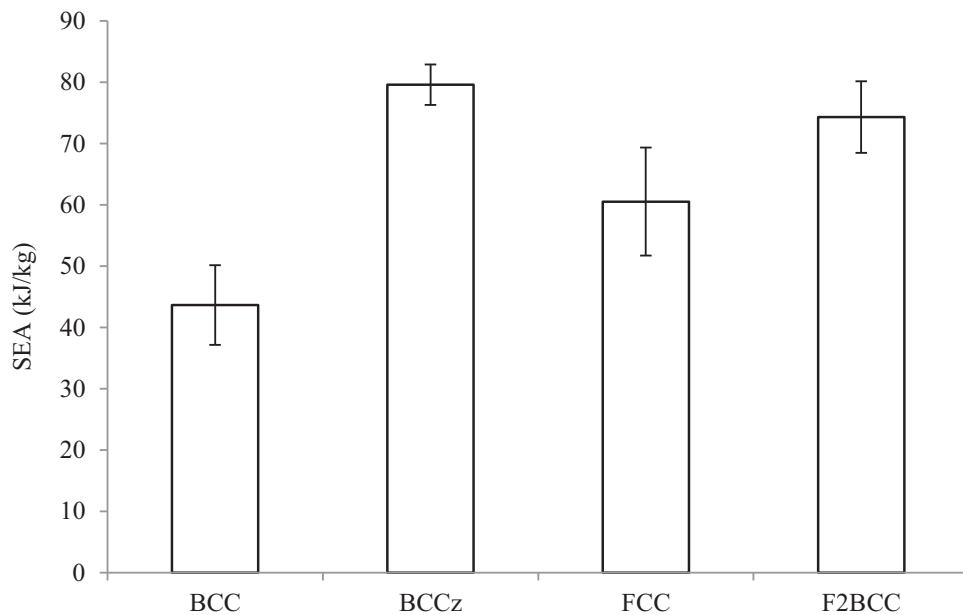


Figure 5.37. Summary of the specific energy absorption values of the four lattice structures.

In the past, many workers have investigated the energy-absorbing capacity of composites, with much of this work focusing on tubular structures. A detailed review of the key findings of many of these studies can be found in the review presented by Jacob *et al* [6]. Concerning carbon fiber reinforced epoxy composites, Hamada *et al* [7] investigated the energy-absorbing characteristics of unidirectional carbon fiber reinforced epoxy tubes (i.e.

a similar fiber orientation to that tested here) and recorded average values of 53 to as high as 110 kJ/kg. A series of impact tests on multidirectional carbon/epoxy by Farley [8] produced SEA values between 60 and 70 kJ/kg, whereas quasi-static tests on bidirectional carbon/epoxy tubes by Thornton yielded values of SEA up to 80 kJ/kg [9]. This evidence suggests that the lattice structures developed here, most particularly (the BCCz and F₂BCC systems) offer potential for use in energy-absorbing structures. It is likely that these values of SEA can be increased further by manufacturing structures with higher values of fiber volume fraction.

5.4 Skin-core Interfacial fracture toughness

This section considers the findings of the interfacial fracture tests undertaken on the modified sandwich structures discussed previously in Section 2.3.

5.4.1 Hybrid GFRP/PET core

A typical load-displacement trace following an interfacial fracture test on a sandwich structure based on a plain unperforated core (Material A) is shown in Figure 5.38. Here, the force increases in a linear fashion up to approximately 200 Newtons, at which point the trace becomes increasingly non-linear up to the peak load value of approximately 310 Newtons. Following the maximum in the load-displacement trace, the force drops suddenly, due to unstable crack propagation along the skin-core interface. An inspection of the failed sample indicated that the crack had propagated through the core close to the skin-core interface to a point beyond the central loading point. The rapid reduction in load highlights the brittle nature of the PET foam. Also included in Figure 5.38 are typical load-displacement traces following tests on Materials B and C.

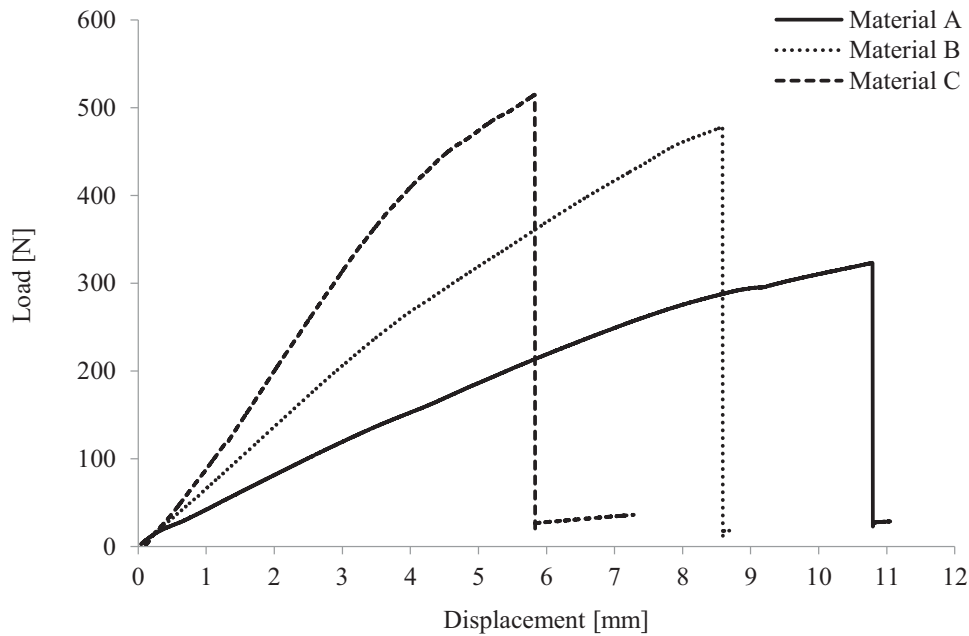


Figure 5.38: Typical load-displacement traces for Materials A, B and C.

Once again, both materials exhibit an initial linear load response, followed by a non-linear response to peak value. Once again, crack growth occurred in an unstable manner at peak load, resulting in the crack propagating rapidly close to the skin-core interface. Differences in the initial slopes of the three samples are due to the fact the initial crack lengths of the three samples were different (50 mm for Material A, 40 mm for Material B and 35 mm for Material C).

Figure 5.39 shows the core and upper skin of failed samples from Materials A, B and C following interfacial fracture testing. The fracture surfaces of the plain sandwich structure, Material A, indicate that the crack propagated at or very close to the skin-core interface. An examination of the composite skins highlights the presence of small amounts of residual PET on the composite. The incorporation of perforations in the core had little effect on the

failure locus, with the crack propagating through the top of the resin columns, Figure 5.39b and Figure 5.39c.

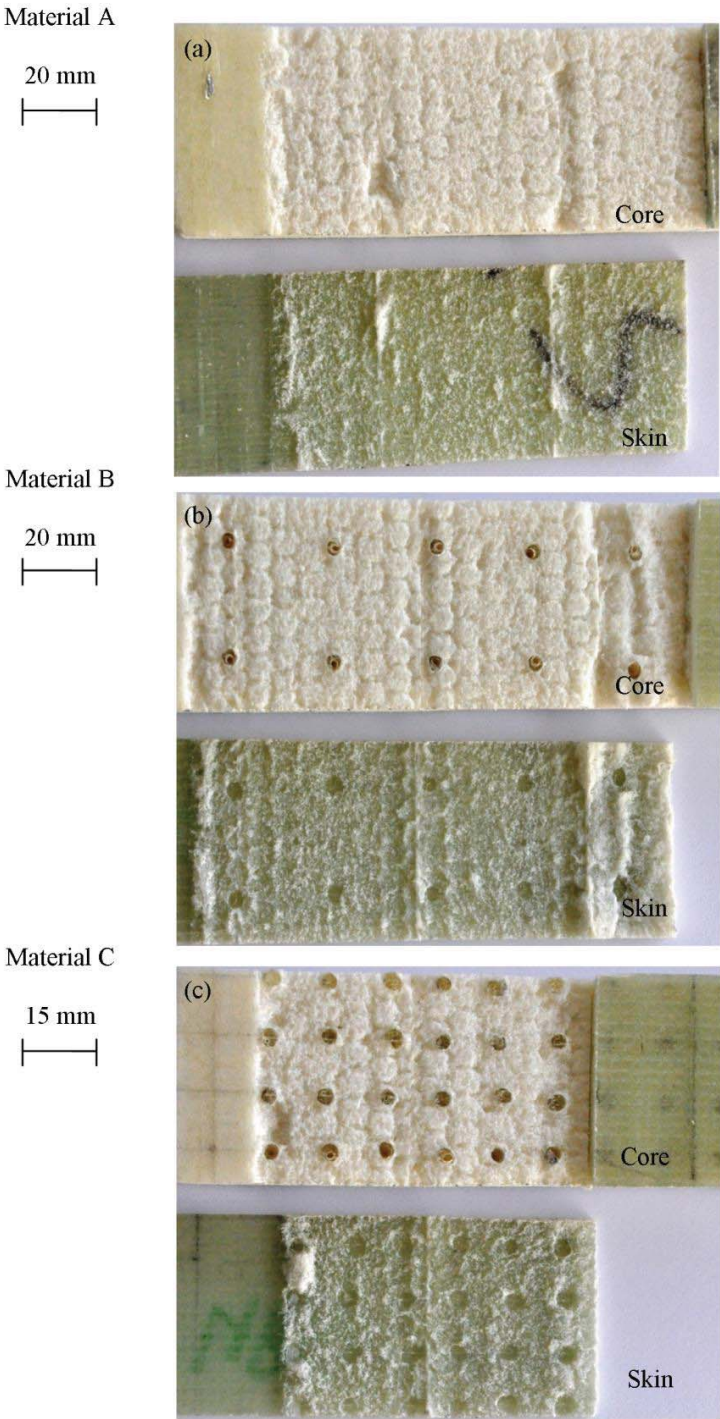


Figure 5.39: Fracture surfaces of Materials A, B, and C following interfacial failure.

Typical load-displacement traces for Materials D-D, E-D and F-D are shown in Figure 5.40. For comparison the load-displacement trace for the plain sandwich structure, Material A, is included in the figure. The three reinforced cores offer similar load-displacement traces. All three samples exhibit an initial failure associated with the crack jumping from the starter defect to the first row of through-thickness reinforcements. At this point, the crack is effectively pinned by the presence of the through-thickness reinforcement, leading to a steady increase and subsequent stabilizing of the applied force.

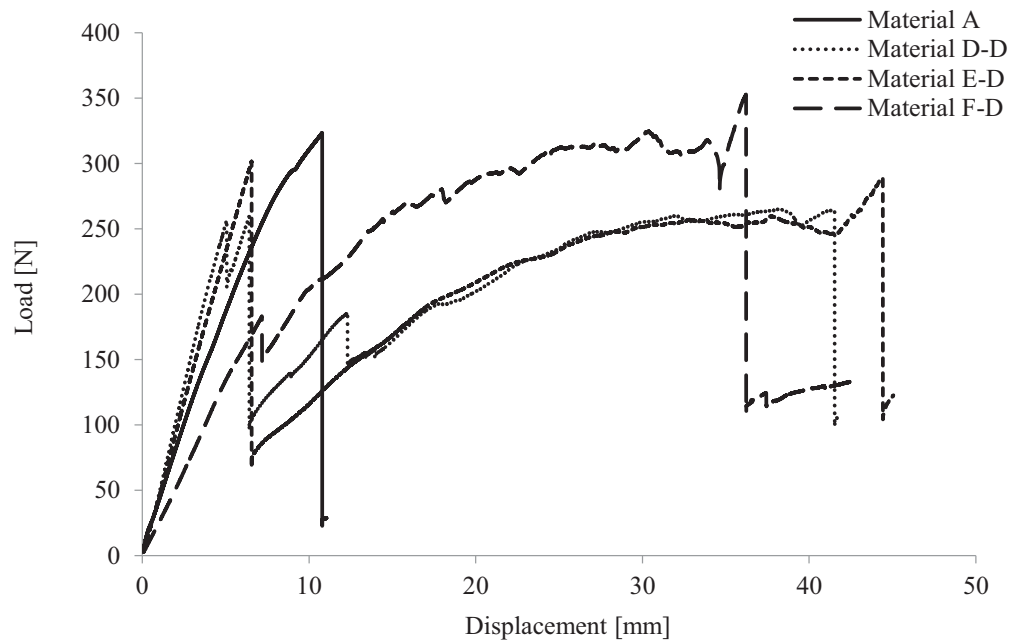


Figure 5.40: Typical load-displacement traces for Materials D-D, E-D and F-D.

This stabilizing process is clearly evident in Figure 5.41, where a photograph of a sample from Material F-D is shown. Here, the presence of large fiber tows linking the skin to the remainder of the sample is clearly evident. It is worth noting that the steady-state force achieved by Material F-D is higher than that associated with Materials D-D and E-D. In all

cases, the load drops abruptly when the vertical reinforcements fracture and the crack jumps ahead to the next line of reinforcements.



Figure 5.41: Photograph of the edge of Material F-D during interfacial fracture testing.

It is worth noting that the load-displacement traces for Materials D-S, E-S and F-S were similar in appearance to those for Materials D-D, E-D and F-D as shown in Figure 5.42.

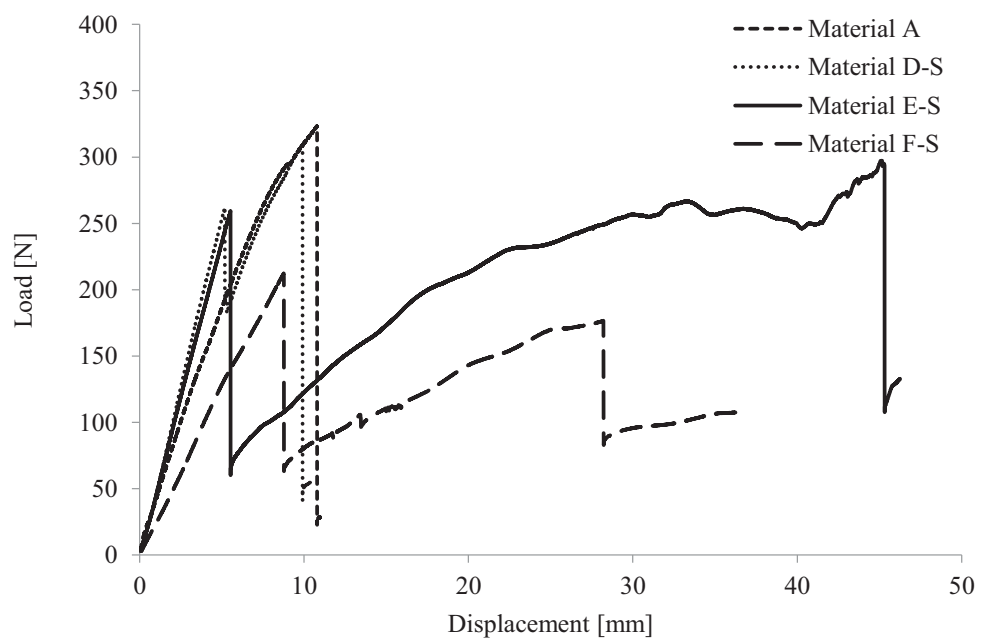


Figure 5.42: Typical load-displacement traces for Materials D-S, E-S and F-S.

The presence of the through-thickness fibers appears to modify the failure characteristics of the sandwich structures, stabilizing the fracture process and subsequently controlling the crack jumping process.

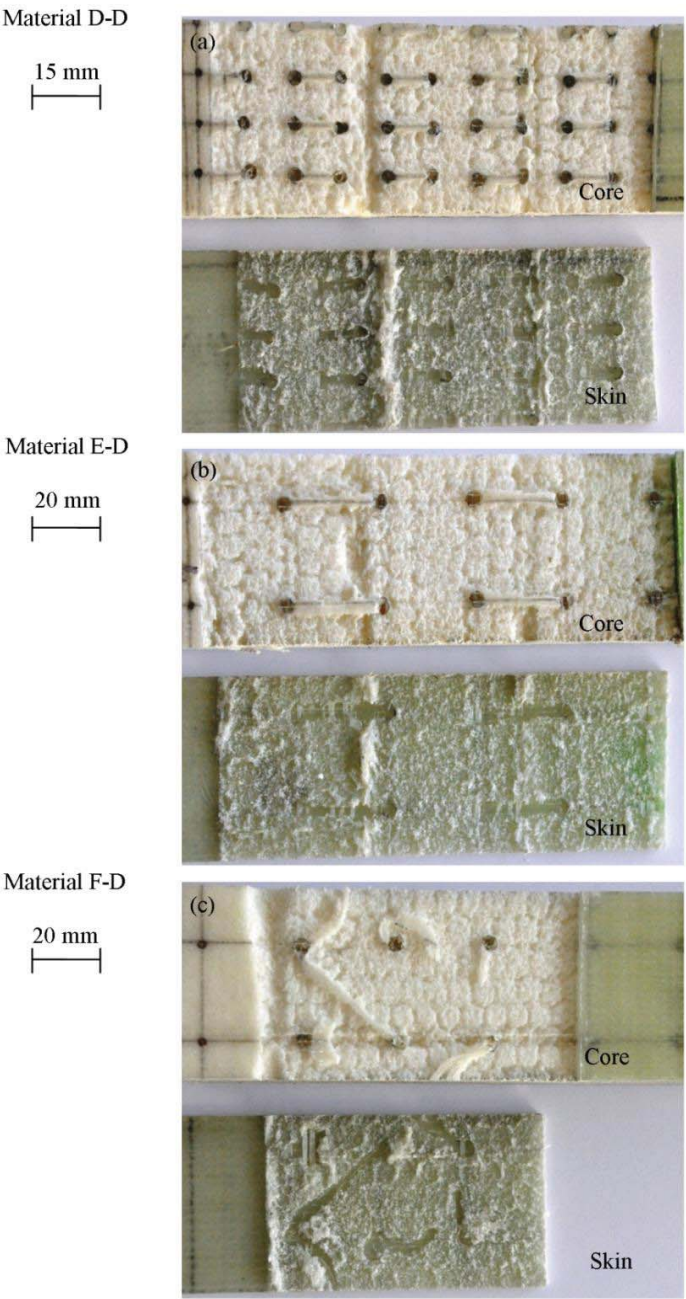


Figure 5.43: Fracture surfaces of Materials D-D, E-D and F-D following interfacial failure.

Figure 5.43 shows the core and upper skin of fractured surfaces of samples from Materials D-D, E-D and F-D following testing. An inspection of the specimens indicates that the primary crack has again propagated at or very close to the skin-core interface. Closer inspection of Materials D-D and E-D indicated that the crack had propagated over the top of the fiber tows that linked the individual perforations, i.e. the reinforcing fibers were not fractured. In contrast, during crack propagation, some of the fibers were fractured in Material F-D, leading to a higher fracture toughness in this system.

Figure 5.44 summarizes the interfacial fracture data for the various sandwich structures tested here. The conventional PET system, Material A, offers an average fracture energy of approximately 675 J/m^2 . Material B, with resin-filled perforations spaced at one inch intervals offers a value of G_c of approximately 857 J/m^2 , some fifty percent higher than the baseline value. Rather surprisingly, Material C, with half inch separations, offers a lower value of 783 J/m^2 , indicating that the higher density of resin columns has not served to enhance the interfacial toughness. It is interesting to note that when core perforations contained fibers, those sandwich structures with a higher perforation density again offered lower values of interfacial fracture toughness. For example, the value of G_c for Material D-S is 849 J/m^2 , compared to 964 J/m^2 for Material E-S. Similarly, the recorded value for Material D-D is 1136 J/m^2 and that for Material E-D is 1364 J/m^2 .

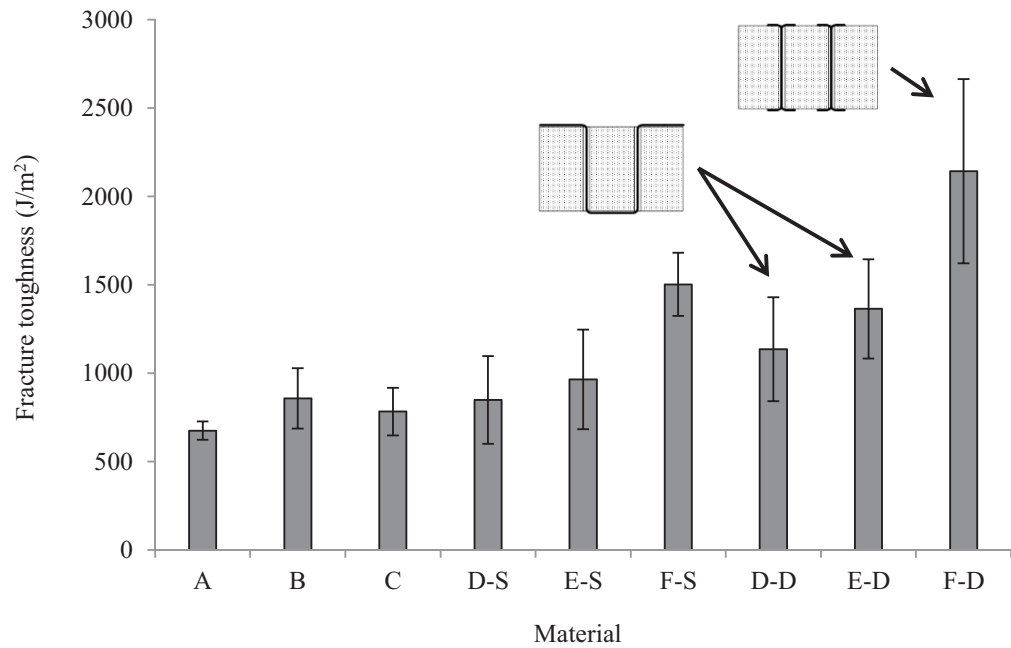


Figure 5.44: Summary of the interfacial fracture properties of the sandwich structures

Finally, Figure 5.44 highlights the benefits gained from spreading the fibers across the top and bottom surfaces of the core. Material F-S offers a value of G_c of approximately 1503 J/m² and Material F-D offers a value of approximately 2143 J/m², similar to values measured following Mode I interlaminar fracture tests on a tough carbon fiber reinforced thermoplastic [10].

References

- [1] L. Y. Mwaikambo, “Tensile properties of alkalised jute fibres”, *BioResources*, vol. 4, pp. 566–588, 2009.
- [2] K. S. Ahmed and S. Vijayaragan, “Elastic property evaluation of jute-glass fibre hybrid composite using experimental and CLT approach”, *Indian J. Eng. Mater. Sci.*, vol. 13, pp. 435, 2006.
- [3] AirBaltekBanova. [Online]. Available: URL <http://www.airexbaltekbanova.com>.
- [4] J. K. Paik, A. K. Thayamballi and G. S. Kim, “The strength characteristics of aluminum honeycomb sandwich panels”, *Thin-walled Struct.*, vol. 35, pp. 205–231, 1999.
- [5] H. S. Lee, S. H. Hong, J. R. Lee and Y. K. Kim, “Mechanical behavior and failure process during compressive and shear deformation of honeycomb composite at elevated temperatures”, *J. Mater. Sci.*, vol. 37, pp. 1265–1272, 2002.
- [6] G. C. Jacob, J. F. Fellers, S. Simunovic and J. M. Starbuck, “Energy absorption in polymer composites for automotive crashworthiness”, *J. Compos. Mater.*, vol. 36, pp. 813–850, 2002.
- [7] H. Hamada, J. C. Coppola, D. Hull, Z. Maekawa and H. Sato, “Comparison of energy absorption of carbon/epoxy and carbon/PEEK composite tubes”, *Composites*, vol. 23, pp. 245–252, 1992.
- [8] G. L. Farley, “The effects of crushing speed on the energy-absorption capability of composite tubes”, *J. Compos. Mater.*, vol. 25, pp. 1314–1329, 1991.
- [9] P. H. Thornton, “Energy absorption in composite structures”, *J. Compos. Mater.*, vol. 13, pp. 247–262, 1979.

- [10] P. Davies, W. Cantwell and H. H. Kausch, “Measurement of Initiation Values of G_{IC} in IM6 / PEEK Composites”, *Compos. Scie. and Techn.*, vol. 35, pp. 301–313, 1989.

Chapter 6: Conclusions and Future Work

6.1 Introduction

The purpose of this work was to develop a suitable manufacturing technique to produce a number of composite lattice core sandwich panel structures and to investigate their mechanical properties. All composite sandwich core specimens were investigated under quasi static compression loading to understand their mechanical response, energy absorption and to highlight the operative failure modes. Analytical models and finite element simulations have been used to predict the initial stiffness and collapse strength of the various lattice configurations under quasi-static compression loading.

6.2 Conclusions

The manufacture of glass fiber reinforced vertical truss structure within a PET foam core sandwich panel using the VARTM process has been investigated. Small cylindrical perforations were introduced into the foam in order to enhance the flow of resin during the infusion process and to create a simple through-thickness lattice structure that would subsequently improve the mechanical properties of the sandwich panel. The manufacturing process was then extended through the development of a lost mold technique for the purpose of eliminating the core, resulting in a free-standing lattice core sandwich structure. The potential of the lost mold technique has been demonstrated by successfully manufacturing and testing of a series of composite lattice core structures with varying degrees of complexity. Composite structures that previously proved to be extremely

challenging to manufacture, have been readily fabricated and these include well known lattice configurations, such as the BCC, BCCz, FCC, F₂BCC and the octet lattice designs. In addition to lattice structures based on a carbon fiber reinforced epoxy composite, the lost mold technique has, for the first time, been used to manufacture a range of environmentally-friendly lattice structures based on jute fibers in an epoxy resin.

Compression tests on samples removed from the hybrid core panels indicated that the presence of the resin-filled (reinforced or plain resin) perforations served to increase the strength of the core. For example, the compression strength of a foam with a simple embedded lattice was up to fifty percent greater than that of the plain core. Compression tests on a vertical lattice based on carbon fiber reinforced epoxy composite have shown that weaving the fibers through the core and across the face sheets greatly improves the lateral stability of the struts, resulting in significant improvements in strength and energy-absorbing capability. Single columns and truss cores based on intermediate and high slenderness ratios failed in a buckling mode at low stresses, with moderate levels of energy absorption. Larger diameter structures, based on higher fiber volume fractions failed in a crushing mode, offering specific energy absorption values above 70 kJ/kg. The mechanical response of the lattice truss cores has been shown to be directly related to the behavior of the individual columns, facilitating predictions of the behavior of larger structures. It has also been shown that it is possible to predict the mechanical response of the individual columns and the associated core using both analytical models and finite element techniques. Additionally, the mechanical properties of the BCC, BCCz, FCC and F₂BCC lattices were predicted using analytical models and the finite element method. Testing has shown that the F₂BCC and BCCz structures offered the highest values of compression

strength when normalized by density, whereas the BCC system offered the lowest values. When normalized by their density, several structures offered mechanical properties that compete favorably with those exhibited by more traditional core materials. The experimentally-determined compression strengths were lower than the values predicted by the finite element and analytical models, due to the presence of defects such as fiber waviness and uneven fiber distribution within the struts and differences in the assumed boundary conditions at the ends of the struts. It has been shown that composite-based lattice structures offer attractive values of specific energy absorption, with values exceeding 75 kJ/kg for both the BCCz and the F₂BCC structures. It is likely that these values can be increased significantly by employing higher values of fiber volume fraction during the manufacturing process, suggesting that these structures could be attractive candidates for use in energy-absorbing structures.

A comparison between the experimental compression strengths of all lattice structures manufactured using the lost mold with available engineering materials is illustrated in Figure 6.1

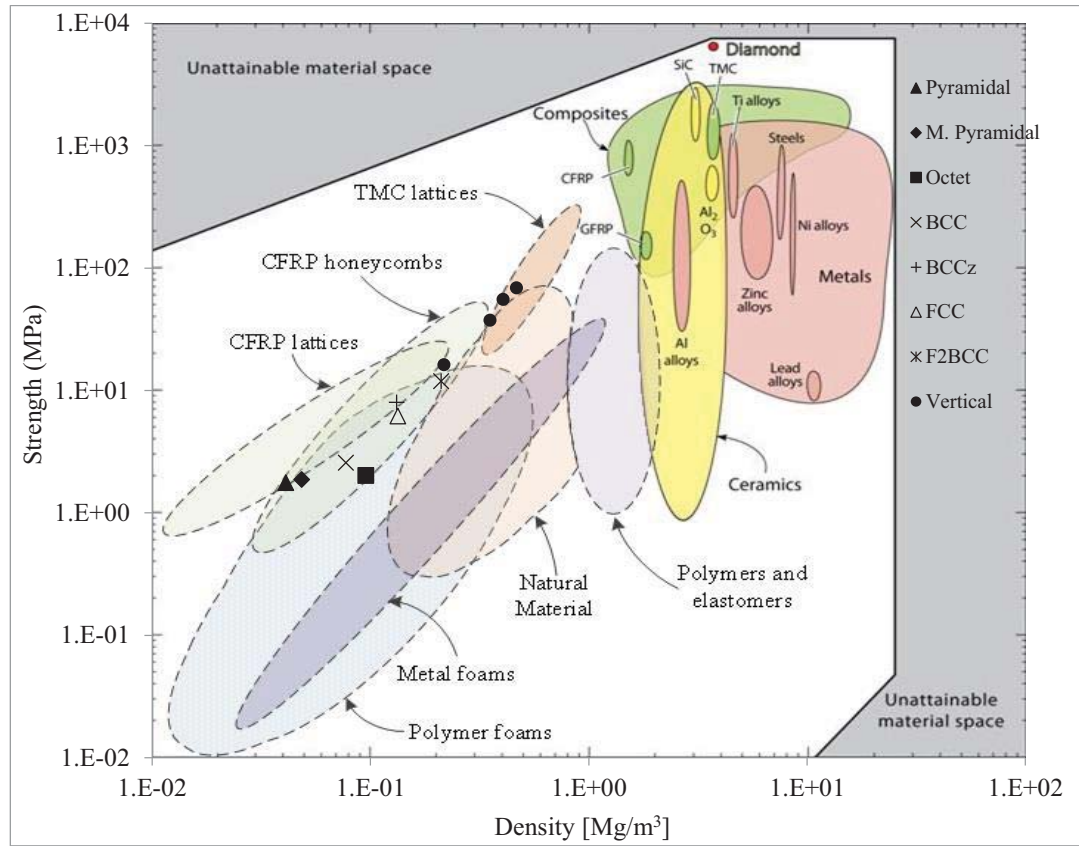


Figure 6.1: An Ashby diagram of strength versus density for engineering materials. The measured compression strengths of the various lattice cores are included [1].

Finally, the skin-core debonding strength of the hybrid core panel was examined in a series of three-point bend test. Introducing small amounts of glass fiber through the core resulted in a 300% increase in interfacial fracture toughness. The presence of the through-thickness fibers served to act as bridges that arrested and subsequently stabilized the crack. It is likely that much larger increases in compression strength and G_c can be achieved by increasing the value of fiber volume fraction above the low values considered here.

6.3 Recommended future work

- Employ higher values of fiber volume fraction during the manufacturing process for improved mechanical properties. The highest fiber volume fraction achieved in this study was 51%, higher values may be achievable. The predicted compression strengths of several lattice structures based on material having a fiber volume fraction of 51% are included in the Ashby plot of strength vs. density for engineering materials. These predictions are based on FE models.

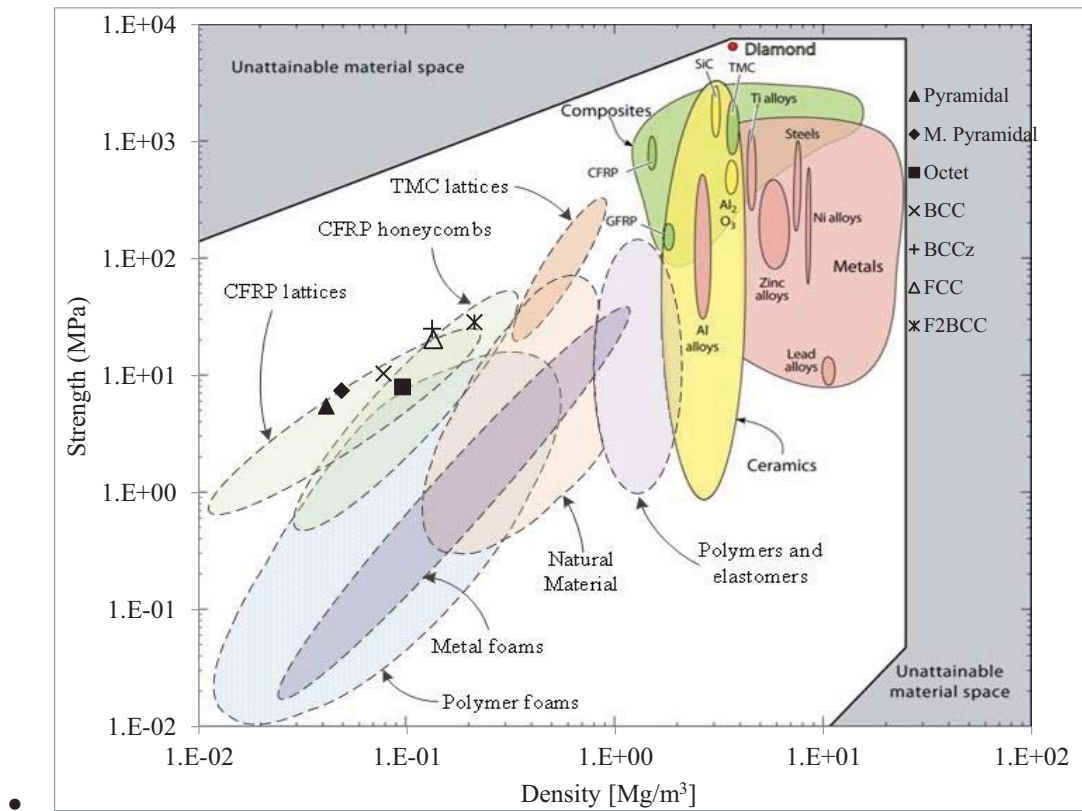


Figure 6.2: An Ashby diagram including the FE model predictions for compression strengths of the various lattice cores made from a material having a 51% fiber volume fraction [1].

The predictions for the initial stiffness are also included in the Ashby plot of elastic modulus vs. density for engineering materials as illustrated in Figure 6.3.

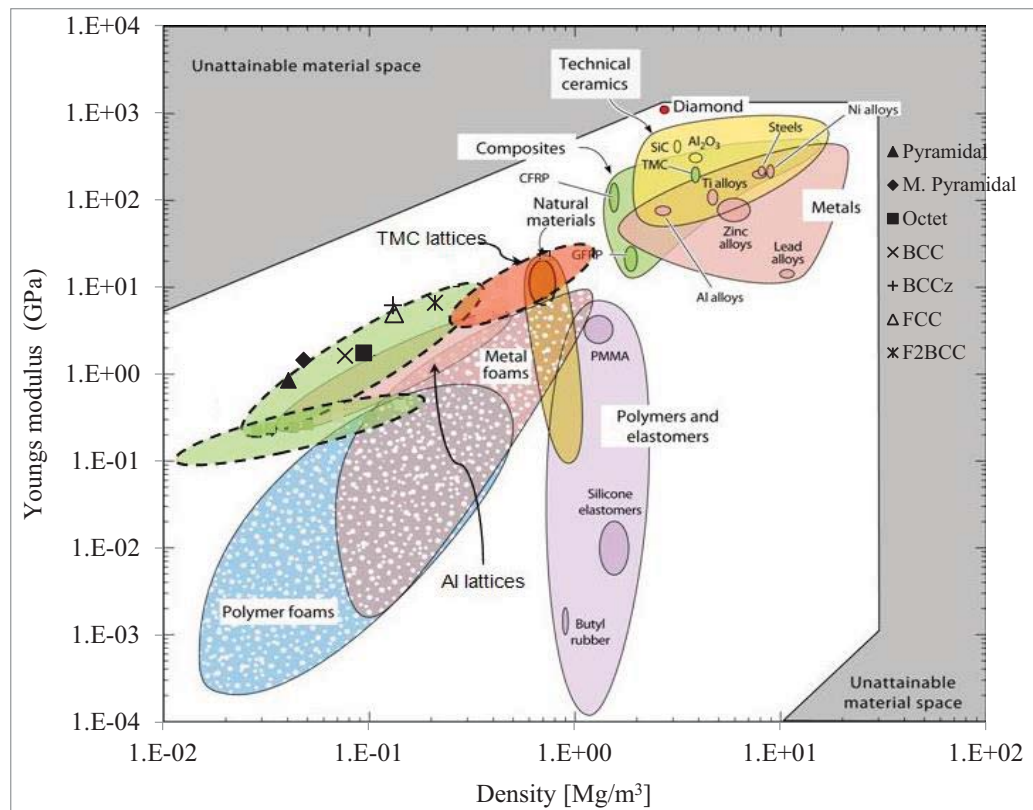


Figure 6.3: An Ashby diagram including the FE model predictions for the elastic modulus of the various lattice cores made from a material having a 51% fiber volume fraction [1].

- Additional testing to be conducted to fully characterize the behavior of the lattice structures under shear, bending and dynamic compression loading conditions. Develop analytical models to for predicting their shear stiffness and strength.
- Each lattice configuration can be optimized for achieving an optimal weight to stiffness/strength ratio.
- The FE models in this work have assumed a perfect bond between the struts within the core and skins. Intersecting struts were also assumed to be perfectly bonded.

More detailed modeling may be achieved using solid and cohesive zone elements to model these strut/strut and strut/skin interfaces.

- More efficient use of the material can be achieved by using hollow cylindrical struts. The lost mold technique can be extended to manufacture an all-composite lattice structure based on hollow cylindrical struts for subsequent testing. Testing to be carried out to fully characterize the behavior honeycomb cores manufactured using the lost mold technique.
- Fiber waviness and misorientation in the longitudinal direction within the individual strut may be introduced during the threading stage or during the infusion process. This may reduce the stiffness and strength properties of the structure. Optical micrographs of the cross section of strut at multiple locations along its length can shed light on how the fiber distribution changes or remains the same along the struts.
- Ultimate failure occurs at peak stress conditions just prior to the collapse of the lattice structure. Nondestructive evaluation such as ultrasound can be used to provide useful information on damage initiation and propagation for the composite lattice structures.

References

- [1] Wadley Research Group. *Ultralight Cellular Materials*. [Online]. Available: URL <http://www.virginia.edu/ms/research/wadley/cellular-materials.html>.

Appendix A

Table A.1: Summary of carbon fiber composite materials used in this study (a) elastic properties and (b) strength characteristics.

Symbol	$V_f = 3.5\%$	$V_f = 7\%$	$V_f = 14\%$	$V_f = 28\%$	$V_f = 42\%$	$V_f = 51\%$	Property
E_1	11 GPa	18 GPa	30 GPa	60 GPa	88 GPa	108 GPa	Elastic modulus in the longitudinal direction (e_1)
E_2	3 GPa	4 GPa	4 GPa	4 GPa	5 GPa	6 GPa	Elastic modulus in the transverse direction (e_2)
E_3	3 GPa	4 GPa	4 GPa	4 GPa	5 GPa	6 GPa	Elastic modulus in the transverse direction (e_3)
G_{12}, G_{13}	1.3 GPa	1.4 GPa	1.4 GPa	1.7 GPa	2.1 GPa	2.5 GPa	Axial shear modulus
G_{23}	1.3 GPa	1.3 GPa	1.4 GPa	1.6 GPa	1.9 GPa	2 GPa	Through-thickness shear modulus
ν_{12}, ν_{13}	0.35	0.35	0.34	0.32	0.30	0.28	Axial Poisson's ratio
ν_{23}	0.36	0.36	0.35	0.34	0.34	0.33	Through-thickness Poisson's ratio

(a)

Symbol	$V_f = 3.5\%$	$V_f = 7\%$	$V_f = 14\%$	$V_f = 28\%$	$V_f = 42\%$	$V_f = 51\%$	Property
X^T	90 MPa*	125 MPa*	200 MPa*	250 MPa*	350 MPa*	400 MPa*	Longitudinal tensile strength
X^C	80 MPa*	105 MPa*	155 MPa	210 MPa	315 MPa	355 MPa	Longitudinal compressive strength
Y^T	50 MPa*	50 MPa*	50 MPa*	65 MPa*	80 MPa*	90 MPa*	Transverse tensile strength
Y^C	50 MPa*	50 MPa*	50 MPa*	65 MPa*	80 MPa*	90 MPa*	Transverse compressive strength
S^L	3 MPa*	3 MPa*	5 MPa*	6 MPa*	7 MPa*	8 MPa*	Transverse shear strength
S^T	8 MPa*	8 MPa*	10 MPa*	12 MPa*	14 MPa*	15 MPa*	Longitudinal shear strength

(b)

Appendix B

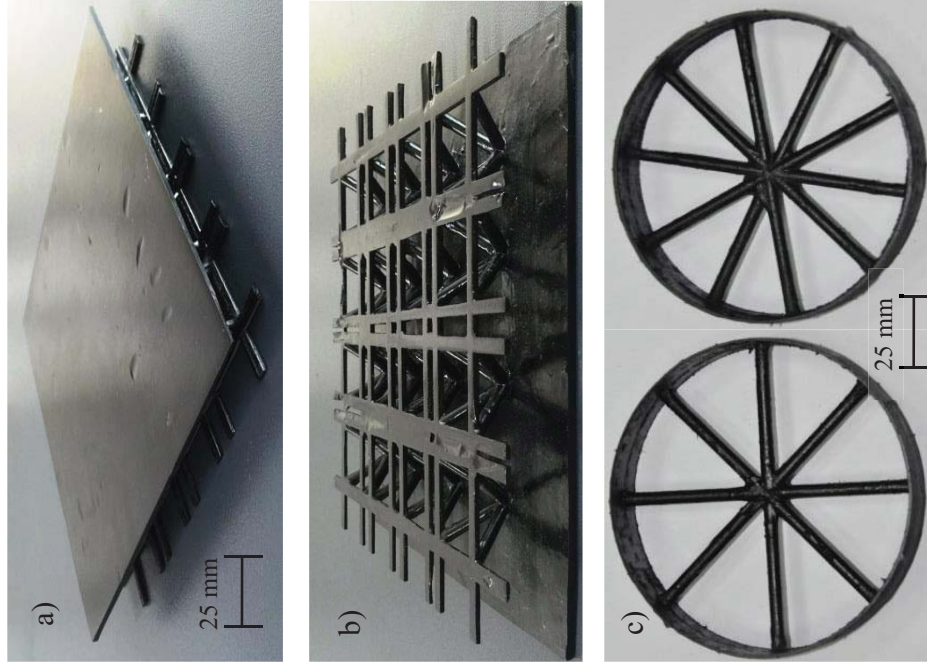


Figure B.1: a) Top view of a single skin sandwich structure (S4), b) skin free side of the S4 structure, c) lattice wheel d) Natural fiber reinforced airfoil and Carbon fiber reinforced airfoil.

Appendix C

Manufacture of an airfoil using the lost-mold technique

The lost mold technique has been used to manufacture a natural fiber reinforced airfoil structures as shown in Figure B.1d in which the core of the structure is based on a vertical truss configuration. Using the same procedure a carbon fiber reinforced airofoil was also manufactured. The airofoil core is reinforced with vertical column lattice as illustrated in Figure B.1e. The process involved a wax block that was initially manufactured by pouring liquid wax in a 500 x 200 x 200 mm mold. After cooling, the block was machined using a CNC milling machine to create a solid 450 mm long NACA 15 airfoil. Holes were drilled in the airfoil with 10 x 3 rows and 4 mm diameter. Two strands of jute fibers were passed through the holes in a continuous fashion. Three layers of jute fiber skins were added over the airfoil structure. The prepared mold was then vacuum bagged and injected using Gurit's Prime 20 Epoxy resin with slow hardener. These airfoils were infused in a ten minute cycle period during which time the resin filled both the skins and vertical columns. The flow front was developed such that the resin flow was from top to bottom facesheets, passing through all vertical columns during the process (Figure C.1). Following curing, the wax mold was removed by heating the structure in an air-circulating oven. Based on these observations, it is believed that this simple lost mold technique can be used to manufacture a wide range of lattice structures based on varying degrees of complexity.



Figure C.1: Photographs showing (a) Jute fibers passing through the holes in the wax mold in a continuous fashion, (b) Natural fiber sheets forming the airofoil skin placed around the mold, (c) airofoil stack sealed in a vacuum bag in preparation for the infusion process (d) and flow front on one side of the airfoil during the VARTM process.

Infusion Process Simulation using PAM-RTM

PAM-RTM is a finite element software that simulates the flow of liquid resin into a reinforcement. Once the mesh is imported, the software requires the input of resin properties including viscosity and density along with the reinforcing fibrous material permeability values and orientation to carry out the analysis. Analysis using PAM-RTM enables the estimation of fill time duration as shown below for the airfoil structure. The structure is a carbon fiber reinforced airfoil structure as shown in Figure B.1e. The laboratory measured fill time was around 26 minutes which is in good agreement with simulated results.

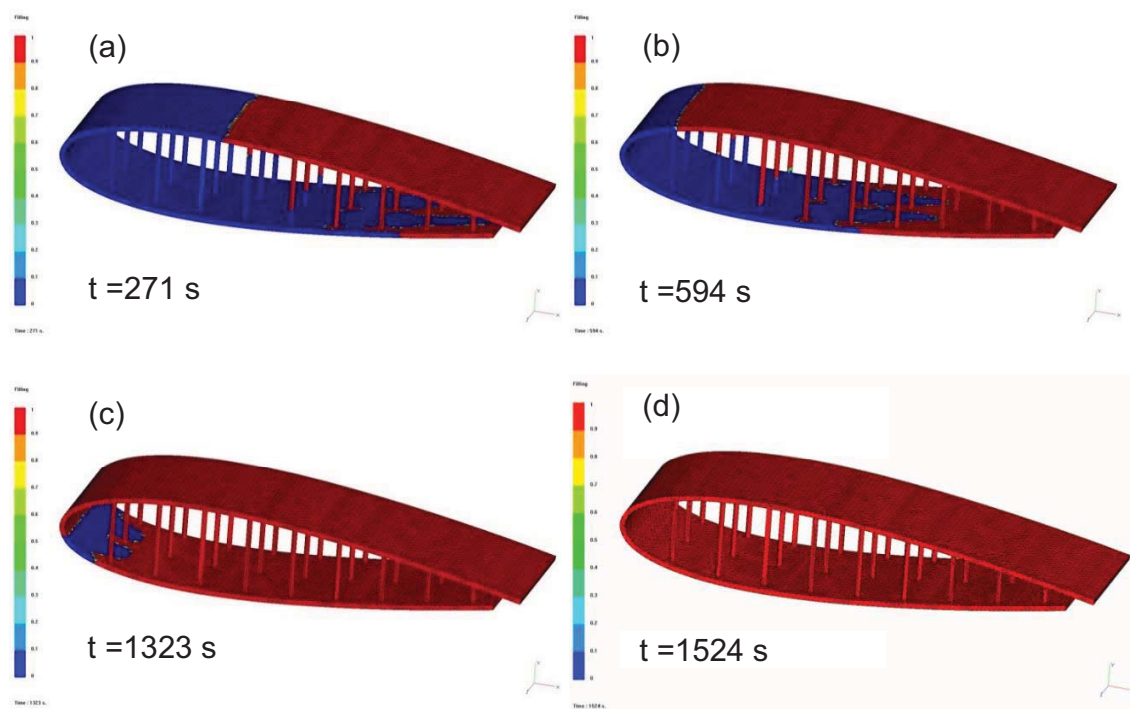


Figure C.2: Snapshots showing the progression of resin through the reinforcement with the blue and red colors indicating dry and resin rich regions respectively.

YOUR KNOWLEDGE HAS VALUE



- We will publish your bachelor's and master's thesis, essays and papers
- Your own eBook and book - sold worldwide in all relevant shops
- Earn money with each sale

Upload your text at www.GRIN.com
and publish for free

